

Investigating Irradiation Damage in Tungsten for Fusion Power

SUCHANDRIMA DAS

Mansfield College

under the supervision of

Prof. Felix Hofmann

This thesis has been submitted to the University of Oxford

for the degree of Doctor of Philosophy

in the Department of Engineering Science

July 2019

Abstract

Tungsten is the front-runner material for armour components in future fusion reactors. In-service, irradiation with fusion neutrons will generate displacement cascades, leaving behind lattice defects. Helium, injected from the plasma and produced by transmutation, aggravates damage by increasing defect retention. These effects can be mimicked using helium-ion-implantation.

Helium-implantation-induced defects are probed here by measuring the lattice strains they cause, using energy- and depth-resolved synchrotron X-ray micro-diffraction. An increase in helium dose from 300 to 3000 appm increases volumetric strain ~ 2.4 times, indicating a ~ 3 times higher defect retention per injected helium at low helium doses. This suggests defect retention is not a simple function of implanted helium dose, but strongly depends on material composition and presence of impurities.

The effect of helium-defects on deformation behaviour is examined by comparing spherical nano-indents in unimplanted and helium-implanted (W-3000He) regions of a <001> tungsten grain. Helium-implantation increases hardness and causes large pile-ups. 3D-resolved X-ray micro-diffraction shows a more confined plastic zone under indents in W-3000He. Localised deformation and slip-channel formation is confirmed through high resolution electron backscatter diffraction and transmission electron microscopy on cross-section lift-outs from indents in W-3000He. Together, the observations suggest a large initial hardening due to helium-defects, followed by localised defect removal and subsequent strain softening.

The hypothesis is examined by implementing it in a crystal plasticity finite element (CPFE) formulation, simulating nano-indentation in <001>-W-3000He. With only one fitting parameter the simulation captures the localised large pile-up and predicts confined fields of lattice distortions beneath indents in quantitative agreement with experimental measurements. Indents in <011> and <111> grains of W-3000He show little pile-up. The same CPFE model captures this orientation dependence of pile-up, suggesting that the underlying strain localisation is orientation-independent and that changes in pile-up arise due to the relative orientations of slip systems, sample surface, and the indenter.

These advances in the understanding of irradiation damage in tungsten, obtained through experimental and modelling techniques, inspire confidence in the feasibility of building predictive models from experimental observations, which can account for irradiation-induced changes when estimating armour component lifetime and in-service performance. This is key for the design of future fusion reactors.

Acknowledgements

This dissertation is dedicated to my father without whose many sacrifices and relentless support in every step of the way, I would not be where I am today. I am deeply grateful to my mother and every member of my family for their unwavering love and encouragement. Without their blessings and their confidence in me, I would not have been able to pursue this academic journey thousands of miles away from home.

I would like to express my whole-hearted thanks to my supervisor Prof. Felix Hofmann, for his patient and diligent guidance throughout the project. Working with him has been a thoroughly enjoyable and enriching experience. Without his help, advice and optimism this project could not have been carried out so smoothly. I certainly cannot think of a better guide for this testing PhD journey.

I am thankful to Dr. Edmund Tarleton for his guidance and inputs at many stages of the project especially for advising on the computational modelling aspect of the project. I am also grateful to Dr. Sergei Dudarev for always showing great interest in my work and contributing with useful discussions, Prof. Alan Cocks and Prof. Alexander Korsunsky for providing insightful advice while examining the progress of my PhD.

I am thankful to my colleagues and office-mates at the Engineering Department for always ensuring an amiable and fun work environment. In particular I am grateful to Marzena Tkaczyk, Elsiddig Elmukashfi, Kurien Parel and Hongbing Yu whose friendship and support have always helped to keep the stress at bay. I would also like to take this opportunity to express my thanks to a number of people in Oxford and elsewhere who have helped and contributed to this project: Prof. David Armstrong, Abdallah Reza, Nicholas Phillips, Robert Paynter, Kalin

Dragnevski, Yevhen Zayachuk, Slava Kuksenko, Anna Kareer, Bo-Shiuan Li, Wenjun Liu, Ruqing Xu and Jon Tischler.

I would also like to thank the staff and my friends from Mansfield College, who have made my stay at Oxford greatly enjoyable.

I would like to acknowledge the funding I received from Leverhulme Trust (RPG-2016-190), the travel grants awarded by Mansfield College and the Engineering Science Department and the beam time allocations at APS at Argonne National Lab, a U.S. Department of Energy (DOE) Office of Science User Facility operated for the DOE Office of Science by Argonne National Laboratory under Contract No. DE-AC02-06CH11357. The David Cockayne Centre for Electron Microscopy, Department of Materials, Oxford, and the LIMA lab, Department of Engineering Science, Oxford were used for the microscopy carried out in this project.

Glossary of abbreviations

AFM	Atomic Force Microscopy
APS	Advanced Photon Source
BCC	Body Centred Cubic
BDTT	Brittle-to-Ductile Transition Temperature
CFC	Carbon Fibre Composite
CPFE-M	Crystal Plasticity Finite Element Modelling
DAXM	Differential Aperture X-ray Microscopy
DEMO	DEMOnstration Reactor
DFT	Density Functional Theory
DPA	Displacements per Atom
FCC	Face Centred Cubic
FEM	Finite Element Modelling
FIB	Focussed Ion Beam
FPY	Full Power Year
FWHM	Full Width at Half Maximum
GND	Geometrically Necessary Dislocations
HFIR	High-Flux Isotope Reactor
HR-EBSD	High Resolution Electron Backscatter Diffraction
ITER	International Thermonuclear Experimental Reactor
JET	Joint European Torus
KB	Kirkpatrick-Baez (Focussing Mirrors)
MATLAB	MATrix LABoratory
PKA	Primary Knock-On Atom
SIA	Self-Interstitial Atom
SEM	Scanning Electron Microscopy
SRIM	Stopping Range of Ions in Matter
SSD	Statistically Stored Dislocations
TEM	Transmission Electron Microscopy

Contents

1.Introduction 1

2.Scientific Background & Methods 7

2.1. Tungsten for fusion 7

2.1.1. Choice of armour materials 7

2.1.2. Tungsten as an engineering material 9

2.1.3. Radiation damage in tungsten 12

2.2. Experimental techniques 28

2.2.1. Nano-indentation 28

2.2.2. X-ray diffraction 32

2.2.3. High-resolution EBSD 37

2.3. Computational Modelling 42

2.3.1. Crystal plasticity 43

3.Probing helium-induced defects through lattice strain measurements 48

3.1. Abstract 48

3.2. Introduction 49

3.3. Experimental details 53

3.3.1. Sample preparation 53

3.3.2. Ion implantation 53

3.3.3. X-ray micro-diffraction measurements 54

3.3.4. Analysis of X-ray diffraction measurements 56

3.3.5. Samples chosen for analysis 59

3.4. Results & Discussion 60

3.5. Implications for Reactor Design 71

3.6. Conclusions 72

4.Effect of helium on deformation behaviour of tungsten 73

4.1. Abstract 73
4.2. Introduction 74
4.3. Sample preparation & ion-implantation 75
4.4. Nano-indentation 76
4.5. SEM micrographs of indents 78
4.6. Laue measurements of lattice distortions 80
5. CPFE modelling of helium-damage in tungsten 85
5.1. Consistent determination of GND: CPFE & Diffraction study in tungsten 86
5.1.1. Abstract 86
5.1.2. Introduction 87
5.1.3. Theoretical Background 92
5.1.3.1. Computing the Curl of a second-order tensor 92
5.1.3.2. Calculation of dislocation tensor 93
5.1.3.3. Calculation of GND density 103
5.1.4. Materials and Methods 105
5.1.4.1. Micro-beam Laue diffraction 105
5.1.4.2. 3D CPFE Model 106
5.1.5. Results and Discussion 113
5.1.5.1. Residual elastic rotations and strains 113
5.1.5.2. Dislocation tensor computation 121
5.1.5.3. GND density computation 125
5.1.6. Conclusions 132
5.2. CPFE formulation for helium-implanted tungsten 134
5.2.1. Abstract 134
5.2.2. Introduction 135
5.2.3. Methods 138
5.2.3.1. Sample Preparation 138

5.2.3.2. Helium Implantation 138
5.2.3.3. Nano-Indentation, AFM & SEM 139
5.2.3.4. Micro-beam Laue diffraction 139
5.2.3.5. FIB Lift-out, HR-EBSD & TEM 140
5.2.3.6. CPFE Modelling 141
5.2.4. Results & Discussion 147
5.2.4.1. Load-displacement curves, indent morphology and defect structures 147
5.2.4.2. Surface morphology of indents: AFM vs CPFE 149
5.2.4.3. Residual elastic lattice rotations 151
5.2.4.4. Residual elastic lattice strains 155
5.2.4.5. GND Density 157
5.2.5. Conclusions 160
5.3. Orientation-dependent deformation of helium-implanted tungsten 162
5.3.1. Abstract 162
5.3.2. Introduction 163
5.1.3. Sample preparation 165
5.3.4. Nano-indentation and AFM 167
5.3.5. CPFE formulation and comparison with experiments 170
6. Conclusions 178
Appendices 185
A. Ion energies and fluence for helium-implantation 185
B. Supplementary materials for Chapter 3 186
EBSD maps of samples 186
Depth resolved strain measurements 186
C. Supplementary materials for Chapter 4 189
Why we need to probe beneath indents? 189
Detailed map of evolving lattice rotations 190

Deviatoric strain on XZ cross-section 191
D. Schematic of lattice rotations during indentation 193
E. Supplementary materials for Chapter 5.1 194
Detailed derivation of three curl definitions 194
Derivation of relation between the three curl definitions 195
Stokes' theorem 198
Values of UMAT parameters 199
F. Use of the effective modulus in indentation 200
G. Burgers' vector & line direction for GND calculation 201
H. Supplementary materials for Chapter 5.2 202
Computation of stress boundary conditions 202
Values of UMAT parameters 203
Values for $\boldsymbol{\rho SSD}$ and $\boldsymbol{\rho m}$ 204
CPFE vs Continuum-mode FEM 204
Line plots from CPFE and Laue strain measurements 205
I. Supplementary materials for Chapter 5.3 206
SEM micrographs of nano-indents 206
CPFE mesh 208
References 209

Chapter 1

Introduction

The predicted rise in global population is anticipated to increase the current energy consumption levels by 48% by 2040 [1]. A large part of future energy needs will have to be met by non-fossil-fuel sources. Renewable sources such as wind, solar, etc. depend on varying environmental conditions and cannot guarantee constant production. Moreover, there are technological and financial difficulties in storing the energy generated from these sources. To ensure regular supply of baseload or to meet unanticipated energy demands, foreseeable and invariant energy sources are needed. Nuclear fusion promises to be such an efficient and reliable energy source. In contrast with fission, it does not face the problems of generating long term radioactive waste, limited fuel supply and lack of public and political tolerance.

However, before fusion reactors can be in full operation and commercially viable, they still require substantial research, particularly in areas of plasma physics, and reactor materials. The largest tokamak currently in operation, the Joint European Torus (JET), has shown the successful operation of a fusion reactor with a deuterium-tritium fuel mixture [2] given by

$$^{2}D + {}^{3}T \rightarrow {}^{4}He + n^{0} \qquad (1.1)$$

JET is a small scale reactor; primarily build to study the behaviour of the plasma under fusion conditions. A new fusion energy project, the ITER, with 10 times the plasma volume of JET, is now being built [3]. The ambitious ITER project, involving several countries,

aims to begin operation in 2035, and is being designed to be the first fusion reactor capable of producing net energy.

The fusion reaction (Eq. 1.1) releases 17.6 MeV of fusion energy, split between a neutron (14.1 MeV) and a charged ^{4}He nucleus [4], [5]. The neutrons generated will be absorbed in a blanket containing lithium. This inner surface or "first wall" is where 85% of the fusion power is deposited. Reaction between lithium and neutrons produce tritium [6], which is re-cycled as input fuel for the reactor. A coolant flowing through the blanket (Figure 1.1) collects the heat energy, to produce electricity by conventional methods. Impurities created during operation, such as eroded particles from the reactor and helium (fusion reaction waste product), must be purged off, in order to sustain the fusion reaction. The divertor (Figure 1.1), located at the bottom of the vacuum vessel, removes these unwanted ions [3] and thus has to sustain the highest surface heat load. It is responsible for exhausting ~ 15% of total fusion power and may experience heat load of 10 – 20 MW/m^2 [6].

The plasma-facing armour components will be exposed not only to high temperatures (> 900 °C) and high heat loads, but also bombardment by the high-energy neutrons [6]. Interaction of the neutrons with the crystal lattice generates collision cascades and defect accumulation in the material [7]. Also it can cause transmutation i.e. the formation of foreign elements (for example in tungsten armour material, rhenium, osmium, tantalum, and even gaseous elements such as hydrogen or helium can be formed [8], [9]). Hydrogen and helium also enter the material through plasma-facing surfaces, exposed to large fluence of both elements [10], [11]. At the anticipated operating temperatures, interstitial mobility of these gasses is high, allowing them to diffuse to defects, cracks or grain boundaries, causing embrittlement and hardening [12].

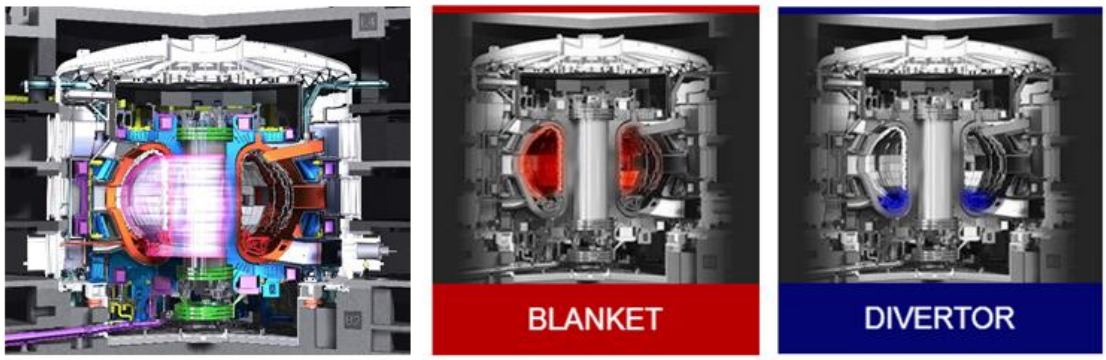


Figure 1.1 – Schematic representation of the Tokamak reactor being build (ITER) highlighting the blanket and the divertor modules [3].

To survive such extreme operating conditions, component materials must possess some key features. To begin with, they must be of low activation type to limit radioactive waste production [13]. Secondly, the material must have an operational temperature window suited for the reactor part. Properties such as thermal load capacity, thermal conductivity, and recrystallisation govern the upper temperature limit, whilst the lower temperature limit is mostly determined by brittleness or irradiation damage considerations [6]. Other deciding factors include the tritium retention rate and the sputtering rate i.e. rate of plasma contamination with eroded materials. Finally the material must be resilient and withstand effects of radiation damage.

Tungsten is a promising candidate material for plasma facing armour due to its high melting point, its strength at high temperatures and low sputtering yield [6], [14], [15]. However, challenges arise from its low fracture toughness, high brittle to ductile transition temperature (BDTT) and poor machinability [16]. Moreover, intense radiation in-service can lower the component lifetime. For a commercially viable fusion reactor the divertor armour material and the first wall component should have a lifetime of at least two and five full-power years respectively [9]. Irradiation by neutrons and helium has the potential to

become life limiting for the armour material, with significant economic consequences for fusion power.

To develop new strategies for improving the irradiation resistance of tungsten components, fundamental understanding of defect generation and property evolution in tungsten is urgently required. This thesis contributes to the development of this understanding, by performing a detailed characterisation of helium irradiation damage in tungsten. As the conditions of the fusion reactor cannot be recreated yet, a surrogate model of helium-ion implanted tungsten is studied using a combination of experimental and finite element modelling techniques. Mechanistic insights about the implanted tungsten layer and associated microstructural alterations are gained by one of the two following ways:

1. Measurement of the lattice distortion induced in the implanted layer

2. Comparative analysis of plastic deformation fields around nano-indents made in implanted and unimplanted tungsten samples.

The sub-micron resolution strain analysis and the examination of the lattice distortions around nano-indents are done using the following, complementary techniques: X-ray micro-diffraction, strain gradient crystal plasticity finite element modelling (CPFE) and high-resolution electron backscatter diffraction (HR-EBSD).

The thesis is arranged into the following chapters in journal publication format (published or in pre-print form) except chapter 2.

Chapter 2 gives an overview of the literature, concentrating on the following topics: choice of armour materials, tungsten as an engineering material, defect

microstructure of irradiated tungsten, alteration in properties of irradiated tungsten, experimental methods (Laue- diffraction, HR-EBSD, nano-indentation) and CPFE.

The investigation on helium-irradiation damage in tungsten is begun in **Chapter 3**, by probing helium-implantation induced defects by measuring the lattice strains they cause. Eigenstrain in helium-implanted tungsten and tungsten-rhenium alloys, is measured using high-resolution mono-beam X-ray diffraction. Observations are discussed in light of helium-induced lattice swelling and defect retention and its variation with dose and presence of rhenium.

In **Chapter 4**, effect of the helium defects on tungsten's deformation behaviour is explored. Alterations in lattice distortions around nano-indents, induced by 3000 appm helium implantation in <001>-oriented tungsten single crystal (W-3000He-<001>), are examined through white beam X-ray micro-diffraction. The chapter ends with a proposed hypothesis to explain the defect-dislocation interaction mechanism underlying the observations in W-3000He-<001>.

Chapter 5, explores this hypothesis using a CPFE formulation which captures the proposed mechanism of defect-dislocation interaction and simulates indentation of W-3000He-<001>. The chapter is split into three sections. The chapter begins by introducing crystal plasticity simulation of indentation in pure tungsten in **Section 5.1**. Predictions of the CPFE model are examined by direct comparison with corresponding observations from Laue diffraction. In this context, fundamental principles associated with the analysis of plastic deformation field, such as computation of fields of lattice distortions and geometrically necessary dislocation (GND) density, including "curl" operation and optimisation techniques for GND computation are discussed in detail. In **Section 5.2**, the CPFE formulation for helium-implanted tungsten is developed. The formulation is assessed

by directly comparing predictions for indentation of W-3000He-<001> with corresponding experimental observations, from HR-EBSD and X-ray diffraction. Finally in **Section 5.3**, the CPFE simulation and experimental techniques are used to examine the orientation-dependence in indentation response of W-3000He.

Every chapter includes a discussion of the corresponding observations. The thesis conclusions are provided in **Chapter 6.** They draw together the most important insights from each chapter, and present them in the context of advances made in the characterisation of radiation damage in tungsten and assessment of the anticipated performance of tungsten armour components.

Chapter 2

Scientific Background & Methods

This chapter provides an overview of the literature on characterising irradiation damage in tungsten and the experimental and modelling techniques relevant to this thesis. Section 2.1 justifies the choice of tungsten as an armour material, and the strengths and limitations of its engineering properties. This section also reviews past studies, examining radiation damage in tungsten, as induced by neutrons and gaseous elements like hydrogen and helium. Section 2.2 reviews experimental techniques used in this project, namely nano-indentation, synchrotron X-ray micro-diffraction and HR-EBSD. The chapter ends with Section 2.3 reviewing the fundamental theory and state of the art of CPFE formulations used for engineering applications.

2.1. Tungsten for fusion

2.1.1. Choice of armour materials

Numerous elements have been considered for fusion energy applications, such as C, Si, W, V, Ta, Cr, and Fe. Given the high temperature that the plasma facing material has to withstand, two materials may be suitable: SiC-CFC (carbon-fibre composites) with a window of ~ 650-950 ^{o}C and tungsten with a window of 800-1300 ^{o}C [17].

Of the two, the CFC materials, have pronounced advantages in terms of high thermal conductivity (200-500 W/mK), minimal plasma contamination (12% allowable plasma concentration) and a capability to withstand cyclic thermal loading of up to 19 MW/m^2 [18]. However, their excellent thermal conductivity reduces to about 50 W/mK

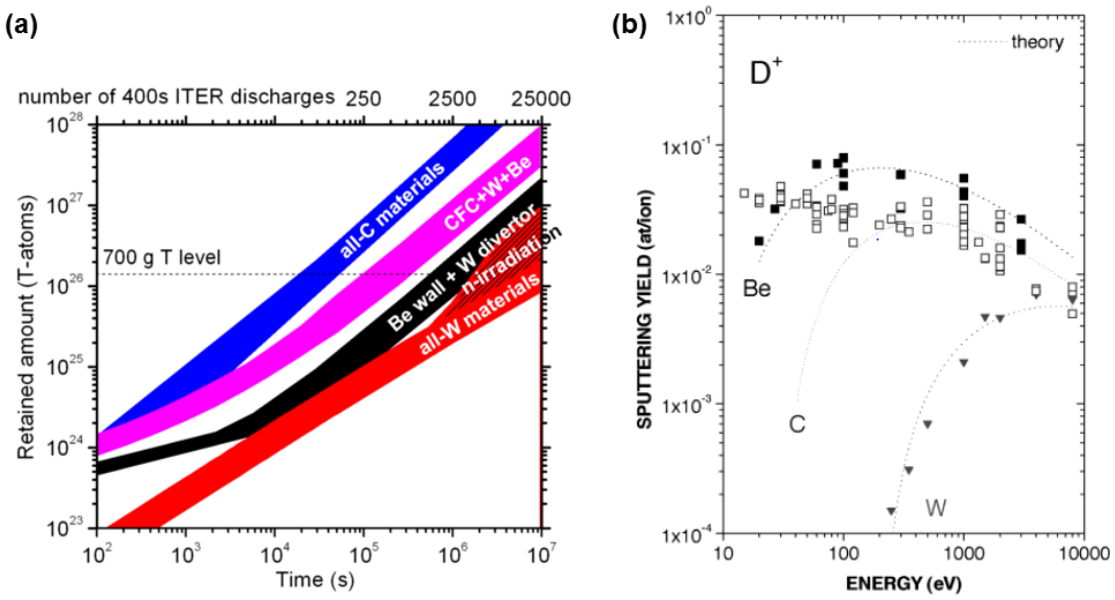


Figure 2.1 – (a) Tritium inventory in ITER for the all-C (blue line), all-W options (red line), the initial material choice (magenta), full-W divertor and Be first wall are included (black line) [19]. (b) Comparison of measured values for the sputtering yield at normalised incidence for beryllium (closed squares), carbon (open squares), and tungsten (closed triangles) by deuterium ions with results from analytical modelling of physical sputtering [20].

when irradiated with a low neutron fluence of 0.2 dpa [18]. Tritium is the fuel for the fusion reactor and being a radioactive element, only a certain inventory limit (~ 700 g) is permitted. It has been seen that CFC has a high tritium retention rate, wherein, the inventory limit can be reached in a few tens of plasma discharges (Figure 2.1 (a)). On the contrary, in tungsten, the inventory limit is not reached even after 18000 plasma discharges (Figure 2.1 (a)) [19].

Another disadvantage of CFC materials is their enhanced erosion due to chemical interaction with the hydrogen plasma. Investigation at plasma gun facilities has shown that a few microns can be eroded with every plasma pulse [21]. The high rate of tritium retention and erosion indicates that CFC materials may have to be frequently repaired and replaced, which makes them commercially unattractive. Thus tungsten, with its high melting point (3422 °C), notable strength at high temperature, low tritium inventory, low sputtering rate

(Figure 2.1 (b)) and the ability to retain these properties after irradiation, has been chosen by ITER for building the divertor [3], [6], [14], [15].

2.1.2. Tungsten as an engineering material

The mechanical properties of pristine tungsten is discussed here to build the foundation for analysis of irradiation induced changes. Traditionally tungsten has been used as a functional material, such as in X-ray targets or in light bulb filaments, owing to its high melting temperature and its electronic structure [22]. The lack of structural use is because tungsten, by virtue of its body centred cubic (bcc) structure, exhibits brittle fracture at low temperature and ductile failure at higher temperatures. The BDTT is largely strain-rate dependent and is typically about 100 °C to 200 °C for tungsten for strain rates 4×10^{-5} to 5×10^{-2} [23] An added disadvantage is its low fracture toughness, with polycrystalline samples having a fracture toughness below 10 MPa$\sqrt{m}$ [24]. This mechanical behaviour is governed by dislocation mobility which is influenced by both intrinsic and extrinsic factors.

The intrinsic factor controlling dislocation mobility is the Peierl's stress, i.e. the minimum required shear stress (theoretically or computationally derived at 0 K) to move a dislocation from one Peierl's valley to the next [25]. The atomic bond strength, the crystal structure, the shear modulus, dislocation width, Burgers' vector and Poisson's ratio, determine the Peierl's stress [26]. Tungsten, with its non-close-packed bcc structure and strong atomic bond, has an inherently high Peierl's stress and consequently a low intrinsic dislocation mobility.

In bcc crystals, screw dislocations glide by nucleation and movement of kink pairs along the dislocation line [27], [28]. Being a thermally activated process, dislocation

mobility and thus BDTT follows an Arrhenius relationship, $T_{BDT} = \frac{E_{BDT}}{k \ln\left(\frac{\dot{\varepsilon}}{A}\right)}$ where T_{BDT} is the brittle-to-ductile transition temperature, E_{BDT} is the corresponding activation energy, k is the Boltzmann constant, $\dot{\varepsilon}$ strain rate and A is a constant. Thus T_{BDT}, depends on the strain-rate and the E_{BDT}. It has been reported that in tungsten, the activation energy for double kink formation on screw dislocations decides E_{BDT} [23]. This could be due to the rate of crystal plasticity being more strongly controlled by screw dislocations than edge, given their much lower mobility as compared to edge dislocations [29]. While E_{BDT} is about 1.05eV for pure tungsten it is seen to increase to about 1.45 eV for impure sintered material [23]. These values of E_{BDT} suggest that the BDTT is sensitive to impurities.

Further, extrinsic factors such as processing of tungsten, can affect its purity which in turn can influence the dislocation mobility and BDTT. Interstitial impurities introduced during processing such as carbon, nitrogen or oxygen can pin both edge and screw dislocations [30]. T_{BDT} in high purity deformed tungsten is found to be ~ 90 K lower than in sintered deformed tungsten for all strain-rates [31]. Solute atoms like phosphorus can gather at grain boundaries and cause tungsten to become more brittle and promote inter-granular failure [24].

Thus in summary, the low mobility of dislocations in tungsten is central to its brittleness at room temperature, high BDTT, and inherently poor mechanical behaviour.

2.1.2.1. Developing tungsten for fusion

Tungsten based armour components require significant development before they can be put to service. Presence of impurities and the type of thermal treatment chosen will influence the fracture behaviour [24]. Tungsten's poor ductility makes it difficult to carry out deep drawing needed to form the divertor components. Further, shattering of the brittle tungsten

in the plasma facing tiles, could result in quenching the fusion reaction, by the introduction of the heavy ions into the plasma.

DFT calculations show that addition of rhenium to tungsten may improve its ductility by changing dislocation core structure, reducing Peierl's stress, increasing the number of available slip planes and reducing the critical stress required for plasticity to set in [32]. However, irradiation-induced clustering of rhenium sets in at high damage doses and leads to substantial hardening as rhenium clusters act as efficient obstacles to dislocation motion [33]–[35]. Other elements such as tantalum, vanadium, molybdenum and titanium can form a solid solution with tungsten. Studies have shown however, that alloys of tungsten with the above elements result in increasing the BDTT and brittle, inter-granular failure along high angle grain boundaries are observed in such alloys [36]. Since alloying tungsten does not have much advantages, an alternative method of forming tungsten fibre reinforced tungsten composites has also been considered to improve the fracture toughness. It is anticipated that controlled cracking and frictional sliding along the fibre matrix interface in such samples, will allow interfacial energy absorption and that the integral effect of such local energy absorption will improve the global toughness [37]. For example, a study compared the bending strength of tungsten-copper composite (W-Cu composite is an important material for building the transition layer between tungsten plasma-facing component and the copper-based heat sink) and tungsten-fibre reinforced W-Cu composite (with ~ 5.5. wt.% tungsten fibres) [38]. It was found that the bending strength of the tungsten fibre reinforced W-Cu composite was 355 MPa as compared to 315 MPa for W-Cu composite [38].

The upper limit of the operating temperature is constrained by properties of recrystallisation and creep. Often the plasmas are seeded with impurities such as nitrogen

to radiate energy and lower the heat load on the divertor. If the recrystallisation temperature of tungsten is improved, concentrations of such impurities in the plasma could be reduced. ODS tungsten alloys have been considered to address this issue. However, addition of the alloying elements and the presence of the oxide particles lowers the fracture toughness of the material. But for instance three-point bending tests in ODS tungsten, W-2%Y_2O_3, showed that the composite is ductile above 400 °C [39]. Also fine grained W-TiC and W-ZrC composites were found to withstand a heat flux 100% higher than pure tungsten while displaying higher tensile strength [40]. These observations inspire confidence that tungsten alloys with rare-earth oxides or carbides are promising materials for further investigation.

In summary, the key improvement areas for tungsten as a fusion material, are increasing ductility, formability and its fracture toughness without adversely affecting the advantageous properties of high thermal conductivity, recrystallisation and creep behaviour. To best judge the degree of improvement needed and estimate the feasibility of the current component designs, it is crucial to understand how properties may change in-service. Thus studying tungsten irradiated by neutrons, hydrogen and helium or corresponding representative models is essential for developing more resilient tungsten armour components.

2.1.3. Radiation damage in tungsten

2.1.3.1. Defect generation

As neutron and other particles bombard the material, the regular crystal lattice is disturbed. The impacting particles knock atoms from their lattice positions, creating primary-knock-on atoms (PKAs). These then produce more lattice displacements (cascade damage) as they move through the material (Figure 2.2 (a)). The vacant site created by a displaced atom is known as a vacancy defect, while the displaced atom itself, accommodated at an interstitial

site, is known as a self-interstitial atom (SIA). The combination of a vacancy and a SIA is known as a Frenkel Pair.

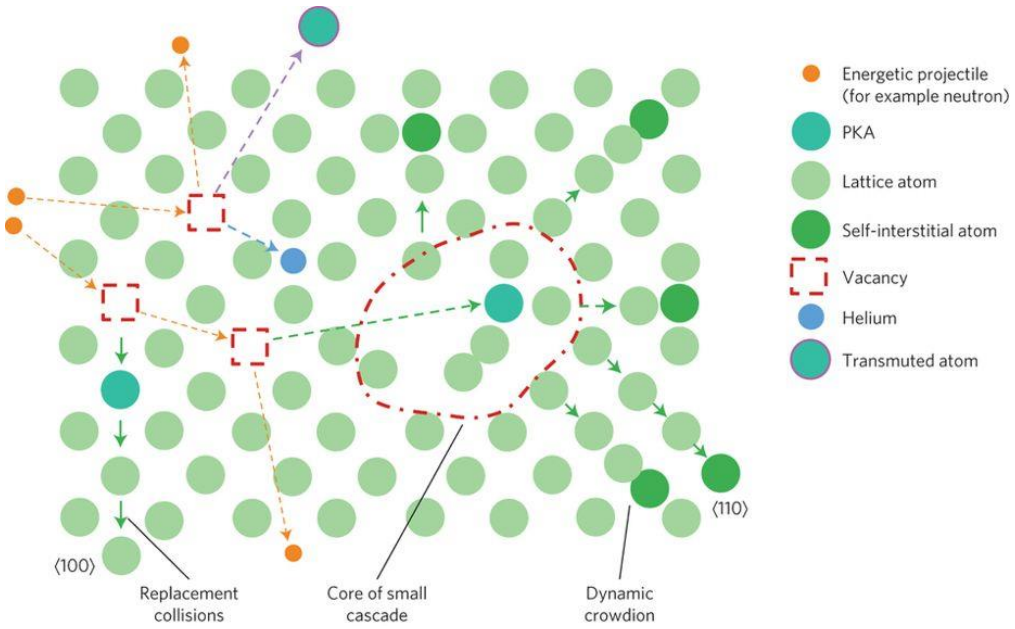


Figure 2.2 – (a) Schematic illustration of irradiation damage [41].

The number of displacements per atom created by the impacting particle i.e. the dpa, is a common measure of radiation damage. However, it must be noted that most of the atomic displacements initiated by the impacting particle, anneal out and only few remain. It was found that for helium implantation, only about 1% of the calculated dpa was retained in the material [42]. Thus there is an element of uncertainty in using dpa as a measure of radiation damage. However, in absence of an acceptable alternative, damage levels in this report will be reported in dpa.

In-service tungsten will be irradiated primarily by two sources: high energy neutrons, and gaseous elements injected from the plasma. Further gaseous elements produced by transmutation can aggravate the radiation damage by their interaction with the irradiation-induced defects.

2.1.3.2. Irradiation by fusion neutrons

Besides point defects, neutron irradiation also creates dislocations, where the crystallographic registry is lost along a line. The interaction between defects and their eventual fate depends on the defect density and their mobility. Several reaction paths are possible: defects can be lost at grain boundaries, can be absorbed by other defect clusters, disappear due to mutual annihilation such as that of vacancy and interstitial or remain in the material [43]. The irradiation-induced defects when retained in the material, create further pinning obstacles for gliding dislocations and in turn cause an increase in the BDTT. Vacancies can accumulate to create volume defects in the form of voids [44], whose diameter can change with the dose [34]. Evolution of loops, voids and other associated phenomena such as creep or swelling depends on the reaction path adopted in the material as the microstructure evolves [43].

Using molecular dynamics simulations, Troev et al. estimated the radiation damage produced by displacement-cascade in tungsten irradiated with neutrons [45]. For a neutron fluence of 2.5×10^{22} n/cm^2, they calculated a dpa of 2.85 in tungsten per full power year (FPY). At energies below 100 keV, at early stages after irradiation, interstitial volume was found to be twice larger than the volume of vacancies. The defect population was seen to be comprised of single vacancies, di-vacancies, interstitials and interstitial clusters containing more than 3 atoms.

As the reactor conditions cannot be recreated yet, alternative means are necessary to experimentally study fusion neutron damage. Fission neutron irradiation can be used to emulate fusion neutron damage [7], [46]. However there remain some concerns about dissimilarities in the energy spectrum of and damage microstructure generated by fission and fusion neutrons. A study evaluated the irradiation conditions in different facilities: the

intense stripping neutron source IFMIF, spallation sources ESS and XADS, fusion prototype reactor DEMO [47] and fission reactors HFR and BOR60 [48]. Comparing the neutron spectra from these different facilities, it was seen that only the IFMIF spectrum was a close replication of the DEMO fusion reactor spectrum (Figure 2.3 (a)). Below 5 MeV, the HFR-8 spectrum, is aligned with the DEMO spectrum but is about five times lower. However, above 5 MeV, while the fusion spectrum goes up to 14 MeV, the fission spectrum drops sharply, indicating the absence of high energy knock-on atoms.

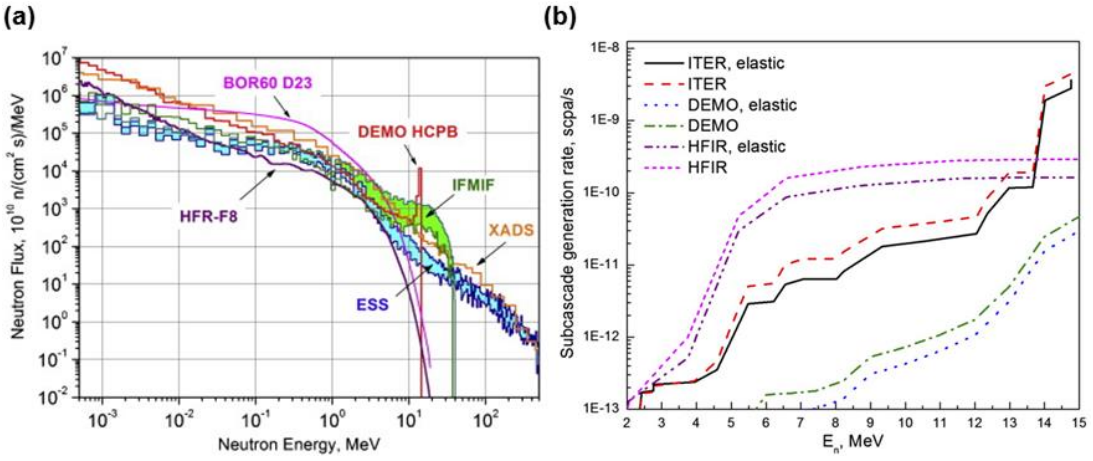


Figure 2.3 - (a) Comparison of neutron spectra from different facilities [49]; (b) Generation rates of sub-cascades for tungsten in HFIR, DEMO and ITER [50].

The PKA energy heavily influences the cascade damage morphology [51]. Beyond a certain PKA, energy cascades can split to create sub-cascades, introducing further complexity in the microstructure. Sub-cascade generation is dependent on the radius of damage zone (R) produced by a secondary knock on atom (SKA). SKAs can be generated by two elastic collisions [52]. If the mean distance λ(E) between two collisions produced by PKA of energy E, is greater than R, then a sub-cascade is generated [52]. Ryazanov et al. found that the sub-cascade generation rate in tungsten in HFIR, particularly for low neutron energies (< 1 keV), is two-three orders of magnitude higher than in DEMO and ITER (Figure 2.3 (b)) [50]. A Monte Carlo binary collision approximation model has

shown that high energy cascade fragments mainly have small defect clusters, while low energy sub-cascades, produce more defects and larger defect clusters [53]. Thus, owing to its higher sub-cascade generation rate, irradiation with fission neutrons, may overestimate the damage produced by fusion neutrons.

Besides creating lattice defects, neutron irradiation can also produce gaseous elements through transmutation. However, for the same neutron fluence, the amount of hydrogen and helium produced in tungsten, differs in fission and fusion environments. For the same neutron fluence of 10^{23} n/cm^2, the relatively softer energy spectrum of the fission neutrons (HFIR) produced only 0.0008 appm/dpa of helium while magnetic confinement (MFE) and inertial confinement fusion (IFE) produced 0.6 and 0.5 appm/dpa of helium respectively [54]. The hydrogen produced is also underestimated by fission neutron irradiation, where HFIR produces 0.003 appm/dpa in comparison with 1.8 and 1.2 appm/dpa produced by MFE and IFE respectively.

Another problem with fission neutron irradiation is that it renders the materials radioactive and unsuitable for regular handling and experiments in the laboratory. Alternatively, ion irradiation, a relatively simpler and more economical technique, can be used to study displacement damage effects. The major benefits are that the sample remains inactive and complex effects of transmutation and gas production are excluded from the study [55]. Moreover, the time frame for producing damage is much shorter. Several dpa can be obtained in a day and materials can be tested to extremely high dpa levels of about 400-500 dpa. However, ions can only penetrate up to a few microns, depending on ion energy and the atomic number of the material being irradiated [55]. Since a shallow damage profile is created, experimental techniques suitable for studying materials at this scale are needed. Also, the PKA energy and the displacement rate (10^{-3} – 10^{-4} dpa/s) from high

energy ion bombardment, is higher than that for fusion neutrons (displacement rate 10^{-7} – 10^{-8} dpa/s) implying differences in damage microtructure induced by ion-implantation and fusion neutrons [56]. Temporal overlap of cascades, caused by the higher displacement rates, are of particular concern, especially in presence of impurites like carbon, which can decelerate the long term damage evolution.

Transmission electron microscopy (TEM) on ion-irradiated tungsten, exposed to different damage levels, has provided useful insights about the evolution of the defect morphology and population, in the neutron-irradiated reactor component, as a function of dose [7]. For example, Yi et al. studied tungsten and W–5 wt.%Re irradiated with 150 keV self-ions at 500 °C, with doses between 10^{16} to 10^{18} $W^{+}m^{-2}$ and ~ 25 nm thick irradiated layer. The first observable defects (predominantly ½<111> vacancy loops) are seen to appear at doses < 0.01 dpa [57]. Between 0.1 - 1 dpa, though defect cluster migration with elastic loop interaction was observed, the number density of loops was found to saturate in the range ~ 10^{15} loops/m^2. In both W and W-5Re, the majority of loops were found to have Burgers' vectors of a/2<111>, with about 25% of loops with <100> Burgers' vector.

The influence of these loops on the mechanical properties are commonly investigated using micro-mechanical tests like nano-indentation and micro-cantilever tests. Nano-indentation on tungsten implanted at 300 °C with 2 MeV tungsten ions showed a saturation in hardness beyond ~ 0.4 dpa (~ 0.8 GPa or 11% hardness increase) (Figure 2.4 (a)) [58]. Also the loop number density was seen to saturate between 0.4 – 33 dpa [58]. Tungsten samples, self-ion implanted at higher temperatures, show higher hardness. For example, in tungsten samples implanted with self-ions to ~ 2 dpa at 800 °C,

~ 20% increase in hardness was observed through micro-cantilever bending tests (loaded to failure under displacement control at a rate of 5 nm s^{-1}) (Figure 2.4 (b)) [59].

Fusion neutron irradiation can result in the formation of transmutation elements such as rhenium, osmium, tantalum [9]. Ion-irradiation of tungsten alloyed with either of these elements can be used to specifically investigate the effect of these transmutation elements on cascade damage behaviour. As such, self-ion implanted tungsten alloys with rhenium or tantalum have been used in several nano-indentation studies. Contrary to self-ion implanted tungsten which saturated in hardness beyond 0.4 dpa at 300 °C, self-ion implanted W-5wt.%Re samples showed ~ 13% hardness increase up to 1.2 dpa and then a further increase of 20% and 40% at 13 and 33 dpa (Figure 2.4 (a)) [58]. These massive increases in hardness are thought to be induced by formation of rhenium clusters which may be precursors of the sigma phase formation [58]. In self-ion implanted W-5wt.%Ta alloy, a different trend is noticed. Large increase of ~ 21% in hardness is noticed for 0.07 dpa damage, but thereafter the hardness increase is less than 14% and saturates beyond 13 dpa [60]. Further, surprising observations of suppressed pile-up around Berkovich indents in these samples, for damage levels 0.07 dpa and 1.2 dpa, is made in contrast to the large pile-up seen aound indents in unimplanted tungsten [60]. A plausible explanation for this observation and the different increases in hardness induced by tantalum and rhenium for low doses like 1.2 dpa are yet to be examined.

To sum up, cascade damage induced lattice defects in tungsten cause significant changes in hardness associated with a loop-dominated defect microstructure. The presence of alloying elements is found to further aggravate the radiation damage effects. However the underlying reasons for these observations, i.e. the mechanism of interaction of the

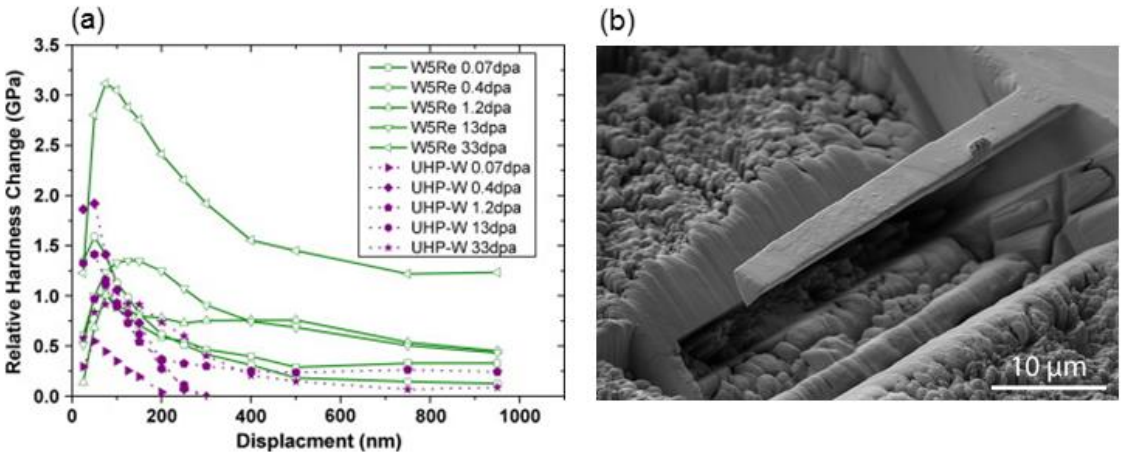


Figure 2.4 – (a) Relative increase in hardness as a function of depth for UHP-W and W5Re implanted to 0, 0.07, 0.4, 1.2, 13 and 33 dpa. A maximum increase in hardness is seen at 125 nm for all doses in both material types [58]. (b) Focussed ion beam (FIB)-machined cantilever produced in tungsten, approximately 30µm in length and 2µm in depth. The cantilever spans approximately 20 grains [59].

induced defects (predominantly loops) with gliding dislocations, as a function of dose and temperature, needs further exploration. Considering the expense and the lengthy process of neutron irradiation, ion irradiation is a practical choice for studying cascade damage models. However, predictive data collected from material irradiated with ions (or fission neutrons), cannot be directly used to represent fusion conditions [61]. Differences in terms of PKA recoil spectrum, transmutation and displacement rates must be analysed. Also the effect of environmental parameters such as stress state, flux pulsing and temperature, must be accounted for if the acquired data is to be used for designing fusion devices.

2.1.3.3. Irradiation by gaseous elements

Hydrogen in tungsten

In tungsten, the retention of hydrogen (and its isotopes) is very low, particularly for doses lower than 10^{22} ions/m^2 [62]. Thermal desorption experiments showed that the majority of deuterium is desorbed between 400 and 600 K [62]. DFT modelling has shown that for

small interatomic distances, the H-H state is unstable[1] [63], suggesting that hydrogen can only be retained and form bubbles/blisters in presence of other defects.

For instance, the presence of helium defects in tungsten can affect its deuterium retention capacity. Iwakiri et al. irradiated tungsten with 8 keV helium at room temperature, followed by 8 keV deuterium at several temperatures (300 to 673 K) [62]. It was found that at 473 K, for a high dose of helium (2×10^{21} ions/m^2), a large number of small helium bubbles form effective trapping sites for deuterium. Thus, the deuterium trapping was three times greater than without helium pre-irradiation.

Deuterium retention is also seen to change in presence of neutron irradiation defects. The deuterium desorption spectra (Figure 2.5) showed only one prominent peak at 550 K for pure tungsten, but an additional peak at 450 K in ion-irradiated tungsten (0.025 dpa), probably due to the irradiation damage trapping deuterium with different activation energies [64]. Another additional peak was observed at 900 K in neutron irradiated tungsten (0.025 dpa). The author hypothesises that this may be caused by deuterium trapped in bulk of the material by neutron-induced defects, rather than only in the near surface region where the ion-irradiation defects are localised.

When retained, hydrogen can bring about reduced pop-in load and increase in hardness (maximum increase of 0.5 GPa) as observed by nano-indentation of tungsten exposed to deuterium plasma at 443 K, with incident ion energy of 35 eV and accumulated fluence of 8.1×10^{25} ions/m^2 [65]. Similar observations of increased hardness were made by Terentyev et al. [66] and Zayachuk et al. [67] in tungsten exposed to deuterium plasma.

[1] at close distance, there is an asymmetric shift of the bonding and anti-bonding state, towards higher energy, thus increasing the interaction energy and resulting in weak repulsion instead of attraction

Complying with the thesis scope, hydrogen irradiation effects are only briefly discussed here and further details can be found in the cited references.

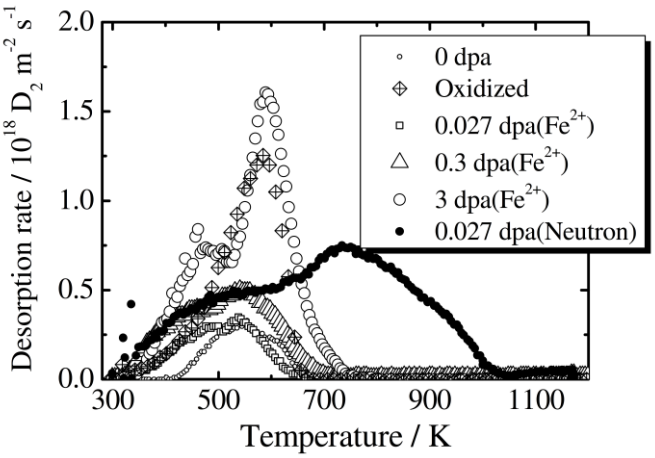


Figure 2.5 - Deuterium TDS spectrum of ion-irradiated and neutron irradiated tungsten [64].

Helium in tungsten

Little helium is formed through transmutation, and it would take more than 300 years for any significant embrittlement through transmuted helium [8]. Thus, the main source of helium will be that implanted from the fusion plasma. Helium-induced damage in tungsten is complex and varies with fluence, implantation energy and implantation temperature. It is also influenced by the amount of helium retained. Grain boundaries act as trapping sites for helium and thus helium retention is greater in polycrystalline tungsten than in single crystals, where a lack of trapping sites allows long range helium diffusion during annealing [68].

DFT calculations have shown that the stable interstitial site for the retained helium is the tetrahedral site and at close separation He-He binding is strong through pure elastic interaction [63]. This enables helium to form stable clusters even in a defect free crystal. As the interstitial helium cluster gets large, it displaces metal atoms from their lattice site

to release the pressure generated by the helium atoms [63]. Frenkel pair defects are formed by this mechanism, which is called trap mutation.

Besides strong interactions with themselves (1.01 eV), helium interacts strongly with defects generated, such as vacancies (4.57 eV), vacancy clusters and impurities [69]. The helium-vacancy bond is particularly strong [70] and DFT calculations showed that mobile vacancy clusters which disintegrate at fusion temperatures, are stabilised by helium atoms which reduces the vacancy emission rates [63]. The helium-vacancy bond which makes the vacancies immobile, can also influence void formation induced by ion-irradiation. Yoshida et al. found that dense interstitial loops and fine voids induced by Cu^{+} implantation in tungsten (at 2.4 MeV to 3 dpa), almost disappear in presence of helium (0.25 keV at 10^{22} He^{+}/m^{2}) [69].

At temperatures below 873 K, helium vacancy complexes with their low thermal migration, form dense fine helium bubbles, by absorbing more and more helium. Beyond a threshold helium dose, at some critical depth from the incident surface, lateral stress induced by local helium bubble swelling together with pressure build-up within a layer of bubbles, may cause them to merge by inter-bubble fracture, and cause blister formation [69], [71]. At higher temperatures (1073 K – 1273 K), when vacancies and helium bubbles can migrate thermally, large helium bubbles form [69]. With increase in helium fluence and temperature, bubbles can evolve into 'nano-fuzz' structures [72], [73] (Figure 2.6).

Even low energy helium ion implantation can cause surface modifications in tungsten (with a displacement threshold energy of 42-44 eV, depending on the crystallographic orientation [74]). For example, micron sized surface pores were seen in tungsten implanted with as low as 10 eV helium ions at 1600°C. For 19 keV helium implanted at ~ 800°C, large blisters were seen to form [11]. Sharafat et al. also observed

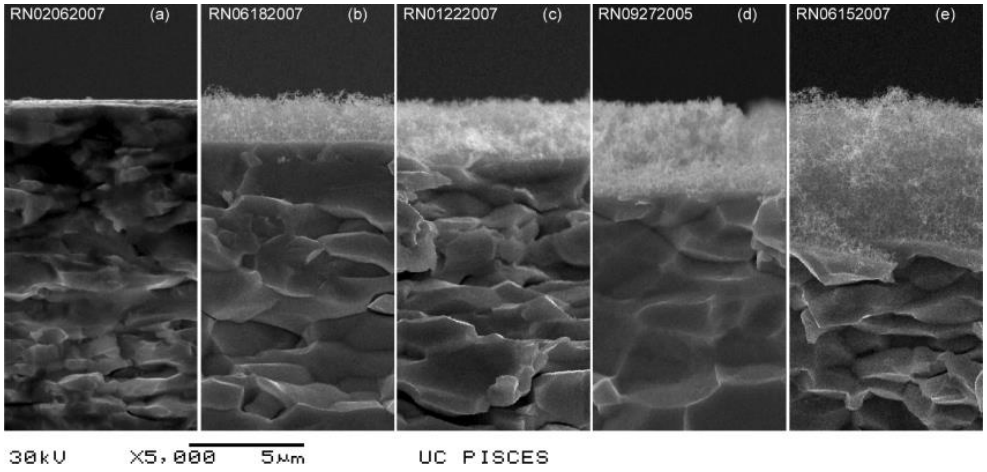


Figure 2.6 - Cross-sectional SEM images of W targets exposed to pure He plasma for exposures times of (a) 300 s, (b) 2.0×10^3 s, (c) 4.3×10^3 s, (d) 9.0×10^3 s and (e) 2.2×10^4 s. Targets were exposed at a fixed temperature of 1120 K. The plasma properties varied slightly in the parameter ranges $n_e = 4 \times 10^{18}$ m^{-3} and $T_e \sim$ 6–8 eV, $\Gamma_{He+} = (4–6) \times 10^{22}$ m^{-2} s^{-1} in order to maintain the constant fixed target temperature [73].

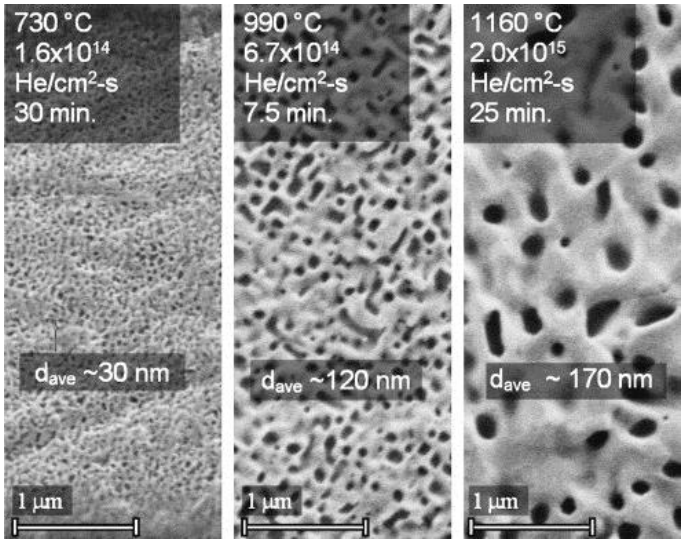


Figure 2.7 - Micrographs of tungsten surfaces implanted with 30 keV He [11].

that 30 keV helium implanted between 730 °C and 1160 °C with doses of about ~ 3×10^{22} m^{-2}, interacted with vacancies, to form large helium bubbles and numerous surface pores (reduced density with increasing temperature), with diameter ranging from 15-150 nm (increasing diameter with temperature) (Figure 2.7). Similar results of a sub-surface semi-porous layer, were observed in polycrystalline tungsten samples, irradiated

with 30 keV helium, at temperature range of 500-900 °C, [75]. The layer was found to reach up to 1000 nm below surface for fluence of about 10^{23} He/m^2.

Helium-defects can significantly impact tungsten's deformation behaviour. High temperature nano-indentation of tungsten samples implanted with ~ 600 appm of helium showed hardness increase (averaged between 150 and 400 nm penetration depth) of about 55% at 523 K [76]. However, beyond 700 K, no significant hardness increase was found (Figure 2.8 (c)) [76]. Even the small helium-induced defects formed at room temperature (few-atom-large V and SIA clusters [77], [78]), formed by relatively low injected dose of ~ 0.3 at. wt.%, can cause a substantial increase in material hardness, degradation of thermal diffusivity and embrittlement [79], [80]. Injected helium concentrations of 0.3 at.% (at 300 K) has been seen to cause 30% increased hardness [81] and 50% reduction of room temperature thermal diffusivity [80]. Further, contrary to suppressed pile-up seen around indents in self-ion implanted tungsten [60], large pile-up was seen around 250 nm deep Berkovich nano-indents in W-0.3 at.% He (implanted at 300 K) (Figure 2.8 (a)-(b)) [81]. This implies that the underlying mechanism of interaction of dislocations with helium-defects is different from that with self-ion implantation induced defects. However, a coherent understanding of how helium-defects interact with the gliding dislocations, is yet unknown. This is primarily due to the difficulty associated with probing the small helium-defects (at room temperature) which are below the sensitivity of TEM (defects below 1.5 nm are not reliably detected) [79], [82]. An alternative way of probing these defects is by measuring the lattice strains they cause.

Hofmann et al. measured the strain in W-1at.%Re alloy, implanted with 3110 appm helium at 573 K, using micro-Laue diffraction [83]. Significant lattice swelling, resulting in an out-of-plane strain of 1.5×10^{-3} was measured in the approximately 2.7 μm thick

implanted layer. By relating the corresponding hydrostatic strain of 2.62 $\times 10^{-3}$ with DFT calculations, the study showed that helium vacancy complexes on average contain a pair of helium atoms. With increase in temperature to 1473 K, the helium-induced lattice swelling was found to extend beyond the implanted layer, suggesting that thermal activation enhances defect migration into the material [12]. These studies inspire confidence in the effectiveness of Laue diffraction in probing the small and complex helium-defect microstructure. Such experimental techniques if combined with microstructural modelling

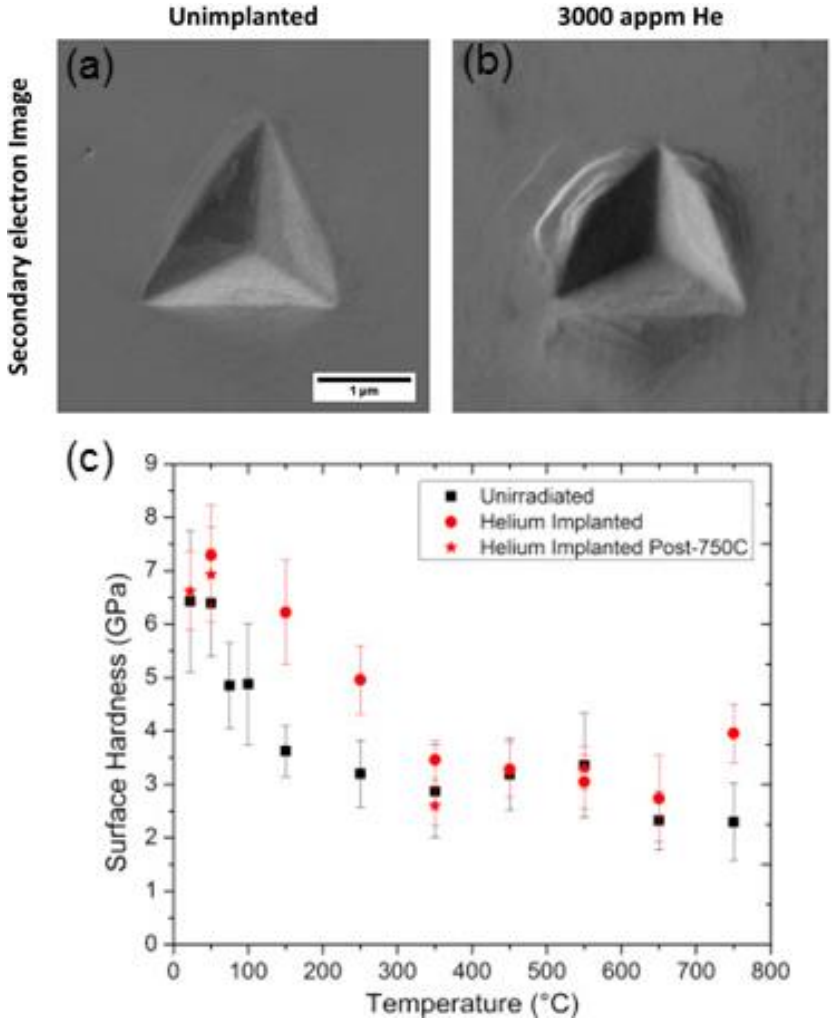


Figure 2.8 - (a)-(b) SEM images of 250 nm deep indents in unimplanted and He + implanted sample respectively[81]. (c) Nano-indentation hardness from shallow indents (averaged between 150 and 400 nm) for an unirradiated sample and the helium-implanted sample [76].

techniques could provide insight into the mechanism of interaction of the helium-defects with mobile dislocations and the overall material microstructural evolution.

In summary, helium induces prominent changes in the microstructure of tungsten, which can influence the deuterium retention and evolution of neutron-induced dimensional change. Unlike hydrogen, helium forms a stable bond with itself to form clusters which are strong enough to create lattice defects. Helium bonds strongly with vacancies and the few atom large helium-vacancy complexes can induce significant lattice swelling and alarming alterations in tungsten's mechanical properties. To control these changes, detailed knowledge of mechanisms governing defect retention and interaction of helium-defects with mobile dislocations is essential.

In this regard, the influence of the following factors requires investigation:

1. Temperature – thermal activation can enhance defect mobility (into the bulk) and defect morphology (bubble and blister formation).
2. Irradiation conditions – fluence and energy changes can alter the defect morphology (bubbles evolving into nano-fuzz).
3. Grain sizes and transmutation elements – Presence of transmutation elements and smaller grain sizes (more grain boundaries) can act as defect nucleation sites and increase helium retention.

2.1.3.4. Summary of literature review

Overall the literature review highlights that tungsten will be embrittled by neutron irradiation as a result of radiation hardening. Helium is anticipated to worsen this problem, owing to its low solubility in the crystal lattice and its affinity for lattice defects, particularly vacancies. Despite limitations, ion-implantation has been shown to be an effective

technique to mimic the radiation damage and enable isolated investigation of damage effects, up to high damage levels (of tens of dpa), without the added complexity of transmutation and material activation. Helium-implantation induced defects at room temperature, which remain "invisible" in TEM, have been shown to be effectively probed by measuring the lattice strains induced by them. Nano-indentation measurements have shown that both helium-ion implantation and self-ion implantation can induce significant hardening along with pile-up and suppression of pile-up around indents respectively. Nano-indentation measurements have also shown that helium-ion implantation had a much greater effect on hardness than collision cascade damage caused by self-ion implantation, suggesting that the presence of helium enhances defect retention and/or increases obstacle strength.

Several important questions arise from these observations reported in the literature: For instance, while helium is known to increase defect retention, the number of defects created by a particular irradiation condition is difficult to ascertain. In particular, the change in defect retention as a function of irradiation dose or presence of impurities, is important to consider to accurately estimate irradiation-induced residual stresses that can affect the fatigue performance of the components. Also, though significant irradiation-induced changes in deformation behaviour have been reported, the mechanism governing these changes i.e. the relationship between defect-dislocation interaction and the mechanical properties, remain unclear. Understanding the underlying physics and integrating this into predictive models is urgently needed for enabling successful predictions of the structural integrity and performance of the tungsten armour components. Predictive models that account for crystallographic orientation-dependence and different irradiation doses are essential for the design and commercial realisation of future fusion reactors beyond ITER.

This thesis aims to address these questions by examining helium-implanted tungsten samples, irradiated to different doses, using a combination of experimental and modelling techniques. A review of the state of the art of the techniques used, namely nano-indentation, X-ray micro-diffraction, HR-EBSD and CPFE modelling follows in the next section.

2.2. Experimental techniques

Ion implantation is a cost- and time-effective way of mimicking radiation damage without making the samples radioactive and unsuitable for laboratory analysis and regular handling. However, as limited ion-penetration depth generates only a few micron thick damage layer (exact thickness depends on the implantation energy), techniques for studying the material at this scale are required. In this project, micro beam X-ray diffraction has been used to non-invasively probe the implantation induced lattice strains in these thin layers. To examine the deformation behaviour of the implanted layer, nano-indentation was used. Subsequently a combination of X-ray diffraction and HR-EBSD was used to measure the deformation field around and beneath indents. In the following sections these experimental techniques are reviewed.

2.2.1. Nano-indentation

Nano-indentation has been used extensively for characterising small-scale mechanical properties [84], [85]. It involves a diamond tip being driven into the material surface whilst measuring both the applied load and displacement. By imposing a small sinusoidal oscillation to the indenter throughout the loading process, hardness and modulus can be measured continuously as a function of indentation depth [85].

A typical load displacement curve is shown in Figure 2.9 (a). The data analysis method proposed by Oliver and Pharr [84] is briefly discussed below. As the material is indented, the combined elastic and plastic deformation of the material beneath the indenter is measured. During unloading, the elastic part of the deformation relaxes and an equation (Eq. (2. 1)) can be fitted to the curve at this point.

$$P = B\ (h - h_f)^m \tag{2. 1}$$

where, P is the load, B and m are power law fitting constants (for example B = 0.141 and m = 1.51 as observed for tungsten from nano-indentation with a Berkovich indenter [85]) and h and h_f are shown in Figure 2.9 (a). The contact depth h_c is obtained from h and the amount of sinking (vertical displacement of the sample surface) in elastic models h_s (assuming negligible pile-up) (h_c and h_s shown in (Figure 2.9 (b)).

$$h_c = h - h_s = h - \in \frac{P_{max}}{S} \tag{2. 2}$$

where, $\in$ is a constant value dependent on the geometry of the indenter. The contact area A can then be defined as an area-function (calibrated by measurement of a reference material for example fused silica to account for deviations from ideal indenter geometry) of h_c. The hardness can then be estimated as

$$H = \frac{P_{max}}{A} \tag{2. 3}$$

The elastic modulus can be determined from A and the measured unloading stiffness using the equation

$$S = \beta \frac{2}{\sqrt{\pi}} E_{eff} \sqrt{A} \quad \text{where} \quad \frac{1}{E_{eff}} = \frac{1 - \upsilon^2}{E} + \frac{1 - \upsilon_i^2}{E_i} \tag{2. 4}$$

where, E_{eff} is the effective elastic modulus, which accounts for the fact that there is elastic deformation in both the specimen (Young's modulus E , Poisson's ratio υ) and the indenter (modulus E_i , Poisson's ratio υ_i).

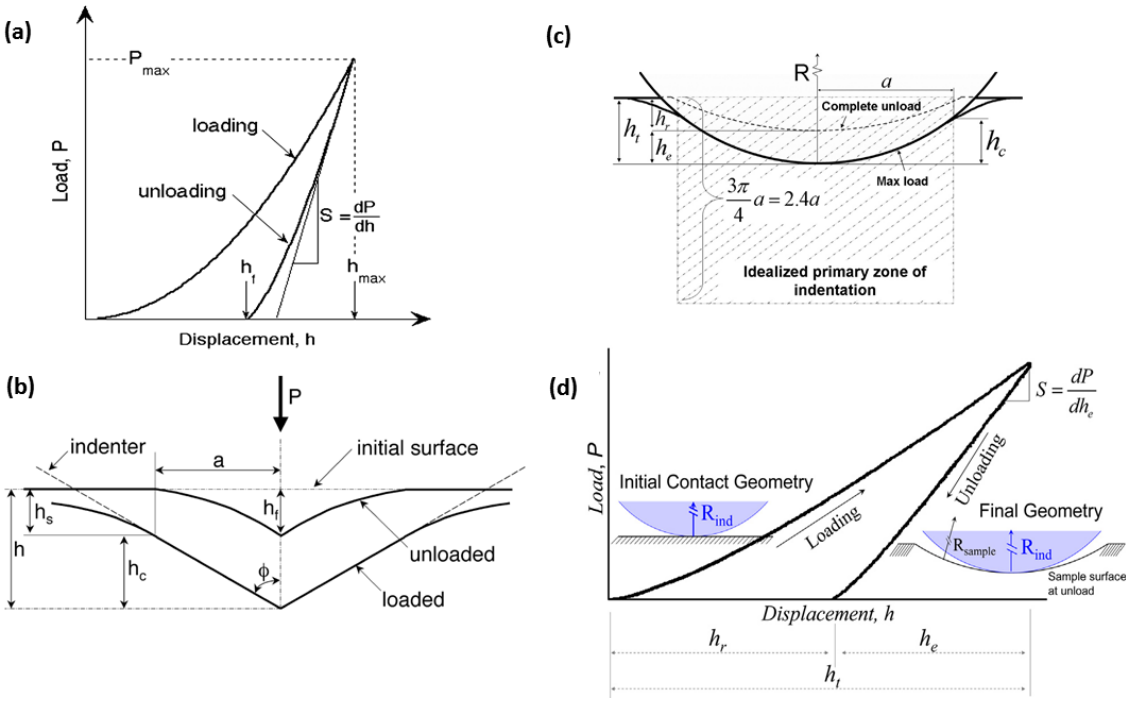


Figure 2.9 - (a) Schematic of indentation load–displacement data showing measured parameters [85]. (b) Schematic of the unloading process showing parameters characterising the contact geometry [85]. (c) Schematic of the indentation zone in spherical indentation [86]. (d) Schematic of a typical measured spherical indentation load–displacement curve with the initial and final contact geometries [86].

For spherical indenters [85], [86], based on the Hertz theory of frictionless contact between two isotropic elastic solids, the load-displacement relation is given by

$$P = {}^{4}/_{3}\sqrt{R_{eff}}E_{eff}\left(h - h_f\right)^{3/2} \quad \text{where} \quad \frac{1}{R_{eff}} = \frac{1}{R} + \frac{1}{R_i} \tag{2. 5}$$

As the displacement is for elastic unloading curve only, depth $h - h_f$ is used instead of h. The effective radius is dependent on the radius of the indenter (R_i) and the radius of the specimen (R). The stiffness during unloading is determined as

$$S = 2\sqrt{R_{eff}}E_{eff}(h - h_f)^{1/2} \quad (2.\ 6)$$

The contact depth (h_c), contact radius (a) and contact area (A_c), as shown in Figure 2.9 (c), (d), are given by

$$h_c = h_t - \frac{3}{4}\frac{P}{S} \quad (2.\ 7)$$

$$a = \sqrt{2h_cR_i - h_c^2} \text{ where } A_c = \pi a^2 \text{ and } E_{eff} = \frac{S}{2a} \quad (2.\ 8)$$

There are several challenges associated with nano-indentation measurements. Well-known is the indentation size effect, where the decreasing indentation size is associated with a substantial increase in hardness [87]. In addition, the shape and size of the elastic and plastic strain fields generated around the indent cannot be easily measured. The stress field around the spherical indenters are relatively less susceptible to experimental uncertainty, compared to "pointed" indenters where small imperfections of the indenter tip can have a large effect [86]. Complexities of the deformation fields such as 'pile up' and sink-in around the indent, which is commonly observed in elastic-plastic materials, are not taken into account for calculations, and can lead to an over- or under-estimation of hardness and modulus. Elastic isotropy is a further assumption, though this is correct for the present study as tungsten, with Zener anisotropy factor of 1.0122, is almost perfectly elastically isotropic [88].

In summary, nano-indentation may not be suitable for extracting stress-strain curves that can be extrapolated to macroscopic properties. However, it is a great qualitative tool that enables probing deformation behaviour on very small scales that could not be otherwise

interrogated. The one key aim of this thesis is to gain mechanistic insights from such measurements.

2.2.2. X-ray diffraction

While electron microscopy techniques offer nano-scale spatial resolution, they are confined to the sample surface or very thin sections. X-ray diffraction is an appropriates tool for examining the micro-nano scale structure in the material bulk, non-invasively. The X-ray wavelength (~ 1 Å) is similar to the spacing between atoms in a crystal, allowing the crystal to act as a 3D diffraction grating, as described by Max von Laue [89]. The Braggs considered constructive interference of X-rays reflected from crystal planes, leading to the well-known Bragg's law [90]. It links the spacing between the lattice planes d_{hkl}, and the incident angle θ, where constructive interference occurs for integer multiple n of wavelength λ (Figure 2.10 (a)).

$$n\lambda = 2d_{hkl}\sin\theta \tag{2. 9}$$

For a cubic crystal with real space lattice vectors $\boldsymbol{a}_1$, $\boldsymbol{a}_2$ and $\boldsymbol{a}_3$, the interplanar spacing d_{hkl}, between planes with Miller indices (*hkl*), is given by

$$\frac{1}{{d_{hkl}}^2} = \frac{h^2}{\boldsymbol{a}_1 . \boldsymbol{a}_1} + \frac{k^2}{\boldsymbol{a}_2 . \boldsymbol{a}_2} + \frac{l^2}{\boldsymbol{a}_3 . \boldsymbol{a}_3} \tag{2. 10}$$

In the reciprocal space, the reciprocal lattice vectors $\boldsymbol{b}_1$, $\boldsymbol{b}_2$ and $\boldsymbol{b}_3$ can be related to the real space lattice vectors using the following equations

$$\boldsymbol{b}_1 = 2\pi\frac{(\boldsymbol{a}_2 \times \boldsymbol{a}_3)}{V};\ \boldsymbol{b}_2 = 2\pi\frac{(\boldsymbol{a}_3 \times \boldsymbol{a}_1)}{V};\ \boldsymbol{b}_3 = 2\pi\frac{(\boldsymbol{a}_1 \times \boldsymbol{a}_2)}{V};$$
$$\text{where } V = \boldsymbol{a}_1.(\boldsymbol{a}_2 \times \boldsymbol{a}_3) \tag{2. 11}$$

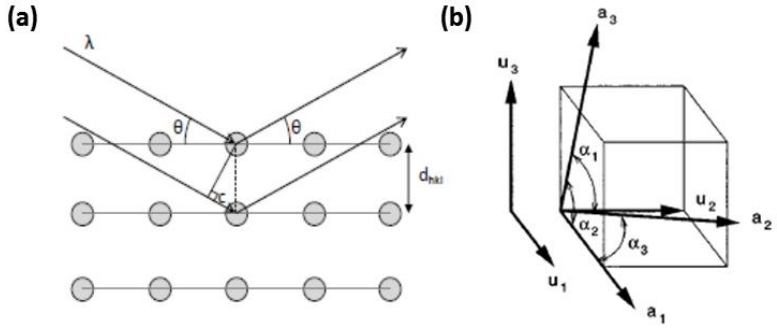


Figure 2.10 – (a) Classical diagram of Bragg diffraction based on simple atom plane model. (b) Cartesian coordinates attached to the real-space unit cell. Here, $\boldsymbol{u}_1 = \boldsymbol{a}_1/|\boldsymbol{a}_1|$; $\boldsymbol{u}_3 = \boldsymbol{a}_1 \times \boldsymbol{a}_2/|\boldsymbol{a}_1 \times \boldsymbol{a}_2|$; and $\boldsymbol{u}_2 = \boldsymbol{a}_3 \times \boldsymbol{a}_1/|\boldsymbol{a}_3 \times \boldsymbol{a}_1|$ [91].

In the reciprocal space, the Bragg plane is characterised by the reciprocal space vector $\boldsymbol{q}_{hkl}$

$$\boldsymbol{q}_{hkl} = h\boldsymbol{b}_1 + k\boldsymbol{b}_2 + l\boldsymbol{b}_3 \tag{2. 12}$$

The diffraction condition is met when

$$\boldsymbol{s} = \boldsymbol{s_0} + \boldsymbol{q}_{hkl} \tag{2. 13}$$

where $\boldsymbol{s_0}$ and $\boldsymbol{s}$ are the incident and scatter beam vectors, respectively, each of length $2\pi/\lambda$. Also, d_{hkl}, can be written in terms of $\boldsymbol{q}_{hkl}$, as

$$d_{hkl} = \frac{2\pi}{|\boldsymbol{q}_{hkl}|} \tag{2. 14}$$

2.2.2.1 Micro-beam Laue diffraction

Micro-beam Laue diffraction is based on the classical Laue diffraction approach where a single crystalline sample is illuminated with a polychromatic X-ray beam. The resulting diffraction pattern consists of a large number of Laue diffraction peaks that are typically collected on an area detector. The diffraction peak positions give information about the lattice orientation and the distortion of the unit cell. By performing these measurements with a micro-focused X-ray beam, detailed maps of the lattice distortions within individual

grains of polycrystalline samples can be measured. The fundamental principles of automated Laue pattern analysis are described by Chung and Ice [91]. Briefly the determination of the lattice strain from the unit cell parameters is described below.

Figure 2.10 (b) shows a unit cell with lattice vectors $\boldsymbol{a}_1$, $\boldsymbol{a}_2$ and $\boldsymbol{a}_3$,, attached to a Cartesian coordinate system $\boldsymbol{u}_1$, $\boldsymbol{u}_2$ and $\boldsymbol{u}_3$. A position in the lattice may be represented by a vector which can be in the Cartesian coordinate system $\boldsymbol{v}_{cart}$, or in unit cell coordinates $\boldsymbol{v}$. The unit cell coordinates can be transformed into the Cartesian coordinates as $\boldsymbol{v}_{cart} = \boldsymbol{A}\boldsymbol{v}$, where, $\boldsymbol{A}$ is given by

$$\boldsymbol{A} = \begin{pmatrix} a_1 & a_2 \cos\alpha_3 & a_3 \cos\alpha_2 \\ 0 & a_2 \sin\alpha_3 & -a_3 \sin\alpha_2 \cos\beta_1 \\ 0 & 0 & 1/b_3 \end{pmatrix} \quad (2.\ 15)$$

where, a_i and α_i are the real space lattice parameters and β_i and b_i are reciprocal lattice parameters[2] (Figure 2.10). By comparing the measured unit cell parameters, $\boldsymbol{A}_{meas}$ with the unstrained reference unit cell $\boldsymbol{A}_0$, the average elastic strain of the scattering volume can be determined. If $\boldsymbol{T}$ is considered to be the transformation matrix that maps the undeformed crystal $\boldsymbol{A}_0$ to the deformed $\boldsymbol{A}_{meas}$, then this term $\boldsymbol{T}$ would contain both the rotation and distortion terms.

$$\boldsymbol{A}_{meas} = \boldsymbol{T}\boldsymbol{A}_0;\ \varepsilon_{ij} = \frac{T_{ij} + T_{ji}}{2} - I_{ij} \quad (2.\ 16)$$

The symmetric component of $\boldsymbol{T}$, then gives the strain in the Cartesian crystal coordinate frame. The strain can be split into distortional and dilatational components. Knowing the lattice parameters in the reciprocal space, the $\boldsymbol{B}$ matrix, equivalent to $\boldsymbol{A}$ matrix (Eq. (2. 15))

[2] Lattice parameters $a_i = |\boldsymbol{a}_i|$ and $b_i = |\boldsymbol{b}_i|$, for i=1,2,3 where $\boldsymbol{a}_i$ and $\boldsymbol{b}_i$ are the real and reciprocal lattice vectors. $\alpha_1 = \arccos\left(\frac{\boldsymbol{a}_2 . \boldsymbol{a}_3}{|\boldsymbol{a}_2||\boldsymbol{a}_3|}\right)$, $\alpha_2 = \arccos\left(\frac{\boldsymbol{a}_3 . \boldsymbol{a}_1}{|\boldsymbol{a}_3||\boldsymbol{a}_1|}\right)$, $\alpha_3 = \arccos\left(\frac{\boldsymbol{a}_1 . \boldsymbol{a}_2}{|\boldsymbol{a}_1||\boldsymbol{a}_2|}\right)$, $\beta_1 = \arccos\left(\frac{\boldsymbol{b}_2 . \boldsymbol{b}_3}{|\boldsymbol{b}_2||\boldsymbol{b}_3|}\right)$, $\beta_2 = \arccos\left(\frac{\boldsymbol{b}_3 . \boldsymbol{b}_1}{|\boldsymbol{b}_3||\boldsymbol{b}_1|}\right)$ and $\beta_3 = \arccos\left(\frac{\boldsymbol{b}_1 . \boldsymbol{b}_2}{|\boldsymbol{b}_1||\boldsymbol{b}_2|}\right)$.

in real space, can be formed. The orientation of the crystal with respect to the lab coordinates is captured by an orientation matrix $\boldsymbol{U}$. The $\boldsymbol{q}_{hkl}$ vector in lab coordinates, for given *hkl* reflection, is

$$\boldsymbol{q}_{hkl} = \boldsymbol{UB}\begin{pmatrix} h \\ k \\ l \end{pmatrix} \tag{2. 17}$$

Two reflections are needed to calculate the orientation matrix, assuming zero strain, while four reflections are needed to determine the orientation and deviatoric elastic strain tensor. By measuring the energy of a single reflection, the dilatational component of the strain can also be determined (details in Chapter 3). The real space plane normal unit direction vector can be written in terms of $\boldsymbol{q}_{hkl}$ as

$$\hat{\boldsymbol{n}} = \frac{\boldsymbol{q}_{hkl}}{|\boldsymbol{q}_{hkl}|} \tag{2. 18}$$

For incident beam unit vector $\widehat{\boldsymbol{s}_0}$, the scattered beam unit vector $\hat{\boldsymbol{s}}$ for this reflection is

$$\hat{\boldsymbol{s}} = \widehat{\boldsymbol{s}_0} + 2\,(\widehat{\boldsymbol{s}_0}.\hat{\boldsymbol{n}}).\hat{\boldsymbol{n}} \tag{2. 19}$$

$\hat{\boldsymbol{s}}$ can be ray-traced to the detector to find the reflection positions. To generate the complete Laue pattern, this computation is carried out for all lattice reflections. The reverse of this procedure is carried out to determine lattice rotation and strain from experimentally measured Laue patterns. Several automated codes to do this are now available (for example XMAS [92], LaueTools [93] or Laue Go (J.Z. Tischler: tischler@anl.gov). Several instrument setups are available for such measurements for example I16, B16 beamlines at Diamond Light Source (DLS), ID22, ID15A beamlines at the European Synchrotron Research Facility (ESRF), 34-ID-E beamline at Advanced Photon Source in Argonne National Laboratory to name a few.

3D measurement of lattice distortion fields, with sub-micron resolution, can be obtained at some Laue instruments, such as at 34-ID-E [94]. The depth resolution in measurements, with a resolution of about 500 nm, can be achieved using the differential aperture X-ray microscopy (DAXM) setup [95]. Here, a platinum wire is scanned in small steps between the detector and the diffracting sample (Figure 2. 11). The depth vs intensity profile for each detector pixel is recovered by subtracting the diffraction images from consecutive wire position increments and triangulating using the wire edge and the line of the incident beam. Such measurements provide a unique way of probing the radiation defects via the lattice strains they cause. As such the effective contribution of defects of all sizes can be probed, even those < 1.5 nm that are "invisible" to TEM [96].

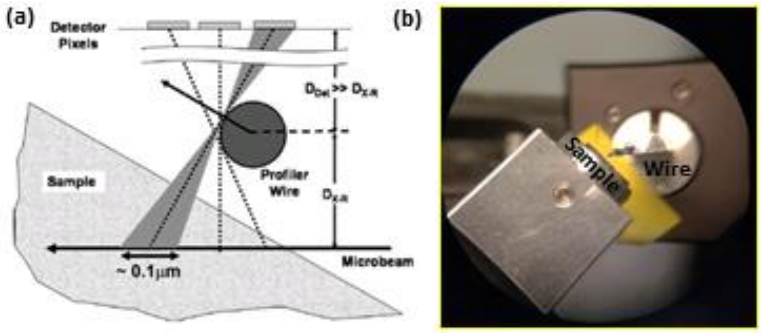


Figure 2. 11 – (a) Schematic view of the differential-aperture profiling geometry (illustration not to scale) [95]. (b) Close-up view of the DAXM setup at the 34-ID-E beamline at the Advanced Photon Source, Argonne National Laboratory.

These measurements are subject to errors in the order of 10^{-4}, caused primarily by experimental geometry; beam-shift, inaccuracy in sample stage positioning, detector shift or change in the misorientation angles of the detector or inaccuracies in peak fitting that occur when the Laue peaks deviate significantly from the functions used for fitting [97]. In particular the measurements of the shear components of strain, especially the out-of-plane shears, are error-prone. These strain components cause out-of-plane tilt of the diffraction

pattern, resulting in only a small change of the diffraction pattern when the conventional detector position is used (90° reflection geometry above the sample). Also, while Laue measurements have high angular resolution [94], [98], [99], their spatial resolution is limited to about 500 nm. Errors arising from inaccurate peak fitting increases further as Laue peaks become streaked [100], in regions of steep strain gradient, due to the underlying population of GNDs generated to accommodate the lattice curvature [101], [102]. In such regions, the strain and lattice rotations cannot be resolved well. As such, HR-EBSD with higher spatial resolution can be used as an effective complementary technique to Laue in order to capture a more complete picture of the lattice distortion fields, particularly in areas with steep strain and rotation gradients.

2.2.3. High-resolution EBSD

HR-EBSD allows calculation of the residual elastic lattice strain and lattice rotation tensors by cross-correlating the shift and distortion of a particular electron diffraction pattern with respect to a number of regions of interest (ROIs) from a reference pattern, within the same grain. This technique was first developed by Wilkinson et al. [103] and is sensitive to orientation changes of approximately 1×10^{-4} rad.

Diffraction patterns are collected, at full resolution, using the conventional EBSD setup with the camera insert as for normal grain orientation mapping. Extra care must be taken to prepare the sample surface as scratches can affect the quality of the pattern obtained and in turn the measurement of lattice distortions. Subsequent analysis of the Kikuchi patterns is done by the XEBSD code provided by A. J. Wilkinson [103]. The method is described briefly here and details can be found elsewhere [103]–[106].

Kikuchi diffraction patterns are direct projections of the lattice planes which will shift with change in interplanar angles or with crystal rotation during deformation. For instance when diffraction vector $\boldsymbol{r}$ gets distorted to $\boldsymbol{r'}$ through displacement $\boldsymbol{Q}$, this reflects as a shift in projected EBSD pattern by $\boldsymbol{q}$ (Figure 2.12) [107].

The relation between $\boldsymbol{q}$ and $\boldsymbol{Q}$ can be written as

$$\boldsymbol{q} = \boldsymbol{Q} - \lambda \boldsymbol{r} \tag{2. 20}$$

where, λ is an unknown scalar. $\boldsymbol{Q}$ can be written as

$$\boldsymbol{Q} = \boldsymbol{r'} - \boldsymbol{r} \tag{2. 21}$$

$\boldsymbol{r'}$ can be derived from $\boldsymbol{r}$ using $\boldsymbol{F^e}$, which is the elastic deformation gradient i.e. the elastic component of the second-order tensor, which maps the undeformed state to the deformed state (details about deformation gradient will be covered in Chapter 5).

$$\boldsymbol{r'} = (\boldsymbol{F^e} - \boldsymbol{I})\boldsymbol{r} \tag{2. 22}$$

Substituting Eq. (2. 21) and (2. 22) into Eq. (2. 20) we get

$$\boldsymbol{q} = (\boldsymbol{F^e} - \boldsymbol{I})\boldsymbol{r} - \boldsymbol{r} - \lambda \boldsymbol{r} \tag{2. 23}$$

λ is unknown in Eq. (2. 23) but can be removed by substituting one of the three simultaneous equations from any of the other two to generate two simultaneous equations.

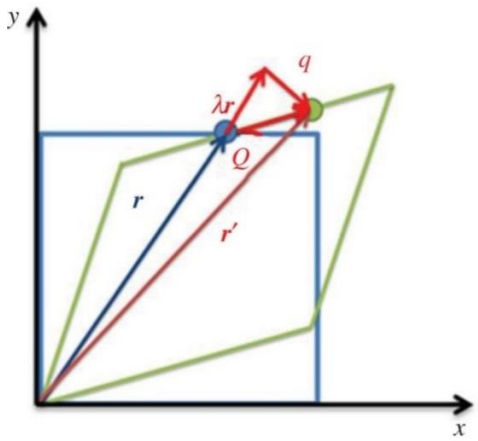


Figure 2.12 - Schematic showing vector $\boldsymbol{r}$ in undeformed 2D lattice structure (blue square) and vector $\boldsymbol{r'}$ in deformed (green square). Displacement due to deformation can be expressed as $\boldsymbol{Q}$ and the resulted shift projected on EBSD detector is represented by $\boldsymbol{q}$ [107].

By measuring the shifts at four or more regions of interest (ROIs), widely spread across the EBSD pattern, eight of the nine components of $\boldsymbol{F}^e$ can be found. To ensure reliable measurement of shift, use of at least 20 ROIs is recommended. The ninth component, corresponding to hydrostatic strain, cannot be measured by HR-EBSD. However, since EBSD measurements are very close to the free surface (within 20-30 nm), by assuming traction free boundary conditions at the surface, the ninth component can be recovered. From $\boldsymbol{F}^e$, the elastic strain ($\boldsymbol{E}^e$) and the rotation ($\boldsymbol{\omega}^e$) can be determined as

$$\boldsymbol{E}^e = \frac{1}{2}(\boldsymbol{F}^{eT}\boldsymbol{F}^e - \boldsymbol{I}) \tag{2. 24}$$

$$\boldsymbol{\omega}^e = \boldsymbol{F}^e\boldsymbol{U}^{e-1} \tag{2. 25}$$

where, $\boldsymbol{U}^e$ can be obtained from the eigenvalues and eigenvectors of the elastic Cauchy green tensor $\boldsymbol{F}^{eT}\boldsymbol{F}^e$ i.e. $\boldsymbol{U}^e = \boldsymbol{Q}^T\boldsymbol{U'}\boldsymbol{Q}$, where $\boldsymbol{Q}$ is the eigenvector matrix of $\boldsymbol{F}^{eT}\boldsymbol{F}^e$ and $\boldsymbol{U'}$ is the square root of the eigenvalues of $\boldsymbol{F}^{eT}\boldsymbol{F}^e$ [107].

The spatial variation of lattice distortions captured can be correlated with the imposed plastic deformation or GND computation using Nye's framework [108]. This was

first attempted by Adams et al. to compute GNDs near grain boundaries in deformed Al bi- and polycrystalline samples [109]. Subsequently, Field et al. also used this same technique to measure GND densities in compressed high purity Al single crystals [110]. Since then, multiple studies have used HR-EBSD measurements to compute GND densities to study the heterogeneous plastic deformation in various loading processes [111]–[113]. Particularly with the development of the cross-correlation technique, the angular resolution of measurement has improved ~ 100 times compared to the conventional Hough-transform-based technique [103], [114], enabling HR-EBSD to measure comparatively low GND densities (~ $10^{10} – 10^{12}$ /m^2).

However, it must be noted that the GND density computation from HR-EBSD measurements involves certain assumptions primarily because the measurement is restricted to the 2D surface. Briefly, the curl operation involved in GND computation (details regarding Nye's framework and GND computation will be discussed later in Chapter 5), requires the derivative of the different components of $\boldsymbol{F}^e$ along X, Y, and Z to obtain a 3 × 3 curl matrix. Since in HR-EBSD, the variation with depth, i.e. along Z is unknown, only three out of nine components of the curl matrix can be accurately determined. By neglecting the contribution of the elastic strain gradients (as lattice rotations generally dominate [108]), five of the nine elements and difference between two elements i.e. in all six components of the curl matrix can be determined [106]. The curl matrix directly relates to the densities of dislocations of different types. Thus if there are more than six types of dislocations (for example considering pure edge or pure screw type of dislocation, in fcc there can be 18 types and in bcc tungsten there can be 16 types for {110}<111> slip systems alone), optimisation techniques are needed to solve the under-determined problem.

Interpretation of the GND computation must also be done with care, accounting for the parameters used and the assumptions made. Most importantly, the step size used for the HR-EBSD measurement, which is directly representative of the considered Burgers' circuit size, must be accounted for when interpreting GND calculations. Dislocations which do not contribute to any lattice curvature at length scales greater than the Burgers' circuit, are the statistically stored dislocations (SSDs). These SSDs consist of dipoles, multi-pole and loops within the Burgers' circuit which do not cause any effective strain field. GNDs on the other hand are the excess dislocations stored within the Burgers' circuit which accommodate the lattice curvature or the closure failure [115]. Thus with reduction in step size, or Burgers' circuit size, the fraction of dislocations which are considered as GNDs will increase (now some dipoles are resolved as GNDs) till finally when the Burgers' circuit becomes smaller than the dipole size, every dislocation will be identified as GND. This problem arises mainly due to the lack of an inherent length scale in conventional plasticity theory. With reduction in step size the noise in the measurement also increases and this could lead to misinterpreting the noise as features that are actually not present in the material [116]. Again using a large step size can reduce the noise but many GNDs will be counted as SSDs and therefore small structures such as dislocation cell walls may not be resolved. Thus the step size must be selected carefully for HR-EBSD analysis depending on the angular resolution, the size of EBSD map and the dislocation density in the sample. While adjusting these variable to optimise the step size, care must be taken to ensure that the measured GND density is above the noise floor (depends on binning, for example when 8×8 binning is used, GND density of the order of 10^{14} m^{-2} arises purely from the noise) [116].

Other parameters for HR-EBSD measurements must also be chosen carefully and as appropriate for the problem in question. Acquiring the high resolution patterns requires about 1 s of exposure time which can limit the size of maps that can be made in the

experiment (for example in 12 hours, a 100 μm × 100 μm area can be measured with 0.5 μm step size) [116]. While this dataset may be sufficient for probing deformation fields around nano-indents or near specific grain boundaries, it cannot be representative of the inhomogeneous deformation in polycrystalline materials. Reduction of the exposure time corresponds to a lowered signal-to-noise ratio. The measurements are also sensitive to the binning size, where increasing binning leads to an improvement in signal to noise ratio, but loss of angular resolution [116].

In summary, HR-EBSD is a powerful tool to non-invasively measure lattice distortions, without difficult sample preparation and in a cost-effective way (can be performed in a regular EBSD setup). While it has high spatial resolution, its sensitivity to small strains is limited. As such it complements very well the Laue diffraction measurements which have slightly lower spatial resolution but good sensitivity to smaller, far-field strains. However, parameters for HR-EBSD measurements must be optimised depending on the given problem and the analysed computations, in particular the GND densities must be interpreted carefully, accounting for the assumptions made and the choice of parameters.

2.3. Computational Modelling

Few practical plasticity problems can be solved analytically, mainly because of irregular geometry, complex boundary conditions and/or loading conditions. An approximate solution of such problems can be obtained by computational mechanics and specifically finite element method (FEM). Herein the solution is obtained by satisfying the boundary conditions while accounting for the conditions of equilibrium, compatibility and the

material's constitutive response. FEM discretises the body into a finite number of elements and nodes with an associated finite number of degrees of freedom.

Plasticity can be modelled at the continuum-level or as microplasticity modelling whereby plastic slip is confined to specific directions consistent with the crystallography of the material. In the engineering industry in particular, the need for fast analysis, time and cost pressures, necessitates most modelling to be done at the continuum-level. There have been great advances made in continuum-level plasticity modelling which can be used to model superplasticity [117], [118], porous plasticity [119], [120], creep in engineering alloys [121], [122] or cyclic plasticity [123]. Details about the fundamentals of time-independent and rate-dependent continuum or phenomenological plasticity can be found elsewhere [124]. In this project, crystal plasticity modelling of single crystals has been used to simulate the experimental observations made from nano-indentation, X-ray diffraction and HR-EBSD. In the following section crystal plasticity modelling technique, its strength, limitations and the current state of the art is described.

2.3.1. Crystal plasticity

Plasticity in crystalline materials takes place through crystal slip, an isochoric process (exceptions include in porous materials[3]), wherein a plane of atoms slides over the adjacent plane by a continuous process of bond breaking and forming i.e. by dislocation motion (Figure 2.13).

[3] In porous metals, volume change occurs due to pore size reduction (from pore closure) and not directly from plastic slip [124].

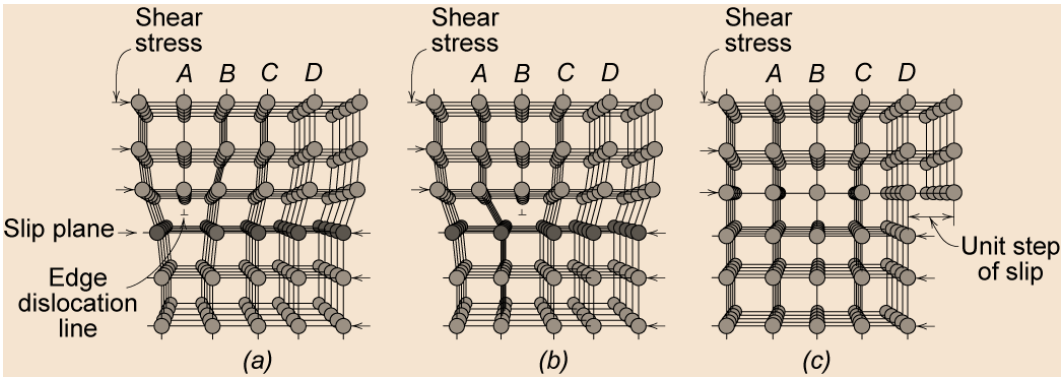


Figure 2.13 – Schematic of dislocation mediated plastic slip, illustrated for an edge dislocation [125].

Dislocations, or these lattice imperfections, are thus often described as a boundary line on the slip plane, demarcating the region where slip has occurred from the region where it has not. They significantly influence properties like hardness, ductility, toughness etc.

Experiments on single crystals have shown that dislocations tend to slip on certain crystal planes and in certain directions which are the most densely packed. This combination of the slip plane and the slip direction constitutes a slip system. Contrary to fcc crystals, bcc tungsten, has several planes that are similarly closely packed; {110}, {112} and {123}. But there is only one distinct close packed direction in tungsten i.e. <111>. Experimental studies have shown that in tungsten, the dominant slip system is the <111>{110} especially at room temperature [126], [127]. Since all the CPFE modelling conducted in this thesis relate to room temperature experiments, only the <111>{110} slip systems were considered here for tungsten.

There can be three types of dislocations; screw dislocation, where the direction of the dislocation line is parallel to the slip direction, edge dislocation where the direction of the dislocation line and the slip direction are orthogonal, and mixed dislocation where the direction of the dislocation line has one component parallel to the slip direction and one component orthogonal to it.

In CPFE formulations, first introduced by Peirce et al. [128], dislocations glide on a given plane when the resolved shear stress τ^{λ} is greater than the critically resolved shear stress (CRSS τ^{C}). Knowing the stress state at a given point in terms of stress tensor $\boldsymbol{\sigma}$, traction vector $\boldsymbol{t}^{\lambda}$ and resolved shear stress τ^{λ} on plane λ are given by

$$\boldsymbol{t}^{\lambda} = \boldsymbol{\sigma}\boldsymbol{n}^{\lambda}; \tau^{\lambda} = \boldsymbol{t}^{\lambda}.\boldsymbol{s}^{\lambda} = \boldsymbol{\sigma}\boldsymbol{n}^{\lambda}.\boldsymbol{s}^{\lambda} \tag{2. 26}$$

where, $\boldsymbol{s}^{\lambda}$ is the slip direction and $\boldsymbol{n}^{\lambda}$, the slip normal. When the yield criterion is satisfied i.e. $\tau^{\lambda} > \tau^{C}$, the amount of crystallographic slip ($\dot{\beta}_{p}^{\lambda}$) on the slip system λ, is determined by a constitutive slip law. Different types of slip laws exist and the choice of the slip law is decided by the specific problem and the material system being modelled. In some instances, a phenomenological power law based slip law is used such as

$$\dot{\beta}_{p}^{\lambda} = \dot{\beta}_{p_0} \left| \frac{\tau^{\lambda}}{\tau^{C}} \right|^{n} \operatorname{sgn}(\tau^{\lambda}) \tag{2. 27}$$

where, $\dot{\beta}_{p_0}$ is a reference strain rate [129].

Alternative physically-based slip laws, accounting for thermally activated movement of dislocations through overcoming obstacles, have also been developed such as

$$\dot{\beta}_{p}^{\lambda} = \rho_{m} \nu (b)^{2} \exp\left(-\frac{\Delta F}{kT}\right) \sinh\left(\frac{\operatorname{sgn}(\tau^{\lambda})(|\tau^{\lambda}| - \tau^{C})V}{kT}\right) \tag{2. 28}$$

where, ρ_m is the density of mobile dislocations, ν the attempt frequency, b the Burgers' vector magnitude, ΔF the activation energy, k the Boltzmann constant, T the temperature in Kelvin, and V the activation volume, which depends on the spacing l between the pinning dislocations [130].

$\dot{\beta}_p^{\lambda}$ can be used to compute $\boldsymbol{F}^p$, which is the plastic deformation gradient i.e. the plastic component of the second-order tensor, which maps the undeformed state to the deformed state (details about $\boldsymbol{F}^p$ will be covered in Chapter 5)

$$\boldsymbol{F}^p = \boldsymbol{I} + \frac{d\boldsymbol{u}^p}{d\boldsymbol{X}} = \boldsymbol{I} + \sum_{\lambda=1}^{j} \beta_p^{\lambda} \boldsymbol{s}^{\lambda} \otimes \boldsymbol{n}^{\lambda} \; ; \qquad \dot{\boldsymbol{F}}^p \approx \sum_{\lambda=1}^{j} \dot{\beta}_p^{\lambda} \boldsymbol{s}^{\lambda} \otimes \boldsymbol{n}^{\lambda}. \tag{2. 29}$$

The plasticity models are often written in rate form as plasticity is an incremental process and thus rather than dealing with the increments in $\boldsymbol{F}^p$, it is more convenient to work with rate of change of $\boldsymbol{F}^p$ i.e. $\dot{\boldsymbol{F}}^p$. To map $\boldsymbol{F}^p$ on to $\dot{\boldsymbol{F}}^p$, a velocity gradient term ($\boldsymbol{L}$) is used

$$\boldsymbol{L} = \frac{d\boldsymbol{v}}{d\boldsymbol{x}} = \dot{\boldsymbol{F}}\boldsymbol{F}^{-1} \; ; \boldsymbol{L}^p \approx \dot{\boldsymbol{F}}^p \; \& \; \boldsymbol{L}^e \approx \boldsymbol{L}\text{-}\boldsymbol{F}^e \boldsymbol{L}^p \boldsymbol{F}^{e-1} \tag{2. 30}$$

Detailed derivations of Eq. (2. 29) and (2. 30) can be found elsewhere [124]. Both $\boldsymbol{L}^p$ and $\boldsymbol{L}^e$ can be split into symmetric and anti-symmetric parts, to give the rate of deformation ($\boldsymbol{D}^e$, $\boldsymbol{D}^p$) and the spin ($\boldsymbol{W}^e, \boldsymbol{W}^p$) respectively. While the rate of deformation is related to the strain increments, the elastic spin is related to the lattice rotation.

Numerous formulations of strain-gradient CPFE have been proposed for example by Fleck and Hutchinson [87], [131], Gao, Huang, Nix and Hutchinson [132], Arsenlis and Parks [133], Cheong and Busso [134], Gurtin and Anand [135], Dunne et al. [130] to name a few. Detailed descriptions of the specific formulations will not be discussed here and can be found in the relevant references. Details of the formulations used in this project will be provided in the relevant chapters.

CPFE formulations help to capture the experimentally observed size-effects [136] and GND production, associated with non-uniform plastic deformation [108], [115]. While

these formulations can be applied to polycrystals [137], for large number of grains, such modelling is infeasible (as of now) at the scale of engineering components. Also CPFE formulations may not explicitly account for the dynamics of interaction between the defect population and gliding dislocations and the resultant evolution of the material microstructure and density of mobile or immobile dislocations. Advances have been made in this regard, by integrating crystal plasticity models with discrete dislocation dynamics [138], [139]. While these models are promising, their complex nature requires multiple fitting parameters and assumptions. A pre-run of dislocation dynamics simulation for the material under consideration may be necessary for estimating necessary parameters. As such, increase in time and cost of computation is unavoidable. Strain gradient CPFE thus offers a good middle path, which, when used with minimal number of fitting parameters and validated with experimental observations, can provide a quantitative estimate of lattice distortions and GND effects [140], [141]. Further, important qualitative insight into the interaction mechanism between defects/precipitates and dislocations, such as irradiation-softening [129] or crack nucleation [142] can also be obtained from such simulations.

Chapter 3

Probing helium-induced defects through lattice strain measurements

This chapter reports a detailed study of helium-implantation-induced lattice strains in tungsten. Helium is known to play a pivotal role in aggravating fusion neutron damage as it strongly binds to vacancies, enhancing defect retention. A key question is how this enhanced defect retention depends on the injected helium dose and whether other elements, such as rhenium, which is the main transmutation product, will have a similar effect. Here we address these issues in a two-step method: using helium-ion-implantation to both produce lattice damage and inject helium into the tungsten matrix and then probing the implantation defects via the lattice strains they cause. The chapter content is in publication format based on article "*S. Das, W. Liu, R. Xu, and F. Hofmann, "Helium-implantation-induced lattice strains and defects in tungsten probed by X-ray micro-diffraction," Mater. Des., vol. 160, pp. 1226–1237, 2018*" [143].

3.1. Abstract

Tungsten is the main candidate material for plasma-facing armour components in future fusion reactors. Bombardment with energetic fusion neutrons causes collision cascade damage and defect formation. Interaction of defects with helium, produced by transmutation and injected from the plasma, modifies defect retention and behaviour. Here we investigate the residual lattice strains caused by different doses of helium-ion-implantation into tungsten and tungsten-rhenium alloys. Energy and depth-resolved synchrotron X-ray micro-diffraction uniquely permits the measurement of lattice strain

with sub-micron 3D spatial resolution and ~ 10^{-4} strain sensitivity. Increase of helium dose from 300 appm to 3000 appm increases volumetric strain by only ~ 2.4 times, indicating that defect retention per injected helium atom is ~ 3 times higher at low helium doses. This suggests defect retention is not a simple function of implanted helium dose, but strongly depends on material composition and presence of impurities. Conversely, analysis of W-1wt.% Re alloy samples and of different crystal orientations shows that both the presence of rhenium, and crystal orientation, have a comparatively small effect on defect retention. These insights are key for the design of armour components in future reactors where it will be essential to account for irradiation-induced dimensional change when predicting component lifetime and performance.

3.2. Introduction

Materials able to withstand the extreme conditions inside future fusion reactors are one of the main challenges for the development of commercial fusion power. Plasma facing armour components will be exposed to high temperatures (above 800 ^{0}C), high heat loads (~ 10-20 MW/m^2 [6]) and intense ion and neutron irradiation [6], [9]. Numerous parameters must be considered when selecting armour materials; low-activation rate to limit radioactive waste production [13], and a suitable operational temperature window, where thermal load capacity, thermal conductivity and recrystallisation govern the upper temperature limit, whilst the lower temperature limit is controlled by ductile to brittle transition and low temperature irradiation resistance [6]. Low tritium retention and good resistance to surface erosion under irradiation are also essential. Tungsten, with an operational window of 800-1300 ^{0}C [17], high melting point of (3422 ^{0}C), low tritium inventory, low sputtering rate and reasonable strength at high temperatures has emerged as the main candidate material for plasma facing fusion armour [14], [15].

Inside the reactor, substantial changes of the properties of tungsten armour components are expected during service. Neutron irradiation causes atomic displacements, leading to the creation and accumulation of defects, and results in hardening, embrittlement and irradiation creep [8]. Nuclear reactions further lead to transmutation and subsequent build-up of rhenium (~ 0.2 at. % $year^{-1}$), tantalum (~ 5000 appm after five year exposure) and osmium (~ 0.1 at. % $year^{-1}$), as well as hydrogen and helium [8], [9]. The material will also be exposed to intense hydrogen and helium bombardment from the plasma (~ 10 MW/m^2) [12]. High interstitial mobility of these gasses, particularly at temperatures above 1000 ^{0}C, allows them to migrate to defects and grain boundaries, where they accumulate and lead to embrittlement and swelling [12]. For a five year operational lifetime, neutron damage in the first wall is anticipated to cause damage of up to 120 displacements per atom (dpa), while the accumulated helium content may reach up to 1200 appm [4].

For commercially viable fusion energy, reliable estimates of the functional properties and integrity of armour components are essential. They require a fundamental understanding of the generation and retention of irradiation-induced defects, and of how they modify material properties. Here helium plays a pivotal role due to its low solubility in the crystal lattice and its strong affinity for lattice defects [8]. A key question is to what extent helium modifies defect retention and whether the presence of other alloying elements, such as rhenium, has a significant effect on this.

Helium ion implantation provides a convenient way of simultaneously mimicking damage formed by energetic neutron irradiation and introducing helium into the tungsten matrix so that its interaction with defects may be studied [12], [42], [144]. Helium-ion implantation induced recoils have predominantly low energy, meaning that the damage micro-structure is dominated by Frenkel pair formation [42]. Probing these defects is

challenging as transmission electron microscopy (TEM) is not sufficiently sensitive to detect them [82]. This is highlighted by high resolution TEM images of tungsten samples implanted with 3000 appm helium at room temperature that do not show any visible defects [79]. Though small, helium-implantation-induced defects have a significant impact on mechanical properties [79], [144] and thermal conductivity of tungsten [80]. To analyse these effects, detailed knowledge of the underlying defect population is required. These studies are further complicated by the limited penetration depth of ions, meaning that implanted layers are generally only a few microns thick.

Several authors have used positron annihilation spectroscopy (PAS) to study vacancy type point defects in crystalline materials such as uranium dioxide or silicon-carbide [145], [146]. This non-invasive technique can effectively be used to ascertain the presence of open-volume defects in which the positrons get trapped altering the positron lifetime. Past studies for example have successfully traced the process of vacancy migration and evolution of vacancy clusters with changing temperature and presence of negatively charged non-vacancy defects generated by proton irradiation [146]. Quantification of the vacancy concentration is also obtainable by the technique. However, interpretation of the PAS measurements requires supportive experimental methods or characterisation techniques such as electron paramagnetic resonance (EPR). Further complexities may include distinction of vacancies from nano-voids or identification of defect combinations of vacancies and self-interstitials.

An alternative approach to probing these implantation-induced "invisible defects" is to measure the lattice strains they cause. This can be done using synchrotron X-ray micro-diffraction which uniquely permits the determination of lattice strain with sub-micron 3D spatial resolution and ~ 10^{-4} strain sensitivity [42], [91], [98], [144]. Using a combination

of this approach and electronic structure calculations, we previously found that implantation of 3000 appm of helium into tungsten produced a defect structure dominated by Frenkel defects [42]. Recombination of Frenkel pairs was prevented by helium occupied vacancies (He_2V), which instead formed a stable configuration where the self-interstitial remains closely bound to the He_2V [77], [147]. Based on the damage microstructure determined from lattice strains, changes in the elastic properties due to defects could then be predicted in very good agreement with experiments [42], [148].

Irradiation-defect-induced lattice strains are also important because of the residual stresses they introduce, which can be on the order of several hundred MPa [42], [149]. These irradiation-induced residual stresses will add to structural in-service loads, creating a stress-offset. It is vital that this is accounted for when estimating the fatigue performance of key components [150]. A key question when estimating the strains, and hence stresses, caused by irradiation damage concerns the number of defects caused by particular irradiation conditions. This is complicated by the fact that generally only a small proportion of the defects produced in collision cascades are retained [42], [151], [152] and the vast majority of defects recombine soon after generation. Kinetic Monte Carlo simulations have shown that the defect retention does not scale linearly with the incident dose and depends on a number of other factors, such as the presence of impurities [153].

In this study, we use micro-beam Laue diffraction to examine the lattice strains caused by different doses of helium-ion implantation. Tungsten and tungsten rhenium alloys are considered to shed light on the importance of alloying elements for irradiation damage retention. The effect of different grain-orientations is considered to assess whether irradiation-induced defects preferentially orient depending on the ion-irradiation direction.

3.3. Experimental details

3.3.1. Sample preparation

Two materials are considered: Polycrystalline, nominally pure (99.99%) tungsten (W), and a polycrystalline tungsten-1wt.%rhenium alloy (W-1Re) manufactured by arc melting from high purity elemental powders [154]. Two samples, ~ 5 mm in size and ~ 1 mm thick, were cut from each material. The sample surfaces were mechanically ground and then polished using diamond paste. A final chemo-mechanical polishing step with 0.1 μm colloidal silica suspension was used to produce a high-quality surface finish. Although polycrystalline, the grain size in the samples was on the order of ~ 1 mm. Thus, as far as the implantation and micro-diffraction measurements are concerned, the samples essentially behave as single crystals. The lattice orientation of grains was determined by electron backscatter diffraction (EBSD).

3.3.2. Ion implantation

Part of each sample was implanted with helium ions using a 2 MeV ion accelerator at the National Ion Beam Centre, University of Surrey, UK. Implantation was carried out at a temperature of 573 K and using a raster scanned beam, to ensure a uniform implantation dose. A range of ion energies (0.05 to 1.8 MeV) and fluences was used to obtain a near uniform helium ion concentration within a ~ 2.8 μm thick implanted layer [12], [42], [154]. Two samples, W and W-1Re were implanted with ~ 3000 appm of helium, while the two other samples, W and W-1Re, were implanted with a lower dose of ~ 300 appm helium. Overall four samples were produced, from here on referred to as W-300He, W-1Re-300He, W-3000He and W-1Re-3000He. Details of the ion energies and fluences used are provided in Appendix A. Figure 3.1 shows the implantation profiles as estimated using

the SRIM code [155] (displacement energy of 68 eV, single-layer calculation model [156]). For W-3000He, between 0 and 2.8 μm depth, a helium ion concentration of ~ 3110 ± 270 appm is obtained with an associated damage of 0.24 ± 0.02 displacements per atom (dpa). For W-300He, between 0 and 2.8 μm depth, a helium ion concentration of ~ 310 ± 30 appm is obtained with an associated damage of 0.02 ± 0.003 displacements per atom (dpa).

3.3.3. X-ray micro-diffraction measurements

To measure lattice swelling due to helium ion implantation, micro-beam Laue diffraction measurements were carried out at beamline 34-ID-E, Advanced Photon Source, Argonne National Lab, USA. A polychromatic X-ray beam (7-30 keV) was focused by KB mirrors to a probe spot of ~ 300 nm full width at half maximum at the sample. The sample was placed at this probe spot in 45° reflection geometry (Figure 3.2). Laue diffraction patterns were recorded on an area detector (Perkin-Elmer, #XRD 1621, pixel size 200 × 200 μm^2) placed ~ 511 mm above the sample.

In micro-beam Laue diffraction, the recorded images correspond to the sum of the intensity scattered by the entire volume illuminated by the incident beam. Thus, the depth along the incident beam from which a specific diffraction signal originated is unknown. Hence, if several grains are illuminated simultaneously, or if there are large lattice distortions, the Laue spots become broadened and difficult to interpret. This instrument uniquely allows measurements of lattice orientation and strain with sub-micron resolution in 3D, using the Differential Aperture X-ray Microscopy (DAXM) technique. Briefly, in the DAXM technique a ~ 50 μm diameter platinum wire is scanned in small steps between the detector and the diffracting sample. The depth vs intensity profile for each pixel on the detector can then be calculated by subtracting the diffraction images from consecutive wire position increments and triangulating using the wire edge and the line of the incident beam.

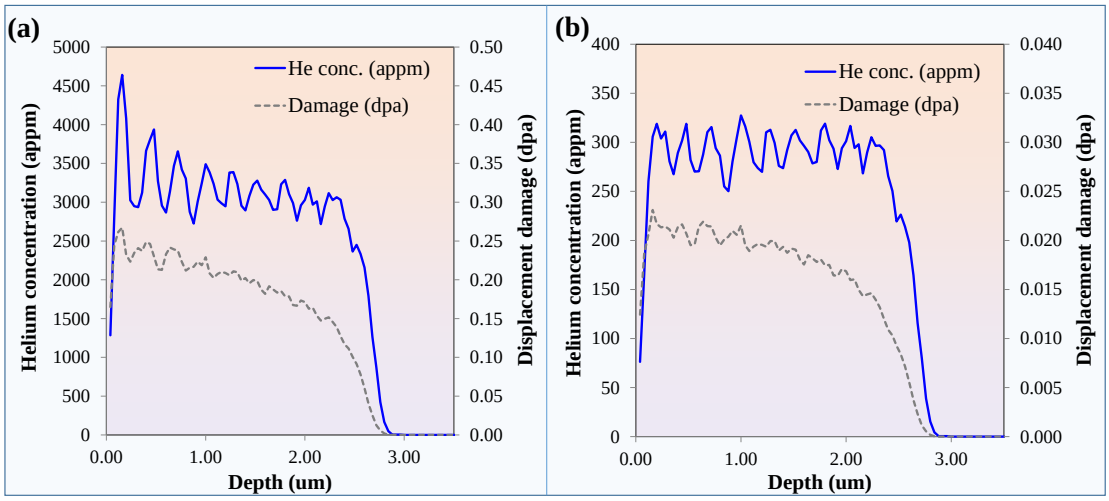


Figure 3.1 - Profile of injected helium ion concentration (dotted grey curve) as calculated by SRIM and implantation-induced displacement damage (solid blue curve) as a function of depth in the sample (a) for tungsten implanted with 3000 appm of helium and (b) for tungsten implanted with 300 appm of helium.

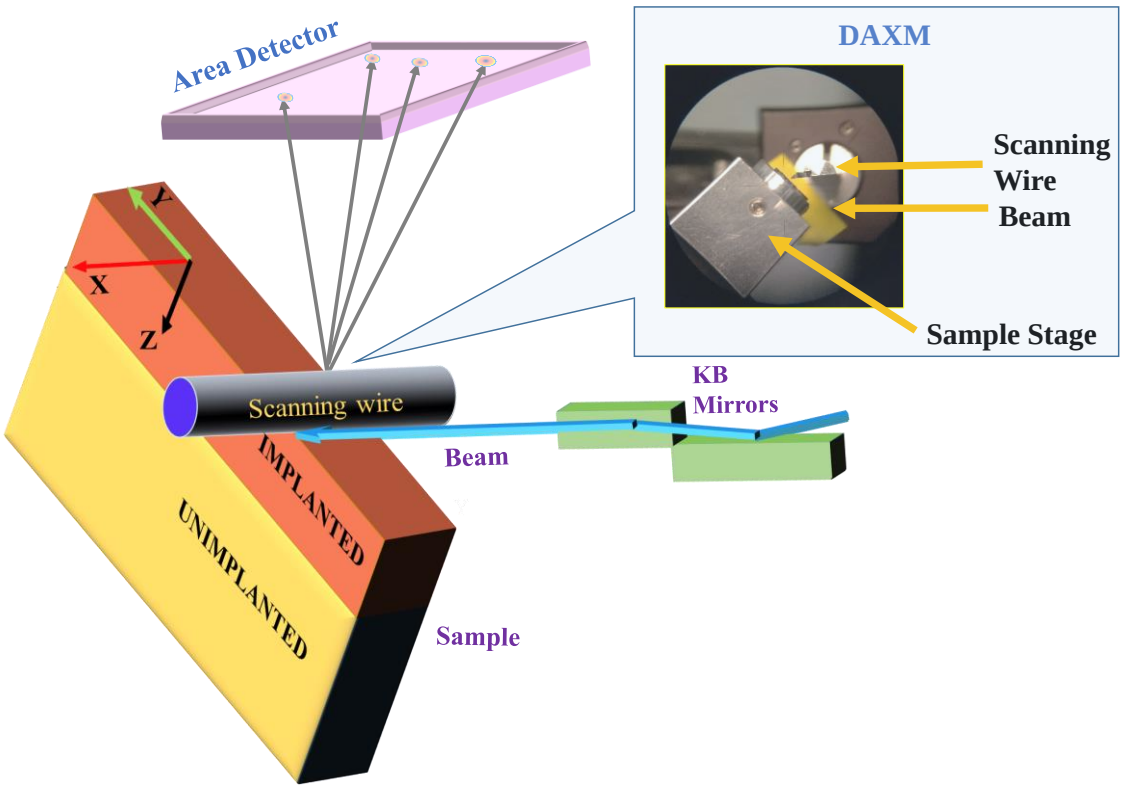


Figure 3.2 – Laue diffraction measurements: Schematic of the experimental configuration illustrating the orientation of the sample with respect to the incident beam, scanning wire and detector, as well as the orientation of the sample coordinate axes.

This allows the reconstruction of depth-resolved diffraction data and hence 3D-resolved strain measurements in crystalline samples. A schematic of DAXM setup is given in Figure 2. 11 and detailed description of the technique and the 34-ID-E instrument is provided elsewhere [94], [98], [157], [158].

3.3.4. Analysis of X-ray diffraction measurements

Polychromatic Laue measurements allow rapid measurement of the deviatoric lattice strain tensor only, as the radial position of diffraction peaks in reciprocal space is not known [91]. By scanning the energy of the incident X-ray beam, the full 3D reciprocal space position of specific reflections can be determined. This can be combined with the deviatoric strain tensor from a white beam measurement to find the full lattice strain tensor [42], [159]. Alternatively the full lattice strain tensor can be determined by measuring the reciprocal space position of at least three non-collinear reflections [91], [160]. This approach offers better sensitivity to small lattice strains and was followed here. For each measurement point photon energy- and depth-resolved scans were performed for six reflections, to ensure that the equations to compute the strain tensor are over determined. Reflections covering the widest possible angular range were chosen. For each reflection an energy range of ~ 80 eV was scanned with an energy step size of 2 eV, and a separate wire scan at each energy. This data was analysed and mapped into a 4 dimensional space (orthogonal reciprocal space Q_x, Q_y, Q_z, and distance along the beam direction) using the LaueGo software package (J.Z. Tischler: tischler@anl.gov).

Figure 3.3 shows the integrated diffracted intensity of a (471) reflection recorded at a point in a <111> oriented grain in the W-1Re-3000He sample. The intensity is plotted as a function of scattering vector magnitude (Q) and depth in the sample. Two distinct peaks

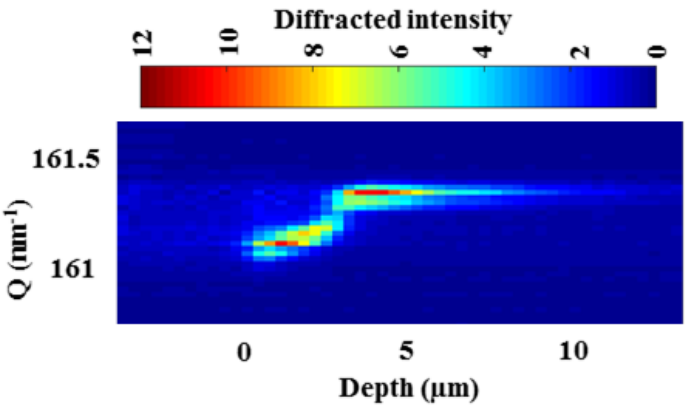


Figure 3.3 – Integrated diffracted intensity on the area detector from a chosen sample point in a <111> oriented grain in the W-1Re-3000He sample as recorded on the detector. The measurement is for a (471) diffraction peak. The intensity is shown as a function of scattering vector magnitude |Q| and depth in the sample.

are visible: A broad peak at lower Q corresponding to the helium-implanted layer (0 to 2.7 μm depth), and a sharp peak from the unimplanted substrate (above 2.7 μm depth). The broadened peak associated with the implanted layer extending approximately 2.7 μm beneath the sample surface is in good agreement with the estimated implanted layer thickness predicted by SRIM (Figure 3.1) [155]. Similar agreement is observed for the other reflections measured in this and the other samples.

A detailed description of full strain tensor determination from three or more reflections with known 3D reciprocal space position can be found elsewhere [91]. Briefly, for each reflection, for each measured point along the depth of the sample, the intensity data was plotted in 3D reciprocal space and the peak centre was found using 3D Gaussian fitting and also confirmed using centre-of-mass. This was repeated for all six reflections at a particular measurement point. Knowing the peak centre for each reflection ($e.g. Qx_{refl1}$, Qy_{refl1}, Qz_{refl1}) and the *h,k,l* indices for that reflection, the **UB** matrix was found, where **U** denotes the orientation matrix and **B** the matrix of reciprocal space lattice vectors.

$$\mathbf{UB}\begin{bmatrix} h_{refl1} & h_{refl2} & : & : & h_{refl7} \\ k_{refl1} & k_{refl2} & : & : & k_{refl7} \\ l_{refl1} & l_{refl2} & : & : & lh_{refl7} \end{bmatrix} = \begin{bmatrix} Qx_{refl1} & Qx_{refl2} & : & Qx_{refl7} \\ Qy_{refl1} & Qy_{refl2} & : & Qx_{refl7} \\ Qz_{refl1} & Qz_{refl2} & : & Qx_{refl7} \end{bmatrix} \quad (3.1)$$

If three non-collinear reflections are used, Eq. (3.1) can be solved directly. If more than three reflections are used Eq. (3.1) is overdetermined. In this case the *hkl* matrix is not invertible. So, to obtain a solution for **UB**, we adopt a minimisation approach, whereby we minimise the difference between the **Q** matrix forward predicted by $\mathbf{UB}\begin{bmatrix} h_{refl1} & : & : & h_{refl7} \\ k_{refl1} & : & : & k_{refl7} \\ l_{refl1} & : & : & lh_{refl7} \end{bmatrix}$ and the actual measured **Q** matrix i.e. $\begin{bmatrix} Qx_{refl1} & : & Qx_{refl7} \\ Qy_{refl1} & : & Qx_{refl7} \\ Qz_{refl1} & : & Qx_{refl7} \end{bmatrix}$.

Here, this was done using the mrdivide function in MATLAB.

From the **UB** matrix, the **U** and the **B** matrices can be found, using the information that $\mathbf{UU}^{\mathrm{T}} = \mathbf{I}$, where **I** is the identity matrix and that the lower triangle of **B** contains zeros [91], [161]. The real-space distorted lattice vectors **A** can then be found from **B** (Eq. (2. 11) and (2. 15)). Comparing **A** to the real-space lattice vectors of an undistorted tungsten crystal, $\mathbf{A}_0$, the deformation gradient, **G**, can be obtained as $\mathbf{A} = (\mathbf{G} + \mathbf{I})\,\mathbf{A}_0$. From **G** the strain tensor, $\boldsymbol{\varepsilon}_{ij}$ for the concerned measured point can be calculated as

$$\varepsilon_{ij} = \frac{1}{2}\left(\mathrm{G}_{ij} + \mathrm{G}_{ji}\right) - \mathrm{I}_{ij} \quad (3.2)$$

The step is repeated for every measured point along the depth in the sample. To find $\mathbf{A}_0$ for the specific materials considered, we assume that the underlying, unimplanted substrate material is not affected by the ion-implantation and can be used as a built-in reference. Hence average data from depths of 7 to 10 µm beneath the sample surface was used to determine $\mathbf{A}_0$ for each material.

3.3.5. Samples chosen for analysis

To assess the influence of the grain orientation, two grains of approximate <111> and <001> surface normal orientation were selected in each sample for micro-diffraction measurements. Thus overall, eight points were studied, as shown by the black dots in Figure B.1 in Appendix B. Table 3.1 shows the out-of-plane orientation of each chosen point and the misorientation of the corresponding point with respect to the perfect <111> or <001> out-of-plane direction.

Sample	**Euler Angles $(\varphi_1, \varphi, \varphi_2)$**[4]	**Out-of-plane orientation**	**Misorientation with <111> or <001> (in degrees)**
W-1Re-300He-<111>	332.2; 54.7; 319.4	[53,62,58]	4
W-1Re-300He-<001>	327.8; 18; 129.4	[24,20,95]	18
W-1Re-3000He-<111>	129.2;120.6;47	[63,59,-51]	5
W-1Re-3000He-<001>	341.4;87;354.1	[-10,99,5]	6.62
W-300He-<111>	225.3; 124.1; 222.4	[-56,-61,-56]	2.43
W-300He-<001>	7.5;76.3;196	[-27, -93, 24]	20.95
W-3000He-<111>	293.8; 55.2; 222	[-55,-61,57]	2.5
W-3000He-<001>	349.3; 14.6; 240.5	[-22,-12,97]	14.6

Table 3.1– List of the out-of-plane orientation of the chosen point in each sample grain and the misorientation of the chosen point with respect to the perfect <111> or <001> out-of-plane direction.

[4] The Euler angle convention used is as follows: $Z1 = \begin{bmatrix} \cos\varphi_1 & \sin\varphi_1 & 0 \\ -\sin\varphi_1 & \cos\varphi_1 & 0 \\ 0 & 0 & 1 \end{bmatrix}$; $X = \begin{bmatrix} 1 & 0 & 0 \\ 0 & \cos\varphi & \sin\varphi \\ 0 & -\sin\varphi & \cos\varphi \end{bmatrix}$; $Z2 = \begin{bmatrix} \cos\varphi_2 & \sin\varphi_2 & 0 \\ -\sin\varphi_2 & \cos\varphi_2 & 0 \\ 0 & 0 & 1 \end{bmatrix}$ and the rotation matrix R = Z1 X Z2.

3.4. Results & Discussion

The Laue diffraction measurements performed on the helium-implanted sample measure the lattice strain, which is a combination of the eigenstrain induced by helium-implantation and the elastic strain generated in the sample in response to the eigenstrain.

The eigenstrain induced by helium can be realised by considering a small cube extracted from the helium-implanted tungsten layer, which is free to deform in all directions (traction free boundary conditions). The introduction of helium into the perfect crystal lattice of this tungsten cube will cause a volumetric expansion. We refer to the strain generated in the process as the volumetric eigenstrain, $\boldsymbol{\varepsilon}^*_{vol}$ (Figure 3.4). Here, we make an assumption that due to random orientation of defects $\boldsymbol{\varepsilon}^*_{vol}$ is purely volumetric, i.e. $\boldsymbol{\varepsilon}^*_{vol} = \begin{bmatrix} \varepsilon^*_{\mathrm{vol}}/3 & 0 & 0 \\ 0 & \varepsilon^*_{\mathrm{vol}}/3 & 0 \\ 0 & 0 & \varepsilon^*_{\mathrm{vol}}/3 \end{bmatrix}$ [162]. With regard to the sample under study (a thick ~ 1 mm underlying tungsten substrate, with a thin helium-implanted layer ~ 2.8 μm sitting on top as shown in Figure 3.4), this implies an expansive strain of $\varepsilon^*_{\mathrm{vol}}/3$ in the X and Y directions. However, the boundary interface between the implanted-layer and the substrate along the in-plane directions, X and Y (indicated by the dotted line AA' and A'B in Figure 3.4), will prevent this expansion due to the need for geometrical continuity in the sample. Thus, an equal and opposite elastic compressive strain will be generated in the X and Y directions due to the presence of the boundary conditions. We refer to this elastic strain, generated in the sample in response to eigenstrain, as the correctional strain, represented by the tensor $\boldsymbol{\varepsilon}_{corr}$ with $\varepsilon_{corr_{11}} = \varepsilon_{corr_{22}} = -\varepsilon^*_{vol}/3$.

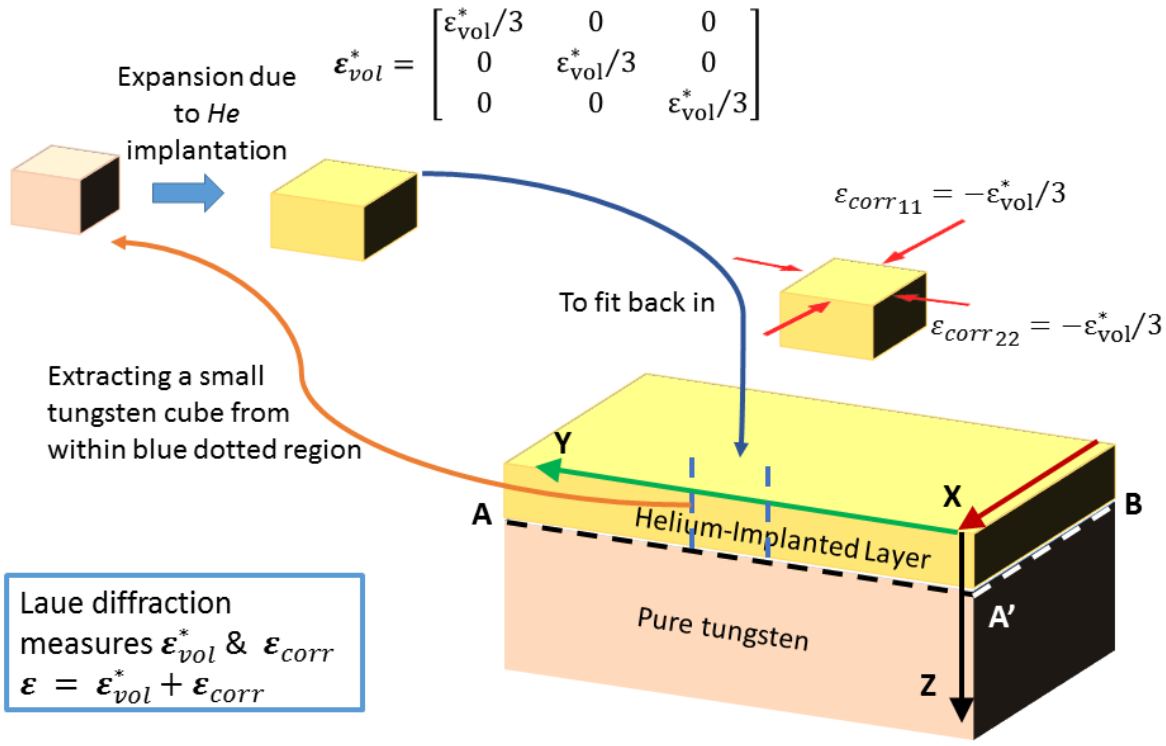


Figure 3.4 – Schematic representation of the volumetric eigenstrain induced by helium-implantation and the correctional elastic strain generated in response to it.

Eigenstrain when originating purely from plastic deformation (as in the case of shot-peening [163]), remains undetected by diffraction measurements as there is no change in the average lattice spacing in the process of plastic deformation. However, the eigenstrain induced in the sample by helium-implantation, brings about a change in the lattice parameter and is thus measurable by the diffraction experiments. It is similar to a thermal strain in this respect. The experimentally measured lattice strain in the sample ($\boldsymbol{\varepsilon}$), is thus an additive combination of $\boldsymbol{\varepsilon}^*_{vol}$ and $\boldsymbol{\varepsilon}_{corr}$. The in-plane components of $\boldsymbol{\varepsilon}^*_{vol}$ and $\boldsymbol{\varepsilon}_{corr}$, being of equal magnitude and opposite sign cancel. Thus, the resultant in-plane strain components, as measured by the diffraction, are approximately equal to zero i.e. $\varepsilon_{xx} = \varepsilon_{yy} \approx 0$. This is consistent with our measurements, as seen in Figure 3.5 and Figure 3.6 and discussed below in further detail.

Figure 3.5 and Figure 3.6 show the average of the direct strains measured (averaged over 0-2.5 μm depth) in the helium-damaged layer of the samples implanted with 300 appm of helium and 3000 appm of helium respectively. The corresponding line plots over the whole depth range of 0-10 μm, are provided in Appendix B in Figure B.2 and Figure B.3 respectively. It is expected that lattice distortion will be close to zero in the X and the Y directions, in order to maintain geometrical continuity with the underlying unimplanted substrate material [42], [164]. Consequently, lattice strains brought about by implantation-induced defects, must be accommodated in the out-of-plane (z) direction. This can be clearly seen for all samples in Figure 3.5 and Figure 3.6, where the out-of-plane ε_{zz} component is positive and significantly larger than the ε_{xx} and ε_{yy} components.

Figure 3.7 and Figure 3.8 show the average shear strains in the 2.5 μm implanted layer measured for samples implanted with 300 and 3000 appm of helium respectively. The corresponding line plots over the whole depth range of 0-10 μm, are provided in Appendix B in Figure B.4 and Figure B.5 respectively. The current experimental configuration and arrangement of the detectors is less sensitive to shear strains than direct strains [97]. Accordingly, the experimental uncertainty associated with the reported shear strains are somewhat larger than those of the direct strains. For example, in Figure 3.8, shear strain ε_{xy} for the W-3000He<111> is measured to be around 1×10^{-3}, contrary to our expectation of near zero deformation in the X and Y direction. However, considering the reduced sensitivity of the current experimental setup to the shear strain measurements, it is difficult to interpret the origin of these observations as they may well be experimental errors. To further analyse this aspect, future study has been planned at a modified experimental setup where we expect to have improved measurements of the shear strain components.

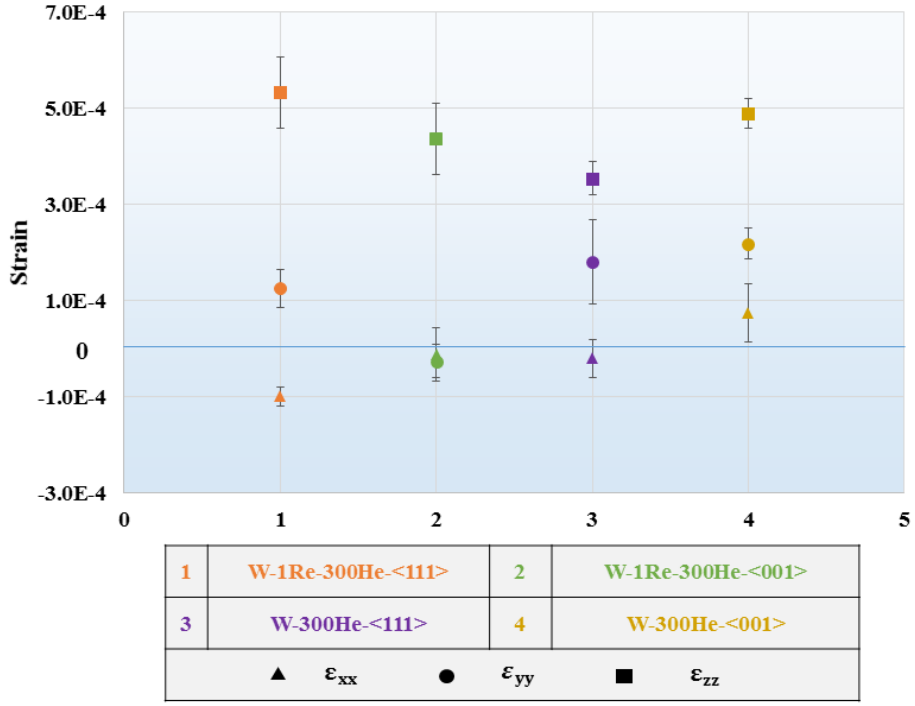


Figure 3.5 – Average of the direct strains in the 2.5 µm helium-implanted layer in the samples implanted with 300 appm of helium. The error bars show ±1 standard deviation.

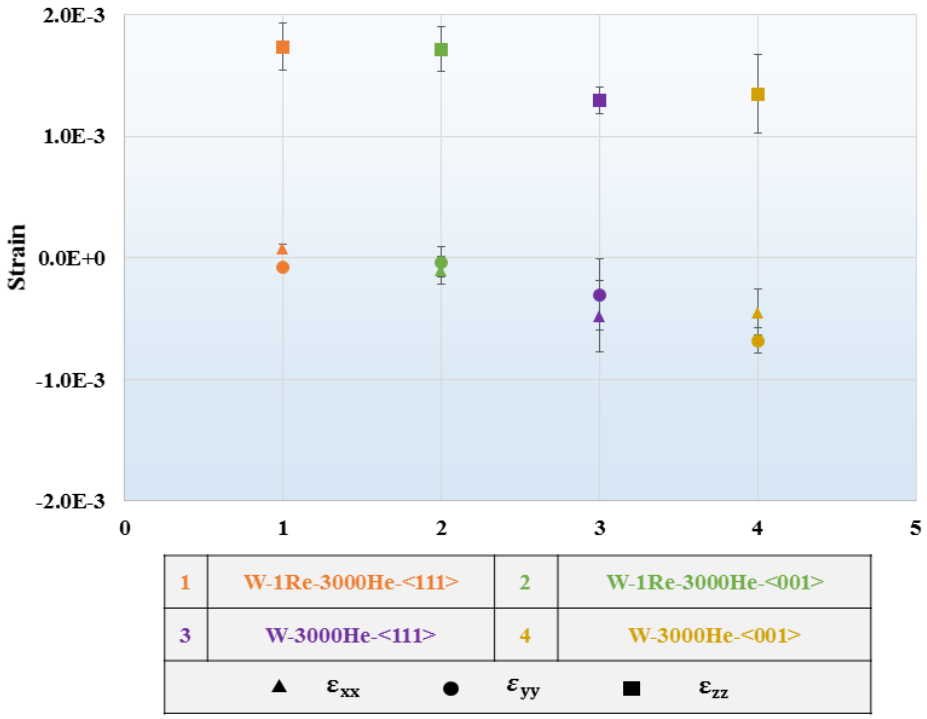


Figure 3.6- Average of the direct strains in the 2.5 µm helium-implanted layer in the samples implanted with 3000 appm of helium. The error bars show ±1 standard deviation.

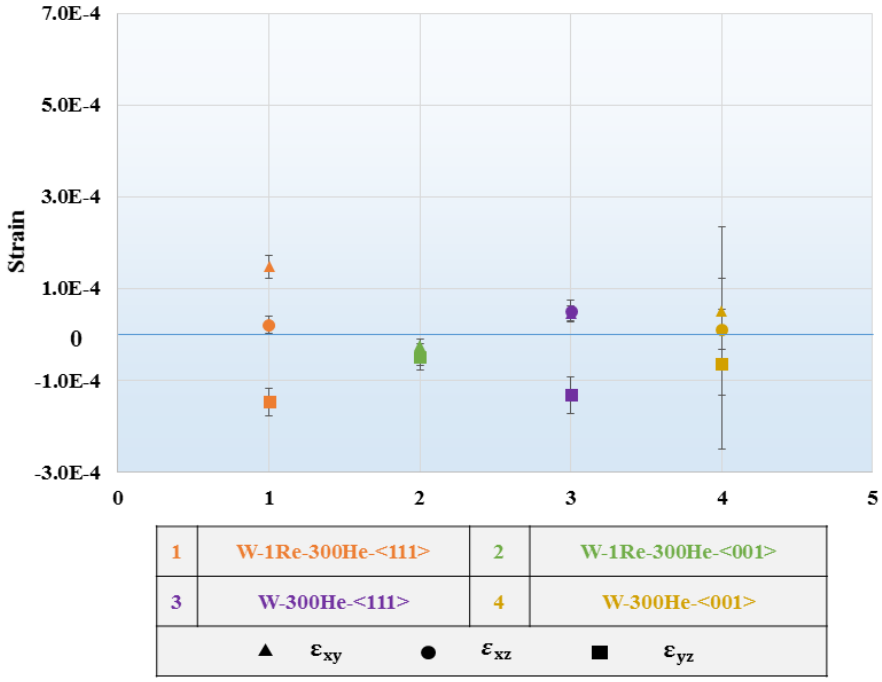


Figure 3.7 - Average of the shear strains in the 2.5 µm helium-implanted layer in the samples implanted with 300 appm of helium. The error bars show ±1 standard deviation.

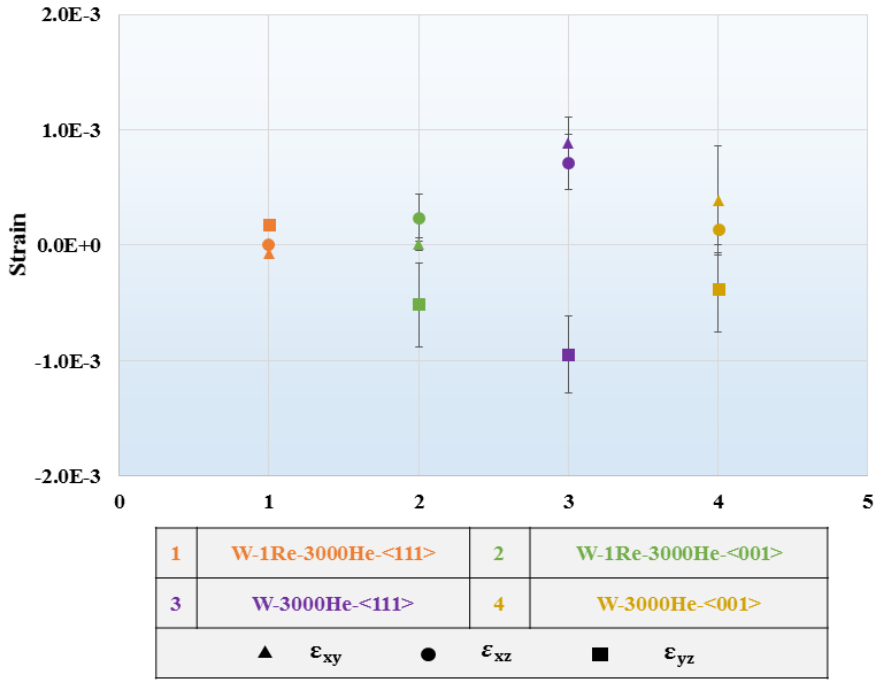


Figure 3.8 - Average of the shear strains in the 2.5 µm helium-implanted layer in the samples implanted with 3000 appm of helium. The error bars show ±1 standard deviation.

The direct strains can be interpreted in terms of lattice swelling associated with helium implantation and lattice defects generated in the process, as discussed below. It is interesting to note that the W-Re sample shows substantially less fluctuation of strains with depth than the W samples. This is particularly noticeable in the line plots in Figure B.2 and Figure B.3. Strain fluctuation in the implanted layer are indicative of a heterogeneous defect population, suggesting that the presence of Re leads to a more homogeneous distribution of defects. It is worth noting that the strains induced by the 300 appm helium implantation are rather small, on the order of a few 10^{-4}. Measurements of such small strains were made possible here by the improved diffraction setup at 34-ID-E, with new, high stability KB mirror mounts [99], [165] and a newly fabricated DAXM wire with reduced shape uncertainty.

At room temperature tungsten is almost perfectly elastically isotropic [88], [166], and hence ε_{zz} can be used to estimate the underlying eigenstrain $\boldsymbol{\varepsilon}^*_{vol}$. Let the lattice strain measured experimentally be given by the tensor $\boldsymbol{\varepsilon}$. The pure volumetric eigenstrain is given by $\boldsymbol{\varepsilon}^*_{vol}$ and the correctional strain tensor term accounting for the lateral constraints on the implanted layer is given by $\boldsymbol{\varepsilon}_{corr}$. In this regime of small strain, $\boldsymbol{\varepsilon}$ may be additively decomposed as

$$\boldsymbol{\varepsilon} = \boldsymbol{\varepsilon}^*_{vol} + \boldsymbol{\varepsilon}_{corr} \tag{3.3}$$

The volumetric eigenstrain tensor $\boldsymbol{\varepsilon}^*_{vol}$, is given by $\begin{bmatrix} \varepsilon^*_{vol}/3 & 0 & 0 \\ 0 & \varepsilon^*_{vol}/3 & 0 \\ 0 & 0 & \varepsilon^*_{vol}/3 \end{bmatrix}$. $\varepsilon_{corr_{11}} = \varepsilon_{corr_{22}} = -\varepsilon^*_{vol}/3$ due to the need for maintaining the geometrical continuity in the sample (shown by schematic in Figure 3.4) and thus we assume $\varepsilon_{xx} = \varepsilon_{yy} \approx 0$.

Considering Poisson effect

$$\varepsilon_{corr_{11}} = -\frac{\varepsilon^*_{vol}}{3} = \frac{1}{E}(\sigma_{corr_{11}} - \upsilon(\sigma_{corr_{22}} + \sigma_{corr_{33}})) \tag{3.4}$$

where, *E* is the elastic modulus and υ the Poisson's ratio. $\sigma_{corr_{33}}$ = 0 as there is a traction free boundary condition in the Z direction and $\sigma_{corr_{11}}$ is considered equal to $\sigma_{corr_{22}}$, owing to symmetry. The assumptions of traction free boundary condition and $\varepsilon_{xx} = \varepsilon_{yy} \approx 0$ are made here as the thickness of the implanted layer is only 0.3% of the total sample thickness i.e. the implanted layer is very thin compared to the substrate. Thus,

$$\varepsilon_{corr_{11}} = -\frac{\varepsilon^*_{vol}}{3} = \frac{1}{E}\left(\sigma_{corr_{11}} - \upsilon\left(\sigma_{corr_{11}} + 0\right)\right) = \frac{\sigma_{corr_{11}}}{E}(1-\upsilon) \tag{3.5}$$

Rearranging we get,

$$\sigma_{corr_{11}} = \frac{-E\varepsilon^*_{vol}}{3(1-\upsilon)} = \sigma_{corr_{22}} \tag{3.6}$$

Now $\varepsilon_{corr_{33}}$, may be written in terms of $\sigma_{corr_{11}}$ and $\sigma_{corr_{22}}$

$$\varepsilon_{corr_{33}} = \frac{1}{E}\left(\sigma_{corr_{33}} - \upsilon\left(\sigma_{corr_{11}} + \sigma_{corr_{22}}\right)\right) = \frac{2\varepsilon^*_{vol}\upsilon}{3(1-\upsilon)} \tag{3.7}$$

As per Eq. (3.3), $\varepsilon_{33} = \varepsilon^*_{vol_{33}} + \varepsilon_{\mathrm{corr}_{33}}$ i.e.

$$\varepsilon_{zz} = \frac{\varepsilon^*_{vol}}{3} + 2\left(\frac{\upsilon}{1-\upsilon}\right)\left(\frac{\varepsilon^*_{vol}}{3}\right) = \frac{\varepsilon^*_{vol}}{3}\left(\frac{1+\upsilon}{1-\upsilon}\right) \tag{3.8}$$

We note here, that the volumetric strain component of $\boldsymbol{\varepsilon}$, i.e. ε_{vol} is given by $(\varepsilon_{xx} + \varepsilon_{yy} + \varepsilon_{zz})$ and is different from the volumetric eigenstrain ε^*_{vol}. $\varepsilon_{vol} = \varepsilon_{zz}$ (as $\varepsilon_{xx} = \varepsilon_{yy} \approx 0$), would be equal to ε^*_{vol}, if $\upsilon = 0.5$. This does not apply for tungsten, which has $\upsilon = 0.28$.

The volumetric eigenstrain for each of the samples, estimated using Eq.(3.8) and the measured ε_{zz} strain, is listed in Table 3.2. Here, in each case, the average of ε_{zz}, measured between 0 - 2.5 μm was considered for the calculations. For the tungsten-rhenium alloy the same Poisson ratio as for pure tungsten (υ = 0.28) was assumed. We note that the addition of rhenium to tungsten [167] does not significantly alter the crystallographic properties of pure tungsten. The lattice constant measured in the tungsten-rhenium alloy samples, at depths greater than 7 μm below the sample surface, is 3.165±0.0009 Å. This is very close to the lattice constant for pure tungsten 3.16522±0.00009 Å [168] and to the value previously measured for material from the same batch of 3.165±0.0007 Å [42].

The effect of the three parameters varying between the samples can now be assessed: the helium dose, the presence of rhenium and the effect of grain orientation. We will deal with each aspect in turn. The average level of lattice strain for 300 and 3000 appm implanted samples (average taken over all four samples with 300/3000 appm helium) is 0.765×10^{-3} and 2.57×10^{-3} respectively. This corresponds to a ~ 240% increase in the underlying volumetric eigenstrain for a ten-fold increase in the implanted helium dose. The volumetric strain is closely linked to the defects produced by the helium-ion-implantation. Our observation suggests that the number of defects retained per injected helium ion in the 300 appm implanted samples is three times greater than in the 3000 appm implanted samples. Interestingly, this is consistent with previous thermal transport measurements on 300 appm and 3000 appm helium-implanted tungsten samples [80]. Here too an

approximately three times higher defect retention per helium ion was observed in the samples exposed to the lower helium dose.

Sample	**Average of ε_{zz} measured between 1-2 μm ($\times 10^{-3}$)**	**Calculated ε^{*}_{vol} ($\times 10^{-3}$)**
W-1Re-300He-<111>	0.533	0.899
W-1Re-300He-<001>	0.436	0.736
W-300He-<111>	0.355	0.599
W-300He-<001>	0.489	0.825
W-1Re-3000He-<111>	1.74	2.934
W-1Re-3000He-<001>	1.72	2.896
W-3000He-<111>	1.30	2.188
W-3000He-<001>	1.35	2.272

Table 3.2 – Volumetric eigenstrain associated with He-implantation in each of the samples, calculated from the measured ε_{zz} strain.

An interesting question concerns the origin of this dose dependence of defect retention per injected helium ion. Calculations and previous experiments [42] suggest that the defects in the implanted layer take the form of vacancies, self-interstitials (SIAs) or small clusters of both [169]. SRIM calculations [155] indicate that, under the present implantation conditions, approximately 60 Frenkel pairs are formed for every injected helium ion. Most of these Frenkel pairs recombine almost immediately and only a small fraction, a few % (although the exact fraction depends on the implanted helium dose), are prevented from recombining by the presence of helium [42]. Since helium has a strong affinity for vacancies and vacancies are in plentiful supply during helium implantation, helium atoms become trapped at vacancies. Once the helium has occupied a vacancy, it prevents recombination of this vacancy with a self-interstitial atom, leading to the retention

of some of the Frenkel pairs formed during implantation [77], [147]. Becquart et al. [153] pointed out, however, that helium only plays a dominant role in defect retention at higher injected concentrations, i.e. when helium is the dominant impurity. For low helium concentrations other impurities present in the sample, most notably carbon, are primarily responsible for preventing the recombination of the Frenkel pairs. This suggests that, in a sample without any impurities, defect retention in the 300 appm helium-implanted samples and the associated volumetric strain should be much lower (~ estimated strain based on 3000 appm value divided by 10) than the volumetric strain we observe. Hence impurities clearly play an important role in controlling implantation-induced lattice strains, especially at low damage doses.

With regard to impurities, the tungsten-rhenium alloys investigated here have an additional impurity in the form of the rhenium atoms. The presence of rhenium is important since it is one of the elements that will build up in tungsten armour components due to transmutation, with an expected concentration of ~ 3.8 at. % after five years of operation [9]. Considering the four samples implanted with 300 appm of helium (rows 1-4 in Table 3.2), and comparing the average volumetric strain across samples with and without rhenium, it is seen that the presence of rhenium is associated with a ~ 15% increase in strain. A similar analysis on the four samples with 3000 appm of helium (rows 5-8 in Table 3.2) shows a ~ 30% increase associated with the addition of rhenium. Next, if we focus on the four tungsten-rhenium alloy samples (W-1Re-300-<111>/<001> & W-1Re-3000He-<111>/<001>), and monitor the change in volumetric strain with the tenfold increase in the helium dose, here a ~ 256% increase in ε_{vol}^{*} is seen. This is slightly higher (relative percentage increase of ~ 35%) than the ~ 213%±5% increase in ε_{vol}^{*} seen in the group of four pure tungsten samples (W-300-<111>/<001> & W-3000He-<111>/<001>) when the helium dose is changed from 300 to 3000 appm.

These observations suggest that, compared to helium (max. concentration 0.3 at. %), rhenium, even at ~ 1 wt. % concentration has relatively little effect on defect retention. From first principle studies [170] it has been seen that Re binds quite weakly to vacancies (binding energy of ~ 0.22 eV), but its binding energy to SIAs is quite high (0.8 eV). Similar estimations have been obtained by object Kinetic Monte Carlo simulations of point defects in tungsten by Becquart et al. [153] and from first principle calculations based on density functional theory (DFT) [171]. Although the Re and the SIA are tightly bound, this mixed-interstitial can migrate easily using a non-dissociative mechanism with a low migration barrier of 0.12 eV [171]. In other words, this implies that even in the presence of Re, the migration of SIAs is not strongly affected i.e. the presence of rhenium will not significantly alter defect retention. Further DFT calculations showed that addition of rhenium to tungsten may improve its ductility by changing dislocation core structure and thereby reducing the critical stress required for plasticity to set in [32]. This is consistent with nano-indentation observations where the presence of rhenium in tungsten had no significant effect on the hardening behaviour [172]. Rather, it has been seen through DFT that presence of rhenium in tungsten actually enhances vacancy-interstitial recombination (suggested that the vacancy suppression occurs at isolated interstitials) and suppression of void swelling, leading to the idea that addition of rhenium to tungsten can improve its radiation-resistance [173]. This of course must be balanced with irradiation-induced clustering of rhenium that sets in at high damage doses and leads to substantial hardening as rhenium clusters act as efficient obstacles to dislocation motion [33], [35], [174].

To assess the effect of lattice orientation, diffraction measurements were made in two grains in each sample, a <111> and a <001> oriented grain. In W-300He sample, the <001> grain shows ~ 38% higher strain than the <111> grain, while the corresponding percentage increase in W-3000He sample is ~ 4%. For the W-1Re-3000He sample no

change in the volumetric strain is noticed between the grains. The W-Re-300He sample, on the other hand, shows a higher ε_{vol}^{*} in the <111> grain compared to the <001> grain. These results, based on a small sample size, are insufficient to provide a definite answer to the question of how the grain orientation influences helium-implantation-induced lattice swelling. However, our results do suggest that the effects of grain orientation are most prominent for low helium concentrations and diminish with increasing the helium dose.

3.5. Implications for Reactor Design

The findings from our experimental study have important implications for the design of future fusion reactors. The large dimensional change (lattice swelling) associated with helium-implantation damage in tungsten, and the associated stresses must be accounted for when estimating armour component fatigue life. In principal, this could be done using the framework recently proposed by Dudarev et al. [164].

A second important finding is the non-linear variation of defect retention as a function of injected helium dose. This effect must be properly characterised and models need to be developed for capturing this behaviour to allow reliable prediction of the evolution of the properties of tungsten armour. The reduced defect retention with increasing helium dose suggests that there may be a saturation regime, similar to observations in self-ion implantation damage in tungsten [58], [60], [175].

We also find that not all transmutation elements have a strong effect on defect retention. For design, one of the next key activities must be to map out the effect of different transmutation elements on defect retention as a function of concentration and damage level. This will require experimental effort, as well as computational models capturing the interaction of defects with transmutation elements. The results will directly feed into reactor

armour design, enabling the estimation of defects produced and retained, and predictions of the resulting distortions.

Finally our results suggest that grain-orientation dependent effects become insignificant, particularly with increasing helium dose, implying that texture control may not be necessary in this regard. This is good news, as it will allow the optimisation of texture to enhance other aspects of fusion armour performance. For example, <111> texture may be used, as it has been seen to have substantially lower erosion yield than <001> oriented grains [176], [177].

3.6. Conclusions

In summary, our results show that energy- and depth-resolved micro-diffraction provides an effective means of probing lattice strains caused even by quite low doses of helium implantation into tungsten. Increasing the dose of helium from 300 appm to 3000 appm causes an increase of ~ 240% in volumetric eigenstrain, indicating that the defect retention per injected helium atom is ~ 3 times higher at low helium doses. This highlights that implantation-induced lattice strains are not simply a linear function of dose, but follow a more complex relationship. Importantly defect retention is strongly depended on material composition and the presence of impurities. Analysis of W-1at.wt.% Re alloy samples showed that the presence of rhenium has a relatively small effect on defect retention in tungsten. Similarly grain orientation appears to only lead to minor changes in the retained defect population. This is important as it means that, at least as far as implantation-induced strains are concerned, tight control of the texture of tungsten armour components may not be necessary.

Chapter 4

Effect of helium on deformation behaviour of tungsten

Probing the defect microstructure produced by helium implantation in tungsten, at room temperature, is challenging since the defects formed are below the sensitivity of TEM (1.5 nm) [79]. Nevertheless, significant changes such as 30% increased hardness [81], 50% reduced thermal diffusivity [80] has been noticed in tungsten samples, with only 0.3 wt.% of helium at room temperature. This chapter examines in detail, the substantial effect helium has on the mechanical properties of tungsten using a combination of nano-indentation and micro-beam Laue diffraction measurements. The chapter content is in publication format and is based on article "*S. Das, D. E. J. Armstrong, Y. Zayachuk, W. Liu, R. Xu, and F. Hofmann, "The effect of helium implantation on the deformation behaviour of tungsten: X-ray micro-diffraction and nanoindentation," Scr. Mater., vol. 146, pp. 335–339, Mar. 2018*" [144].

4.1. Abstract

The effect of helium-implantation-induced defects on deformation behaviour is examined by comparing spherical nano-indents in unimplanted and helium-implanted regions of a tungsten single crystal. Helium-implantation increases hardness and causes large pile-ups. 3D-resolved X-ray micro-diffraction uniquely allows examination of the complex lattice distortions beneath specific indents. In the ion-implanted material we find reduced lattice rotations and residual strains due to indentation, indicating a more confined plastic zone. Together, our observations suggest that helium-induced defects initially act as efficient

obstacles to dislocation motion, but are weakened by the subsequent passage of dislocations, causing a reduction in work hardening capacity.

4.2. Introduction

Tungsten is a promising candidate material for plasma facing components in future fusion reactors due to its high melting point, its strength at high temperatures and low sputtering yield [6], [14], [15]. However, challenges arise from its low fracture toughness, high brittle to ductile transition temperature (BDTT) [16] and poor machinability.

In the fusion reactor environment, armour components will be exposed to high temperatures (> 900 °C) and bombardment with high-energy fusion neutrons (14.1 MeV) [6]. Interaction of these energetic neutrons with the tungsten lattice leads to collision cascades and the subsequent formation of defects in the material [7]. Furthermore, it causes transmutation, resulting in the formation of rhenium, osmium and tantalum, as well as hydrogen (H) and helium (He) [8], [9]. At the anticipated operating temperatures, interstitial mobility of these gasses is high, allowing them to diffuse to defects, cracks or grain boundaries, resulting in embrittlement and hardening [12]. Hydrogen and helium will also be introduced into the material at plasma-facing surfaces exposed to large fluences of both elements [10], [11].

The defect microstructure in tungsten is heavily influenced by the strong binding of helium to vacancies [169]. Previously nano-indentation showed a substantial increase in the hardness of tungsten after helium-ion implantation [79]. Interestingly helium ion implantation had a much greater effect on hardness than collision cascade damage caused by self-ion bombardment. This suggests that the presence of helium enhances defect retention and/or increases obstacle strength [79].

The effect of helium implantation on the mechanical properties of tungsten is potentially life limiting for the divertor, with significant economic consequences for fusion power. Resolving this problem requires a clear picture of the mechanisms governing the interaction of implantation defects with dislocation-mediated inelastic deformation. Experimentally these interactions are challenging to probe and at present remain poorly understood.

In this study, we consider spherical nano-indents in helium-implanted and unimplanted regions of the same tungsten single crystal, enabling a direct comparison and ensuring that any observed changes between the two regions are solely due to helium-implantation-induced defects. Using synchrotron X-ray micro-diffraction we are able to probe the lattice rotations and residual lattice strains beneath specific indents. These measurements uniquely provide access to the full, complex 3D lattice distortion field, whereas FIB lift-out and SEM/TEM observations, for example, only capture one slice though the indent. Importantly, since these X-ray measurements are non-destructive, the residual stress state remains unaltered. This 3D information is essential to unambiguously assess the underlying deformation fields that lead to the changes in surface morphology examinable by AFM or SEM (see exemplary finite element simulation in Appendix C). Our results reveal striking differences that are discussed in terms of the interaction between helium-induced defects and dislocations.

4.3. Sample preparation & ion-implantation

A 5 mm diameter, 0.8 mm thick disk with [001] out-of-plane orientation was cut from a tungsten single crystal (99.99% purity). The [001] surface was mechanically ground and then polished using diamond paste. A final chemo-mechanical polishing step with 0.1 μm colloidal silica suspension produced a high quality surface finish.

Part of the sample was implanted with helium ions at 298 K using a 2 MeV ion accelerator at the National Ion Beam Centre, University of Surrey, UK. Implantation was carried out at room temperature (298 K) and using a raster scanned beam to ensure a uniform implantation dose. A combination of different ion energies and fluences was used to obtain a near uniform helium ion concentration in excess of 3000 appm (details in Appendix A) within a ~ 2.8 μm thick implanted layer [12], [42], [154]. Figure 4.1 (a) shows the implantation profile estimated using the SRIM code [155] (displacement energy of 68 eV, single-layer calculation model [156]). Between 0 and 2.8 μm depth, a helium ion concentration of ~ 3110 ± 270 appm is obtained with an associated damage of 0.24 ± 0.02 displacements per atom (dpa). Recoils induced by helium implantation have predominantly low energy, suggesting Frenkel pair formation as the main damage mechanism [42]. Since vacancy mobility is low at room temperature little defect clustering is expected [79], [178], [179].

4.4. Nano-indentation

Nano-indentation was performed using a MTS NanoXp with a spherical, ~ 4.2 μm radius diamond indenter tip. Indents were made to a maximum displacement of 500 nm with a 50 μm spacing between indents. Use of a spherical, axi-symmetric indenter removes the additional complexity, associated with in-plane indenter orientation relative to the crystal, found in Berkovich indentation. Figure 4.1 (b) shows the load-displacement curves of the two indents considered in more detail below.

The load displacement curves show an initial Hertzian elastic response that is almost identical in the unimplanted and implanted material. This is as expected since ion-implantation-induced changes in elastic modulus are small [42], [148]. At ~ 25 nm depth the unimplanted sample shows a large pop-in, indicative of dislocation nucleation in the

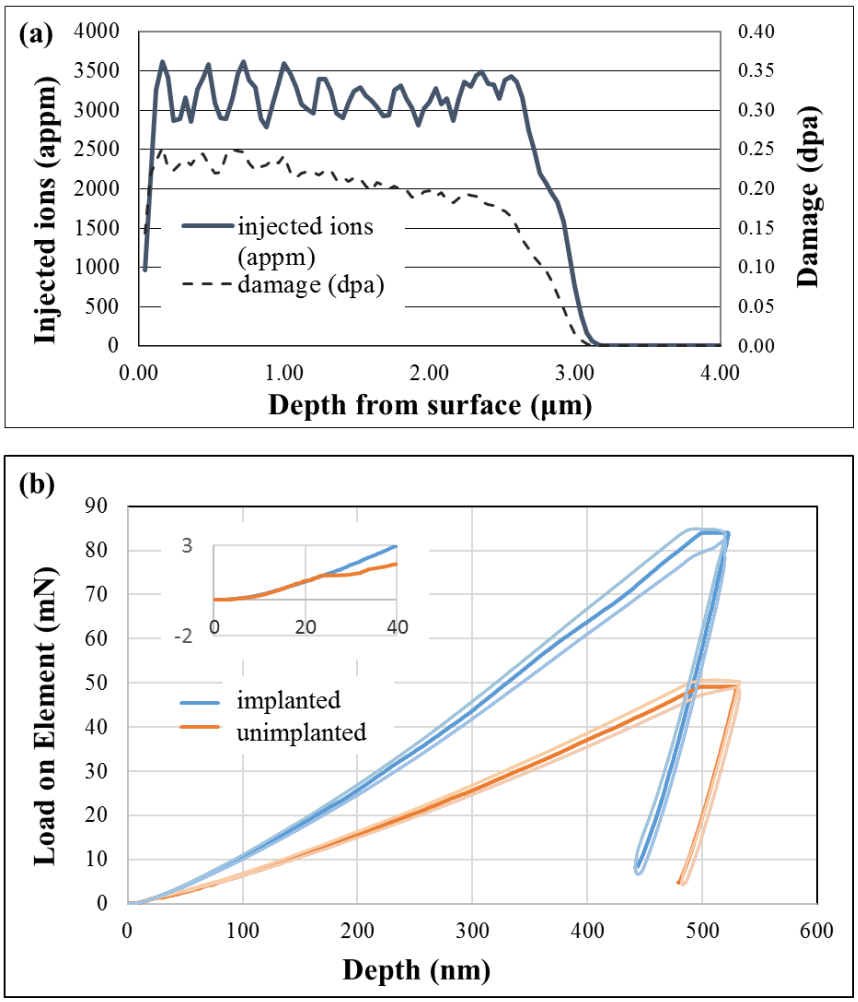


Figure 4.1 – (a) Profile of injected helium ion concentration calculated by SRIM (solid line) and the anticipated displacement damage (dashed line) plotted as a function of depth in the sample. (b) Load versus displacement curves for spherical indentation of the unimplanted and helium-implanted sample (faint lines = mean ± one standard deviation computed over 16 indents).

initially relatively defect free material at the onset of plastic deformation [180]. In the implanted sample, there are no obvious pop-ins. This indicates an easier nucleation of initial dislocation loops due to the presence of helium-implantation-induced defects. At larger indentation depths the implanted sample shows a significantly greater indentation load than the unimplanted material, suggesting a substantial hardening due to helium-implantation-induced defects. This behaviour agrees well with previous Berkovich indentation of helium-implanted tungsten [79], [81], [154].

4.5. SEM micrographs of indents

SEM micrographs of the nano-indents, recorded using a Zeiss Merlin FEG SEM, are shown in Figure 4.2 (a) and (b). Little pile up is present in the unimplanted sample. The implanted material, on the other hand, shows a much larger, localised pile up around the indent tip. A similar trend was observed by Beck et al. who reported a substantial increase in pile up around Berkovich indents in helium-implanted tungsten of unidentified orientation [81]. Unfortunately, in their work the relative contributions of ion-implantation defects and indentation geometry to this effect could not be distinguished. Interestingly, in our study, the effects of crystallography are clearly visible: The pile-up shows a strong dependence on the in-plane crystal orientation. Along <100> directions the pile-up is relatively small, whilst along <110> directions a larger pile-up is present. This is very clear in the implanted sample, where, due to the orientation dependent large pile up, the indenter impression assumes a square shape (sides of the square are along the <100> direction). Such pile up patterns, localised in defined zones around the indent, and exhibiting a four-fold symmetry of out of plane displacement profile, have been previously observed in nano-indented <001> oriented Cu single crystals [181], [182]. It can further be noted that the pile-up in the implanted material shows a number of distinct steps indicated by small arrows in Figure 4.2 (b). This suggests a slip localisation, similar to the dislocation channel formation reported in irradiation-damaged fcc metals [68], [183].

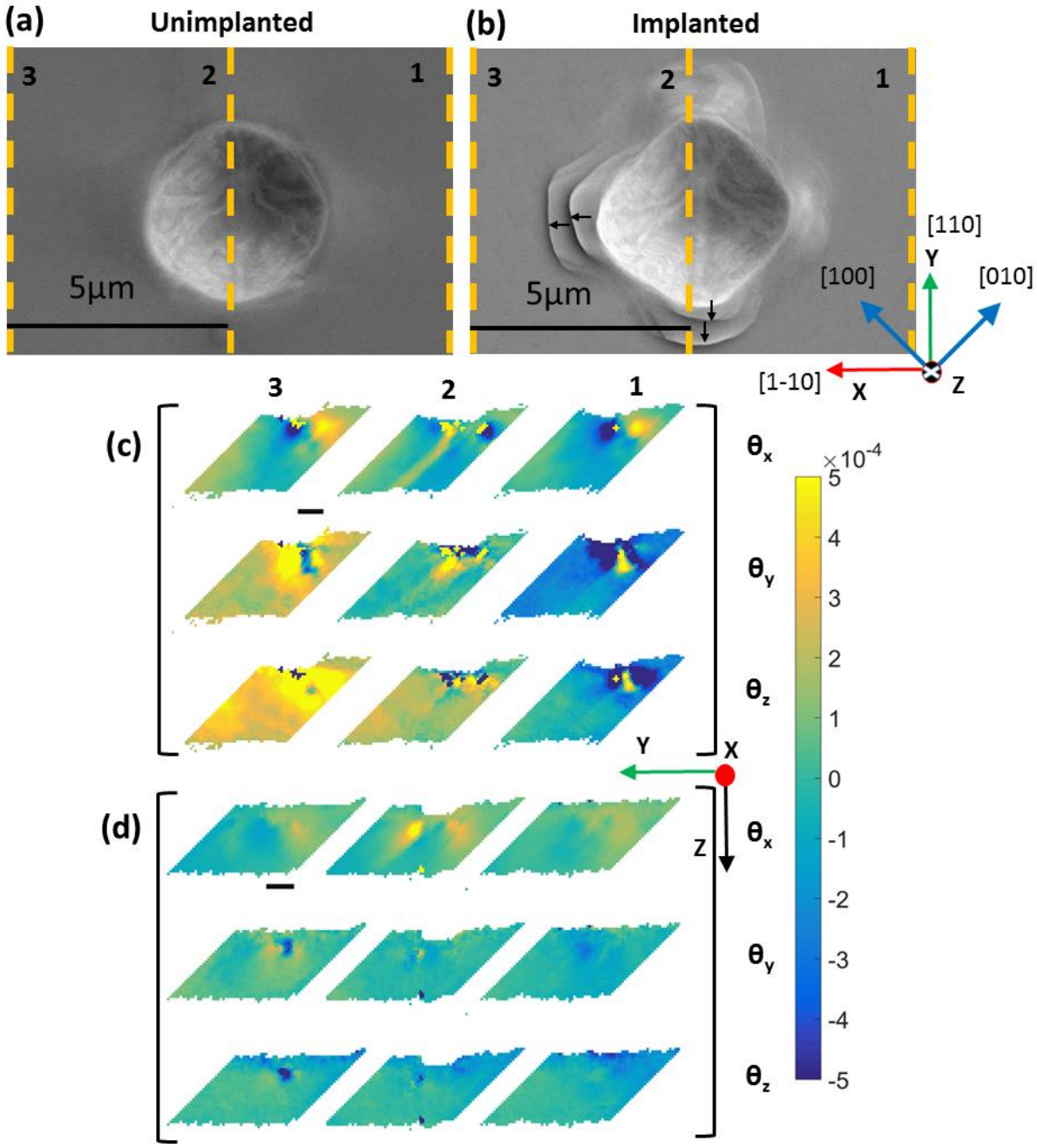


Figure 4.2 – (a) and (b) SEM micrographs of the sample with the X, Y, Z coordinate frame superimposed and showing the relative orientations of [100] and [010] crystal axes. (a) Shows an indent in the unimplanted region, whilst (b) shows an indent in the implanted material. (c) and (d) Lattice rotations in radians about the X, Y, and Z axes (rows) shown on virtual Y-Z slices through the sample at 3 different X positions for each indent. The locations of slices are shown as yellow lines in the SEM micrographs. Scale-bars correspond to 5 µm.

4.6. Laue measurements of lattice distortions

Micro-beam Laue diffraction measurements were carried out at beamline 34-ID-E, Advanced Photon Source, Argonne National Lab, USA. This instrument allows measurements of lattice orientation with sub-micron 3D resolution using the Differential Aperture X-ray Microscopy (DAXM) technique. A detailed description of the DAXM technique and the 34-ID-E instrument is provided in Section 2.2.2.1, Section 3.3.3 and elsewhere [94], [157], [158]. Here a polychromatic X-ray beam (7 – 30 keV), focussed to a size of ~ 500 nm, was used and measurements were carried out to a depth of 20 µm beneath the ion-implanted surface. Laue diffraction patterns contained 30+ peaks and were indexed and fitted using the LaueGo software package (J.Z. Tischler: tischler@anl.gov) to extract both lattice orientation and the full deviatoric lattice strain tensor at each measurement point in 3D space.

Lattice rotations, θ_x, θ_y and θ_z, due to nano-indentation, refer to changes in crystal orientation compared to the pristine (unimplanted and undeformed) single crystal. The right-handed coordinate frame used here, and the corresponding crystal directions, are shown in Figure 4.2 (a) and (b). Figure 4.2 (c) and (d) show lattice rotation maps about all three axes for indents in the unimplanted and implanted material respectively. These rotations are plotted on virtual YZ slices through the sample at three X positions (indicated by dashed yellow lines Figure 4.2 (a) and (b)). Positions 1 and 3 correspond to slices 5 µm before and after the indent centre respectively, while position 2 corresponds to a slice through the indent centre.

In the unimplanted sample, lattice rotations are significantly larger than in the implanted material. However, both show similar patterns of lattice rotation variation at the different X positions (seen clearly in Figure C.2 in Appendix C). Schematic of the lattice

rotations expected to be induced by nano-indentation is shown in Appendix D. The lattice rotations observed here are as expected; θ_y is negative (anti-clockwise rotation) before the indent centre (position 1) and positive after the indent centre (position 3). For θ_x a similar pattern is observed with a positive lobe to the right and a negative lobe to the left at positions 1 and 3. At the indent centre, rather than clear positive and negative lobes, a rapidly varying arrangement of lattice rotations is observed beneath the indent.

A common assumption in spherical indentation is that, compared to sharper indenters, there is a smooth, well-defined stress state under the indenter tip [86], [184]. In fact, tungsten, being almost perfectly elastically isotropic, is perfect for illustrating this. However, the measured lattice rotations show that in fact even a small amount of plasticity can lead to much more complex lattice distortions. At the indent centre, the implanted and unimplanted materials show completely different lattice rotation structures. The magnitude of lattice rotations far from the indent centre is substantially larger in the unimplanted than the implanted material, suggesting a more confined plastic zone in the implanted case.

Strain information was extracted from the Laue diffraction data using the method described by Chung and Ice [91]. As the lattice strain tensor is symmetric, six strain components are shown in Figure 4.3. Figure 4.3 (a) and (b) show visualisations of the measured sample volume, coloured according to the diffracted intensity. The indent centre is indicated by the intersection of the XZ and YZ planes superimposed on Figure 4.3 (a) and (b). Experimentally measured lattice strains on these planes in the unimplanted and implanted sample are shown in Figure 4.3 (c) - (f). Strain plots for the XZ plane are shown in Figure C.3 in Appendix C.

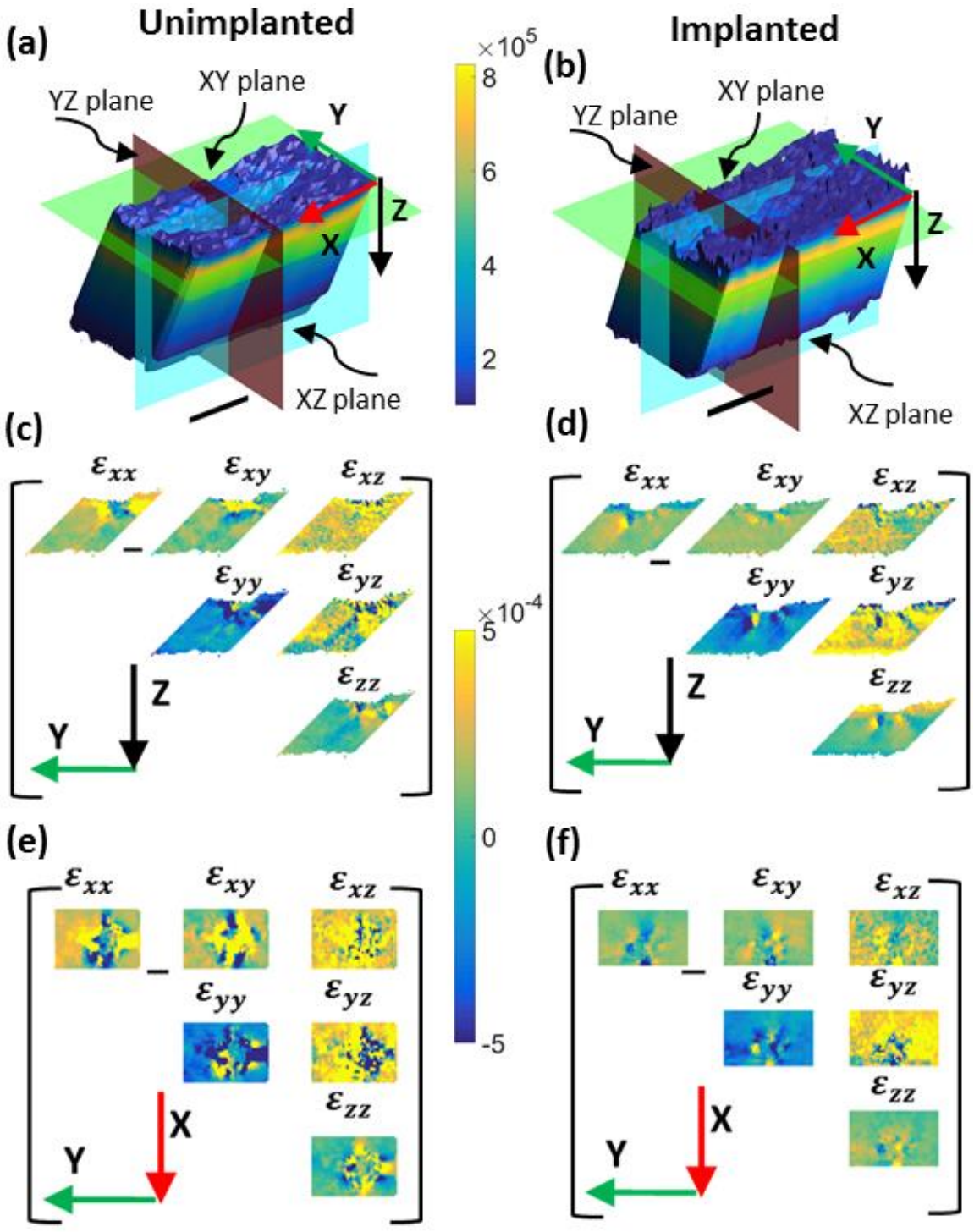


Figure 4.3 – (a) and (b) Three-dimensional rendering of the measured sample volume, coloured by scattered intensity. The top of the rendered volume corresponds to the sample surface, parallel to the XY plane. The intersection of XZ and YZ planes marks the indent centre. Six components of the measured deviatoric elastic strains tensor plotted on the YZ plane, (c) and (d), and on the XY plane, (e) and (f). (a), (c) and (e) are for the unimplanted sample; (b), (d) and (f) are for the implanted sample. Scale-bars correspond to 5 μm.

The differences in the residual elastic strain fields beneath the indent in the unimplanted and implanted material are striking. Strain magnitudes, particularly for the direct strain components and the ε_{xy} shear component, are significantly smaller in the implanted sample, suggesting a more confined plastic zone. The trend of compressive and tensile strains is similar in both, with the unimplanted sample showing large strain fields even far away from the indent centre. In the XY plane (parallel to the sample surface Figure 4.3 (e) – (f)), four-fold symmetry of the strain distribution can be seen, consistent with the pile-up patterns in SEM micrographs (Figure 4.2 (a) and (b)).

Implantation with helium results in the formation of small di-helium-vacancy complexes to which the self-interstitial atoms remain strongly attached [42], [77]. The greater hardness of the implanted material shows that the small helium-induced defects, unresolvable by TEM [79], act as surprisingly strong obstacles to dislocation motion. Here the presence of slip steps in the implanted material is interesting, as it indicates a localisation of deformation and supports the formation of dislocation channels. We hypothesise that gliding dislocations help to recombine vacancies and self-interstitial atoms, thus sweeping out channels with reduced defect density in which subsequent dislocations can propagate more easily, thus resulting in slip-step formation.

In other neutron-irradiated bcc materials, for instance vanadium, dislocation channels have been observed on {112} and {110} planes, even at low damage levels of 0.012 dpa [185]. The slip steps observed here in <110> directions in Figure 4.2 (b) are consistent with this. The formation of dislocation channels with reduced obstacle concentration has been previously reported to lead to reduced strain hardening capacity [186] or work softening[187]. This is consistent with the increase in pile-up we observe in

the implanted material. Indeed simulations by Oliver and Phar have previously linked increase pile-up to reduced work hardening capacity [85].

In summary, we have observed localisation of pile-up, formation of dislocations channels and a more confined plastic zone associated with spherical nano-indents in helium-implanted tungsten. Our results suggest that helium-implantation-induced defects initially act as efficient obstacles to dislocation motion, but are removed by interaction with passing dislocations. This behaviour differs markedly from observations in heavy ion irradiated tungsten where the opposite effect, i.e. a suppression of pile-up, has been reported [60]. This raises the question why the interaction of dislocations with helium filled implantation-induced defects is so different to interaction with defects without helium. The exact mechanism that governs this interaction and the fate of the helium remain unclear. We hope that these new detailed observations will stimulate the interest of the modelling community to elucidate the interaction of implantation-induced defects with glide dislocations. This is of particular importance since increased hardness and reduced work hardening capacity are detrimental to material ductility, a key concern for long-term structural integrity of future tungsten based diverter concepts.

Chapter 5

CPFE modelling of helium-damage in tungsten

In Chapter 4, we hypothesised that helium irradiation in tungsten results in hardening followed by strain-softening during deformation. This is considered to be the cause for confined distortion fields and slip steps around indents in helium-implanted tungsten. This chapter focusses on exploring this hypothesis using a CPFE formulation which captures the key mechanisms of interaction of the helium irradiation defects with the gliding dislocations. The chapter is broken into three sections.

Section 5.1 introduces crystal plasticity simulation of indentation in pure tungsten. Predictions of the CPFE model are examined by direct comparison with corresponding observations from Laue diffraction. In this context, fundamental principles associated with the analysis of plastic deformation field, such as computation of fields of lattice distortions and geometrically necessary dislocation (GND) density, including "curl" operation and optimisation techniques for GND computation are discussed in detail. In **Section 5.2**, the CPFE formulation of helium-implanted tungsten is developed. Indentation is simulated for 3000 appm helium-implanted <001>-oriented tungsten single crystal. Accuracy of predictions is examined by direct comparison with corresponding experimental observations, from HR-EBSD and X-ray micro-diffraction. The chapter ends with **Section 5.3**, where the viability of the CPFE formulation is assessed by performing simulations of indentation of implanted-tungsten samples of various orientations and comparing with experimental observations.

5.1. Consistent determination of GND: CPFE & Diffraction study in tungsten

This section is in publication format and is based on article "*S. Das, F. Hofmann, and E. Tarleton, "Consistent determination of geometrically necessary dislocation density from simulations and experiments," Int. J. Plast., vol. 109, pp. 18–42, May 2018*" [188].

5.1.1. Abstract

The use of Nye's dislocation tensor for calculating the density of geometrically necessary dislocations (GND) is widely adopted in the study of plastically deformed materials. The "curl" operation involved in finding the Nye tensor, while conceptually straightforward has been marred with inconsistencies and several different definitions are in use. For the three most common definitions, we show that their consistent application leads to the same result. To eliminate frequently encountered confusion, a summary of expressions for Nye's tensor in terms of elastic and plastic deformation gradient, and for both small and large deformations, is presented. A further question when estimating GND density concerns the optimisation technique used to solve the under-determined set of equations linking Nye's tensor and GND density. A systematic comparison of the densities obtained by two widely used techniques, L^1 and L^2 minimisation, shows that both methods yield remarkably similar total GND densities. Thus the mathematically simpler, L^2, may be preferred over L^1 except when information about the distribution of densities on specific slip systems is required. To illustrate this, we compare experimentally measured lattice distortions beneath nano-indents in pure tungsten, probed using 3D-resolved synchrotron X-ray micro-diffraction, with those predicted by 3D strain-gradient crystal plasticity finite element calculations. The results are in good agreement and show that the volumetric component of the elastic strain

field has a surprisingly small effect on the determined Nye tensor. This is important for experimental techniques, such as micro-beam Laue measurements and HR-EBSD, where only the deviatoric strain component is measured.

5.1.2. Introduction

Before the development of crystal plasticity finite element formulations, phenomenological continuum models were used to describe plastic deformation in materials. Without delving into the underlying microstructural processes, these approaches, calibrated by experiments, could capture plasticity at the macroscopic scale [124], [189]. Their great advantage is simplicity, however a lack of physical basis severely limits their predictive capabilities, especially for processes where microstructural heterogeneity is important.

Crystal plasticity finite element (CPFE) formulations address this issue by explicitly modelling plasticity in terms of crystallographic slip at the grain scale [190]. Popularity of these formulations has increased dramatically as they directly account for complex interactions between individual grains of polycrystals and the resulting locally heterogeneous loading. Beginning from 1982, when it was first introduced by Peirce et al. [128], the CPFE technique has developed to span a range of constitutive and numerical formulations, applicable to a large number of problems. For example CPFE has been used to simulate the development of microstructures and the consequent effect on the macroscopic material response [191], to simulate surface roughening in thin film mechanics problems [192], grain-boundary and interface mechanics [193], [194], strain-gradient effects [130], [195], polycrystalline morphology and texture, the necessary conditions (energy) for crack nucleation [196], geometrically necessary dislocations (GNDs) [197], creep and high temperature deformation [198], texture formation [199], deformation twinning [200], multiphase mechanics [201] etc. Importantly CPFE methods can be easily

adapted to different material systems, simply by modifying the crystallographic slip law. CPFE has been applied to a diverse range of not only metals [195], [198], [201], [202], but also rocks [203]. Furthermore CPFE has been used across a range of length scales, from single crystals [182], [204] to polycrystals [137] and multiscale applications combined with ab initio calculations [205]. CPFE has also been used with other modelling techniques such as continuum dislocation dynamics, and nonlinear thermoelasticity to simulate the response of materials under extreme dynamic loading [206].

In the early 70s, empirical viscoplastic formulations were primarily used, based on the "flow-potential" approach proposed by Rice [207] for time-dependent plastic deformation. Subsequent works of Rice and Asaro [199] and Peirce and Needleman [128], focused on the analysis of non-uniform, localised deformation of ductile crystals, where crystal slip was simulated by a rate-independent, elastic-plastic relation, following the Schmid law. Owing to computational restrictions, their simulations involved a simplified scenario of a single slip, or two symmetric slip systems.

With increasing computational power, a wide range of microstructure-based multi-scale plasticity models has emerged. These include various grain- and sub-grain scale problems, as well as complex 2D, 3D grain morphologies. The introduction of strain gradient terms in the constitutive law marked a major step forward, making it possible to capture experimentally observed size effects. Numerous strain gradient plasticity (SGP) formulations have been proposed, for example by Fleck and Hutchinson [87], [131], Gao, Huang, Nix and Hutchinson [132], Arsenlis and Parks [133], Cheong and Busso [134], Gurtin and Anand [135], Dunne et al. [130] and Fleck and Willis [208], [209]. These approaches have enabled accurate simulations of inelastic, scale-dependent deformation phenomena such as the increasing hardness of metals and ceramics with decreasing indenter

size in indentation simulations [182], or Hall-Petch grain size strengthening effect [140], [192], [210]. SGP phenomenological formulations have also been extended to calculate the fraction of the rate of plastic work converted into heat, by taking into account a strain dependent factor to include the locked in strain energy around statistically stored dislocations [211].

In particular, SGP formulations helped to numerically simulate the length-scale effects and production of GNDs associated with non-uniform plastic deformation. Smaller characteristic length-scales lead to steeper strain gradients and hence higher GND densities, causing a size effect as flow stress depends on dislocation density [108]. Liu et al. [212] compared experimental and theoretical evaluations (using tension and torsion on polycrystalline copper wires) of three phenomenological theories of strain gradient plasticity, to show that the size effects seen in plastic flow is primarily due to the GND density generated as a result of plastic strain gradients. Using both mechanism-based and phenomenological SGP theories, Paneda et al. [213] showed localised strain hardening near crack tips, promoted by GNDs. Compelling as the results are, experimental techniques are required to confirm these numerical simulations. Recently, another method, the critical thickness theory (CTT) has been used to give a physical insight into the size-effect, particularly at the initial yield stage, when distinct strain gradient and GNDs may not be present [214]. By considering the misfit strain between an epitaxial layer and substrate, CTT aims to establish the thickness of the misfitting epitaxial layer, beyond which an enhancement in yield strength is expected. The authors propose that by comparing the CTT predicted yield strength to the strain-gradient enhanced yield strength predicted by SGP theory, a link between the material length-scale in SGP and physical quantities (e.g. Burgers' vector magnitude) may be established [214].

In strain gradient CPFE formulations, plastic deformation is accounted for by dislocation glide on active slip systems and the deformation gradient is linked to the lattice curvature and in turn to the additional GNDs, generated in the slip systems, to accommodate this lattice curvature. The length-scale effect within the concept of GNDs is captured here by using Nye's formulation of the dislocation tensor [108]. In a recent study, Lyu et al. [210] modelled crystal plasticity using a continuum dislocation dynamics model (CDD) and used this together with a viscoplastic self-consistent model to study the evolution of dislocation densities in multi-phase steels.

To calculate GND density, the closure failure of a suitable Burgers' circuit can be considered [108], [115]. Using Stokes theorem, this can be recast as the computation of the "curl" of the deformation gradient to form the dislocation or Nye tensor [108]. Whilst straightforward conceptually, this step has been marred with inconsistencies. A review of the literature reporting GND density calculations shows a wide range of different curl definitions being used, often with erroneous applications of ± signs, misplaced indices and missing transpose operations. These errors will lead to unphysical results. For example a missing transpose operation effectively corresponds to swapping of Burgers' vector and line direction, resulting in incorrect dislocation densities. If a minus sign is erroneously placed then left handed screw densities become right handed and edge dislocation densities have their extra half plane on the opposite side of the slip plane. The first key goal of this paper is to compare the three most commonly used curl definitions and to establish the correct expressions to be used.

A further question in the computation of GND density concerns the optimisation technique used to solve the under-determined set of equations linking the curl of the deformation gradient and GND density. Two optimisation techniques, L^1 and L^2, are

commonly employed. Each yields a different solution and very few studies [111], [215] have investigated the differences in the results they produce. Here we carry out a systematic comparison of the GND densities predicted by both methods to determine their applicability in different scenarios.

For the validation of strain gradient CPFE models, a direct comparison to experiments performed at the same length-scale is essential. Here we present experimental measurements and strain gradient CPFE calculations of the lattice distortions beneath a spherical nano-indent in a tungsten single crystal. Experimental techniques such as electron back-scattered diffraction (EBSD), high-resolution EBSD (HR-EBSD), high-resolution digital image correlation (HR-DIC) are commonly used to measure lattice distortions in two-dimensions, for example studies by [216], [197], [217], [142], [218], [219] etc. Barabash et al. [220] showed how GNDs and the effective strain gradient change the white beam Laue patterns of shocked materials. With the aim of capturing the GND formation in plastic deformation, we use the synchrotron X-ray micro-Laue diffraction technique to non-destructively probe the full lattice rotation and residual elastic strain field with 3D spatial resolution, and without altering the residual stress state. Using strain gradient CPFE calculations we carry out a detailed 3D simulation of the same experiment. The experimentally measured and predicted lattice rotations, strains and GND densities are compared in detail. This gives rise to several interesting questions, for example concerning the effect of the volumetric elastic strain on GND density calculations, since Laue diffraction only measures the deviatoric lattice strain tensor [91]. This question is examined by modelling the experimentally recorded data using the strain gradient CPFE calculations.

We begin by describing the different definitions for calculating the curl of a second-order tensor. This is followed by a review of the theoretical framework of the computation

of the dislocation tensor and GND density. Based on this the expressions for the dislocation tensor in terms of elastic or plastic deformation gradient, as well as lattice strains and rotations, are discussed. Next, a comparison of nano-indentation-induced lattice distortions measured by Laue diffraction and predicted by strain gradient CPFE simulations is presented. Finally, the effects of L^1 or L^2 optimisation techniques, and volumetric elastic strain on the computation of GND densities are explored.

5.1.3. Theoretical Background

5.1.3.1. Computing the Curl of a second-order tensor

As noted by Robert W. Soutas [221], there are several different definitions in use for computing the curl of a second order tensor. Here, three different approaches to the curl computation are discussed. Importantly we show that, if used consistently, they all lead to the same end result.

Let $\boldsymbol{P}$ and $\boldsymbol{V}$ be general second-order tensors. The *km* component of the pre-curl of $\boldsymbol{P}$ is denoted as $(\nabla \times \boldsymbol{P})_{km}$, while the post-curl is $(\boldsymbol{V} \times \nabla)_{km}$ [221]. In component form these may be stated as

$$\text{Precurl: } R_{km} = (\nabla \times \boldsymbol{P})_{km} = \in_{ijk} P_{jm,i} \tag{5.1.1}$$

$$\text{Postcurl: } S_{km} = (\boldsymbol{V} \times \nabla)_{km} = -\in_{ijm} V_{kj,i} \tag{5.1.2}$$

where, $\in_{ijk}$ is the permutation tensor. An alternative third definition (referred to as "curl3" through-out this text) is commonly used in computational crystal plasticity studies, for example by Arsenlis and Parks [133] and Cermelli and Gurtin [222]:

$$\text{curl3: } Q_{km} = (\nabla \times \boldsymbol{V})_{km} = \in_{ijk} V_{mj,i} \tag{5.1.3}$$

The derivation of each of these three curl formulae, in tensor notation, is shown in Appendix E. **Comparing the precurl (Eq. (5.1.1)) and curl3 (Eq. (5.1.3)), it can be seen that R_{km}, the precurl of $\boldsymbol{P}$, will be equal Q_{km}, the curl3 of $\boldsymbol{V}$, when $\boldsymbol{V} = \boldsymbol{P}^{\mathrm{T}}$.**

$$R_{km} = (\nabla \times \boldsymbol{P})_{km} = \in_{ijk} P_{jm,i} = \in_{ijk} P^{\mathrm{T}}_{mj,i} = \in_{ijk} V_{mj,i} = (\nabla \times \boldsymbol{V})_{km} = Q_{km} \quad (5.1.4)$$

The post-curl definition is the negative transpose of curl3. This can be shown as

$$\begin{aligned} \text{Postcurl: } S_{km} &= (\boldsymbol{V} \times \nabla)_{km} = -\in_{ijm} V_{kj,i} = -(\in_{ijk} V_{mj,i})^{T} \\ &= -(Q_{km})^{T}. \end{aligned} \quad (5.1.5)$$

Explicit versions of Eq. (5.1.4) and (5.1.5), in component form, are provided in Appendix E. In summary, for any second-order tensor $\boldsymbol{V}$, the curl computation using each of the three discussed conventions, may be equated as

$$\textbf{curl3}\ (\boldsymbol{V}) = \textbf{Precurl}\ (\boldsymbol{V}^{\mathrm{T}}) = -(\textbf{Postcurl}\ (\boldsymbol{V}))^{\mathrm{T}} \quad (5.1.6)$$

5.1.3.2. Calculation of dislocation tensor

A geometrical link between the lattice curvature and the distribution of GNDs is given by the dislocation tensor (also known as the Nye tensor), $\boldsymbol{\alpha}^{Nye}$, proposed by Nye [108]. Nye initially formulated $\boldsymbol{\alpha}^{Nye}$ using only the lattice rotation gradients, assuming that no long-range elastic strain fields are present. Kroner and Ashby further developed this approach, by adding elastic strain gradients to the formulation of the dislocation tensor [133]. Below a summary of this theory is provided.

The analysis below, for small deformations, closely follows the derivation by Fleck and Hutchinson [131] in their study establishing the concept of strain gradient plasticity. Figure 5.1.1 (b) shows a representative crystal lattice within an imaginary solid,

with a chosen Cartesian reference frame as depicted. We assume that plastic flow occurs by dislocation motion and that the lattice is stretched and rotated during elastic deformation.

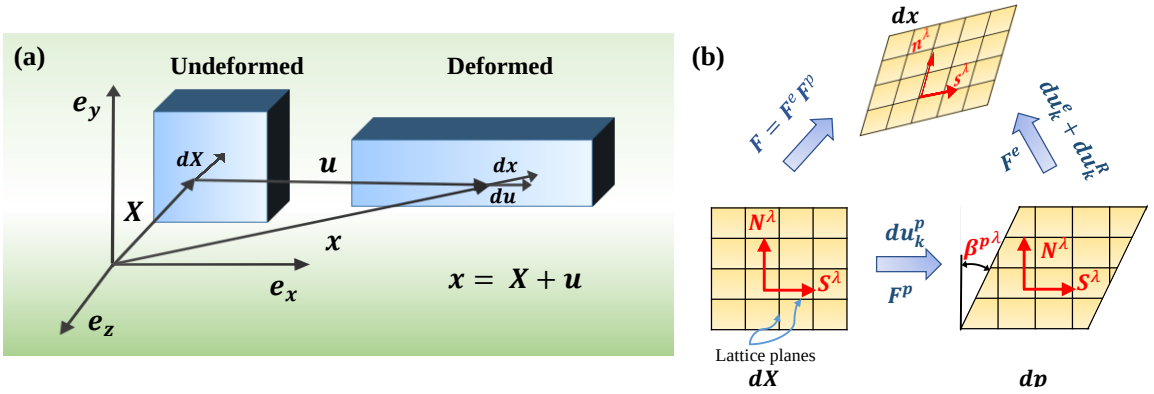


Figure 5.1.1 – (a) Schematic representation of the deformation of a body. $\boldsymbol{u}$ contains the information about whether the deformation is a translation, rigid body rotation or stretch, or a combination of these. (b) Schematic showing the multiplicative decomposition of the deformation gradient as the crystal lattice deforms from the initial state *dX* to the intermediate imaginary state *dp* (where only plastic deformation has taken place) and finally to state *dx*.

Let us consider the relative displacement, $d\boldsymbol{u}$, of two material points which are separated by $d\boldsymbol{X}$ as shown in Figure 5.1.1 (a). This relative displacement can be split into three components [131] as follows

$$d\boldsymbol{u} = d\boldsymbol{u}^p + d\boldsymbol{u}^R + d\boldsymbol{u}^e \tag{5.1.7}$$

where,

$$du_k^p = \beta_{kj}^p dX_j \tag{5.1.8}$$

$$du_k^R = \omega_{kj} dX_j \tag{5.1.9}$$

$$du_k^e = \varepsilon_{kj}^e dX_j \tag{5.1.10}$$

$d\boldsymbol{u}^p$ is the relative displacement caused by slip and described by the slip tensor $\boldsymbol{\beta}^p$. $d\boldsymbol{u}^R$ is caused by lattice rotation $\boldsymbol{\omega}$ and $d\boldsymbol{u}^e$ is due to elastic strain, $\boldsymbol{\varepsilon}^e$. For a specific slip systems, λ, defined by slip direction $\boldsymbol{s}^\lambda$ and slip plane normal $\boldsymbol{n}^\lambda$, and crystallographic slip $\beta^{p\lambda}$, the slip tensor $\boldsymbol{\beta}^p$, is given by the contribution from each of the active slip systems.

Thus,

$$\boldsymbol{\beta}^{p} = \sum_{\lambda} \beta^{p\lambda}\, \boldsymbol{s}^{\lambda} \otimes \boldsymbol{n}^{\lambda} \tag{5.1.11}$$

Following Nye's reasoning [108] the closure failure of a Burgers' circuit, *c*, on surface *S* with plane normal $\boldsymbol{N}$ (see Figure 5.1.3 (b)) can be used to link the crystallographic slip to the resultant Burgers' vector, $< \boldsymbol{B} >$:

$$< B >_k = \oint_c du_k^p = \oint_c \beta_{kj}^p dX_j \tag{5.1.12}$$

Using Stokes' theorem this can be rewritten as:

$$< B >_k = \iint_S (\in_{ijm} \beta_{kj,i}^p).N_m\, dS = \iint_S \alpha_{km}^{Nye}.N_m\, dS \tag{5.1.13}$$

where $\boldsymbol{\alpha}^{Nye}$ is the dislocation tensor defined by Nye. Thus, the Nye tensor corresponds to the curl of the slip tensor [131]:

$$\alpha_{km}^{Nye} = \in_{ijm} \beta_{kj,i}^p \tag{5.1.14}$$

Nye [108] related $\boldsymbol{\alpha}^{Nye}$ to the dislocation distribution inside the crystal. Given q dislocations per unit area with Burgers' vector $\boldsymbol{b}$ and unit line direction $\boldsymbol{l}$ threading the plane, with surface unit normal $\boldsymbol{N}$, $\boldsymbol{\alpha}^{Nye}$ may be written as

$$\alpha_{km}^{Nye} = q\, b_k l_m \tag{5.1.15}$$

Defining $\rho_m = q\, l_m$ means $\alpha_{km}^{Nye} = b_k \rho_m$. So, Nye's dislocation tensor may be written as

$$\boldsymbol{\alpha}^{Nye} = \sum_{\lambda} (\boldsymbol{b}^{\lambda} \otimes \boldsymbol{\rho}^{\lambda}) \tag{5.1.16}$$

where λ is a general slip system.

Here, it is important to note that the total displacement $d\boldsymbol{u}$, along any closed circuit must be zero. Thus, the closure failure brought about by crystallographic slip $< B >_k = \oint_c du_k^p$, has to be balanced by an equal and opposite displacement incompatibility, i.e. $\oint_c (du_k^R + du_k^e)$. This relation between the closure failure due to slip (i.e. plastic displacement) and that due to elastic displacement can be described by the concept of the deformation gradient as outline below:

Figure 5.1.1 (a) shows an imaginary material in the undeformed configuration with a line vector *d**X***. After deformation, this line vector is transformed to *d**x***. From here on we distinguish between undeformed and deformed coordinate systems. **Variables in upper case correspond to undeformed coordinates, while lower case refers to the deformed coordinates.**

The deformation gradient, $\boldsymbol{F}$, can be defined as a second-order tensor that maps the undeformed state to the deformed state of a sample. This can be written as

$$\boldsymbol{F} = \frac{\partial \boldsymbol{x}}{\partial \boldsymbol{X}} = \boldsymbol{I} + \frac{\partial \boldsymbol{u}}{\partial \boldsymbol{X}} = \boldsymbol{I} + \boldsymbol{\beta} \tag{5.1.17}$$

where, $\boldsymbol{u}$ is the displacement, $\boldsymbol{I}$ is the identity matrix and $\boldsymbol{\beta}$ the displacement gradient. $\boldsymbol{\beta}$ contains information about whether the deformation involves a rigid body rotation or a shape change or both [124]. When the deformation includes both elastic and plastic contributions, the deformation gradient can be split into elastic ($\boldsymbol{F}^e$) and plastic ($\boldsymbol{F}^p$) parts, where each of the gradients may contain both stretch and rigid body rotation.

In Eq. (5.1.14) $\boldsymbol{\alpha}^{Nye}$, is defined as a curl computation of the slip tensor. The plastic deformation gradient $\boldsymbol{F}^p$ captures the deformation by crystallographic slip, which is the same as the deformation captured by the slip tensor (Eq. (5.1.8)). In fact, $\boldsymbol{F}^p = \boldsymbol{I} + \boldsymbol{\beta}^p$.

Hence Nye's dislocation tensor may be written in terms of $\boldsymbol{F}^p$ as $\alpha_{mk}^{Nye} = \in_{ijm} F_{kj,i}^p$. Kroner [223] and Bilby [224] expressed the dislocation density tensor as the negative of the expression adopted by Nye (Eq. (5.1.14)). Consequently, Arsenlis and Parks [133] and Cermelli and Gurtin [222] used the curl3 convention to find the dislocation density tensor from the plastic deformation gradient. Rewriting $\boldsymbol{\alpha}^{Nye}$ (Eq. (5.1.14)) in terms of the curl3 formula gives

$$\alpha_{km}^{Nye} = \in_{ijm} F_{kj,i}^p = \left(\in_{ijk} F_{mj,i}^p\right)^T = ((\text{curl3 } (\boldsymbol{F}^p))^T)_{km} \tag{5.1.18}$$

From here onwards, unless otherwise specified, the curl operation signifies performing the curl computation using the curl3 convention. Owing to the contribution made by several researchers to the concept of the dislocation density tensor, from here on we adopt the notation of $\boldsymbol{\alpha}$ to represent it.

Eq. (5.1.18) can also be arrived at considering the following approach: To separate the elastic ($\boldsymbol{F}^e$) and the plastic ($\boldsymbol{F}^p$) deformations, an intermediate imaginary configuration $d\boldsymbol{p}$ can be introduced (Figure 5.1.1 (b)), where the sample has undergone purely plastic deformation. The transformation of $d\boldsymbol{X}$ to $d\boldsymbol{p}$ is captured by $\boldsymbol{F}^p$

$$d\boldsymbol{p} = \boldsymbol{F}^p d\boldsymbol{X} \tag{5.1.19}$$

$d\boldsymbol{p}$ can then be mapped to the vector $d\boldsymbol{x}$ by the elastic deformation gradient

$$d\boldsymbol{x} = \boldsymbol{F}^e d\boldsymbol{p} \tag{5.1.20}$$

and equating Eq. (5.1.19) and (5.1.20)

$$d\boldsymbol{p} = \boldsymbol{F}^p d\boldsymbol{X} = \boldsymbol{F}^{e^{-1}} d\boldsymbol{x}. \tag{5.1.21}$$

Rewriting Eq. (5.1.21) the multiplicative decomposition of the deformation gradient is obtained as proposed by Lee et al. [225]

$$\boldsymbol{F} = \frac{\partial \boldsymbol{x}}{\partial \boldsymbol{X}} = \boldsymbol{F}^e \boldsymbol{F}^p. \tag{5.1.22}$$

Substituting $\boldsymbol{F}^e$ and $\boldsymbol{F}^p$ into Eq. (5.1.17) and introducing elastic and plastic parts of the displacement gradient, $\boldsymbol{\beta}^e$ and $\boldsymbol{\beta}^p$ respectively, gives

$$\boldsymbol{F} = I + \boldsymbol{\beta} = \boldsymbol{F}^e \boldsymbol{F}^p = (I + \boldsymbol{\beta}^e)(I + \boldsymbol{\beta}^p) = I + \boldsymbol{\beta}^e + \boldsymbol{\beta}^p + \boldsymbol{\beta}^e \boldsymbol{\beta}^p. \tag{5.1.23}$$

For small deformations, the $\boldsymbol{\beta}^e \boldsymbol{\beta}^p$ term is negligible and thus the displacement gradient for small strains may be written as

$$\boldsymbol{\beta} \cong \boldsymbol{\beta}^e + \boldsymbol{\beta}^p. \tag{5.1.24}$$

From the kinematics of deformation, closure failure of a region can be defined as the change in length of a path on the surface due to generation of dislocations in the volume. Acharya and Bassani [226] defined closure failure with respect to deformed configuration $\boldsymbol{x}$, where $\boldsymbol{x} = \boldsymbol{X} + \boldsymbol{u}$, as

$$< \boldsymbol{b} >= \oint_c \boldsymbol{F}^{e-1} d\boldsymbol{x} \tag{5.1.25}$$

where <$\boldsymbol{b}$> is the net Burgers' vector of the dislocation lines passing through closed loop *c*. This is analogous to Eq. (5.1.12) in the deformed configuration. Using Stokes theorem, the integration around *c* may be replaced by integration over any surface patch *s,* bounded by *c* and with plane normal $\boldsymbol{n}$, so that

$$< \boldsymbol{b} >= \oint_c \boldsymbol{F}^{e-1} d\boldsymbol{x} = \iint_s (\text{curl}\, \boldsymbol{F}^{e-1})^T \boldsymbol{n} ds \cong \iint_s (-\text{curl}\, \boldsymbol{F}^e)^T \boldsymbol{n} ds \tag{5.1.26}$$

where, curl $\boldsymbol{F}^{e-1} \cong -\text{curl}\, \boldsymbol{F}^e$ for small elastic strains because

$$\boldsymbol{F}^{e-1} = (\boldsymbol{I} + \boldsymbol{\beta}^{e})^{-1} \cong \boldsymbol{I} - \boldsymbol{\beta}^{e} \text{ so curl } \boldsymbol{F}^{e-1} \cong -\text{curl } \boldsymbol{F}^{e} \tag{5.1.27}$$

as curl of the identity matrix is zero.

Re-writing in terms of the displacement gradient,

$$< \boldsymbol{b} >= \iint_{S} (\text{curl } (\boldsymbol{F}^{e-1}))^{T} \boldsymbol{n} ds \cong \iint_{S} (-\text{curl } (\boldsymbol{\beta}^{e}))^{T} \boldsymbol{n} ds \tag{5.1.28}$$

The transpose in Eq. (5.1.28) is introduced when applying Stokes' theorem to higher order tensors, as proved by Cermelli and Gurtin (details in Appendix E) [222]. The closure failure, represented in terms of the non-vanishing cumulative Burgers' vector of all dislocations, can also be written in terms of the undeformed configuration $\boldsymbol{X}$. Computation of curl in the undeformed configuration, $d\boldsymbol{X}$, will be referred to as "CURL" from here on.

$$\begin{aligned} < \boldsymbol{b} >= \oint_{c} \boldsymbol{F}^{e-1} d\boldsymbol{x} = \oint_{c} \boldsymbol{F}^{e-1} \boldsymbol{F} d\boldsymbol{X} = \oint_{c} \boldsymbol{F}^{e-1} \boldsymbol{F}^{e} \boldsymbol{F}^{p} d\boldsymbol{X} = \oint_{C} \boldsymbol{F}^{p} d\boldsymbol{X} \\ = \iint_{S} (\text{CURL } \boldsymbol{F}^{p})^{T} \boldsymbol{N} dS = < \boldsymbol{B} > \end{aligned} \tag{5.1.29}$$

Here <$\boldsymbol{b}$> and <$\boldsymbol{B}$> refers to the resultant Burgers' vector in the deformed and undeformed coordinate frame respectively. Rewriting Eq. (5.1.29) in terms of the plastic displacement gradient,

$$< \boldsymbol{B} >= \iint_{S} (\text{CURL } (I + \boldsymbol{\beta}^{p}))^{T} \boldsymbol{N} dS = \iint_{S} (\text{CURL } (\boldsymbol{\beta}^{p}))^{T} \boldsymbol{N} dS \tag{5.1.30}$$

Thus, in summary, the closure failure can be represented in terms of either the elastic or plastic displacement gradient as

$$< \boldsymbol{B} >= \iint_S (\mathrm{CURL}\,(\,\boldsymbol{\beta}^p))^T\ \boldsymbol{N}dS \cong \iint_s \left(-\mathrm{CURL}\,(\boldsymbol{\beta}^e)\right)^T \boldsymbol{N}dS$$
$$\cong \iint_s \left(-\mathrm{curl}\,(\boldsymbol{\beta}^e)\right)^T \boldsymbol{n}ds = < \boldsymbol{b} > \tag{5.1.31}$$

where for small deformation we do not need to distinguish between the initial and deformed system. Equating Eq. (5.1.16) and Eq. (5.1.31), the dislocation tensor may be re-written to again arrive at Eq. (5.1.18).

$$\boldsymbol{\alpha} = \sum_i (\boldsymbol{b}^i \otimes \boldsymbol{\rho}^i) = (\mathrm{CURL}\,(\,\boldsymbol{F}^p))^T\ = (\mathrm{CURL}\,(\,\boldsymbol{\beta}^p))^T \cong (-\mathrm{curl}\,(\boldsymbol{\beta}^e))^T$$
$$\cong (-\mathrm{CURL}\,(\boldsymbol{\beta}^e))^T \tag{5.1.32}$$

The elastic strain $\boldsymbol{\varepsilon}^e$, and lattice rotation $\boldsymbol{\omega}^e$, are related to the displacement gradient tensor by

$$\boldsymbol{\varepsilon}^e = \tfrac{1}{2}\,(\boldsymbol{\beta}^e + \boldsymbol{\beta}^{eT});\ \boldsymbol{\omega}^e = \tfrac{1}{2}\,(\boldsymbol{\beta}^e - \boldsymbol{\beta}^{eT}) \tag{5.1.33}$$

Thus, Eq. (5.1.32) may further be re-written as

$$\boldsymbol{\alpha} \cong (-\mathrm{curl}(\,\boldsymbol{\varepsilon}^e + \boldsymbol{\omega}^e))^T \cong (-\mathrm{CURL}(\,\boldsymbol{\varepsilon}^e + \boldsymbol{\omega}^e))^T \tag{5.1.34}$$

for the case of small deformation. Given the deformation gradients, $\boldsymbol{F}^e$ or $\boldsymbol{F}^p$, or displacement gradients, $\boldsymbol{\beta}^e$ or $\boldsymbol{\beta}^p$, $\boldsymbol{\alpha}$ can be computed using any of the three curl definitions discussed above (Eq. (5.1.1), (5.1.2) & (5.1.3)). Following Eq. (5.1.6) a summary of expressions for in terms of the three curl definitions is provided in Table 5.1.1.

$\boldsymbol{\alpha}$	In terms of: CURL ($\boldsymbol{\beta}^p$) or CURL ($\boldsymbol{F}^p$) for all deformations	In terms of: curl ($\boldsymbol{\beta}^e$) for small deformations curl ($\boldsymbol{F}^{e-1}$) for large deformations
Using "curl3"	$(\text{CURL}\,(\boldsymbol{F}^p))^T = (\text{CURL}\,(\boldsymbol{\beta}^p))^T$ where, $\text{CURL}\,(\boldsymbol{\beta}^p)_{km} = \in_{ijk} \beta^p_{mj,i}$	$(\text{curl}\,(\boldsymbol{F}^{e-1}))^T \cong (-\text{curl}\,(\boldsymbol{\beta}^e))^T$ where, $\text{curl}\,(\boldsymbol{\beta}^e)_{km} = \in_{ijk} \beta^e_{mj,i}$ $\text{curl}\,(\boldsymbol{F}^{e-1})_{km} = \in_{ijk} F^{e-1}_{mj,i}$
Using "Pre-curl"	$\left((\text{CURL}\,(\boldsymbol{F}^{p\text{T}})\right)^T = (\text{CURL}\,(\boldsymbol{\beta}^{p^T}))^T$ where, $\text{CURL}(\boldsymbol{\beta}^{p^T})_{km} = \in_{ijk} (\beta^{p^T})_{jm,i}$	$(\text{curl}\,\boldsymbol{F}^{e-1^T})^{\text{T}} \cong (-\text{curl}\,(\boldsymbol{\beta}^{e^T}))^T$ where,$\text{curl}\,(\boldsymbol{\beta}^{e^T})_{km} = \in_{ijk} (\beta^{e^T})_{jm,i}$ $\text{curl}\,(\boldsymbol{F}^{e-1^T})_{km} = \in_{ijk} (F^{e-1^T})_{jm,i}$
Using "Post-curl"	$(-(\text{CURL}\,(\boldsymbol{F}^p))^T)^T = -\text{CURL}\,(\boldsymbol{F}^p) = -\text{CURL}\,(\boldsymbol{\beta}^p)$ where, $\text{CURL}\,(\boldsymbol{\beta}^p)_{km} = -\in_{ijm} \beta^p_{kj,i}$	$\left(-\left(\text{curl}\left(\boldsymbol{F}^{e-1}\right)\right)^T\right)^T = -\text{curl}\left(\boldsymbol{F}^{e-1}\right) \cong \text{curl}\,(\boldsymbol{\beta}^e)$ where, $\text{curl}\,(\boldsymbol{\beta}^e)_{km} = -\in_{ijm} \beta^e_{kj,i}$ $\text{curl}\,(\boldsymbol{F}^{e-1})_{km} = -\in_{ijm} F^{e-1}_{kj,i}$

Table 5.1.1 – Summary of computation of dislocation tensor using the three common different definitions of curl in terms of $\boldsymbol{\beta}$ and $\boldsymbol{F}$.

For small strains the dislocation tensor may be explicitly written in terms of the plastic ($\boldsymbol{\beta}^p$) or elastic ($\boldsymbol{\beta}^e$) displacement gradients:

$$\boldsymbol{\alpha} \cong \begin{bmatrix} \frac{\partial \beta_{13}^p}{\partial x_2} - \frac{\partial \beta_{12}^p}{\partial x_3} & \frac{\partial \beta_{11}^p}{\partial x_3} - \frac{\partial \beta_{13}^p}{\partial x_1} & \frac{\partial \beta_{12}^p}{\partial x_1} - \frac{\partial \beta_{11}^p}{\partial x_2} \\ \frac{\partial \beta_{23}^p}{\partial x_2} - \frac{\partial \beta_{22}^p}{\partial x_3} & \frac{\partial \beta_{21}^p}{\partial x_3} - \frac{\partial \beta_{23}^p}{\partial x_1} & \frac{\partial \beta_{22}^p}{\partial x_1} - \frac{\partial \beta_{21}^p}{\partial x_2} \\ \frac{\partial \beta_{33}^p}{\partial x_2} - \frac{\partial \beta_{32}^p}{\partial x_3} & \frac{\partial \beta_{31}^p}{\partial x_3} - \frac{\partial \beta_{33}^p}{\partial x_1} & \frac{\partial \beta_{32}^p}{\partial x_1} - \frac{\partial \beta_{31}^p}{\partial x_2} \end{bmatrix} \tag{5.1.35}$$

$$\boldsymbol{\alpha} \cong \begin{bmatrix} \frac{\partial \beta_{12}^e}{\partial x_3} - \frac{\partial \beta_{13}^e}{\partial x_2} & \frac{\partial \beta_{13}^e}{\partial x_1} - \frac{\partial \beta_{11}^e}{\partial x_3} & \frac{\partial \beta_{11}^e}{\partial x_2} - \frac{\partial \beta_{12}^e}{\partial x_1} \\ \frac{\partial \beta_{22}^e}{\partial x_3} - \frac{\partial \beta_{23}^e}{\partial x_2} & \frac{\partial \beta_{23}^e}{\partial x_1} - \frac{\partial \beta_{21}^e}{\partial x_3} & \frac{\partial \beta_{21}^e}{\partial x_2} - \frac{\partial \beta_{22}^e}{\partial x_1} \\ \frac{\partial \beta_{32}^e}{\partial x_3} - \frac{\partial \beta_{33}^e}{\partial x_2} & \frac{\partial \beta_{33}^e}{\partial x_1} - \frac{\partial \beta_{31}^e}{\partial x_3} & \frac{\partial \beta_{31}^e}{\partial x_2} - \frac{\partial \beta_{32}^e}{\partial x_1} \end{bmatrix} \tag{5.1.36}$$

The displacement gradient can also be written in terms of the lattice rotation and lattice strain as

$$\boldsymbol{\beta}^e = \boldsymbol{\omega}^e + \boldsymbol{\varepsilon}^e \tag{5.1.37}$$

This leads to the following form for the dislocation tensor:

$$\begin{aligned} \boldsymbol{\alpha} \cong & \begin{bmatrix} \frac{\partial \omega_{12}^e}{\partial x_3} - \frac{\partial \omega_{13}^e}{\partial x_2} & \frac{\partial \omega_{13}^e}{\partial x_1} & \frac{\partial \omega_{21}^e}{\partial x_1} \\ \frac{\partial \omega_{32}^e}{\partial x_2} & \frac{\partial \omega_{23}^e}{\partial x_1} - \frac{\partial \omega_{21}^e}{\partial x_3} & \frac{\partial \omega_{21}^e}{\partial x_2} \\ \frac{\partial \omega_{32}^e}{\partial x_3} & \frac{\partial \omega_{13}^e}{\partial x_3} & \frac{\partial \omega_{31}^e}{\partial x_2} - \frac{\partial \omega_{32}^e}{\partial x_1} \end{bmatrix} \\ & + \begin{bmatrix} \frac{\partial \varepsilon_{12}^e}{\partial x_3} - \frac{\partial \varepsilon_{13}^e}{\partial x_2} & \frac{\partial \varepsilon_{13}^e}{\partial x_1} - \frac{\partial \varepsilon_{11}^e}{\partial x_3} & \frac{\partial \varepsilon_{11}^e}{\partial x_2} - \frac{\partial \varepsilon_{12}^e}{\partial x_1} \\ \frac{\partial \varepsilon_{22}^e}{\partial x_3} - \frac{\partial \varepsilon_{23}^e}{\partial x_2} & \frac{\partial \varepsilon_{23}^e}{\partial x_1} - \frac{\partial \varepsilon_{21}^e}{\partial x_3} & \frac{\partial \varepsilon_{21}^e}{\partial x_2} - \frac{\partial \varepsilon_{22}^e}{\partial x_1} \\ \frac{\partial \varepsilon_{32}^e}{\partial x_3} - \frac{\partial \varepsilon_{33}^e}{\partial x_2} & \frac{\partial \varepsilon_{33}^e}{\partial x_1} - \frac{\partial \varepsilon_{31}^e}{\partial x_3} & \frac{\partial \varepsilon_{31}^e}{\partial x_2} - \frac{\partial \varepsilon_{32}^e}{\partial x_1} \end{bmatrix} \end{aligned} \tag{5.1.38}$$

where, considering the asymmetric nature of $\boldsymbol{\omega}^e$, the ω_{ii}^e components are 0. In general, the lattice rotation gradients are substantially greater than the elastic strain gradients and make a more significant contribution to the dislocation tensor.

5.1.3.3. Calculation of GND density

Eq. (5.1.16) relates the dislocation tensor to the densities of geometrically necessary dislocations. The 3×3 $\boldsymbol{\alpha}$ tensor can be reshaped as a 9×1 column vector. A linear operator $\boldsymbol{A}$ is formed (9×j matrix, for j types of dislocations), where the j^{th} column contains the dyadic product of the Burgers' vector and line direction of the j^{th} dislocation type. Representing the densities of the j dislocation types as a column vector $\boldsymbol{\rho}$, the quantities $\boldsymbol{\alpha}$, $\boldsymbol{\rho}$ and $\boldsymbol{A}$ may be used to recast Eq. (5.1.16) as

$$\boldsymbol{A\rho} = \boldsymbol{\alpha} \tag{5.1.39}$$

Explicitly this may be written as

$$\sum_j \left(\boldsymbol{b}^j \otimes \boldsymbol{\rho}^j\right) = \begin{bmatrix} \boldsymbol{b}_1^1\boldsymbol{l}_1^1 & \boldsymbol{b}_1^2\boldsymbol{l}_1^2 & \boldsymbol{b}_1^3\boldsymbol{l}_1^3 & \cdots & \boldsymbol{b}_1^j\boldsymbol{l}_1^j \\ \boldsymbol{b}_1^1\boldsymbol{l}_2^1 & \boldsymbol{b}_1^2\boldsymbol{l}_2^2 & \boldsymbol{b}_1^3\boldsymbol{l}_2^3 & \cdots & \boldsymbol{b}_1^j\boldsymbol{l}_2^j \\ \boldsymbol{b}_1^1\boldsymbol{l}_3^1 & \boldsymbol{b}_1^2\boldsymbol{l}_3^2 & \boldsymbol{b}_1^3\boldsymbol{l}_3^3 & \cdots & \boldsymbol{b}_1^j\boldsymbol{l}_3^j \\ \boldsymbol{b}_2^1\boldsymbol{l}_1^1 & \boldsymbol{b}_2^2\boldsymbol{l}_1^2 & \boldsymbol{b}_2^3\boldsymbol{l}_1^3 & \cdots & \boldsymbol{b}_2^j\boldsymbol{l}_1^j \\ \boldsymbol{b}_2^1\boldsymbol{l}_2^1 & \boldsymbol{b}_2^2\boldsymbol{l}_2^2 & \boldsymbol{b}_2^3\boldsymbol{l}_2^3 & \cdots & \boldsymbol{b}_2^j\boldsymbol{l}_2^j \\ \boldsymbol{b}_2^1\boldsymbol{l}_3^1 & \boldsymbol{b}_2^2\boldsymbol{l}_3^2 & \boldsymbol{b}_2^3\boldsymbol{l}_3^3 & \cdots & \boldsymbol{b}_2^j\boldsymbol{l}_3^j \\ \boldsymbol{b}_3^1\boldsymbol{l}_1^1 & \boldsymbol{b}_3^2\boldsymbol{l}_1^2 & \boldsymbol{b}_3^3\boldsymbol{l}_1^3 & \cdots & \boldsymbol{b}_3^j\boldsymbol{l}_1^j \\ \boldsymbol{b}_3^1\boldsymbol{l}_2^1 & \boldsymbol{b}_3^2\boldsymbol{l}_2^2 & \boldsymbol{b}_3^3\boldsymbol{l}_2^3 & \cdots & \boldsymbol{b}_3^j\boldsymbol{l}_2^j \\ \boldsymbol{b}_3^1\boldsymbol{l}_3^1 & \boldsymbol{b}_3^2\boldsymbol{l}_3^2 & \boldsymbol{b}_3^3\boldsymbol{l}_3^3 & \cdots & \boldsymbol{b}_3^j\boldsymbol{l}_3^j \end{bmatrix} \begin{bmatrix} \boldsymbol{\rho}_1 \\ \boldsymbol{\rho}_2 \\ \boldsymbol{\rho}_3 \\ \vdots \\ \boldsymbol{\rho}_j \end{bmatrix} = \begin{bmatrix} \boldsymbol{\alpha}_{11} \\ \boldsymbol{\alpha}_{12} \\ \boldsymbol{\alpha}_{13} \\ \boldsymbol{\alpha}_{21} \\ \boldsymbol{\alpha}_{22} \\ \boldsymbol{\alpha}_{23} \\ \boldsymbol{\alpha}_{31} \\ \boldsymbol{\alpha}_{32} \\ \boldsymbol{\alpha}_{33} \end{bmatrix} \tag{5.1.40}$$

where, $\boldsymbol{l}$ is the line direction. Since generally j > 9 there is no unique solution for $\boldsymbol{\rho}$. Instead, knowing $\boldsymbol{\alpha}$ and $\boldsymbol{A}$, optimisation methods may be used to obtain $\boldsymbol{\rho}$. The mathematically simplest is the L^2 optimisation scheme [133], which minimises the sum of squares of

dislocation densities i.e. $\sum_j \rho_j^2 = \boldsymbol{\rho}^T . \boldsymbol{\rho}$. Using the right pseudo inverse, the solution may be written as

$$\boldsymbol{\rho} = \boldsymbol{A}^T (\boldsymbol{A}\boldsymbol{A}^T)^{-1} \boldsymbol{\alpha} \tag{5.1.41}$$

When using the L^2 optimisation, it is essential to construct $\boldsymbol{A}$ including all possible slip systems not just the active ones (i.e. the calculation is independent of the resolved shear stress). For example, in a bcc crystal, if {110}<111> slip systems are being considered, all 16 possible dislocation types (12 edge + 4 screw) must be included, leading to an $\boldsymbol{A}$ matrix with dimensions [9×16]. The disadvantage of this optimisation scheme is a lack of any physical basis.

An alternative optimisation method, here referred to as L^1, minimises the total dislocation elastic energy, i.e. $(1-\upsilon)^{-1} \sum_j \rho_j^{edge} + \sum_j \rho_j^{screw}$, to obtain a solution for Eq. (5.1.39). In the example above, since all the dislocations have the same Burgers' vector magnitude, and assuming elastic isotropy, differences arise only due to the ratio of energies for edge and screw dislocations [215]:

$$\frac{E_{edge}}{E_{screw}} = \frac{1}{1-\upsilon} \tag{5.1.42}$$

where, υ is the Poisson's ratio. The "linprog" algorithm, implemented in Matlab (The Mathworks Inc.; www.mathworks.com) was used to perform the L^1 optimisation.

A key assumption is that dislocations are either pure edge or pure screw. Other methods for solving Eq. (5.1.40) involve minimising the total dislocation density [109], [227], [228], or minimisation the equivalent line length [215]. A thorough, in-depth comparison all these minimisation norms is beyond the scope of this paper. Instead we focus on a comparison of the two most commonly used methods, L^1 and L^2 minimisations. For both these optimisations, the solution obtained represents only one of the infinite

number of solutions to Eq. (5.1.39). The total dislocation density is obtained by summing the magnitudes of the densities of all *j* dislocation types.

5.1.4. Materials and Methods

To illustrate the concepts discussed above, we now consider the lattice distortions, dislocation tensor and GND density beneath a spherical nano-indent in a pure tungsten single crystal. A direct comparison is made between experimental measurements and numerical predictions from a strain-gradient CPFE model of the indentation process.

5.1.4.1. Micro-beam Laue diffraction

A <001>-oriented high purity tungsten single crystal (99.99 wt.%) was mechanically polished using diamond paste and colloidal silica to produce a near defect-free mirror finish. 500 nm deep indents were made using a MTS NanoXp indenter with a spherical, ~ 4.2 μm radius diamond tip. Synchrotron X-ray micro-beam Laue diffraction was used to probe the residual lattice distortions beneath a specific indent with sub-micron (~ 0.5 microns) 3D resolution. Details about the diffraction measurements can be found in Section 2.2.2.1 and Section 3.3.3. Measurements were done to a depth of 20 μm beneath the sample surface. Laue diffraction patterns contained 30+ peaks and were indexed and fitted using the LaueGo software package (J.Z. Tischler: tischler@anl.gov) to extract both lattice orientation and the deviatoric elastic strain tensor at each measured point in 3D space. The measured strain and rotation gradients were then used to calculate the dislocation tensor and GND density.

5.1.4.2. 3D CPFE Model

A 3D finite element model was constructed to simulate the nano-indentation experiment in Abaqus (Dassault Systèmes, Providence, RI, USA). Here we are modelling indentation of <001> oriented crystal which should exhibit a four-fold symmetry. So, we use an indentation model (Figure 5.1.2) comprised of a 3D single crystal tungsten cube ($20\times20\times20$ μm^3), which represents a quarter of the experimental setup. The indentation experiment we are aiming to simulate here is expected to produce lattice rotations < 0.08° (as estimated from Section 4.6 where we experimentally measured lattice rotations for pure tungsten, indented under similar conditions). Thus, these small indentation-induced lattice rotations are assumed not to disturb the four-fold symmetry, assumed for the initially <001>-oriented crystal. However, it is to be noted here, that for distinctly different crystallographic orientations, the indentation model has to be updated accordingly. For example, for <011> and <111> oriented crystal, which shows two-fold and three-fold symmetry respectively, indentation model representing half and one-third of the experimental setup should be used respectively (as will be shown later in Chapter 5.3).

The boundary conditions imposed on the sample block included symmetric boundary conditions on the XZ and YZ surfaces near the indent, a traction free top surface, and fixed displacement and rotation boundary conditions on the remaining surfaces. The modelled spherical indenter (4.2 μm radius) was assumed to be a discrete rigid part to avoid a full meshing and increase in simulation size. Contact between the sample and indenter was defined using the Abaqus node to surface contact algorithm and the contact was considered to be frictionless as past studies have shown that the mechanical response of the underlying substrate is not significantly affected by the coefficient of friction [182]. The results of indentation load reached, were scaled with an effective modulus E_{eff} to account

for the fact that elastic displacements may occur in both the indenter tip and the specimen [202] (details in Appendix F).

A refined finite element mesh (applied edge bias 0.1 to 2 μm) with >15700 20-noded, reduced integration (8 integration point) 3D quadratic elements (C3D20R) was used. Figure 5.1.2 shows the Von Mises stress (after unloading) in the simulated model, mirrored about the YZ plane. Consistent with the nano-indentation experiment, in the simulation, a displacement of 0.5 μm was applied to the indenter followed by complete unloading to account for relaxation of the elastic part of the deformation and any reverse plastic deformation that may be taking place.

Strain gradient crystal plasticity was implemented with a user material subroutine (UMAT). In the UMAT, the mechanical response of the tungsten bcc crystal under indentation was predicted using a constitutive law incorporating crystallographic slip. A brief description of the constitutive law, originally developed by Dunne et al. [130], [195], is provided here.

Recalling Eq. (5.1.22), it is known that the deformation gradient $\boldsymbol{F}$, splits multiplicatively into its elastic and plastic parts. Plastic deformation occurs on a slip system, λ, when the resolved shear stress τ^{λ} is greater than the critically resolved shear stress (CRSS). $\boldsymbol{F}^{p}$ can be defined in terms of the crystallographic slip $\boldsymbol{\beta}^{p}$ (relative displacement of two slip planes separated by a unit distance), slip direction $\boldsymbol{s}$ and

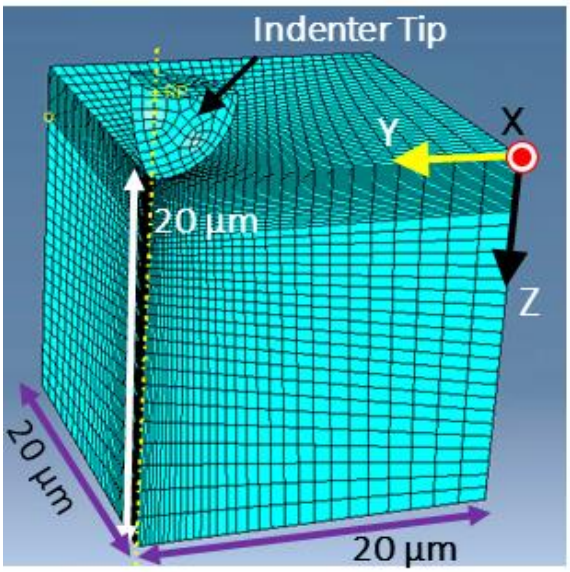


Figure 5.1.2 - CPFE mesh of the quarter model created in Abaqus for simulation of the nano-indentation experiments with a 4.2 µm radius spherical indenter. Superimposed are the X, Y, Z coordinate frame.

slip plane normal $\boldsymbol{n}$. The crystallographic plane normals and the slip directions are updated as the crystal lattice undergoes deformation. For a finite number of slip systems, $\boldsymbol{F}^p$ is given by the sum of the contribution of the slip systems to the resultant slip

$$\boldsymbol{F}^P = \boldsymbol{I} + \frac{\partial \boldsymbol{u}^P}{\partial \boldsymbol{X}} = \boldsymbol{I} + \boldsymbol{\beta}^p = \boldsymbol{I} + \sum_{\lambda} \beta^{p\lambda}\left(\boldsymbol{s}^\lambda \otimes \boldsymbol{n}^\lambda\right) \tag{5.1.43}$$

The rate of change of $\boldsymbol{F}^p$ is thus

$$\dot{\boldsymbol{F}}^p = \sum_{\lambda} \dot{\beta}^{p\lambda}\left(\boldsymbol{s}^\lambda \otimes \boldsymbol{n}^\lambda\right) \tag{5.1.44}$$

where $\dot{\beta}^{p\lambda}$ is the crystallographic slip rate on slip system λ. The velocity gradient $\boldsymbol{L}$ is given by

$$\boldsymbol{L} = \frac{\partial \boldsymbol{v}}{\partial \boldsymbol{x}} = \dot{\boldsymbol{F}}\boldsymbol{F}^{-1} \tag{5.1.45}$$

The velocity gradient can be split into symmetric and anti-symmetric components to give the rate of deformation $\boldsymbol{D}$ and the continuum spin $\boldsymbol{W}$ respectively. The total rate of deformation can be written as a sum of the elastic and plastic rates of deformation

$$\boldsymbol{D} = \boldsymbol{D}^e + \text{sym}\left(\boldsymbol{F}^e \boldsymbol{L}^p \boldsymbol{F}^{e-1}\right) \cong \boldsymbol{D}^e + \text{sym}(\boldsymbol{L}^p) \cong \boldsymbol{D}^e + \boldsymbol{D}^p \tag{5.1.46}$$

$\boldsymbol{D}^e$ is computed using Hooke's law, while $\boldsymbol{D}^p$ is approximated by the symmetric part of $\boldsymbol{L}^p$. $\boldsymbol{L}^p$ can be written as

$$\begin{aligned} \boldsymbol{L}^p = \dot{\boldsymbol{F}}^p \boldsymbol{F}^{p-1} &= \sum_\lambda \dot{\beta^p}^\lambda \left(\boldsymbol{s}^\lambda \otimes \boldsymbol{n}^\lambda\right) \left(\boldsymbol{I} + \sum_\lambda \beta^{p\lambda} \left(\boldsymbol{s}^\lambda \otimes \boldsymbol{n}^\lambda\right)\right)^{-1} \\ &\cong \sum_\lambda \dot{\beta^p}^\lambda \left(\boldsymbol{s}^\lambda \otimes \boldsymbol{n}^\lambda\right) \left(\boldsymbol{I} - \sum_\lambda \beta^{p\lambda} \left(\boldsymbol{s}^\lambda \otimes \boldsymbol{n}^\lambda\right)\right) \\ &\cong \sum_\lambda \dot{\beta^p}^\lambda \left(\boldsymbol{s}^\lambda \otimes \boldsymbol{n}^\lambda\right) \cong \dot{\boldsymbol{F}^p} \end{aligned} \tag{5.1.47}$$

where, the higher products are ignored for small deformations.

When the UMAT is called by Abaqus, the UMAT is provided with the deformation gradient ($\boldsymbol{F}$) at the beginning and end of the time increment and the internal state variables at the beginning of the time increment. The UMAT returns the updated values of the state variables at the end of the time increment, the updated stress state ($\boldsymbol{\sigma}_{t+\Delta t}$) and the material Jacobian $\left(\frac{\partial \Delta \sigma}{\partial \Delta \varepsilon}\right)$. $\boldsymbol{D}^p$ approximated from $\boldsymbol{L}^p$ (Eq. (5.1.46)), gives the increment in the plastic strain ($\Delta \boldsymbol{\varepsilon}_p = \boldsymbol{D}^p \Delta t$), and the increment in the total strain can be computed from the known value the deformation gradient ($\Delta \boldsymbol{\varepsilon}$ = sym ($\dot{\boldsymbol{F}}\, \boldsymbol{F}^{-1}$)$\Delta t$). $\boldsymbol{\sigma}_{t+\Delta t}$ can then be written in terms of a trial stress ($\boldsymbol{\sigma}_{tr}$) and a plastic corrector term as follows

$$\boldsymbol{\sigma}_{t+\Delta t} = \boldsymbol{C}' \left(\boldsymbol{\varepsilon}_t^e + \Delta \boldsymbol{\varepsilon}^e\right) = \boldsymbol{C}' \left(\boldsymbol{\varepsilon}_t^e + \Delta \boldsymbol{\varepsilon} - \Delta \boldsymbol{\varepsilon}^p\right) = \boldsymbol{\sigma}_{tr} - \boldsymbol{C}' \Delta \boldsymbol{\varepsilon}^p \tag{5.1.48}$$

where $\boldsymbol{C}'$ is the stiffness matrix rotated into the sample coordinate system. The UMAT used here solves these equations implicitly, i.e. all quantities are written at the end of the time increment and the stress is forced to converge back onto the yield surface within a tolerance of 10^{-12} MPa using the plastic corrector term $\boldsymbol{C}'\Delta\boldsymbol{\varepsilon}^{p}$. The reduction of this stress residual ($\Psi = \boldsymbol{\sigma}_{t+\Delta t} - \boldsymbol{\sigma}_{tr} + \boldsymbol{C}'\Delta\boldsymbol{\varepsilon}^{p}$) is done using the Newton-Raphson iterative method. Further details can be found in [130].

The physically based slip law used here determines the slip rate on the slip system by considering the thermally activated process of movement of dislocations, overcoming pinning obstacles. For a slip system with average dislocation glide speed $\langle v\rangle^{\lambda}$ Burgers' vector magnitude b^{λ}, with q dislocations per unit area h-L as shown in Figure 5.1.3 (a), the crystallographic slip rate maybe written using the Orowan equation

$$\dot{\beta}^{p\,\lambda} = q\frac{\langle v\rangle^{\lambda} b^{\lambda}}{Lh} = \rho_{m}^{\lambda} b^{\lambda}\langle v\rangle^{\lambda} \tag{5.1.49}$$

where, ρ_{m}^{λ} is the density of mobile dislocations.

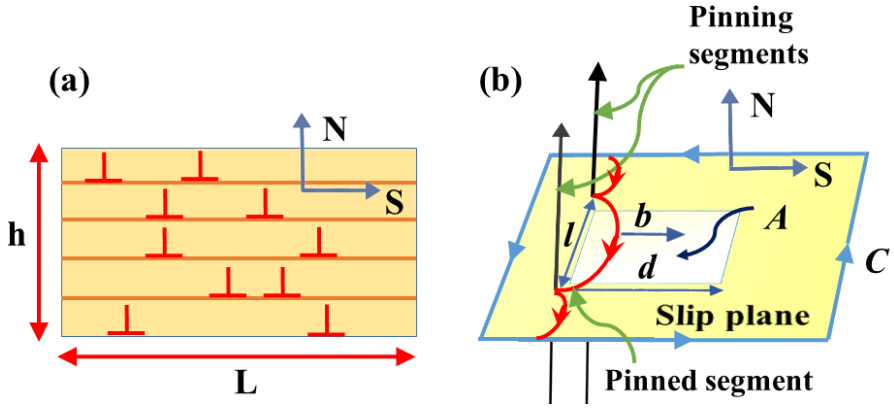


Figure 5.1.3 – (a) Schematic diagram of a set of slip planes, viewed edge on, each comprising of a random distribution of dislocations on one slip system (b) One of the slip planes from (a), viewed in cross-section, with slip plane normal ***N*** and slip direction ***S***. *C* represents the closed circuit path around the slip plane used to determine the Burgers' vector of the black cutting dislocations. An edge dislocation (shown in red), pinned by cutting dislocations from another slip system, where *l* is the distance between the pinning points and *d* the distance jumped by the dislocation on overcoming the pinning dislocations.

The thermal activation process influences the glide velocity by enabling the pinned dislocations to overcome the energy barriers produced by obstacles. Figure 5.1.3 (b) shows an edge dislocation, pinned by cutting dislocations from another slip system, where l is the distance between the pinning points and d the distance jumped by the dislocation on overcoming the pinning dislocations. Average glide velocity is given by

$$\langle v \rangle = d\Gamma \tag{5.1.50}$$

where, Γ is the rate of escape of dislocations given by

$$\Gamma = \frac{\nu b^{\lambda}}{2l} \exp\left(-\frac{\Delta G}{kT}\right) \tag{5.1.51}$$

where, ν is the frequency of dislocation jumps, G is the Gibbs free energy, k the Boltzmann constant and T the temperature in Kelvin. In terms of activation energy (ΔF) and applied stress field τ, the Gibbs free energy is

$$\Delta G = \Delta F - \tau V \tag{5.1.52}$$

where, V is the activation volume. Substituting this expression of ΔG into Eq. (5.1.50) and taking into account the forward and backward activation, and the critically resolved shear stress τ_c, the slip rate for a slip system λ, maybe written as,

$$\dot{\beta^p}^{\lambda} = \rho_g \nu \left(b^{\lambda}\right)^2 \exp\left(-\frac{\Delta F^{\lambda}}{kT}\right) \sinh\left(\frac{\mathrm{sgn}(\tau^{\lambda})(\left|\tau^{\lambda}\right| - \tau_c^{\lambda})V^{\lambda}}{kT}\right) \tag{5.1.53}$$

V depends on the spacing between the pinning dislocations l . Here, a lengthscale dependent mechanical response is considered where the strain rate and subsequent plastic deformation reduces as the GND density increases. l is considered to be a function of the density of SSDs (ρ_{SSD}) and GNDs (ρ_{GND})

$$l = \frac{1}{\sqrt{\Psi(\rho_{GND} + \rho_{SSD})}} \tag{5.1.54}$$

where, Ψ is the probability of pinning or the percentage of GNDs and SSDs contributing to hardening. It is to be noted here that Eq. 5.1.53 can also be written as $\dot{\beta p}^{\lambda} = \propto \sinh\left(\mathrm{sgn}(\tau^{\lambda})(|\tau^{\lambda}| - \tau_c^{\lambda})\varphi\right)$, where $\propto = \rho_g \nu (b^{\lambda})^2 \exp\left(-\frac{\Delta F^{\lambda}}{kT}\right)$ and $\varphi = \frac{V^{\lambda}}{kT}$ are simply constants, since none of the parameters constituting $\propto$ and φ are changed as the deformation progresses (the only parameters in the slip law which are changing are τ^{λ} and τ_c^{λ}). Here, we mention the thermal activation aspects of $\propto$ and φ, for the sake of completeness. However, thermal activation aspect of the slip rule is not relevant for the sample material under consideration as values of ΔF and V are chosen to minimise the strain-rate sensitivity (values in Table E.1 in Appendix E).

To compute GNDs at each of the eight gauss points of C3D20R, the following steps are adopted in the UMAT. We know from Section 5.1.3.3 that to compute GNDs we need to know the dislocation tensor and therefore the CURL ($\boldsymbol{F}^p$). At each gauss point, the UMAT computes $\boldsymbol{F}^p$. So, after each of the gauss points of a given element has been analysed by the UMAT, $\boldsymbol{F}^p$ will be known at each of the eight points. The aim however is to obtain CURL ($\boldsymbol{F}^p$) at each of these points (i.e. capture the spatial variation in $\boldsymbol{F}^p$ within the element). To do this a linear 3D element is considered within the C3D20R element, such that the nodes of the linear element are co-incident with the gauss points of C3D20R element. So $\boldsymbol{F}^p$ is now known at each node of the linear element. CURL ($\boldsymbol{F}^p$) is then computed at the eight integration points of this linear element and these results are extrapolated back to the eight gauss points of C3D20R (i.e. the nodes of the linear element) using linear shape functions. Further details about this method can be found in [130], [195]. Following this method, CURL ($\boldsymbol{F}^p$) at a gauss point of C3D20R can only be obtained once

$\boldsymbol{F}^p$ is known at each of the eight gauss points of an element. Thus, a common block is used to share data ($\boldsymbol{F}^p$) between gauss points of each element. For a given time increment, once $\boldsymbol{F}^p$ is known at all eight gauss points of a given element, the method described above is used to compute CURL ($\boldsymbol{F}^p$) at each of the gauss points. Thus, in the UMAT, at a given time increment, GND density at a particular gauss point of an element, is computed using the CURL ($\boldsymbol{F}^p$) known at that gauss point, from the previous time increment.

The experimentally measured nano-indentation load-displacement data was used to refine the critically resolved shear stress parameter (CRSS), used in the slip law, to ensure accurate reproduction of the load-displacement curve. Values of all other UMAT parameter used for this model are provided in Table E.1 in Appendix E. Assumptions of isotropic elasticity and small deformations were made in the numerical simulation.

Lattice rotations and residual elastic strain fields beneath the indents were extracted from these simulations and were directly compared with the corresponding experimental measurements. The model was constructed with the initial crystallographic orientation of the sample. Both, experimental and the simulated results are presented in the same sample coordinate frame to enable a direct comparison.

5.1.5. Results and Discussion

5.1.5.1. Residual elastic rotations and strains

Lattice orientation of all sample points, captured by rotation matrix $\boldsymbol{R}$, was measured experimentally by Laue diffraction and also predicted by the CPFE simulations. The average of the rotation matrix $\boldsymbol{R}$, of points located between 22-25 μm beneath the indent was chosen as the reference $\boldsymbol{R}_{ref}$, and the changes in orientation $\boldsymbol{R}_{dif}$, of all other points were calculated with respect to $\boldsymbol{R}_{ref}$ (Eq. (5.1.56)). $\boldsymbol{R}_{ref}$ captures the combined effect of

right handed rotations about the X, Y and Z axis, θ_x, θ_y and θ_z respectively. The sequence of rotations is θ_x first, then θ_y and finally θ_z . Given the rotation matrix $\boldsymbol{R}_{dif}$ for every point in the sample, and provided that $R_{dif_{31}} \neq \pm 1$, the lattice rotation angles were computed for each sample point using the expressions in Eq. (5.1.57) provided in [229]:

$$\boldsymbol{R} = \boldsymbol{R}_{dif}\boldsymbol{R}_{ref} \tag{5.1.55}$$

$$\boldsymbol{R}_{dif} = \boldsymbol{R}\boldsymbol{R}_{ref}^{-1} \tag{5.1.56}$$

$$\theta_x = \tan^{-1}\left(\frac{R_{dif_{32}}}{R_{dif_{33}}}\right), \quad \theta_y = -\sin^{-1}\left(R_{dif_{31}}\right), \quad \theta_z = \tan^{-1}\left(\frac{R_{dif_{21}}}{R_{dif_{11}}}\right) \tag{5.1.57}$$

Figure 5.1.4 shows the lattice rotations predicted by CPFE and those measured experimentally, plotted on sections in the YZ plane at different position along the X-axis. Appendix D shows a schematic representation of the nano-indentation process and depicts the lattice rotations expected due to indentation. The lattice rotation directions we observe (Figure 5.1.4) agree very well with this. Kysar et al. [216] used electron back-scatter diffraction (EBSD) to measure lattice rotations (spatial resolution of ~ 3 μm) in a single crystal nickel, indented with a wedge indenter. However, in their study, a two-dimensional deformation state was purposely introduced to eliminate all out-of-plane deformation gradients (within experimental error), such that the resultant dislocation tensor had only two non-zero components. Using the advanced technique of Laue diffraction, we have been able to measure the out-of-plane components of the lattice distortions and therefore the elastic portion of the deformation gradient with sub-micron resolution.

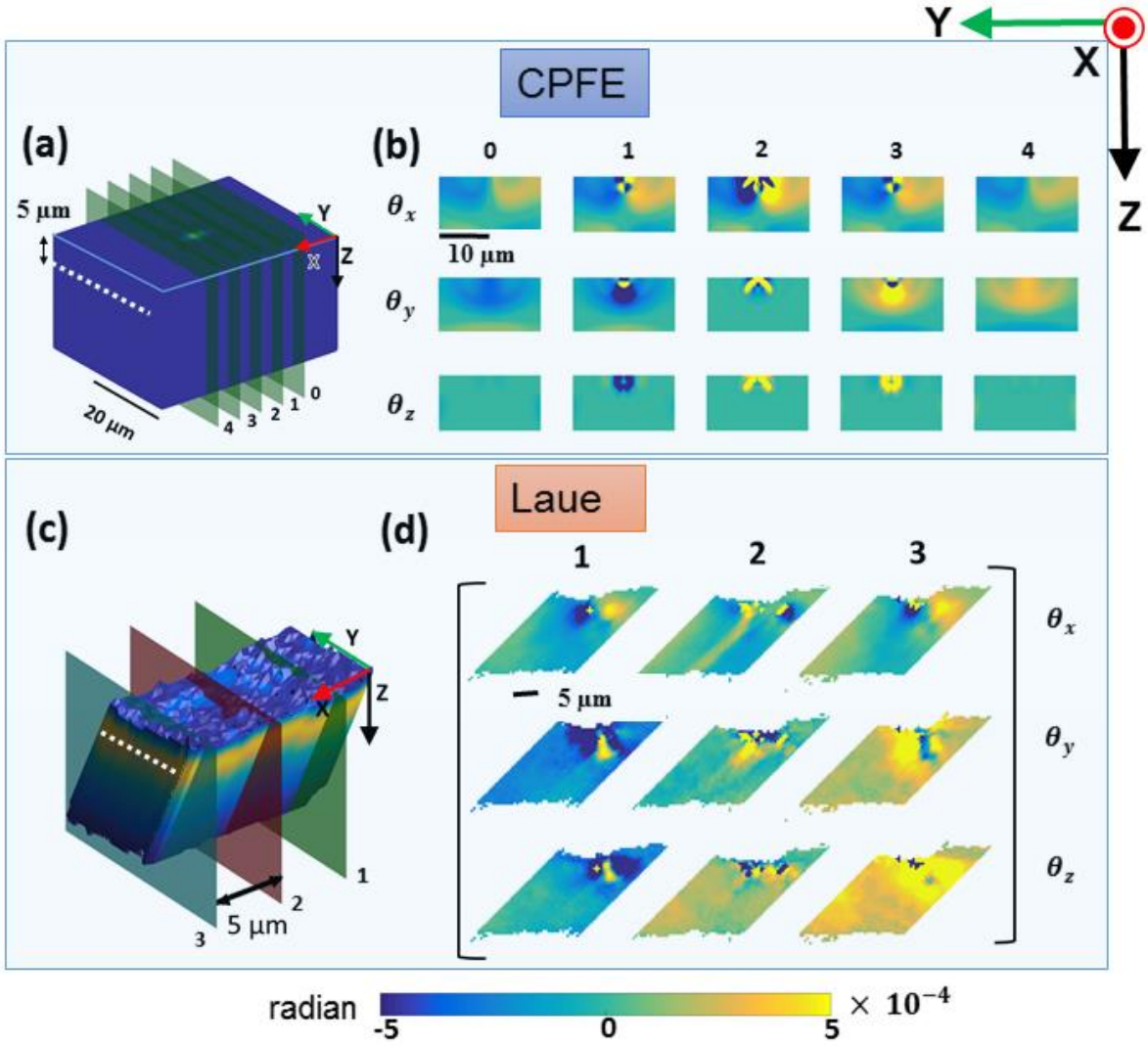


Figure 5.1.4 – **CPFE data**: (a) 3D rendering of the simulated volume coloured according to the predicted displacement magnitude along the Z axis of the indented tungsten block. X, Y and Z axes are superimposed. Slices 0-4, drawn on the block, represent the five sections along the X-axis (slice 2 being the indent centre), on which the lattice rotations predicted by CPFE are plotted in (b). **Laue experimental data**: (c) Visualisation of the measured sample volume, coloured according to the experimentally measured intensity. Superimposed are the X, Y, and Z axes, as well as the slices on which the measured lattice rotations in (d) are plotted. With respect to the initial crystallographic coordinates, the X axis points in [1 -1 0] direction, the Y in [1 1 0] direction and the Z in the [001] direction. Slices 1-3 in experiments and simulations are at the same spatial positions and data in (b) and (d) are displayed on the same length- and colour-scale. The dotted white lines through (a) and (c) represent the depth at which the line plots in Figure 5.1.5 were extracted.

As seen in Figure 5.1.4, CPFE predictions match well with the experimental results, for all three rotation components, except at the indent centre (Figure 5.1.4, slice 2), where a rapid variation of lattice rotations is seen. A quantitative comparison between the CPFE and the experimental results are made in Figure 5.1.5 where line plots corresponding to the contour plots in Figure 5.1.4 (b) and (d), have been extracted at a depth of 5 µm beneath the indent (shown by white dotted lines in Figure 5.1.4 (a) and (c)). The results for both CPFE calculations and Laue measurements are superimposed.

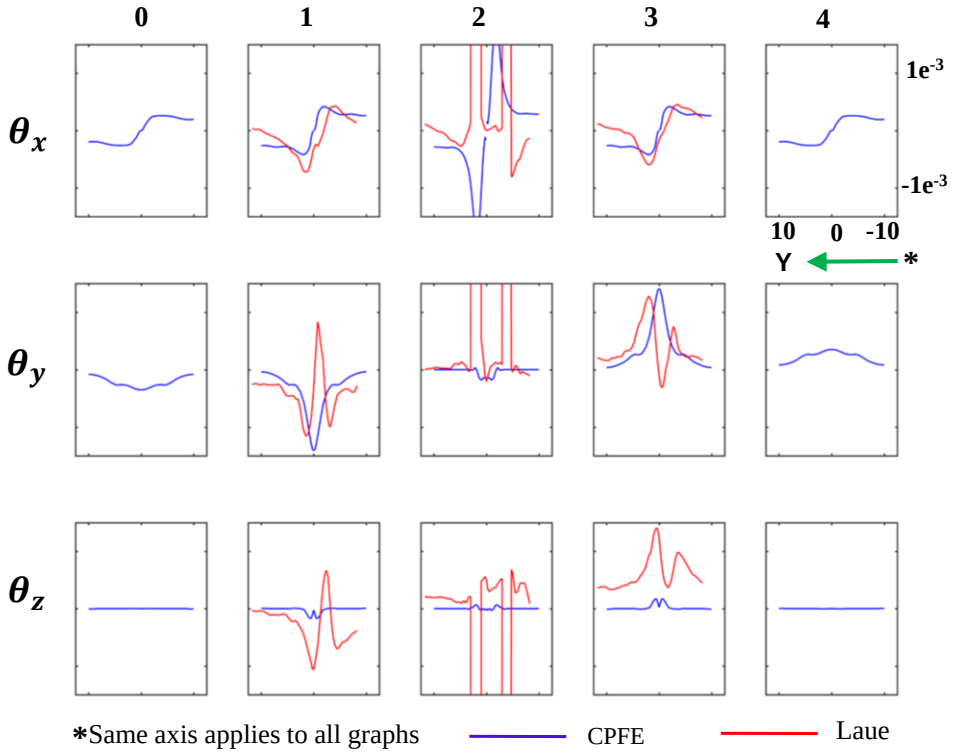


Figure 5.1.5 – Line plots corresponding to the contour plots in Figure 5.1.4 (b) and (d). Lattice rotations are plotted along a horizontal line 5 µm below the indent (line shown by dotted white lines in Figure 5.1.4 (a) and (c)). The slices (0-4) represent the five sections along the X-axis (slice 2 being the indent centre), shown by the YZ planes drawn in Figure 5.1.4 (a) and (c).

In Figure 5.1.5, agreement between CPFE predictions and the Laue measurements is quite good, particularly in slices 1 and 3 (slices 5 µm away, on either side of the indent centre) for the θ_x component. In slices 1 and 3, reasonable agreement is noticed for θ_y

component as well. However, θ_z predicted by CPFE does not agree with that measured by Laue. While Laue measurements show magnitude of θ_z to be almost comparable to that of θ_x and θ_y, this is not captured in CPFE, which shows θ_z to be near zero.

At the indent centre significant discrepancies are visible, likely the result of steep strain gradients which cannot be captured properly due to limited spatial resolution in our measurements. A similar effect, although at a lower spatial resolution (> 2μm), of strong discontinuities in the lattice rotation fields below indents in fcc single crystal nickel, were made by Dahlberg et al. [197] using 2D CPFE and EBSD measurements.

The experimental Laue measurements only provide the deviatoric lattice strain tensor ($\boldsymbol{\varepsilon}^e_{dev}$), which is related to the total strain tensor ($\boldsymbol{\varepsilon}^e$) by

$$\boldsymbol{\varepsilon}^e = \boldsymbol{\varepsilon}^e_{dev} + \boldsymbol{\varepsilon}^e_{vol} = \boldsymbol{\varepsilon}^e_{dev} + 1/3\ \mathrm{Tr}\,(\boldsymbol{\varepsilon}^e)\boldsymbol{I} \tag{5.1.58}$$

To make a direct comparison with the experimental measurements, the dilatational and plastic strains were removed from the total strain predictions from CPFE. Figure 5.1.6 shows the direct components of $\boldsymbol{\varepsilon}^e_{dev}$ predicted by CPFE and as well as the experimentally measured strains, plotted on the same YZ sections at different positions along the X-axis.

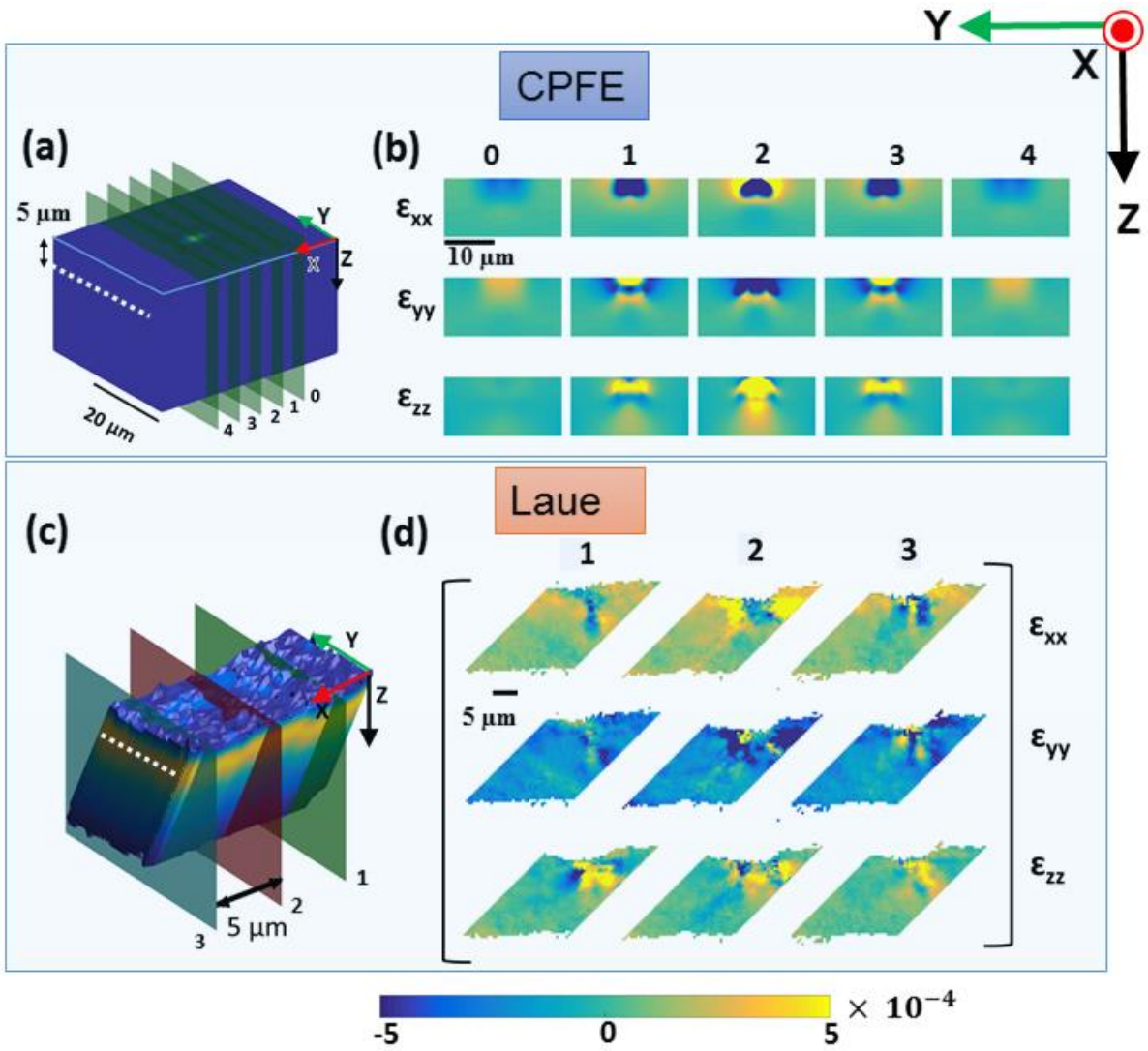


Figure 5.1.6 - **For the CPFE data**: (a) The slices 0-4 drawn on the block represent the five sections along the X-axis (slice 2 being at the indent centre) on which the residual deviatoric elastic strains predicted by CPFE are shown in (b). **For the Laue data**: Visualisation of the measured sample volume. Superimposed are the X, Y, and Z axes, as well as the slices on which the measured deviatoric elastic lattice strains in (d) are plotted. With respect to the initial crystallographic coordinates, the X axis points in [1 -1 0] direction, the Y in [1 1 0] direction and the Z in the [001] direction. Slices 1-3 in experiments and simulations are at the same spatial positions and data in (b) and (d) is displayed on the same length- and colour-scales. The dotted white lines through (a) and (c) represent the depth at which the line plots in Figure 5.1.7 were extracted.

Qualitatively there is quite good agreement, especially for the ε_{zz} out-of-plane strain component. A quantitative comparison between the results is made through comparing line plots (Figure 5.1.7), corresponding to the contour plots in Figure 5.1.6 (b) and (d), extracted

at depth of 5 μm beneath the indent (white dotted lines in Figure 5.1.6 (a) and (c)). The agreement of the lattice strains is not as clear as for the lattice rotations, but similar features can be identified in the measured and predicted profiles. This is especially the case for slices 1 and 3, i.e. slightly (5 μm away) away from the indent centre.

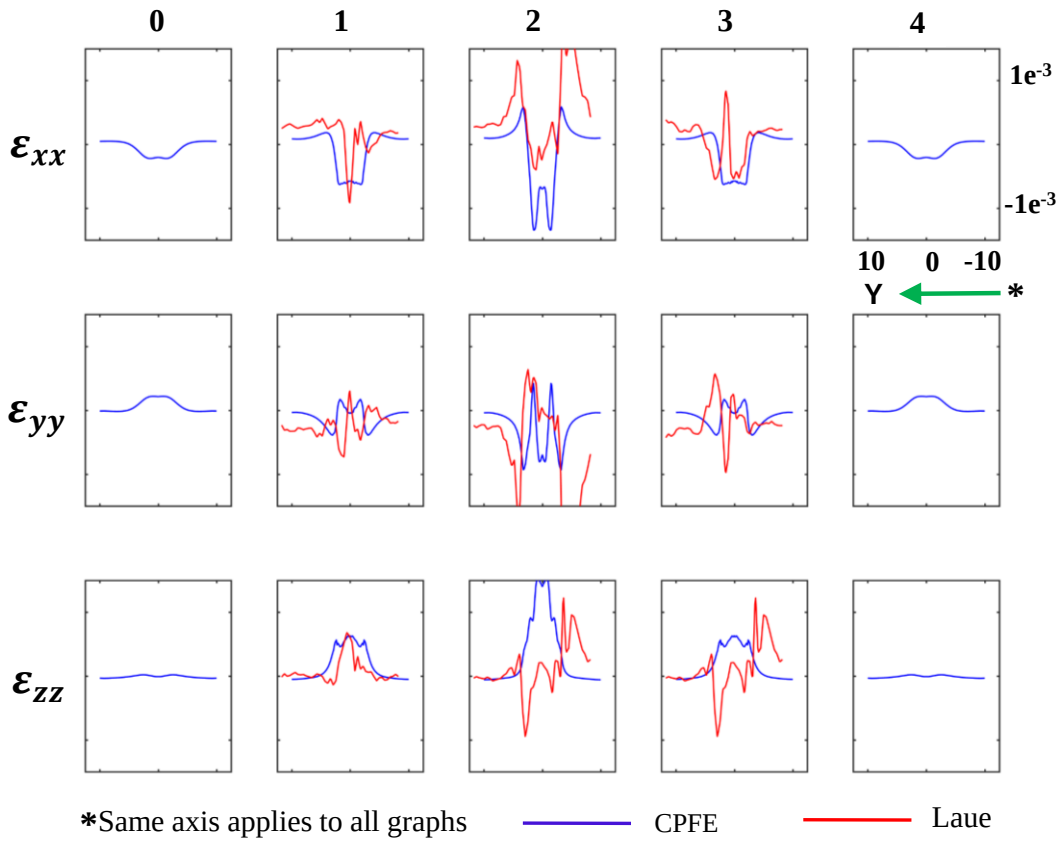


Figure 5.1.7 - Line plots corresponding to contour plots in Figure 5.1.6 (b) and (d) extracted at a depth of 5 μm below the indent (dotted white lines in Figure 5.1.6 (a) and (c)). The slices (0-4) represent the five sections along the X-axis (slice 2 being the indent centre), shown by the YZ planes drawn in Figure 5.1.6 (a) and (c).

Figure 5.1.8 shows all the components of the symmetric deviatoric strain tensor plotted on XZ and XY planes through the indent centre. Apart from the shear components, ε_{xz} and ε_{yz}, the strains predicted by CPFE and those measured experimentally agree quite well. In particular the symmetry of the deformation fields is reproduced. Experimental data

for the ε_{xz} and ε_{yz} components is noisy as the experimental configuration is relatively insensitive to these strain components [158].

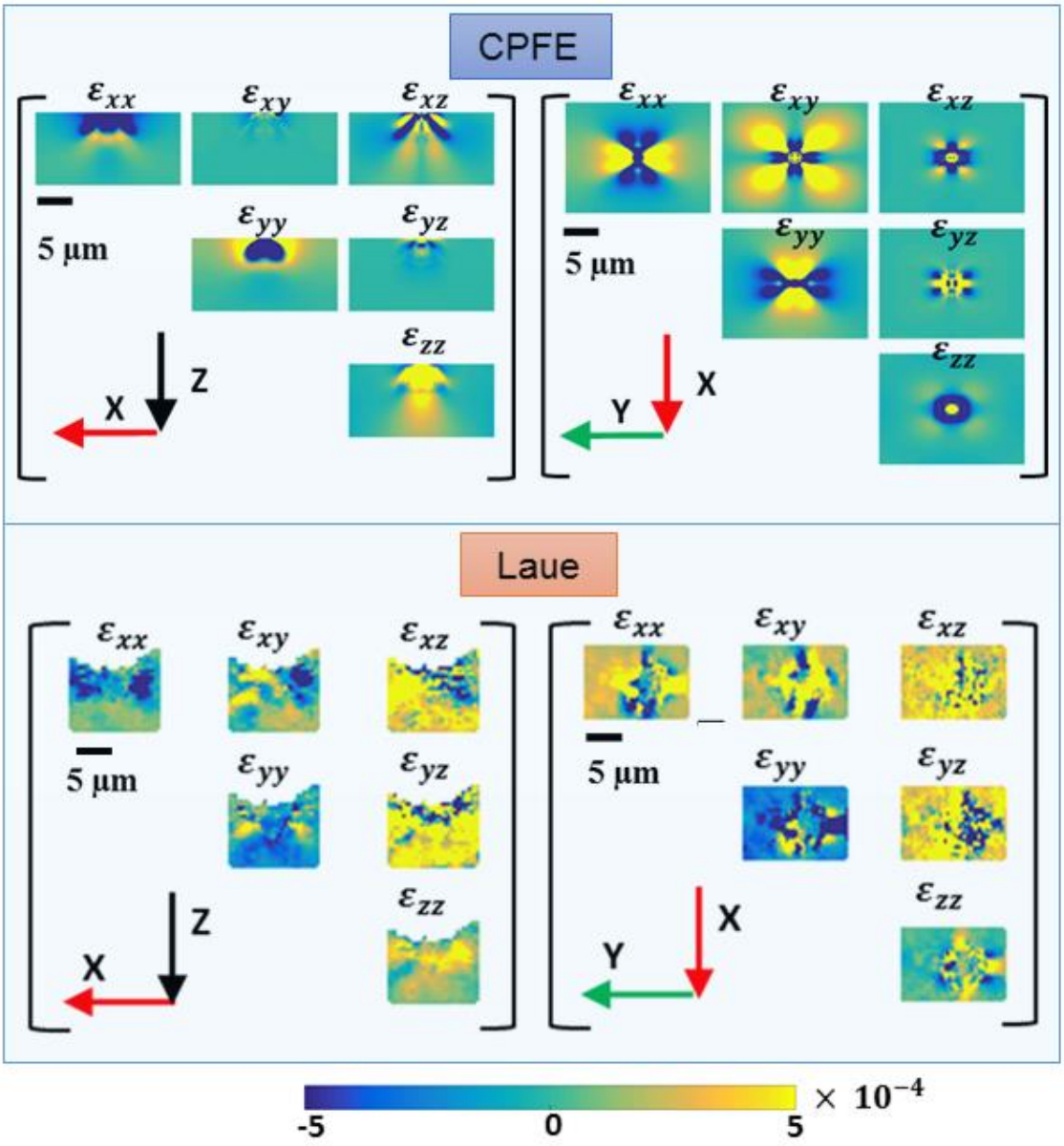


Figure 5.1.8 – Residual deviatoric elastic lattice strains predicted by CPFE simulation and experimentally measured by Laue-diffraction. The strains are plotted on sections through the indent centre in the XZ plane and at the indented free surface, the XY plane. Numerical predictions and experimental measurements are shown using same length- and colour-scales.

Several recent studies have used high-resolution electron backscatter diffraction (HR-EBSD) or high-resolution digital image correlation (HR-DIC) in conjunction with

CPFE simulations, to understand strain fields in crystals. For example, Guan et al. [219] used HR-DIC and CPFE simulations to investigate the development of strain fields and strain localisation in single crystal and oligocrystal nickel subjected to three-point beam bending with cyclic loading. Measurements were restricted to a two-dimensional area on the sample surface and qualitative agreement of only the three in-plane strain components in the XY plane were obtained. Kartal et al [217] used HR-EBSD, on the free surface of a nickel sample, to extract the full residual elastic strain tensor resulting from differences in thermal expansivities between the nickel matrix and a carbide particle embedded within it. A direct comparison of the deviatoric strain measurements from HR-EBSD and CPFE simulations only showed good agreement for the shear component ε_{xy}. In a similar study, Zhang et al. [142], used HR-DIC, HR-EBSD and CPFE simulations to assess the residual strain fields in a polycrystal nickel alloy embedded with a non-metallic agglomerate. They too only find qualitative agreement of the in-plane strains.

The key limitation of HR-EBSD and HR-DIC is their lack of depth-resolved information, thereby allowing examination of the deformation field only at the sample surface. In contrast, micro-beam Laue measurements allows 3D – resolved strain measurement with very good sensitivity of ~ 10^{-4}. However, its spatial resolution (~ 0.5 to 1 µm in 3D) is lower than HR-EBSD (~ 0.05 µm). Our measurements show surprisingly good agreement between the measured lattice rotations and strains, and those predicted by CPFE (Figure 5.1.4 and Figure 5.1.6), inspiring some confidence in the use of this combination of techniques for analysing crystal scale deformation.

5.1.5.2. Dislocation tensor computation

Next we compare the dislocation tensor $\boldsymbol{\alpha}$, found from Laue diffraction experiments with that predicted by CPFE calculations. Laue diffraction only measures the deviatoric residual

elastic strain ($\boldsymbol{\varepsilon}^e_{dev}$), while the CPFE simulations provide the full residual strain tensor (both elastic and plastic components). To allow a direct comparison, $\boldsymbol{\alpha}$ was computed from CPFE and experiments using only $\boldsymbol{\varepsilon}^e_{dev}$. The elastic component of the displacement gradient ($\boldsymbol{\beta}^e_{dev}$) was calculated using $\boldsymbol{\varepsilon}^e_{dev}$ and lattice rotation ($\boldsymbol{\omega}^e$) measurements:

$$\boldsymbol{\beta}^e_{dev} = \boldsymbol{\omega}^e + \boldsymbol{\varepsilon}^e_{dev} \tag{5.1.59}$$

$\boldsymbol{\omega}^e$ and $\boldsymbol{\varepsilon}^e_{dev}$ predicted by CPFE and measured from Laue were interpolated onto a regularly spaced grid using the triangulation-based linear interpolation function in MATLAB. Using Eq. 5.1.59, $\boldsymbol{\beta}^e_{dev}$ was then computed at each point of the regularly spaced grid. $\boldsymbol{\alpha}$ was then found by taking the curl of $\boldsymbol{\beta}^e_{dev}$ as stated in Eq. 5.1.35. The required gradients of $\boldsymbol{\beta}^e_{dev}$ (for e.g. $\frac{\partial \beta^e_{dev_{12}}}{\partial x_3}$ $-\frac{\partial \beta^e_{dev_{13}}}{\partial x_2}$) were computed using the gradient function in MATLAB (for example $\frac{\partial \beta^e_{dev_{11}}}{\partial x_1}$, $\frac{\partial \beta^e_{dev_{11}}}{\partial x_2}$ and $\frac{\partial \beta^e_{dev_{11}}}{\partial x_3}$ is considered to be the difference in $\beta^e_{dev_{11}}$ between consequent points on the uniform grid, along X, Y and Z directions respectively, divided by the grid step size). $\boldsymbol{\beta}^p$ obtained directly from the CPFE simulation, was also subjected to a similar interpolation onto a uniform grid using MATLAB and the same gradient function was then used to compute $\boldsymbol{\alpha}$ from curl of $\boldsymbol{\beta}^p$.

Figure 5.1.9 shows the dislocation tensor, calculated from CPFE and experimental measurements, plotted on YZ, XZ and XY sections, through the indent centre. From Eq. (5.1.32), $\boldsymbol{\alpha} = (\text{curl}\ (\boldsymbol{\beta}^p))^T \approx -(\text{curl}\ (\boldsymbol{\beta}^e))^T$ for small strains. The plots of $(\text{curl}\ (\boldsymbol{\beta}^p))^T$ and $-(\text{curl}\ (\boldsymbol{\beta}^e_{dev}))^T$, computed from CPFE simulations, are remarkably similar. The CPFE and experimental measurements, both show large and rapid variations of the dislocation tensor near the indent. However, the details of the components of $\boldsymbol{\alpha}$ clearly are quite different. The limited spatial resolution in experiments is likely the main reason. This

is particularly the case since the curl operation takes the gradient of the measured lattice strains and rotations, making it very sensitive to experimental uncertainties, especially in the presence of steep strain gradients. Interestingly the XY plots clearly show the same symmetry in both experiments and simulations.

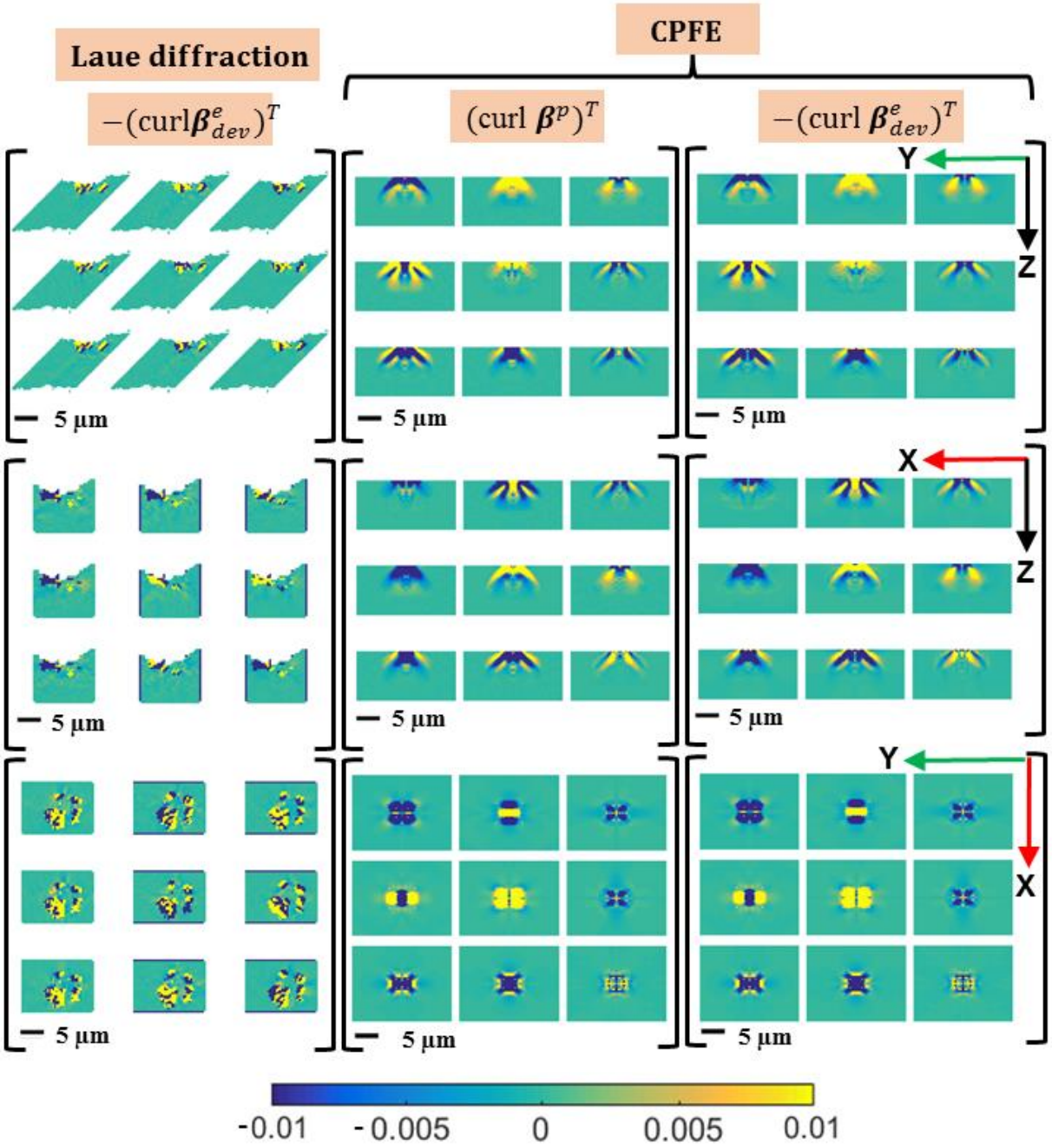


Figure 5.1.9 - The dislocation tensor $\boldsymbol{\alpha}$ of the deformation field beneath spherical indents in pure tungsten. Plots are shown on sections thought the indent centre on YZ, XZ and the XY planes. Colour scale has units of 1/µm and $\boldsymbol{\alpha}$ is represented as $\begin{bmatrix} \alpha_{11} & \alpha_{12} & \alpha_{13} \\ \alpha_{21} & \alpha_{22} & \alpha_{23} \\ \alpha_{31} & \alpha_{32} & \alpha_{33} \end{bmatrix}$.

An important question concerns the error incurred by neglecting the volumetric component of the elastic lattice strain. Consider the difference, δ, between $(-\text{curl}\,(\boldsymbol{\beta}^e))^T$ and $(-\text{curl}\,(\boldsymbol{\beta}^e_{dev}))^T$, which both provide approximations to $\boldsymbol{\alpha}$:

$$\boldsymbol{\alpha} \cong (-\text{curl}\,(\boldsymbol{\beta}^e))^T = (-\text{curl}\,(\boldsymbol{\varepsilon}^e + \boldsymbol{\omega}^e))^T = (-\text{curl}\,(\boldsymbol{\varepsilon}^e_{dev} + \boldsymbol{\varepsilon}^e_{vol} + \boldsymbol{\omega}^e))^T \quad (5.1.60)$$

$$\boldsymbol{\alpha} \cong (-\text{curl}\,(\boldsymbol{\beta}^e_{dev}))^T = (-\text{curl}\,(\boldsymbol{\varepsilon}^e_{dev} + \boldsymbol{\omega}^e))^T \quad (5.1.61)$$

The difference, δ, corresponds to the curl of the volumetric strain component $(\boldsymbol{\varepsilon}^e_{vol})$:

$$\begin{aligned}\delta &= \left(-\text{curl}\,(\boldsymbol{\varepsilon}^e_{dev} + \boldsymbol{\varepsilon}^e_{vol} + \boldsymbol{\omega}^e)\right)^T - \left(-\text{curl}\,(\boldsymbol{\varepsilon}^e_{dev} + \boldsymbol{\omega}^e)\right)^T \\ &= \left(-\text{curl}\,(\boldsymbol{\varepsilon}^e_{vol})\right)^T\end{aligned} \quad (5.1.62)$$

Figure 5.1.10 shows plots of δ, computed from the CPFE simulations, on the same YZ, XZ and the XY planes through the indent centre as used in Figure 5.1.9. A comparison of Figure 5.1.9 (column 3: depicting the components of $\boldsymbol{\alpha}$ calculated using $\left(-\text{curl}\,(\boldsymbol{\beta}^e_{dev})\right)^T$) and Figure 5.1.10 shows that the magnitude of δ is substantially smaller than that of $\boldsymbol{\alpha}$. This suggests that effect of $\left(-\text{curl}\,(\boldsymbol{\varepsilon}^e_{vol})\right)^T$ on the calculated components of $\boldsymbol{\alpha}$ is small.

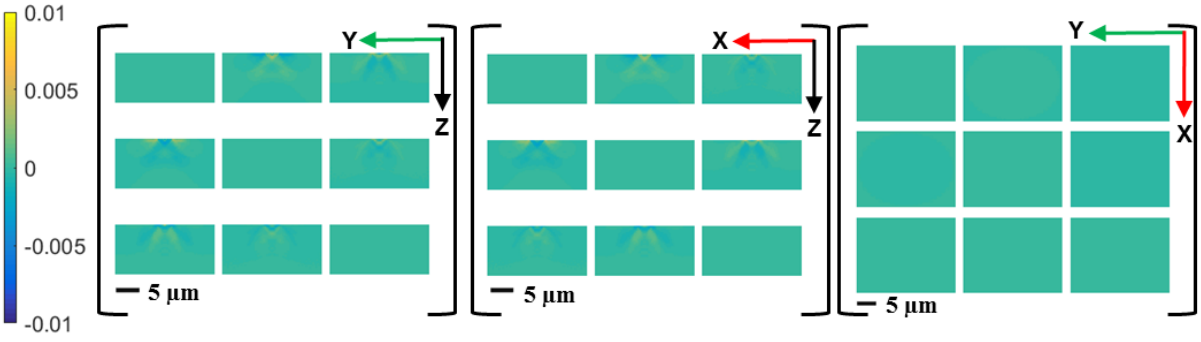


Figure 5.1.10 – Plot of $\delta = (-\text{curl}\,(\boldsymbol{\beta}^e))^T - \left(-\text{curl}\,(\boldsymbol{\beta}^e_{dev})\right)^T$ at the indent centre, on the YZ, XZ and XY planes. The colour scale has units of 1/µm and the representation of the components of δ is the same as that of $\boldsymbol{\alpha}$ in Figure 5.1.9.

The lack of sensitivity of $\boldsymbol{\alpha}$ to the volumetric part of the elastic strain tensor is an important result since many experimental techniques (for example Micro-beam Laue diffraction, HR-EBSD) can only readily measure deviatoric elastic strain. Nye's original formulation [108] only considered lattice rotations, implying that for small deformations the effect of lattice rotations dominates over that of lattice strains. The volumetric component of the elastic strain tensor is expected to play an even smaller part since plastic deformation, accommodated by crystallographic slip, is an isochoric process.

The 3D depth-resolved measurements of deviatoric lattice strain and rotation, possible with micro-beam Laue diffraction, allow determination of all nine components of the dislocation tensor. This is in contrast to surface techniques, such as HR-EBSD [215], [113], [112], [218] or micro-Laue diffraction without depth resolution [230], where terms of the dislocation tensor Eq. (5.1.38) depending on $\frac{\partial}{\partial x_3}$ remain unknown. Hence, without depth-resolution, only three of the nine elements of $\boldsymbol{\alpha}$ can be explicitly determined. If the assumption is made that the effect of lattice strains is negligible, five components may be determined [106]. This means that GND densities determined from 2D surface methods will always constitute a lower bound estimate.

5.1.5.3. GND density computation

GND density was computed using L^2 and L^1 optimisation techniques for both experimental measurements and CPFE simulations. For tungsten we assume that deformation is accommodated by dislocations with a/2<111> Burgers' vector slipping on {110} planes [127], [231] (list of Burgers' vectors and line directions in Appendix G). Furthermore, we assume dislocations to have either pure edge or pure screw character. This results in 16

distinct dislocation types; four screw types with <111> line directions and twelve edge type with <112> line directions.

L^1 vs L^2 Optimisation

The GND densities of all sixteen dislocation types, determined using the L^2 optimisation method (Eq. (5.1.39) and (5.1.41)), are shown in Figure 5.1.11 and Figure 5.1. 13 for experiments and CPFE simulations respectively. In both figures dislocation densities are plotted on YZ, XZ and XY sections through the indent centre. GND densities, determined using the L^1 optimisation method (Eq. (5.1.39) and (5.1.42)), are shown in Figure 5.1.12 and Figure 5.1.14 for experiments and CPFE simulations respectively. For the L^2 optimisation the GND density is distributed (almost evenly) over all slip systems. The reason is that minimisation of $\sum_j \rho_j^2 = \boldsymbol{\rho}^T.\boldsymbol{\rho}$ associates a larger penalty with slip systems that have high dislocation density. Thus a solution where dislocation density is distributed amongst slip systems is favourable. In contrast, the L^1 scheme minimises the total energy (weighted line length) namely $(1-\upsilon)^{-1}\sum_j \rho_j^{edge} + \sum_j \rho_j^{screw}$. Here a much greater variation of dislocation density distribution between slip systems is observed.

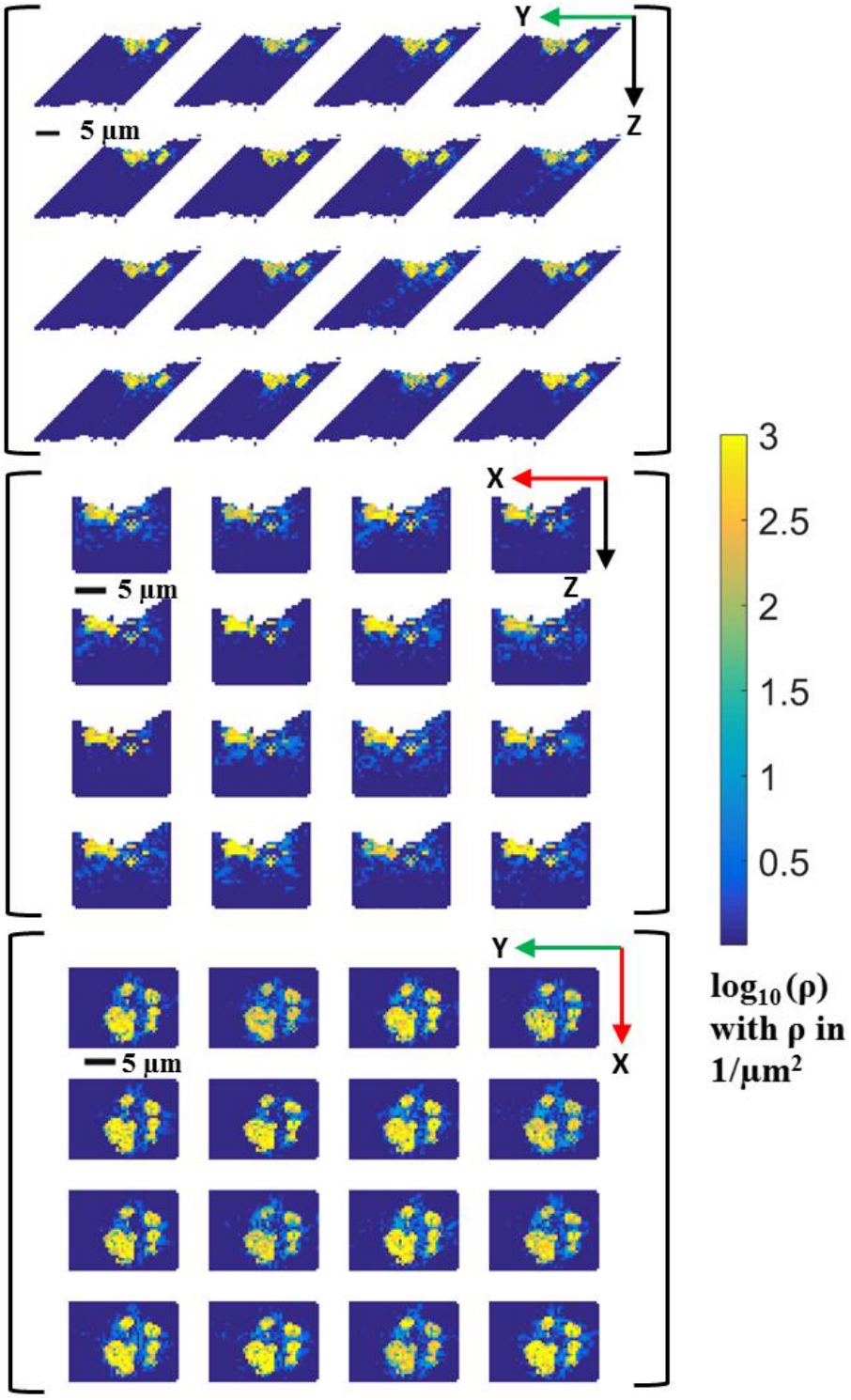


Figure 5.1.11 – Experimental dislocation densities obtained by L^2 optimisation method plotted at the indent centre on the YZ, XZ and the XY plane. For each plane, the 16 dislocation densities plotted correspond to $\begin{bmatrix} \text{Edge 1} & \text{Edge 2} & \text{Edge 3} & \text{Edge 4} \\ \text{Edge 5} & \text{Edge 6} & \text{Edge 7} & \text{Edge 8} \\ \text{Edge 9} & \text{Edge 10} & \text{Edge 11} & \text{Edge 12} \\ \text{Screw 1} & \text{Screw 2} & \text{Screw 3} & \text{Screw 4} \end{bmatrix}$. Colour scale shows $\log_{10}(\rho)$ with ρ in $1/\mu m^2$. Scale bar = 5 µm.

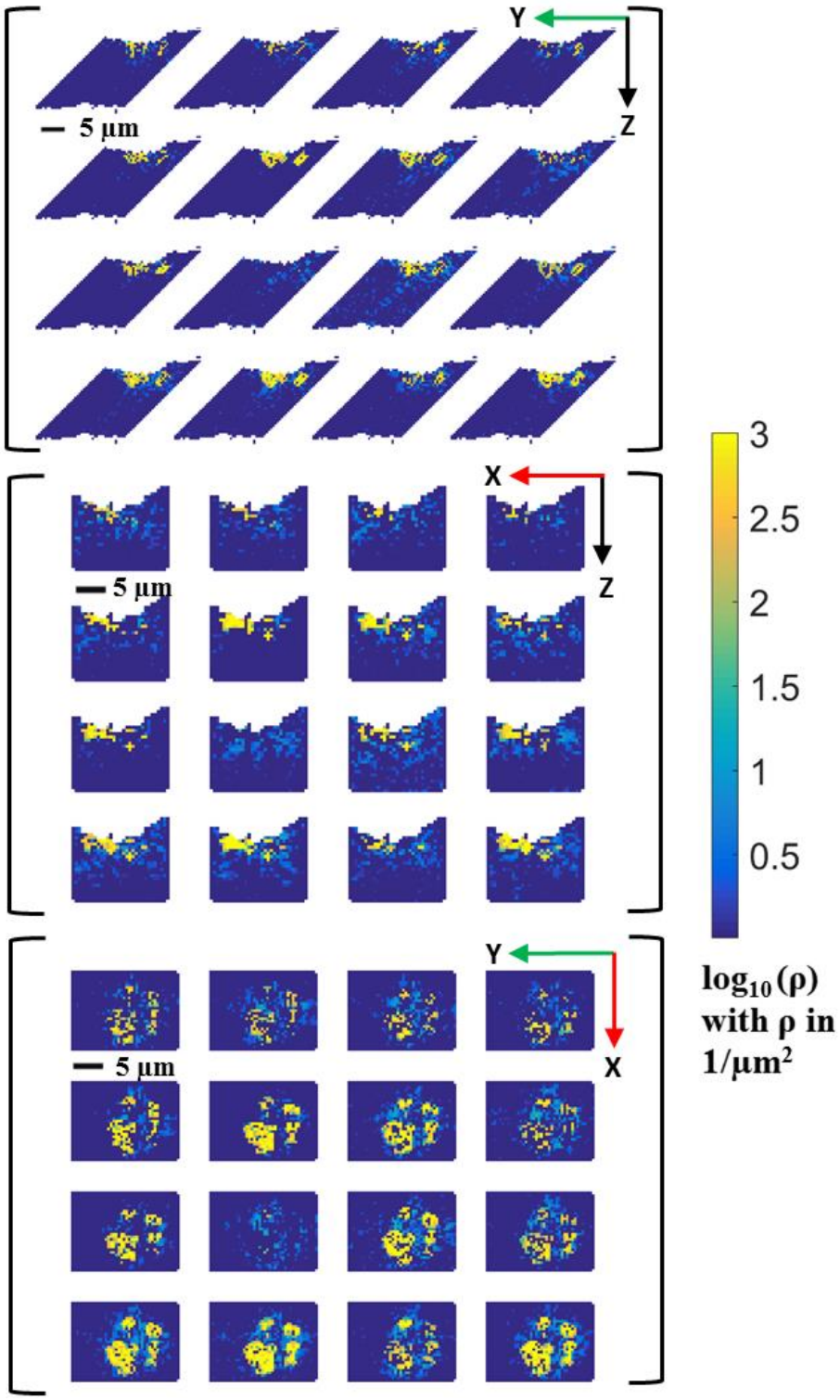


Figure 5.1.12 – Experimental dislocation densities obtained by L^1 optimisation method plotted at the indent centre on the YZ, XZ and the XY plane. For each plane, the 16 dislocation densities plotted correspond to $\begin{bmatrix} \text{Edge 1} & \text{Edge 2} & \text{Edge 3} & \text{Edge 4} \\ \text{Edge 5} & \text{Edge 6} & \text{Edge 7} & \text{Edge 8} \\ \text{Edge 9} & \text{Edge 10} & \text{Edge 11} & \text{Edge 12} \\ \text{Screw 1} & \text{Screw 2} & \text{Screw 3} & \text{Screw 4} \end{bmatrix}$. Colour scale shows $\log_{10}(\rho)$ with ρ in $1/\mu m^2$. Scale bar = 5 µm.

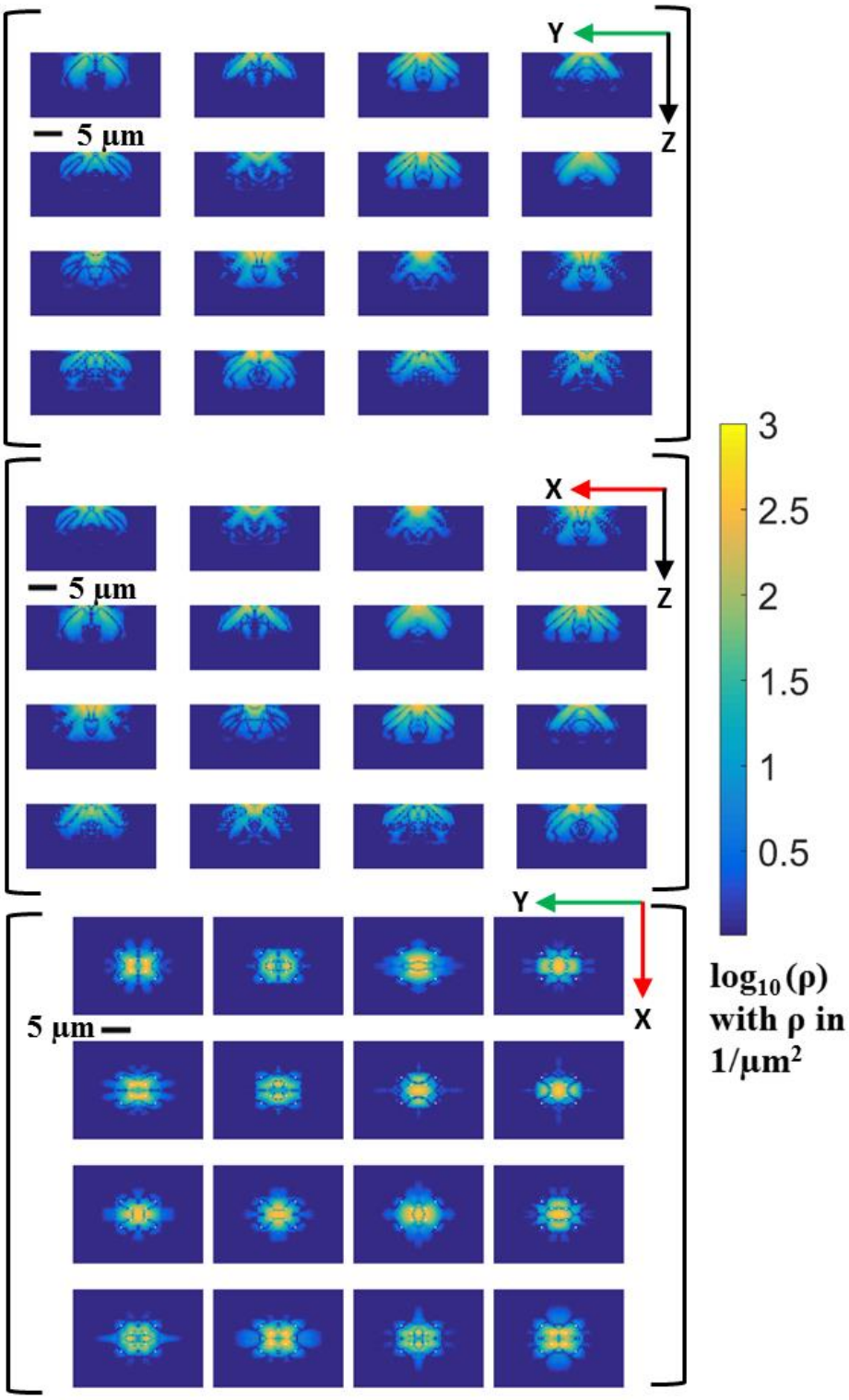


Figure 5.1. 13 – CPFEM Dislocation densities obtained by L^2 optimisation method plotted at the indent centre on the YZ, XZ and the XY plane. For each plane, the 16 dislocation densities plotted correspond to $\begin{bmatrix} \text{Edge 1} & \text{Edge 2} & \text{Edge 3} & \text{Edge 4} \\ \text{Edge 5} & \text{Edge 6} & \text{Edge 7} & \text{Edge 8} \\ \text{Edge 9} & \text{Edge 10} & \text{Edge 11} & \text{Edge 12} \\ \text{Screw 1} & \text{Screw 2} & \text{Screw 3} & \text{Screw 4} \end{bmatrix}$. Colour scale shows $\log_{10}(\rho)$ with ρ in $1/\mu m^2$. Scale bar = 5 µm.

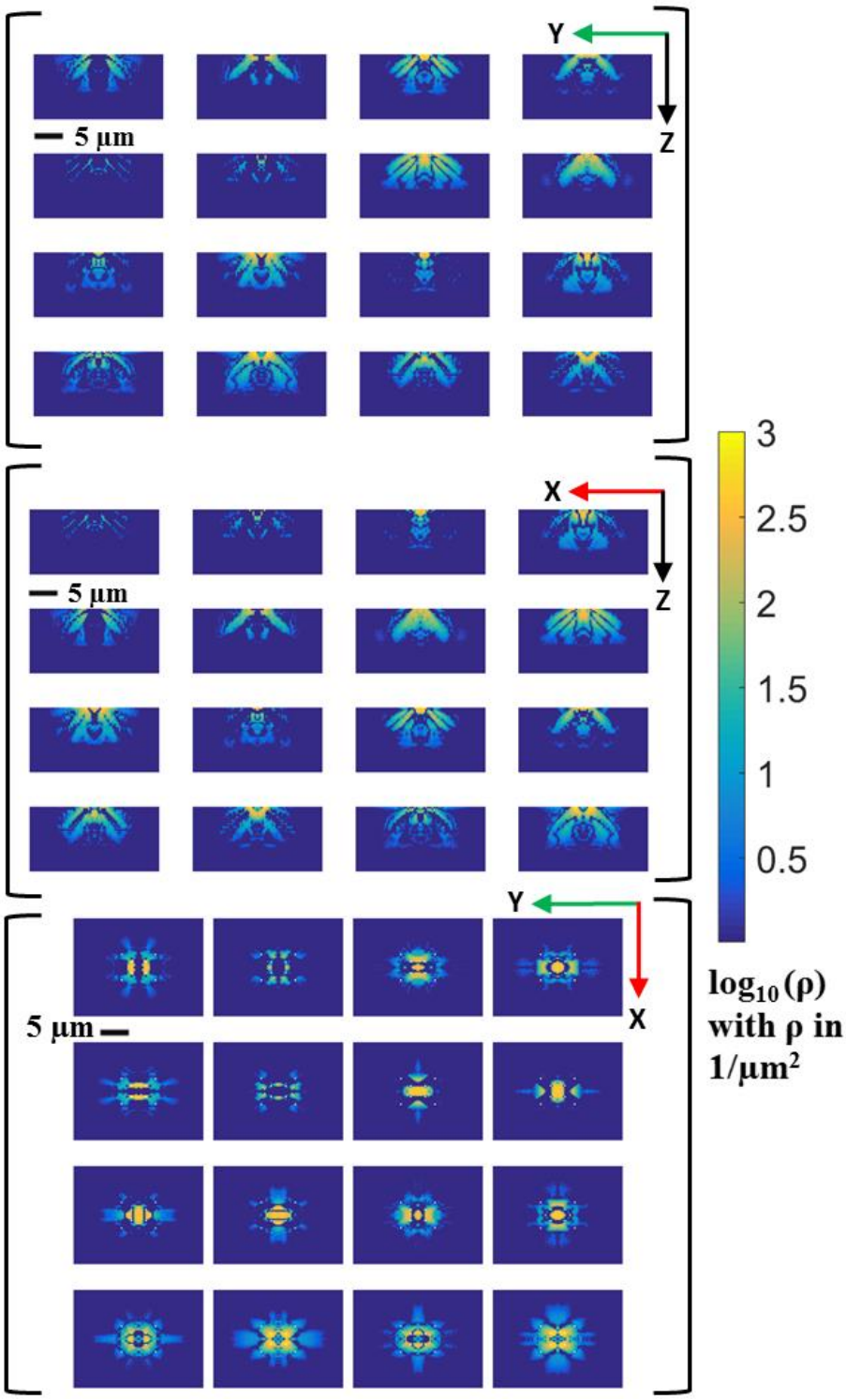


Figure 5.1.14 – CPFEM Dislocation densities obtained by L^1 optimisation method plotted at the indent centre on the YZ, XZ and the XY plane. For each plane, the 16 dislocation densities plotted correspond to $\begin{bmatrix} \text{Edge 1} & \text{Edge 2} & \text{Edge 3} & \text{Edge 4} \\ \text{Edge 5} & \text{Edge 6} & \text{Edge 7} & \text{Edge 8} \\ \text{Edge 9} & \text{Edge 10} & \text{Edge 11} & \text{Edge 12} \\ \text{Screw 1} & \text{Screw 2} & \text{Screw 3} & \text{Screw 4} \end{bmatrix}$. Colour scale shows $\log_{10}(\rho)$ with ρ in $1/\mu m^2$. Scale bar = 5 µm.

Arsenlis and Parks [133] compared L^1 and L^2 optimisation techniques for a fcc crystal and found that L^1 produced more accurate results for a dislocation structure consisting of two dislocation lines. In contrast, the L^2 method predicted complex dislocation structures with multiple dislocation lines. Randman et al. [215] and Ruggles et al. [218] also observed that L^1 minimisation generates an uneven distribution of GND density over individual slip systems. However, in their study, no corresponding comparison was made to densities obtained using the L^2 method. Our direct comparison of L^1 and L^2 methods, for both experimental and CPFE datasets, is consistent with these observations. It highlights that L^2 optimisation leads to an unphysical spreading of dislocation density over many slip systems, making the use of the L^1 method for accurate estimation of GND densities on individual slip systems essential. This effect will be of particular importance for crystal plasticity simulations where a distinction between the cutting density and mobile density associated with particular slip system is made [190].

The total dislocation density (i.e. summed over all slip systems) computed through both methods is remarkably similar. This is shown in Figure 5.1.15 where the total GND densities (calculated using L^1 and L^2 optimisations) from experiments and CPFE are plotted on YZ, XZ and XY sections through the indent centre. Thus, if only the total dislocation density in the sample is required, either of the optimisation techniques may be used. In this case, the L^2 optimisation, which is far more straightforward to implement and is computationally cheaper, is preferable.

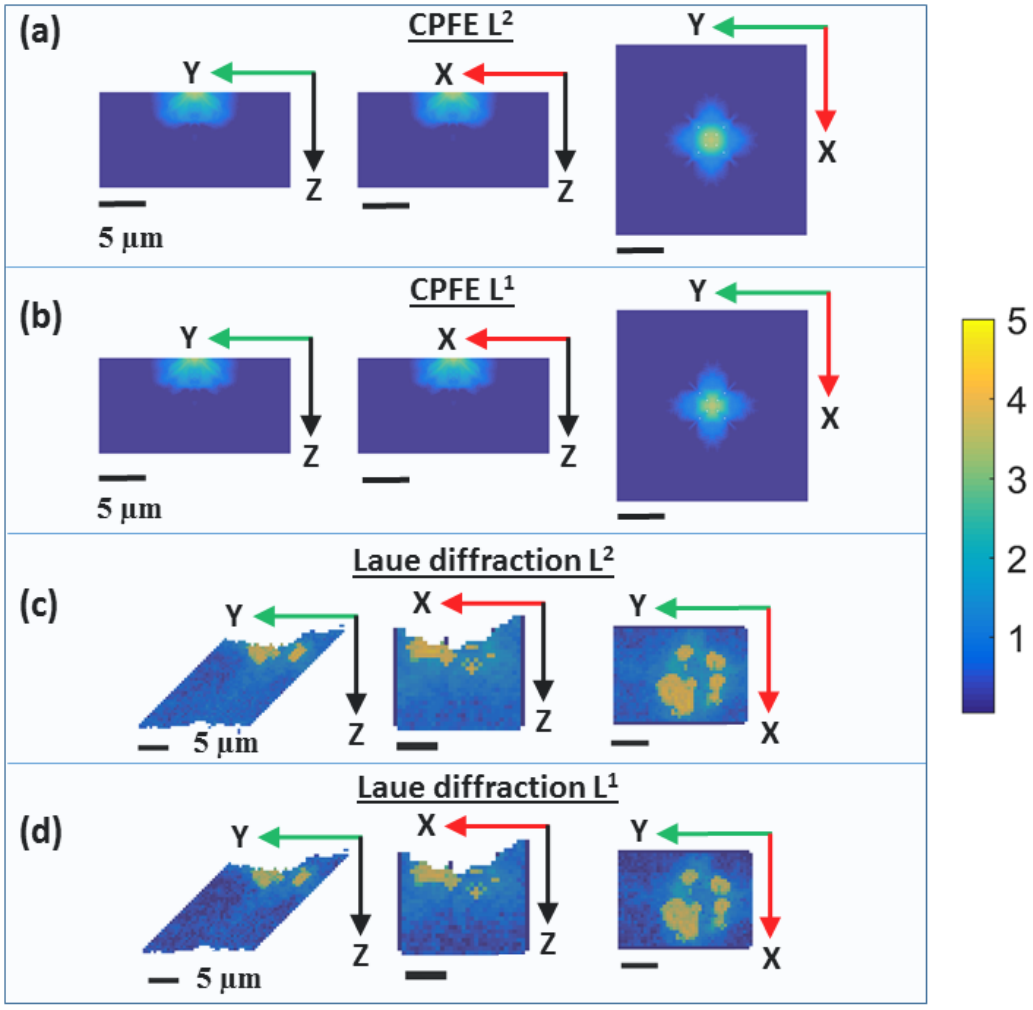


Figure 5.1.15 - Total dislocation density plotted on YZ, XZ and XY sections through the indent centre. The GND densities predicted by L^2 and L^1 optimisation based on CPFE data are shown in (a) and (b) respectively. L^2 and L^1 results from the experimental measurements are plotted in (c) and (d) respectively. The colour scale shows $\log_{10}(\rho)$ with ρ in lines/μm^2.

5.1.6. Conclusions

The dislocation tensor captures the dislocation population required to accommodate inhomogeneous plastic deformation. It is linked to the density of geometrically necessary dislocations (GNDs), and can be equated to lattice deformation in the form of lattice rotations and lattice strains. This provides a very useful relationship between GND density and the lattice curvature it accommodates. Here we have provided a comprehensive review of the theoretical background of the computation of Nye's dislocation tensor and the

underlying GND density in plastically deformed materials. Comparing CPFE simulations and X-ray diffraction measurements of lattice distortions associated with spherical nano-indents in tungsten, a number of important conclusions can be reached:

The relationship between different curl definitions, used to compute the dislocation tensor, has been explored.

- Table 5.1.1 provides a summary of the dislocation tensor in terms of both elastic and plastic deformation gradients, for cases of small and large deformations. Importantly the different curl definitions in use, if applied consistently, all lead to the same result.
- Lattice rotations and lattice strains beneath a spherical nano-indent in a tungsten single crystal are considered. CPFE and synchrotron X-ray micro-beam Laue measurements show good qualitative agreement, particularly for the 3D distribution of lattice rotations.
- The contribution of $\left(-\text{curl}\left(\boldsymbol{\varepsilon}_{vol}^{e}\right)\right)^{T}$, the curl of the volumetric part of the elastic strain tensor, to the dislocation tensor is small. This is an important result since many experimental strain measurement techniques, such as white-beam Laue diffraction and HR-EBSD, can only measure the deviatoric lattice strain tensor.
- L^1 optimisation recovers a more heterogeneous distribution of GND density over individual slip systems. In contrast L^2 optimisation distributes GND density almost uniformly over all slip systems. Thus, if GND density on specific slip systems is required, the physically-based L^1 minimisation should be used.
- The total GND density determined by either L^1 or L^2 minimisation is remarkably similar. Thus the computationally simpler L^2 optimisation may be used if only total GND density is required.

5.2. CPFE formulation for helium-implanted tungsten

This section is in publication format and is based on article "*S. Das, H. Yu, E. Tarleton, and F. Hofmann, "Hardening and Strain Localisation in Helium-Ion-Implanted Tungsten," arXiv Prepr. arXiv1901.00745, Dec. 2018*" [232]. The article is currently under review in the journal Scientific Reports.

5.2.1. Abstract

Tungsten is the main candidate material for plasma-facing armour components in future fusion reactors. In-service, fusion neutron irradiation creates lattice defects through collision cascades. Helium, injected from plasma, aggravates damage by increasing defect retention. Both can be mimicked using helium-ion-implantation. In a recent study on 3000 appm helium-implanted tungsten (W-3000He), we hypothesised helium-induced irradiation hardening, followed by softening during deformation. The hypothesis was founded on observations of large increase in hardness, substantial pile-up and slip-step formation around nano-indents and Laue diffraction measurements of localised deformation underlying indents. Here we test this hypothesis by implementing it in a crystal plasticity finite element (CPFE) formulation, simulating nano-indentation in W-3000He at 300 K. The model considers thermally-activated dislocation glide through helium-defect obstacles, whose barrier strength is derived as a function of defect concentration and morphology. Only one fitting parameter is used for the simulated helium-implanted tungsten; defect removal rate. The simulation captures the localised large pile-up remarkably well and predicts confined fields of lattice distortions and geometrically necessary dislocation underlying indents which agree quantitatively with previous Laue

measurements. Strain localisation is further confirmed through high resolution electron backscatter diffraction and transmission electron microscopy measurements on cross-section lift-outs from centre of nano-indents in W-3000He.

5.2.2. Introduction

There is an ongoing search for plasma facing armour materials for critical components in future fusion reactors, such as the main wall and the divertor. Tungsten is a promising candidate due to its high melting point, reasonable strength at high temperatures and low sputtering yield [6], [14], [15]. Within the fusion reactor, armour components will be exposed to high temperatures (> 1200 K) and irradiated by high energy neutrons (14.2 MeV, ~ 2 dpa per year for tungsten) which will generate lattice defects [6], [8]. Foreign elements like hydrogen and helium will accumulate within initially pure tungsten components due to transmutation and migration from the fusion plasma [8]. The presence of helium in tungsten is particularly worrying because of its low solubility and strong affinity for lattice defects [78], [153].

Ideally, tungsten irradiated in the fusion reactor should be studied to examine the role played by helium in deciding the evolution of its properties. However, such samples being radioactive, are difficult to access and unsuitable for regular laboratory experiments. Helium-ion implantation can mimic the fusion induced radiation damage by creating irradiation-damage-like lattice defects. The injected helium further interacts with the lattice defects to create helium-defects. Such helium-implanted tungsten has been widely studied through both simulations and experiments for varying conditions of temperature and helium fluence [11], [69], [72], [75]. At room temperature, it has been seen that an energetic helium ion, creates numerous Frenkel pairs. While, most Frenkel pairs recombine immediately, a few are prevented from recombining, as helium occupies vacancies to form stable di-

helium-vacancy complexes [77], [153]. An important question concerns the fate of the SIAs. Recent DFT calculations and experiments show that the SIAs remain near to and form a stable configuration with the helium-filled vacancies [42], [77], [147].

Experimentally, these few atom large helium-defects formed at room-temperature, are challenging to probe. Surprisingly, high-resolution Transmission Electron Microscopy (TEM) micrographs of 0.3 at.% helium-implanted samples showed no visible damage [79] suggesting that the defects are smaller than 1.5 nm, the sensitivity limit of TEM to lattice defects [233]. An interesting question which arises here, is whether these tiny defects, "invisible" in TEM, can induce any significant changes in physical and mechanical properties.

Nano-indentation has been widely used to gain mechanistic insight into the shallow helium-damaged layers. Nano-indentation of 0.3 at.% helium-implanted samples showed a 30% increase in hardness [81]. Corresponding observations of 50% lower thermal diffusivity (at room temperature) [80] were also made. Helium-induced changes were also distinctly visible in the indent morphology. Large pile-up and slip steps were noticed around indents in helium-implanted tungsten as compared to shallow pile-up around indents in pure tungsten. This was seen for both Berkovich indents (250 nm deep, in 0.3 at.wt.% helium-implanted [81]) and spherical indents (~ 500 nm deep in 3000 appm helium-implanted (Chapter 4)). Moreover, 3D resolved micro-beam Laue diffraction measurement of residual lattice distortions beneath the indents showed a significantly smaller deformation zone in the implanted material (Chapter 4).

These observations from past studies make the following clear; helium can significantly aggravate cascade damage by enhancing defect retention due to its strong affinity for vacancies [153]. The resulting helium-defect-complexes, despite their small

size, can significantly alter mechanical properties. However, the mechanisms underlying these observations remain unclear. To prevent these undesirable helium-induced changes, it is essential to understand how helium-defects interact with the surrounding microstructure and evolve. This is also vital for enabling accurate predictions of the evolution of structural and functional properties and the lifetime of irradiated tungsten armour components; a critical aspect for the successful design of commercially viable fusion reactors.

We hypothesise that initially helium-defects strongly obstruct dislocation motion causing the observed pronounced hardening. As deformation progresses, gliding dislocations help to recombine helium-filled Frenkel defects, facilitating easier glide of subsequent dislocations through defect-free channels and creating the slip steps seen near nano-indents in the implanted material (observations in Chapter 4). The objective of this study is to explore this hypothesis using a combination of modelling and experimental techniques. A model built on this hypothesis will capture the physics of the internal damage mechanism. In the long term, such models could be useful for predicting the lifetime of engineering components, or to conduct virtual experiments.

Here we consider a <001>-oriented tungsten single crystal, partly implanted with 3000 appm of helium at room temperature. Nano-indentation with a spherical indenter tip was done on both helium-implanted and unimplanted parts of the sample. The physical morphology of the indent surface and region beneath the indents was examined using atomic force microscopy (AFM), scanning electron microscope (SEM) and transmission electron- microscopy (TEM) to assert the prior observations of helium-induced changes (in Chapter 4).

To test the hypothesis, a crystal plasticity finite element (CPFE) formulation was developed to simulate indentation in helium-implanted tungsten. A physically-based constitutive law is implemented in the model to effectively capture the mechanism of interaction between glide dislocations and helium-defects. CPFE predictions of lattice distortions beneath indents are compared to corresponding observations from X-ray micro-beam Laue diffraction and high-resolution electron backscatter diffraction (HR-EBSD) measurements. The spatial distribution of geometrically necessary dislocations (GNDs) beneath indents is calculated from both simulations and experiments as an indicator of the extent of plastic deformation. The results are discussed in light of the proposed mechanism for the interaction of helium-implantation-induced defects and glide dislocations in tungsten.

5.2.3. Methods

5.2.3.1. Sample Preparation

A 2.5 mm radius, 0.8 mm thick disc with [001] out-of-plane orientation was cut from a tungsten single crystal (99.99% purity). A high-quality surface finish was obtained by mechanical grinding, polishing with diamond paste and final chemo-mechanical polishing with 0.1 µm colloidal silica suspension.

5.2.3.2. Helium Implantation

Implantation was performed at the National Ion Beam Centre, University of Surrey, UK. The sample was partly implanted with helium at 298 K, using a 2 MeV ion accelerator, and a raster scanned beam, to ensure a uniform implantation dose. Using a combination of different ion energies and fluences (Appendix A), a near uniform helium ion concentration of ~ 3000 appm within a ~ 2.8 µm thick implanted layer was obtained [12], [42], [154].

The SRIM estimated implantation profile [155] (displacement energy of 68 eV, single-layer calculation model [156]) is shown in Figure 4.1 (a). A helium ion concentration of ~ 3100 ± 410 appm, with an associated damage of 0.20 ± 0.03 displacements per atom (dpa) was obtained between 0-2.8 μm depth. Frenkel pair formation is the main damage mechanism, since helium implantation induced recoils at energies < 2 MeV have predominantly low energy [42]. Little defect clustering is expected, given that the mobility of vacancies at room temperature is low [79], [178], [179], [234].

5.2.3.3. Nano-Indentation, AFM & SEM

Nano-indentation was performed on a MTS NanoXp, with a spherical diamond tip (~ 4.2 μm radius, 90° cone angle, from Synton MDP) to a maximum displacement of 500 nm with 50 μm spacing between indents. Indent impressions were imaged using a Zeiss Merlin FEG SEM. Surface morphology was determined using a Digital Instruments Dimension 3100 AFM in contact mode using Bruker CONTV-A tips (nominal tip radius 10 nm).

5.2.3.4. Micro-beam Laue diffraction

X-ray micro-diffraction was carried out at beamline 34-ID-E, Advanced Photon Source, Argonne National Lab, USA. This instrument allows measurements of lattice orientation with sub-micron 3D resolution using the Differential Aperture X-ray Microscopy (DAXM) technique. A detailed description of the DAXM technique and the 34-ID-E instrument is provided in Section 2.2.2.1 and Section 3.3.3. A polychromatic X-ray beam (7-30 keV) was focused by KB mirrors to a sub-micron probe spot (500 nm (vertical) × 400 nm (horizontal) full width at half maximum near Lorentzian shape). With the sample placed at the probe focus in 45° reflection geometry, diffraction patterns were recorded on an area detector (Perkin-Elmer, #XRD 1621, with pixel size 200×200 μm) placed ~ 511 mm above the

sample. Material up to 20 μm beneath the ion-implanted surface was measured with 0.5 μm 3D spatial resolution. Laue diffraction patterns containing 30+ peaks were indexed and fitted using the LaueGo software package (J.Z. Tischler: tischler@anl.gov) to extract both lattice orientation and the full deviatoric lattice strain tensor at each measured point in 3D space.

5.2.3.5. FIB Lift-out, HR-EBSD & TEM

Focused ion beam (FIB) lift-out cross-section samples (~ 3 μm thick) were made from the indent-centre in the implanted and unimplanted samples using a Zeiss Auriga FIB-SEM. For HR-EBSD measurements, lift-outs were thinned from one side to ~ 1.5 μm thickness using a 30 kV, 240 pA ion beam, followed by low energy ion beam polishing (2 kV, 200 pA, 10 minutes) to remove FIB damage. For TEM characterisation, the lift-out specimens were further thinned to ~ 100 nm using FIB, and then flash polished (1% NaoH aqueous solution, 0.05 s, 8 V, 298 K). Though the FIB lift-out preparation removes constraints perpendicular to the foil, the in-plane lattice strains and rotations are expected to remain largely unchanged.

HR-EBSD measurements were performed on a Zeiss Merlin FEG SEM equipped with a Bruker eFlash detector. The Kikuchi pattern at each point is recorded at the full detector resolution. The 2D spatial variation of lattice distortions is obtained by cross-correlating the EBSD pattern collected at each point in a map with a pattern collected at a nominally strain-free reference position (chosen far away from the indent (> 10 μm) in the unimplanted substrate material) [197], [216], [217]. From this the deviatoric lattice strain ($\sim 1 \times 10^{-3}$), lattice rotation ($\sim 1 \times 10^{-3}$ rads) and the GND density for each point was found [108], [133], [182], [188]. Analysis of the Kikuchi patterns was carried out using the XEBSD code provided by A. J. Wilkinson [103].

TEM characterisation was performed on a JEOL 2100 TEM at 200 keV. The TEM micrographs were taken under a two-beam bright field condition.

5.2.3.6. CPFE Modelling

The indentation experiments were simulated using a strain-gradient CPFE model based on the model proposed by Dunne et al. [130], [195] where plastic deformation is constrained to occur only in directions consistent with crystallographic slip. Recently we successfully demonstrated the use of strain-gradient CPFE for performing 3D simulations of nano-indentation in pure tungsten (Section 5.1). Here, we use a modified version of this UMAT to simulate nano-indentation in helium-implanted tungsten.

The CPFE Model

A 3D model consisting of a 20×20×20 μm^3 deformable block and a rigid 4.2 µm radius spherical indenter was simulated using Abaqus 2016 (Dassault Systèmes, Providence, RI, USA) (Figure 5.2.1 (a)). A refined finite element mesh (applied edge bias 0.1 to 2 µm) with 39500, 20-noded, reduced integration (8 integration points) 3D quadratic elements (C3D20R) was used. The 20 µm high simulation block was partitioned into two layers: a 3 µm thick implanted layer at the free surface and a 17 µm thick substrate. Considering the four-fold symmetry of <001>-oriented grains [182], only one quarter of the experiment was simulated. Mirror boundary conditions were applied on the XZ and YZ planes. The top surface was traction free and remaining surfaces of the sample block were fixed. Additional boundary conditions, $\sigma_{xx}^{BC} = \sigma_{yy}^{BC} \approx$ -260 MPa are applied to the helium-implanted layer to account for the restricted in-plane displacement (Section 3.4) to maintain geometrical continuity between the implanted layer and substrate (calculations in Appendix H). The indenter was subjected to a displacement of 0.5 µm into the sample block followed by

complete unloading to account for relaxation of the elastic part of the deformation and any reverse plastic deformation that may be taking place.

The indenter was assumed to be a discrete rigid part to avoid a full meshing and increase in simulation size. Contact between the sample and indenter was defined using the Abaqus node to surface contact algorithm and the contact was considered to be frictionless as past studies have shown that the mechanical response of the underlying substrate is not significantly affected by the coefficient of friction [182]. The results of indentation load reached, were scaled with an effective modulus E_{eff} to account for the fact that elastic displacements may occur in both the indenter tip and the specimen [202] (details in Appendix F).

The CPFE Framework

Crystal plasticity was implemented using a user material subroutine (UMAT) that shares data between gauss points using a common block. The UMAT code is based on the user element (UEL) originally developed by Dunne et al. [130]. Detailed description of this can be found in Section 5.1.4.2. Briefly, a physically based slip law [130] was used to approximate the crystallographic slip rate $\dot{\beta}_p^\lambda$ for each slip system λ, by considering the thermally activated glide of mobile dislocations ρ_m in a field of pinning dislocations

$$\dot{\beta}_p^\lambda(\tau^\lambda) = \begin{cases} \rho_m \nu \left(b^\lambda\right)^2 \exp\left(-\frac{\Delta F}{kT}\right) \sinh\left(\frac{\mathrm{sgn}\left(\tau^\lambda\right)\left(\left|\tau^\lambda\right| - \tau_c\right)V}{kT}\right), & \tau^\lambda > \tau_c \\ 0\,, & \tau^\lambda < \tau_c \end{cases} \tag{5.2.1}$$

where ν is attempt frequency, b^λ the Burgers' vector magnitude, ΔF the activation energy, k the Boltzmann constant, T the temperature, τ_c the critically resolved shear stress (CRSS considered the same for all slip-systems), τ^λ the resolved shear stress on slip system λ and

V the activation volume, which depends on the spacing between the pinning dislocations l. We assume $l = \frac{1}{\sqrt{\Psi \rho_{SSD}}}$, where, coefficient Ψ represents probability of pinning and ρ_{SSD}, the density of statistically stored dislocations (SSD). Values of the UMAT parameters are listed in Table H.1 in Appendix H. In the simulation we make assumptions of isotropic elasticity, small elastic deformations and that all parameters on the RHS in Eq. (5.2.1) remain constant (other than τ_c and the independent variable τ^{λ}).

Strain hardening was implemented at end of each time increment Δt, using a Taylor hardening law [236], [237].

$$\tau_c = \tau_c^0 + C' G\, b \sqrt{\rho_{GND}} \tag{5.2.2}$$

where G is the shear modulus of tungsten, τ_c^0 the initial CRSS, ρ_{GND} the sum of the GNDs produced across all slip-systems and C' the percentage of GNDs considered contributing to hardening. For the implanted layer, an additional term τ_H (with initial value τ_H^0 at $t = 0$), is included in Eq. (5.2.2), to account for the increased resistance to dislocation glide by the helium-implantation-induced defects.

$$\tau_c = \tau_c^0 + C' G\, b \sqrt{\rho_{GND}} + \tau_H \tag{5.2.3}$$

Strain-softening i.e. removal of helium-defects, is implemented by reducing τ_H at end of Δt

$$\beta_p^{t+\Delta t} = \beta_p^t + \sum_{\lambda=1}^{n} \dot{\beta}_p^{\lambda} \Delta t \tag{5.2.4}$$

$$\tau_H^{t+\Delta t} = \tau_H^0 e^{-(\beta_p^{t+\Delta t}/\gamma)} \tag{5.2.5}$$

where β_p^t and $\beta_p^{t+\Delta t}$ are the accumulated crystallographic slip summed over all slip systems at the start and end of Δt and γ the softening rate. Rate of decrease of τ_H is estimated to be proportional to its current value i.e. the current helium defect concentration $\left(\left.\frac{\partial \tau_H}{\partial \beta_p}\right|_{t+\Delta t} = -\tau_H/\gamma\right)$ suggesting the exponential softening rate in Eq. (5.2.5).

Fitting Parameters for the UMAT

Only two UMAT parameters, τ_c^0, and C', were fitted to the experimental results of the unimplanted sample. When simulating indentation of the unimplanted material, both layers of the block were assigned identical material properties including the two fitting parameters C' and τ_c^0. To simulate helium-implanted tungsten, the 17 μm thick substrate was left unaltered and the implanted layer was assigned material parameters of the substrate along with the two additional parameters, γ and τ_H^0. Only γ, is fitted to the experimental result of the implanted sample while τ_H^0 is physically-based.

To determine τ_H^0 a slip-plane interspersed with helium-defects is considered (Figure 5.2.1 (b)). In Figure 5.2.1 (b), each circle represents a defect (helium-vacancy complex with SIA attached to it (He_2V-SIA) [42]), separated from each other by a spacing L and resisting dislocation glide. Thus, in order to glide, the dislocation must exert a force, F_S given by

$$\tau_H^0 bL = F_S \tag{5.2.6}$$

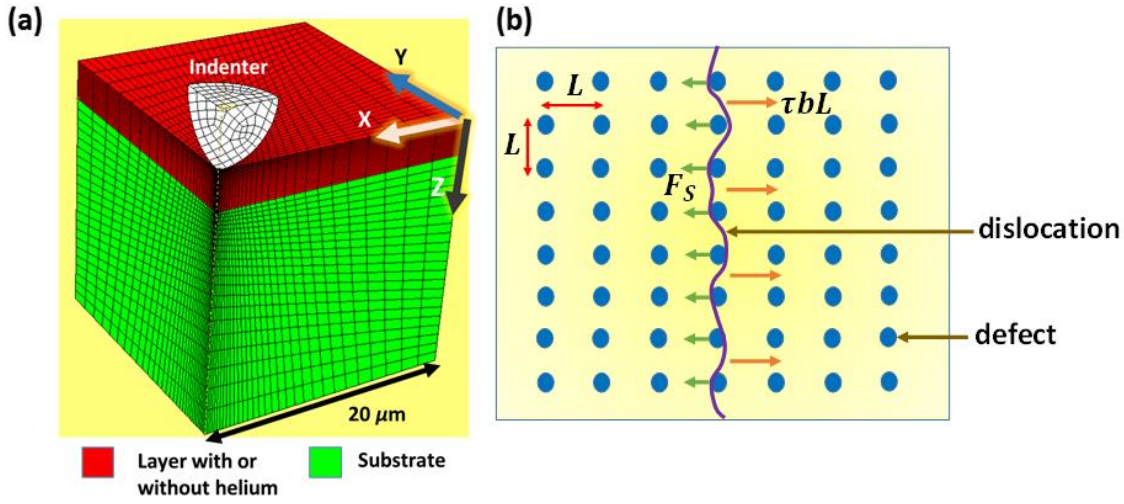


Figure 5.2.1 – (a) Refined mesh for the 3D crystal plasticity finite element simulation of the tungsten sample indented by a 4.2 μm radius spherical indenter with the X, Y, Z coordinate frame superimposed. (b) View of the slip plane interspersed with helium-implantation induced defects with a dislocation line trying to pass through.

An area L^2 of the slip plane contains one defect. This area also contains $(L/b)^2$ atoms in total, so knowing defect concentration c Eq. (5.2.6) can be re-written as

$$\tau_H^0 = \frac{F_S}{bL} = \frac{F_S\sqrt{c}}{b^2} \tag{5.2.7}$$

To estimate the force F_S, we hypothesize a mechanism of interaction between these defects and gliding dislocations which can lead to the experimentally observed changes of increased hardness and large pile-up around the indents. We hypothesize that He_2V-SIA defect complexes can strongly obstruct dislocation motion owing to the strong binding energy of the di-helium-vacancy complex of ~3.1 eV (which makes it difficult to cut through the He_2V-SIA obstacle) [153]. However, as deformation progresses, there comes a stage when gliding dislocations can exert enough force (F_S) on He_2V-SIA pinning obstacles, to dissociate the helium from the helium-vacancy complex. The SIA component of the defect complex may then quickly jump into the vacancy, annihilating the Frenkel-

pair which was retained by the helium. This would then allow the dislocation to cut through, while the released, now interstitial helium, should be free to traverse the microstructure. Thus, F_S may be considered a function of the energy required for the dissociation of helium from the He_2V-SIA complex i.e.

$$2r_W F_S \approx \Delta E \tag{5.2.8}$$

where, ΔE is the dissociation energy (which includes the binding energy for the helium-vacancy complex and the migration energy of the released helium ion) and r_W the atomic radius. The defect complex, primarily involving nearest neighbours [147], is estimated to be twice the size of the atomic radius of tungsten. Based on ab-initio studies of the stability of He_2V, ΔE is estimated to be approximately 2.5 eV [238]. Given the helium-implantation dose of 3000 appm, the concentration of defects c, is estimated as 1.5×10^{-3} (assuming on average 2 helium atoms per Frenkel pair) [42]. Knowing the values of b, ΔE, r_W (135 pm [239]) and c, τ_H^0 can be estimated as

$$\tau_H^0 = \frac{\Delta E\sqrt{c}}{2r_W b^2} = 750 \text{ MPa} \tag{5.2.9}$$

The fate of the released helium ion is not apparent from the current experimental observations. It is not unreasonable to assume that on its own the released helium ion may not have enough energy to create new displacement defects with which it can bind to create new pinning obstacles in the form of He_2V-SIA complex and cause further hardening. Based on this assumption the released helium ion is not considered to contribute to the evolution of τ_H. Further study using molecular dynamics simulation focussing on the interaction of the He_2V-SIA complex with gliding dislocation may help to shed light on the unknown fate of the released helium ion.

5.2.4. Results & Discussion

5.2.4.1. Load-displacement curves, indent morphology and defect structures

Figure 5.2.2 (a)-(b) show SEM micrographs of spherical nano-indents in the unimplanted and implanted sample respectively. To ensure reproducibility, two indents are made in the helium-implanted sample as shown in Figure 5.2.2 (b). In striking contrast to the unimplanted sample, a large, localised pile up is seen around both indents in the implanted material. Black arrows in Figure 5.2.2 (b) indicate slip steps, sugestive of slip localisation and slip channel formation. Figure 5.2.2 (c) shows the load versus displacement curves for nano-indentation to 500 nm depth in helium-implanted and unimplanted parts of the <001>-oriented tungsten single crystal. The implanted sample is seen to reach ~ 73% higher load than the unimplanted sample. This substantial increase in hardening may be attributed to both the helium-defects, as well as the increase in pile-up, with an associated increase in contact area. These results are reassuringly similar to previously observed helium-induced changes in tungsten (Chapter 4) on which the hypothesis outlined above is based.

It is interesting to compare the CPFE predicted load-displacement curves for the implanted material with and without the implantation-induced stress boundary conditions (Appendix H), keeping all other UMAT parameters the same. The indentation load predicted without the residual stresses is ~ 16% lower than the experimental observation. This suggests that large residual stresses (here ~ 75% of τ_c^0) must be accounted for to yield accurate results. Prior studies on hardness of mild steel, probed through micro-indentation, showed a similar dependence on residual stress state [240]. Interestingly our CPFE calculations highlight that the impact of residual stress on indentation response continues to be important even at the nano-scale.

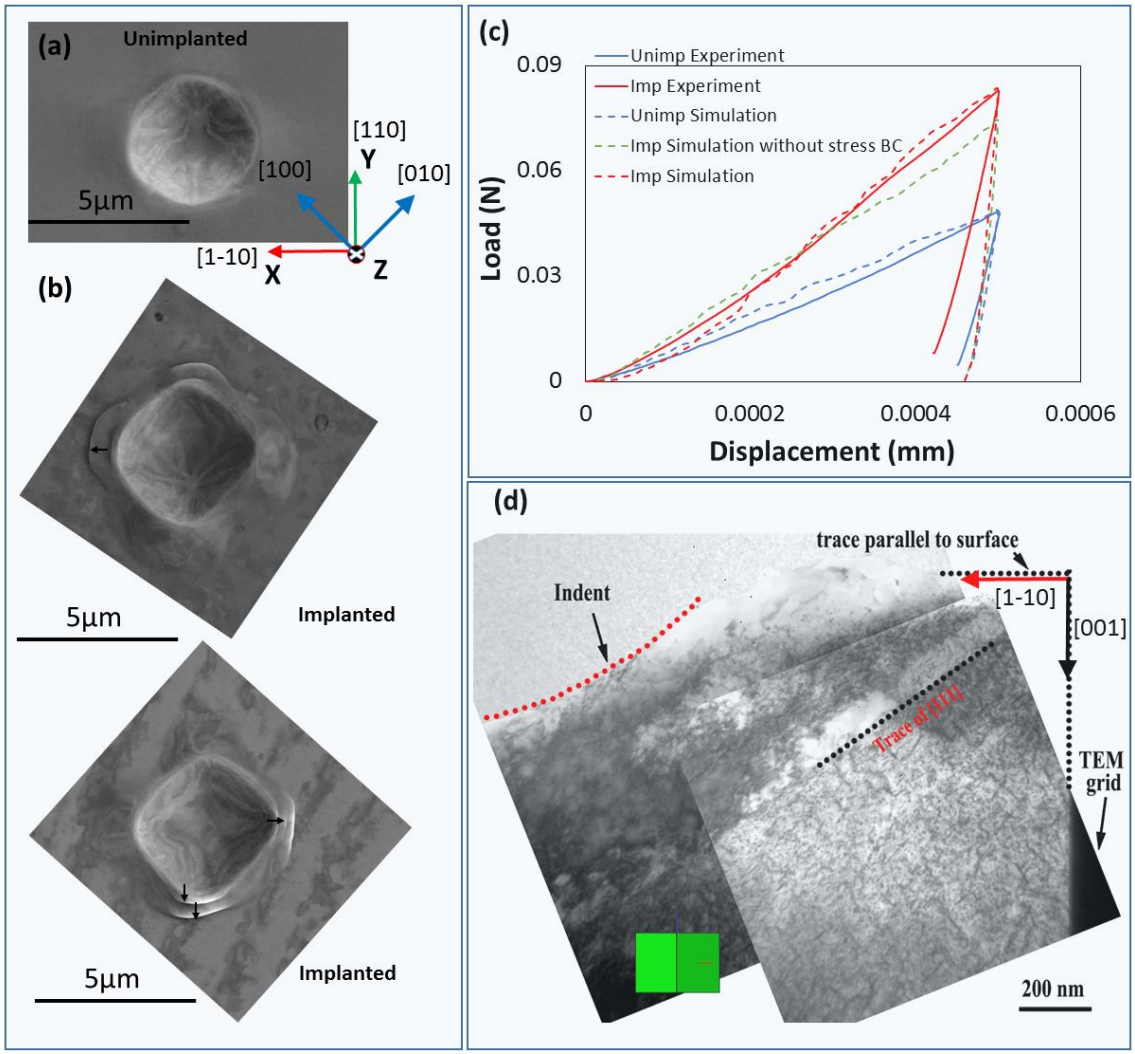


Figure 5.2.2 – (a) SEM micrographs of the nano-indent made with a 4.2 µm radius spherical indenter tip in the unimplanted part of sample and (b) SEM of two indents made in the helium-implanted part of sample. The X, Y and Z axes superimposed applies to both (a) and (b). (c) Load versus displacement curve for the unimplanted and helium-implanted tungsten sample as obtained from nano-indentation and predicted by CPFE. (d) TEM micrographs of a FIB-lift-out cross-section from the indent-centre in the implanted sample, showing the presence of slip channels beneath the indent. The green cube represents the crystal orientation of the TEM lamella, also indicated by red (X axis) and black (Z axis) arrows showing the same coordinate frame as in (a).

Cross-section TEM micrographs through the centre of a nano-indent in the implanted material clearly show defect free zones (Figure 5.2.2 (d)), inspiring confidence in the proposed mechanism of defect removal by glide dislocations in localised areas. These slip channels are found to be parallel to the [111] direction and are cleared of almost all visible defects. This observation is similar to slip channels observed in irradiated fcc

materials [241]. However, slip channels in neutron-irradated copper [187], [241], self-ion irradiated stainless steel [242], [243], or neutron-irradiated pure Fe [244], all appear much more clearly demarcated, with sharp boundaries. In contrast, the slip channels we observe have a less well-defined boundary with the surrounding, higher defect density material. Rather the channels seen here more closely resemble those in 0.12 dpa neutron-irradiated bcc vanadium [245]. In vanadium channeling increased with damage level, with wider, river-pattern shaped channels forming in 0.69 dpa irradiated material [245]. Stacking fault energy (SFE) plays a key role in controlling the mechanism of strain localisation [246], and the high SFE of bcc metals [247] may explain the observed differences in the slip channels morphology between bcc and fcc metals.

5.2.4.2. Surface morphology of indents: AFM vs CPFE

The displacement of the top surface (XY-surface) of the indentation model in the Z-direction (Figure 5.2.1 (a) shows the co-ordinate frame) as predicted by CPFE, reflects the change in the pile-up pattern around the indent. Experimentally AFM measurements were performed to quantify the pile-up induced by indentation. The reference point for the AFM measurement was taken to be a point on the sample surface 14 μm away from the indent centre, which being sufficiently far from the indent is considered to be unaffected by the indentation-induced change in surface displacement. Surface displacement around the indents, with respect to this reference point is shown in the AFM plots in Figure 5.2.3.

The large increase in pile-up in the helium-implanted material predicted by CPFE agrees very well with the surface height profile measured by AFM (Figure 5.2.3). Line plots were made from AFM and CPFE contour plots in the <100> and the <110> directions i.e. direction with minimum and maximum pile-up respectively (Figure 5.2.3 (e)-(f)). From the

line plots, ~ 172 % increase in pile-up height is seen in the <110> direction in the implanted sample.

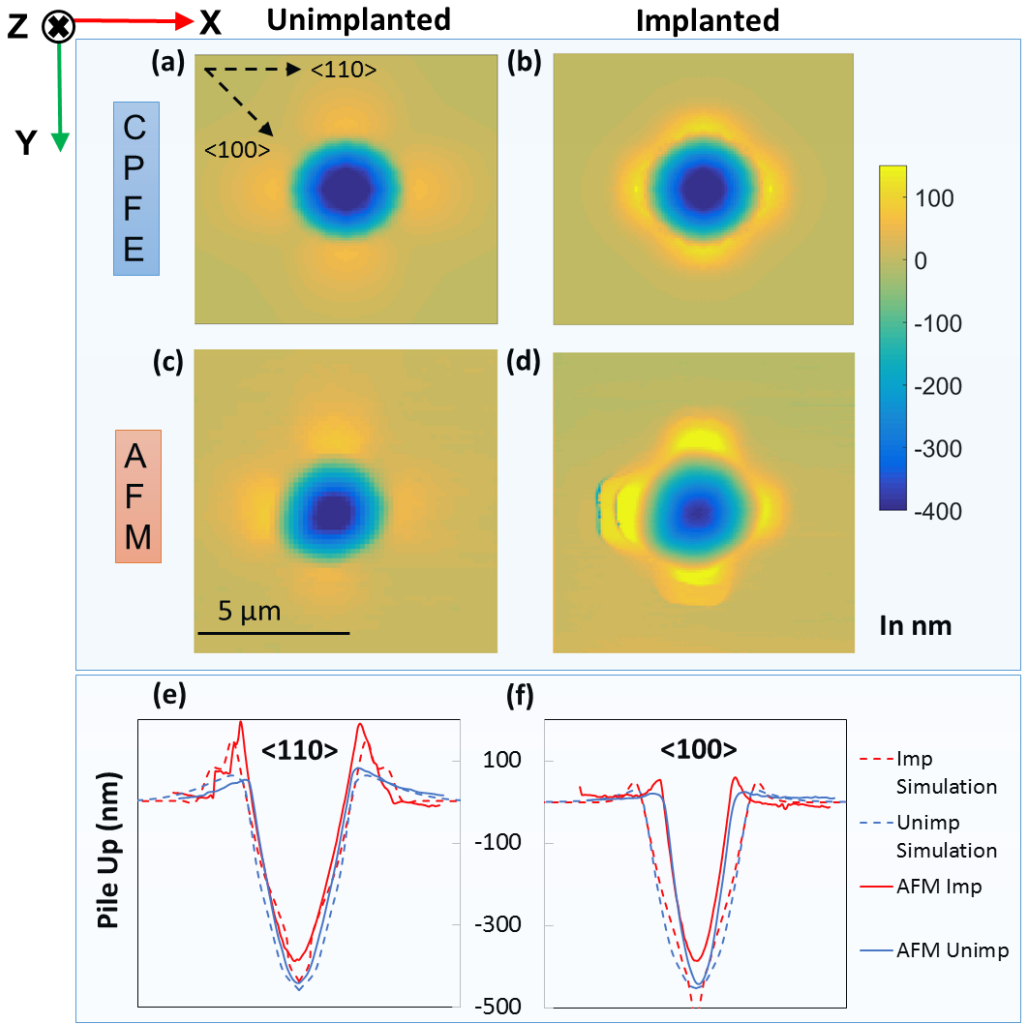


Figure 5.2.3 – Surface profiles of the nano-indents; (a) and (b) as obtained through CPFE formulation for the unimplanted and the helium-implanted tungsten sample respectively, (c) and (d) as obtained through AFM measurements for the unimplanted and helium-implanted tungsten sample respectively. (e) and (f) show line profiles of surface height extracted along <110> and <100> directions respectively for the unimplanted and implanted material. Also shown are the surface profiles predicted by CPFE.

A relatively shallower residual indent impression in the implanted sample is consistent with the observed increase in hardness. We note in passing that CPFE uniquely predicts the experimentally observed four-fold pile-up pattern by constraining slip to the applicable crystallographic slip systems. The contrasting, unphysical uniform distribution

of pile-up around the indent, predicted by an isotropic continuum finite element (FEM) model, is displayed in Figure H.1 (Appendix H) for comparison.

5.2.4.3. Residual elastic lattice rotations

The residual elastic lattice rotations induced by nano-indentation around and beneath indents (represented by rotation matrix $\boldsymbol{R}$) were predicted by CPFE and compared with HR-EBSD and Laue diffraction measurements (Laue data used from prior study for comparison (Section 4.6)). The average orientation of points in the unimplanted material, far from the indent (22-25 μm and 10 μm below surface for Laue and HR-EBSD respectively) was considered as the orientation of the un-deformed material, $\boldsymbol{R}_0$. For CPFE the input orientation was considered as $\boldsymbol{R}_0$. The indentation-induced change in crystal orientation from $\boldsymbol{R}_0$ to $\boldsymbol{R}$ at each point in space was then calculated as:

$$\boldsymbol{R}_t = \boldsymbol{R}\,\boldsymbol{R}_0^{-1} \tag{5.2.10}$$

Using the convention in [229], $\boldsymbol{R}_t$ accounts for the combined effect of sequential rotation about the X, Y and then Z axis by the rotation angles θ_x, θ_y and θ_z. Note we use the common convention for example $\theta_x > 0$ if anticlockwise when viewed looking down the X-axis towards to origin (i.e. right handed rotations). The lattice rotations in Figure 5.2.4 are plotted on virtual YZ slices, at different X positions, for both samples. For HR-EBSD only rotation about the out-of-plane axis θ_x, is considered for one YZ slice through the indent centre. Rotations about the other two axes are not considered as they may have been modified due to stress-relaxation during FIB-lift-out preparation. HR-EBSD and Laue diffraction, respectively, have the advantage of high spatial resolution and high angular resolution, and are compared with the CPFE predictions using the same colour and length-scales.

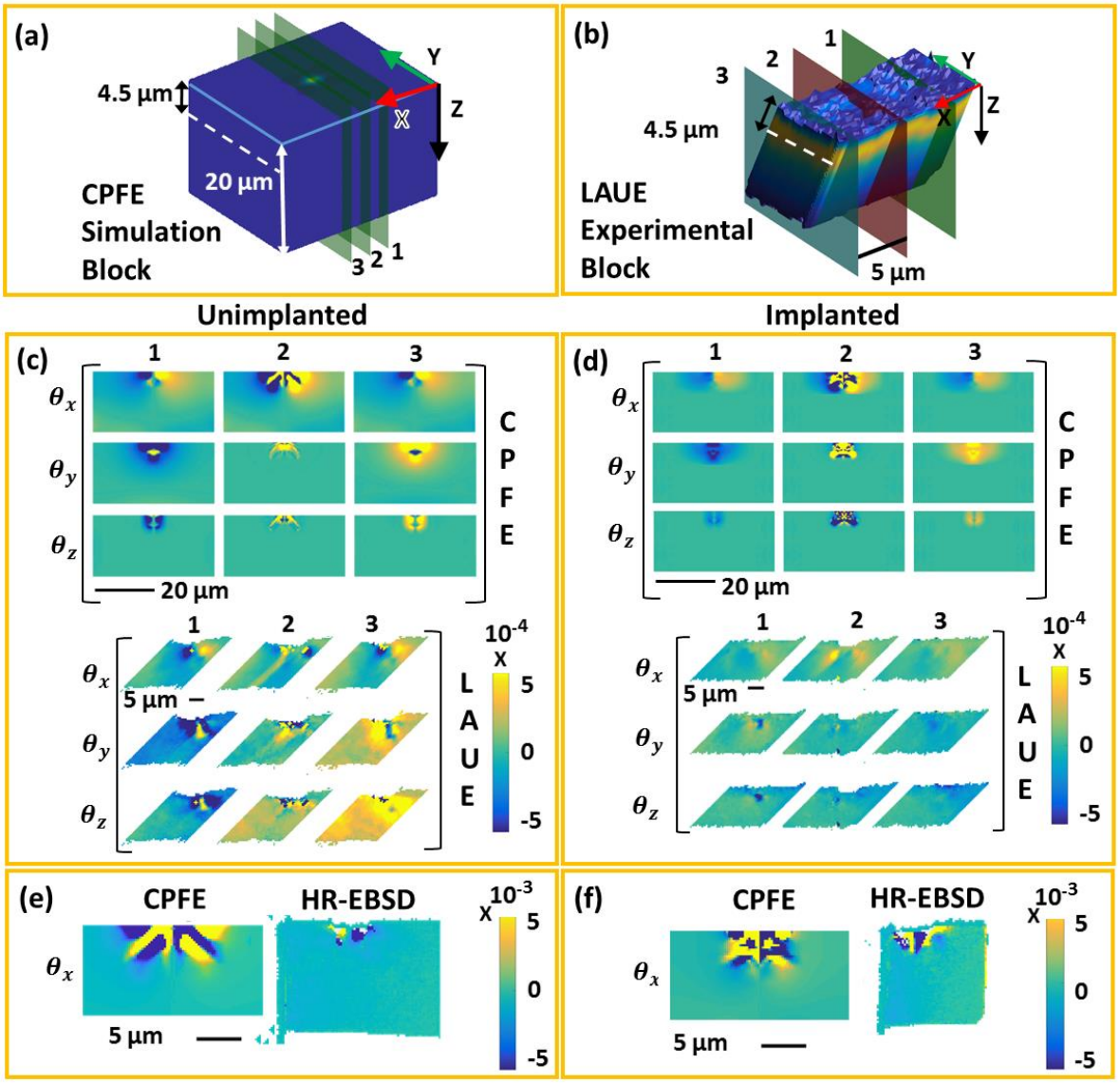


Figure 5.2.4 – (a) 3D rendering of the CPFE simulated volume coloured according to the predicted displacement magnitude along the Z axis of the indented tungsten block. X, Y and Z axes are superimposed. Slices 1-3, drawn on the block, represent the three sections along the X-axis (indent centre - slice 2), on which the lattice rotations predicted by CPFE are plotted. (b) Visualisation of the sample volume measured by Laue diffraction, coloured according to the experimentally measured intensity. Superimposed are the X, Y, and Z axes, as well as the slices on which the measured lattice rotations are plotted. Comparison of lattice rotations predicted by CPFE and measured by Laue for the (c) unimplanted sample and (d) the helium-implanted sample. Comparison of lattice rotation as predicted by CPFE and measured by HR-EBSD for the (e) unimplanted sample and (f) the helium-implanted sample. With respect to the initial crystallographic coordinates, the X axis is [1 -1 0], Y is [1 1 0] and Z is [001]. Data from CPFE simulations, Laue diffraction and HR-EBSD experiments are displayed on the same length- and colour-scale. The dotted white lines in (a) and (c) represent the depth at which the line plots in Figure 5.2.5 were extracted. Lattice rotations are plotted in radians.

The Laue data and CPFE predictions of lattice rotations (Figure 5.2.4 (a)-(d)) agree reasonably well, particularly for θ_x. Interestingly, agreement is better for slices 5 μm away from the indent centre (positions 1 and 3 in Figure 5.2.4 (c)-(d)). The disparity between CPFE and Laue data in position 2 is due to the presence of steep strain gradients and rapid variation of lattice rotation at the indent centre. In positions 1 and 3, rotations in the unimplanted sample, particularly θ_x, are significantly larger than in the implanted sample.

For quantitative analysis, line plots were extracted, for these two slices, at depths of 4.5 μm from the sample surface, from both Laue and CPFE results and superimposed (Figure 5.2.5). The line plots distinctly show the smaller lattice rotations in the implanted sample, suggesting a more localised deformation. The θ_x line plots from CPFE and Laue agree very well in the far field, where small changes in lattice orientation are well captured by the high angular resolution of Laue measurements [94], [98], [99]. However, in the highly deformed volume directly beneath the indent, where steep strain gradients exist, Laue peaks become streaked [100]. This streaking is linked to the underlying GND population within the probed volume, as described for example by Barabash et al. [101], [102]. Unfortunately streaked Laue peaks cannot be fitted as accurately, leading to a loss of strain and lattice rotation resolution in this region. For example, in Figure 5.2.5, CPFE predicts rapid variations of lattice rotation immediately below the indent that are not resolved by Laue diffraction. The high spatial resolution of HR-EBSD [103], [104] complements the Laue measurements by giving detailed information in this region.

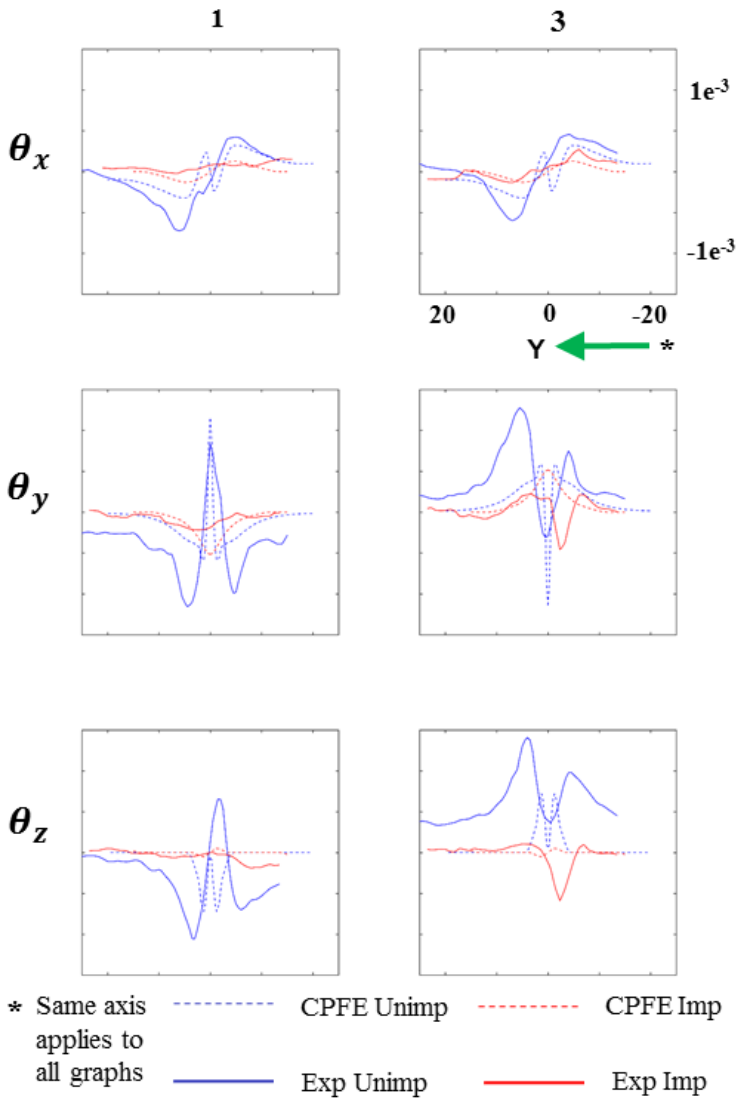


Figure 5.2.5 – Line plots corresponding to the contour plots in Figure 5.2.4 (c)-(d). Lattice rotations are plotted along a horizontal line 4.5 µm below the indent (line shown by dotted white lines in Figure 5.2.4 (a) and (b)). Slices 1 and 3 represent the YZ sections drawn 5 µm away from the indent centre, on either side, along the X-axis in Figure 5.2.4 (a) and (b).

Quite good agreement between HR-EBSD and CPFE (Figure 5.2.4 (e)-(f)) is seen for both samples in terms of the geometry of the deformation field. However, CPFE predicts a slightly wider spread of the rotation field than measured by HR-EBSD. This may be attributed to stress release during FIB-lift-out preparation. Importantly, comparison of CPFE and HR-EBSD shows that the magnitude of the rotation field immediately below the indent is similar for both the implanted and unimplanted material. Thus, the major

difference between the implanted and unimplanted material lies in the far-field rotations captured by Laue diffraction.

It is worth noting that using only HR-EBSD or Laue diffraction could lead to incomplete measurement of the deformation field in the far-field or near the indent respectively. This underlines the importance of the use of complementary techniques for gaining a complete picture of crystal scale deformation at the nano-scale.

5.2.4.4. Residual elastic lattice strains

The deviatoric residual lattice strain ($\boldsymbol{\varepsilon}^e_{dev}$) is measured by both Laue diffraction (Laue data used from prior study for comparison (Section 4.6)) and HR-EBSD. To directly compare the CPFE predictions with the experimental measurements, $\boldsymbol{\varepsilon}^e_{dev}$ is calculated from the total elastic strain tensor ($\boldsymbol{\varepsilon}^e$) given by CPFE:

$$\boldsymbol{\varepsilon}^e_{dev} = \boldsymbol{\varepsilon}^e - \boldsymbol{\varepsilon}^e_{vol} = \boldsymbol{\varepsilon}^e - 1/3\ \mathrm{Tr}\,(\boldsymbol{\varepsilon}^e)\boldsymbol{I} \tag{5.2.11}$$

where $\boldsymbol{\varepsilon}^e_{vol}$ is the volumetric strain. Helium-implantation induces an out-of-plane lattice swelling i.e. positive ε^e_{zz}, while constraints imposed on the implanted layer along X and Y directions (to maintain continuity with the substrate) means that $\varepsilon_{xx} = \varepsilon_{yy} \approx 0$ (Section 3.4). As $\mathrm{Tr}\,(\boldsymbol{\varepsilon}^e_{dev}) = 0$, it may be estimated that, far from the indent in the implanted material, $\varepsilon^e_{dev_{xx}} = \varepsilon^e_{dev_{yy}} = -0.5\varepsilon^e_{dev_{zz}}$. This implantation-induced deviatoric strain is clearly seen in Laue measurements of the implanted sample (Figure 5.2.6 (d)); a tensile $\varepsilon^e_{dev_{zz}}$ (~ 5.5×10^{-4}) and compressive $\varepsilon^e_{dev_{xx}}$ and $\varepsilon^e_{dev_{yy}}$ (~ -2.75×10^{-4}) in the implanted layer (Figure 4.3). It is worth noting that the CPFE formulation for the implanted sample does not explicitly include the helium-induced lattice swelling. Rather the corrective stress, arising due to restricted deformation in the X and Y directions, is included in the CPFE

model as an additional boundary condition (details in Section 5.2.7.1). Consequently, the CPFE predicted strains are purely indentation-induced (direct components of the indentation-induced deviatoric strain referred to as ε_{xx}, ε_{yy} and ε_{zz}). Thus, the CPFE predicted out-of-plane strain for the implanted layer is somewhat smaller than that measured by Laue, where both indentation and implantation induced strains are captured (Figure 5.2.6 (d)). ε_{xx}, ε_{yy} and ε_{zz}, predicted by CPFE and measured by Laue diffraction, are shown in Figure 5.2.6, plotted on virtual YZ slices through the sample at different X positions.

Good qualitative agreement is observed between Laue measurements and CPFE predictions and interestingly both show a localisation of indentation induced lattice strain in the implanted sample. Distinctly noticeable is the tightly confined ε_{zz}, at positions 5 μm away from the indent centre (slices 1 and 3 in Figure 5.2.6 (d)). The localisation of strain fields is further quantified by line plots (Figure H.2 in Appendix H) drawn for the corresponding contour plots in Figure 5.2.6 at depth of 4.5 μm from the sample surface. The agreement between CPFE predictions and experimental measurements inspires confidence in the CPFE formulation for helium-implanted tungsten (with only one fitting parameter) and its foundation hypothesis; localised deformation in slip channels arising from interactions of dislocations with helium-defects.

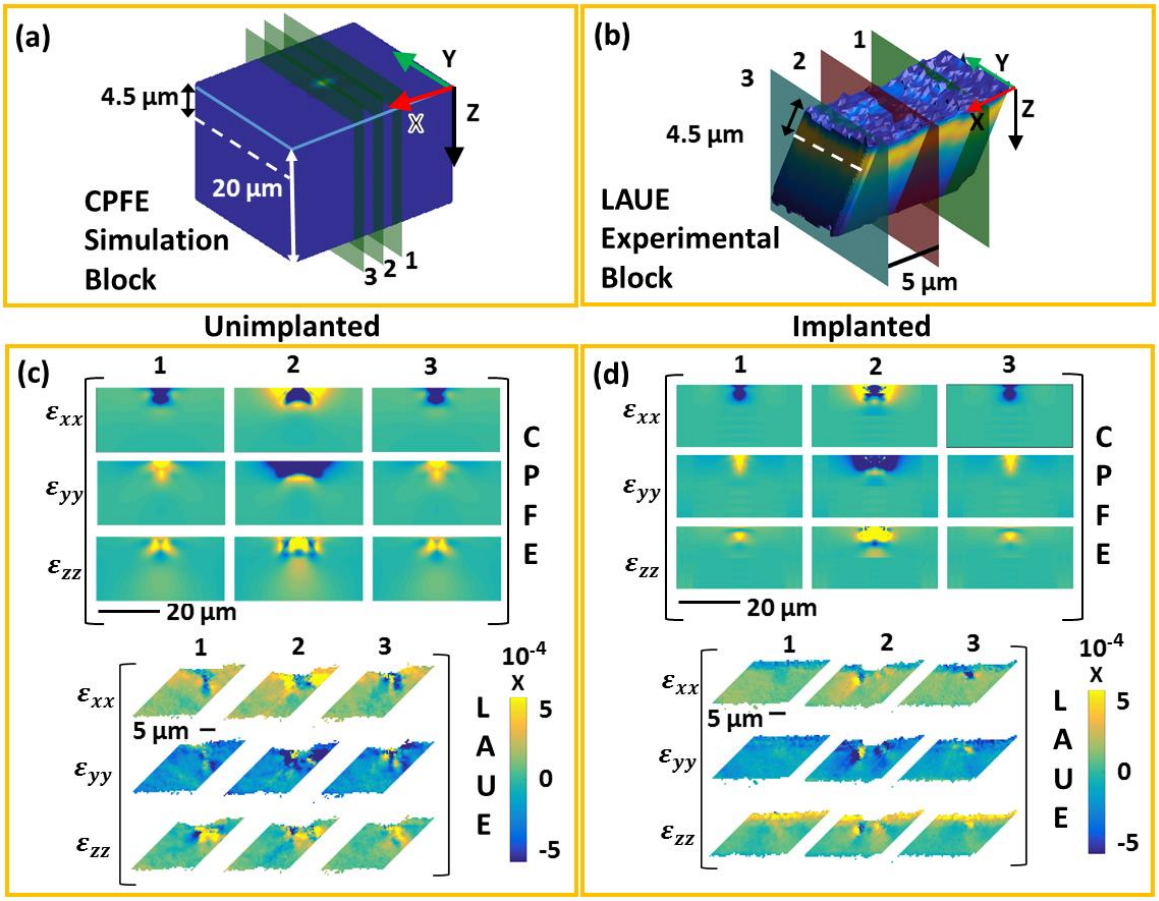


Figure 5.2.6 – **For the CPFE data**: (a) Slices 1-3 drawn on the block represent the three sections along the X-axis (slice 2 being at the indent centre) on which the residual deviatoric elastic strains predicted by CPFE are shown in (c) unimplanted sample and in (d) helium-implanted sample. **For the Laue data**: (b) Visualisation of the measured sample volume. Superimposed are the X, Y, and Z axes, as well as the slices on which the measured deviatoric elastic lattice strains in (c) the unimplanted sample and (d) the helium-implanted sample are plotted. With respect to the initial crystallographic coordinates, X is [1 -1 0] direction, Y is [1 1 0] and Z is [001]. Slices 1-3 in experiments and simulations are at the same spatial positions and data in (c) and (d) is displayed on the same length- and colour-scales. The dotted white lines through (a) and (b) represent the depth at which the line plots in Figure H.2 in Appendix H were extracted.

5.2.4.5. GND Density

Hardening is implemented in the CPFE formulation as a function of evolving GND density (Eq.(5.2.3)). For the implanted sample, the hardening is accompanied by a strain softening due to removal of helium-implantation-induced defects by glide dislocations (Eq. (5.2.5)). The fine-tuned combination of hardening and softening in the UMAT is vital for the

quantitative agreement observed between the CPFE predictions and experimental results for the lattice distortions. The explicit incorporation of GNDs in the formulation is key for introducing length-scale effects as originally proposed by Ashby [115]. Further, the GND distribution can provide insights into the plastic zone size, which can be directly compared to experiments. Following Nye's theory [108], GND densities are thus computed from both HR-EBSD and Laue measurements and compared with the CPFE predictions.

Details of the GND density computation can be found in Section 5.1.3.3. Here, the GND density $\boldsymbol{\rho}$ was computed using the L^2 optimisation technique [133], which minimises the sum of squares of dislocation densities i.e. $\sum_j \rho_j^2 = \boldsymbol{\rho}^T.\boldsymbol{\rho}$. Previous work showed that L^2, while mathematically simpler, can reliably predict the sum of GND densities over all slip systems (Section 5.1.5.3). We assume, consistent with the CPFE calculations, that deformation in bcc tungsten is accommodated by dislocations with a/2<111> Burgers' vector gliding on {110} planes [127], [231] (list of Burgers' vector and line directions considered in Appendix G). We assume dislocations to be of either pure edge (with <112> line directions) or pure screw type (with <111> line directions), resulting in 16 dislocation types in total.

Figure 5.2.7 shows the total GND density computed from HR-EBSD, Laue diffraction and CPFE datasets, plotted on the YZ, XZ and the XY cross sections at the indent centre. To enable a direct comparison with both Laue and HR-EBSD measurements, the CPFE predictions are plotted on two different length scales. Complementing each other, the high angular resolution of Laue measurements [94], [158] and high spatial resolution of HR-EBSD measurements [103], [105] detect the far-field and near-field deformation respectively. In the unimplanted sample, a small zone of high GND density is seen close to the indent (Figure 5.2.7 (d)), with a surrounding larger zone of low GND density

(Figure 5.2.7 (c)). In contrast, the implanted sample shows a relatively larger zone of high GND density surrounding the indent (Figure 5.2.7 (h)), with a surprisingly sharp boundary and very low GND density outside this region (Figure 5.2.7 (g)). The experimental observations show a similar picture, consistent with the predictions from CPFE.

The CPFE formulation for the helium-implanted sample was based on the hypothesis of removal of helium-implantation-induced obstacles by the progressive passage of dislocations. This leads to defect-free slip channels that accommodate deformation in the implanted zone, near the indent, and give rise to a large pile up. As a result, a more compact plastic zone is expected in the implanted material, which is clearly seen in the spatial variation of GND density predicted by CPFE and observed in experiments.

An important point to note from Figure 5.2.7 is the size of the plastic zone surrounding each indent. The results show that, although the indent is only 500 nm deep, the affected zone extends beyond the ~ 3 μm thick implanted layer. This implies that the underlying substrate can have a significant impact on the results, even when the indentation depth is < 20% of the implanted layer thickness. Generally, when nano-indentation is performed on thin film on substrates, the contribution of the underlying substrate is carefully accounted for [248]–[250]. However, in most studies investigating the indentation response of irradiated materials, indentation depth of ~ 20 % of the implanted layer thickness is used and the effect of the underlying unimplanted material is not considered explicitly [251]–[253]. Our result highlights that to ensure fidelity it is important to account for the combined effect of the implanted layer and substrate. An analysis whereby the implanted layer is approximated as an infinite half space may render inaccurate results.

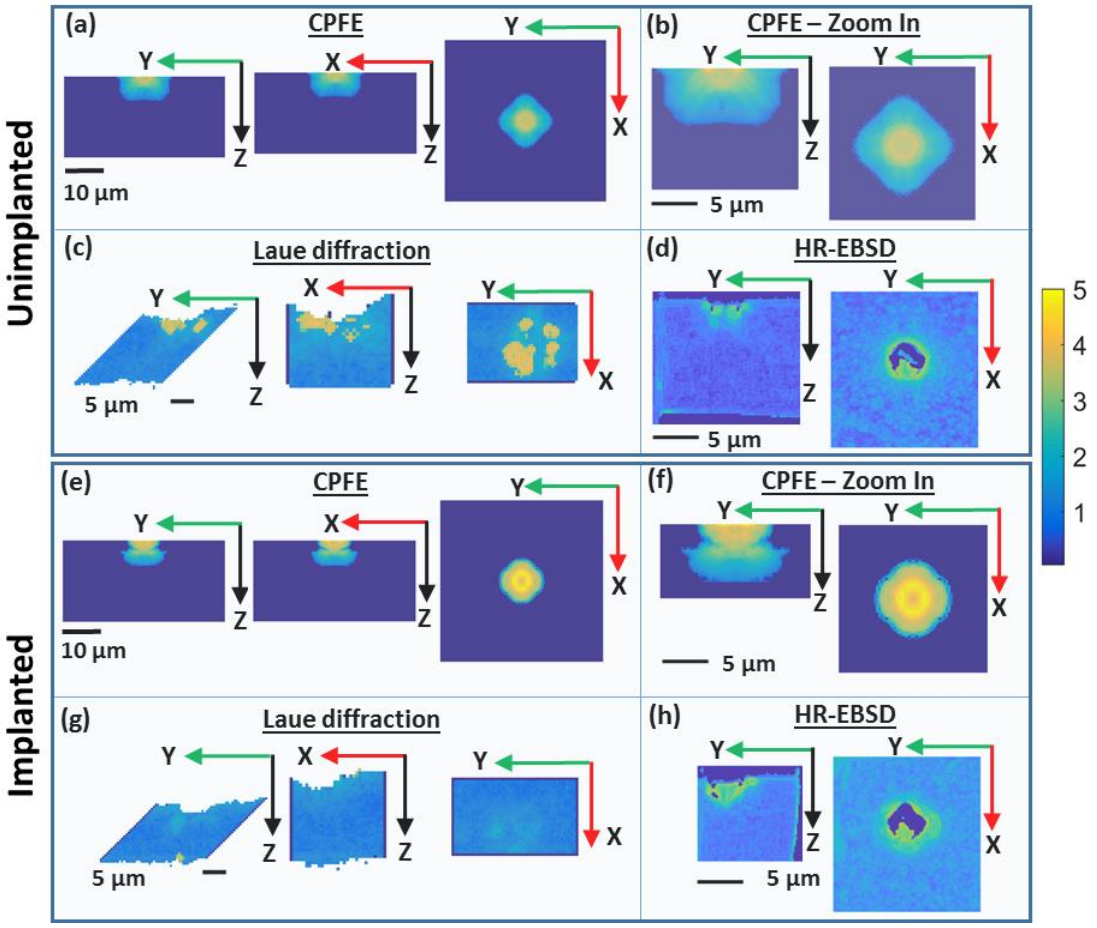


Figure 5.2.7 – Total GND density plotted on YZ, XZ and the XY cross-sections through the indent centre. GND density was calculated using L^2 optimisation. Predictions from CPFE calculations are shown in (a) and (b) for the unimplanted sample, and (e) and (f) for the helium-implanted sample. GND density computed from Laue diffraction measurements for the unimplanted and implanted samples are shown in (c) and (g) respectively. GND density determined by HR-EBSD for the unimplanted and the implanted sample is shown in (d) and (h) respectively. The same colour scale is used for all plots showing $\log_{10}(\rho)$ with ρ in $1/\mu m^2$. (a), (c), (e) and (f) are plotted on the same length scale. (b), (d), (f) and (h) show magnified plots of GND density and are also all shown on the same length scale.

5.2.5. Conclusions

We have presented a comprehensive analysis of the effect of helium-implantation damage on the mechanical properties of tungsten. TEM of the cross-section of an indent in the implanted sample showed that dislocations "sweep out" helium-implantation-induced defects, leaving behind low defect density zones/channels. This "sweeping out" leads to a localisation of deformation and a softening of the material with increasing plastic

deformation. Qualitatively this explains the substantial increase in pile-up and the localisation of deformation leading to slip steps. A physically-based CPFE model was constructed where initial hardening due to interaction of dislocation with irradiation defects, as well as subsequent softening is accounted for. Importantly this model has only one additional fitting parameter, for simulating helium-implanted tungsten, besides fitting parameters for CRSS and hardening co-efficient which are needed to simulate pure tungsten. It successfully captures the changes in load-displacement curve, changes in pile-up structure, lattice rotations and residual lattice strains, as well as GND population in remarkably good agreement with our experimental observations. The results highlight that even a comparatively small concentration of irradiation/implantation induced defects – 1500 appm – can produce dramatic changes in the mechanical behaviour, with strain hardening being replaced by a large increase in the initial hardness followed by strain softening. Understanding these changes in detail and having physically-based models that capture these effects will be key to determining the evolution of mechanical properties in fusion reactor armour components and assessing their in-service performance.

5.3. Orientation-dependent deformation of helium-implanted tungsten

This section is in publication format and is based on article "*S. Das, H. Yu, E. Tarleton, F. Hofmann, Orientation-dependent indentation response of helium-implanted tungsten, Appl. Phys. Lett. 114 (2019) 221905. doi:10.1063/1.5097403*" [254].

5.3.1. Abstract

A literature review of studies investigating the topography of nano-indents in ion-implanted materials reveals seemingly inconsistent observations, with reports of both pile-up and sink-in. This may be due to the crystallographic orientation of the measured sample point, which is often not considered when evaluating implantation-induced changes in the deformation response. Here we explore the orientation dependence of spherical nano-indentation in pure and helium-implanted tungsten, considering grains with <001>, <110> and <111> out-of-plane orientations. Atomic force microscopy (AFM) of indents in unimplanted tungsten shows little orientation dependence. However, in the implanted material a much larger, more localised pile-up is observed for <001> grains than for <110> and <111> orientations. Based on the observations for <001> grains, we hypothesise that a large initial hardening due to helium-induced defects is followed by localised defect removal and subsequent strain softening. A crystal plasticity finite element model of the indentation process, formulated based on this hypothesis, accurately reproduces the experimentally-observed orientation-dependence of indent morphology. The results suggest that the mechanism governing the interaction of helium-induced defects with glide dislocations is orientation independent. Rather, differences in pile-up morphology are due to the relative orientations of the crystal slip systems, sample surface and spherical indenter.

This highlights the importance of accounting for crystallographic orientation when probing the deformation behaviour of ion-implanted materials using nano-indentation.

5.3.2. Introduction

Ion-implantation is commonly used to mimic irradiation damage in materials. This cost-effective technique allows examination of specific irradiation factors. For example helium-implantation introduces irradiation-like defects, while enabling examination of the interaction of these defects with the implanted helium [42], [143], [255]. Similarly self-ion implantation has been extensively employed to emulate the cascade damage caused by neutron irradiation [57], [58].

Nano-indentation is often used to gain insight into the mechanical properties of the few-micron-thick ion damaged layers. Marked changes in pile-up morphology around nano-indents have been observed in irradiated materials, even for low damage levels. A review of several studies reveals seemingly contradictory observations. For example, large pile-up around 250 nm deep Berkovich nano-indents was observed in 0.3 at.% helium-implanted W-1 at. % Re [81]. But for HT9 ferritic/martensitic steel, implanted with both helium and protons, there was no noticeable difference in indent surface profile [256]. A suppression of pile-up was noticed around indents in 2 MeV W^+ ion implanted W-5 wt.%Ta (0.04 dpa) [60]. On the other hand Fe^+ implantation of Fe-12 wt.%Cr lead to a distinct increase in pile-up [257].

This raises the question why implantation with helium or self-ions causes pile-up increase in some materials and suppression in others. Generally, pile-up and sink-in are, respectively, associated with low and high strain-hardening potential [84], [250]. Different annealing conditions could lead to differences in strain-hardening potential and

consequently different surface profiles. Interestingly, nano-indentation in annealed single crystals has shown a strong dependence of the deformation pattern on the crystallographic orientation of the crystal [258]–[260]. This was also seen in atomistic simulations concentrating on the early stages of nano-indentation in fcc crystals [261].

In most nano-indentation studies of ion-implanted material crystallographic orientation is not considered. This raises the question whether the pile-up morphology and consequently the measured hardness may be orientation-dependent. If this is the case, then conclusions drawn from indentation of material with unknown crystal orientation could be misleading.

Here we concentrate on tungsten, the main candidate material for fusion reactor armour due to its high melting point (3422 °C) and strength at high temperature [6], [14], [15]. Helium-defects are known to cause substantial property changes in tungsten, for example increased hardness [79], lattice swelling [12], [42], [143] and reduced thermal diffusivity [80]. Recently, comparing spherical nano-indents in 0.3 at.% helium-implanted and unimplanted parts of the same tungsten <001> single crystal, we found a large, localised increase in pile-up around indents in the helium-implanted material (Chapter 4). Here, we examine whether this helium-induced change in pile-up morphology is dependent on grain orientation. For each crystal orientation, besides the indent surface morphology, the deformation field beneath specific indents is investigated using a physically-based crystal plasticity finite element (CPFE) model.

5.1.3. Sample preparation

A tungsten poly-crystal (99.99% purity, ~ 180 μm grain size) was recrystallised in vacuum at 1400 °C. The surface was mechanically ground and then polished using diamond paste. Final chemo-mechanical polishing with 0.1 μm colloidal silica suspension produced a high quality surface finish. Part of the sample was implanted with helium at the National Ion Beam Centre, University of Surrey, UK. Implantation was performed at 298 K using a 2 MeV ion accelerator and a raster scanned beam to ensure a uniform implantation dose. The implantation profile, estimated using SRIM [155] (displacement energy of 68 eV, single-layer calculation model [156]), is provided in Figure 4.1 (b). Using a combination of different ion energies and fluences (Appendix A) an almost uniform helium ion concentration > 3000 appm (associated damage of ~ 0.24 dpa) was obtained within a ~ 2.8 μm thick implanted layer. Frenkel pair formation is likely to be the main damage mechanism as helium-implantation-induced recoils have predominantly low energy [42]. Little defect clustering is expected given that vacancies in tungsten have low mobility at room temperature [178], [179], [234].

Using electron back-scatter diffraction (EBSD), grains with near <001>, <110> and <111> orientation were selected in both the unimplanted and implanted regions of the sample. Table 5.3.1 shows the out-of-plane orientations of the twelve selected grains and their misorientation with respect to the perfect <111>, <110> or <001> out-of-plane direction.

Implanted part of sample	**Euler Angles $(\varphi_1, \varphi, \varphi_2)$**[5]	**Out-of-plane orientation**	**Misorientation with <001> or <011> or <111> (in degrees)**
(001) Grain 1	290.4,13.5,74.7	[22.52,6.16,97.24]	13.5
(001) Grain 2	42.6,9.6,301.3	[14.25,8.66,98.6]	9.6
(011) Grain 1	351.1,37.4,358.2	[1.91,60.1,79.44]	7.69
(011) Grain 2	161.3,35.3,190	[-10.03, -56.91,81.6]	11.62
(111) Grain 1	40.3,56.8,312.9	[-61.3,56.96,54.76]	2.69
(111) Grain 2	51.3,49.7,320.7	[-48.31,59.02,64.68]	6.75
Unimplanted part of sample	**Euler Angles $(\varphi_1, \varphi, \varphi_2)$**	**Out-of-plane orientation**	**Misorientation with <001> or <011> or <111> (in degrees)**
(001) Grain 1	267.1,8.1,273.9	[-14.06,0.96,99]	8.1
(001) Grain 2	151,11.9,32	[10.93,17.49,97.85]	11.9
(011) Grain 1	290.7,38,273.3	[-61.46,3.54,78.8]	7.33
(011) Grain 2	168.6,42.3,4.7	[5.51,67.07,73.96]	4.22
(111) Grain 1	186.5,46.5,323.6	[-43.05,58.38,68.84]	10.57
(111) Grain 2	34.6,48.3,132.2	[55.31,-50.15,66.52]	6.79

Table 5.3.1 – List of the out-of-plane orientation and misorientation of the twelve grains considered in this study. Misorientation is calculated with respect to the perfect <111>, <110> or <001> out-of-plane direction.

[5] The Euler angle convention used is as follows: $\mathbf{Z}^{(1)} = \begin{bmatrix} \cos\varphi_1 & \sin\varphi_1 & 0 \\ -\sin\varphi_1 & \cos\varphi_1 & 0 \\ 0 & 0 & 1 \end{bmatrix}$; $\mathbf{X} = \begin{bmatrix} 1 & 0 & 0 \\ 0 & \cos\varphi & \sin\varphi \\ 0 & -\sin\varphi & \cos\varphi \end{bmatrix}$; $\mathbf{Z}^{(2)} = \begin{bmatrix} \cos\varphi_2 & \sin\varphi_2 & 0 \\ -\sin\varphi_2 & \cos\varphi_2 & 0 \\ 0 & 0 & 1 \end{bmatrix}$ and the rotation matrix $\mathbf{R} = \mathbf{Z}^{(1)}\mathbf{X}\mathbf{Z}^{(2)}$.

5.3.4. Nano-indentation and AFM

Four 500 nm deep spherical nano-indents were made for each orientation for both implanted and unimplanted areas (MTS NanoXp, Synton ~ 5 μm radius diamond tip, 50 μm spacing between indents). Use of a spherical indenter tip removes the additional complexity of in-plane indenter orientation relative to the crystal associated with non-rotationally symmetric tips, for example Berkovich. SEM micrographs (Zeiss Merlin FEG SEM) of the nano-indents in <111>, <001> and <110> grains in the helium-implanted and unimplanted material are shown in Appendix I. They clearly show that consistent results are obtained across the indents for each crystal orientation.

To quantify pile-up morphology, AFM was carried out on one indent per grain orientation in the implanted and unimplanted material (Figure 5.3.1). AFM measurements were done in contact mode using a Digital Instruments Dimension 3100 AFM with Bruker CONTV-A tips (10 nm nominal tip radius). Little difference is seen between indents in different grains of the unimplanted sample (Figure 5.3.1 (d)-(f)). However, in the implanted samples there are striking orientation-dependent variations in pile-up morphology (Figure 5.3.1 (j)-(l)). The <001> grain shows the characteristic large pile-up and distinct slip steps we previously observed (Figure 4.2). Surprisingly indents in <011> and <111> grains, though in the same polycrystalline implanted sample, show very little pile-up. Indeed comparing AFM measurements of indents in <011> and <111> grains of the unimplanted and helium-implanted material could lead to the incorrect conclusion that helium does not significantly modify the deformation behaviour of tungsten.

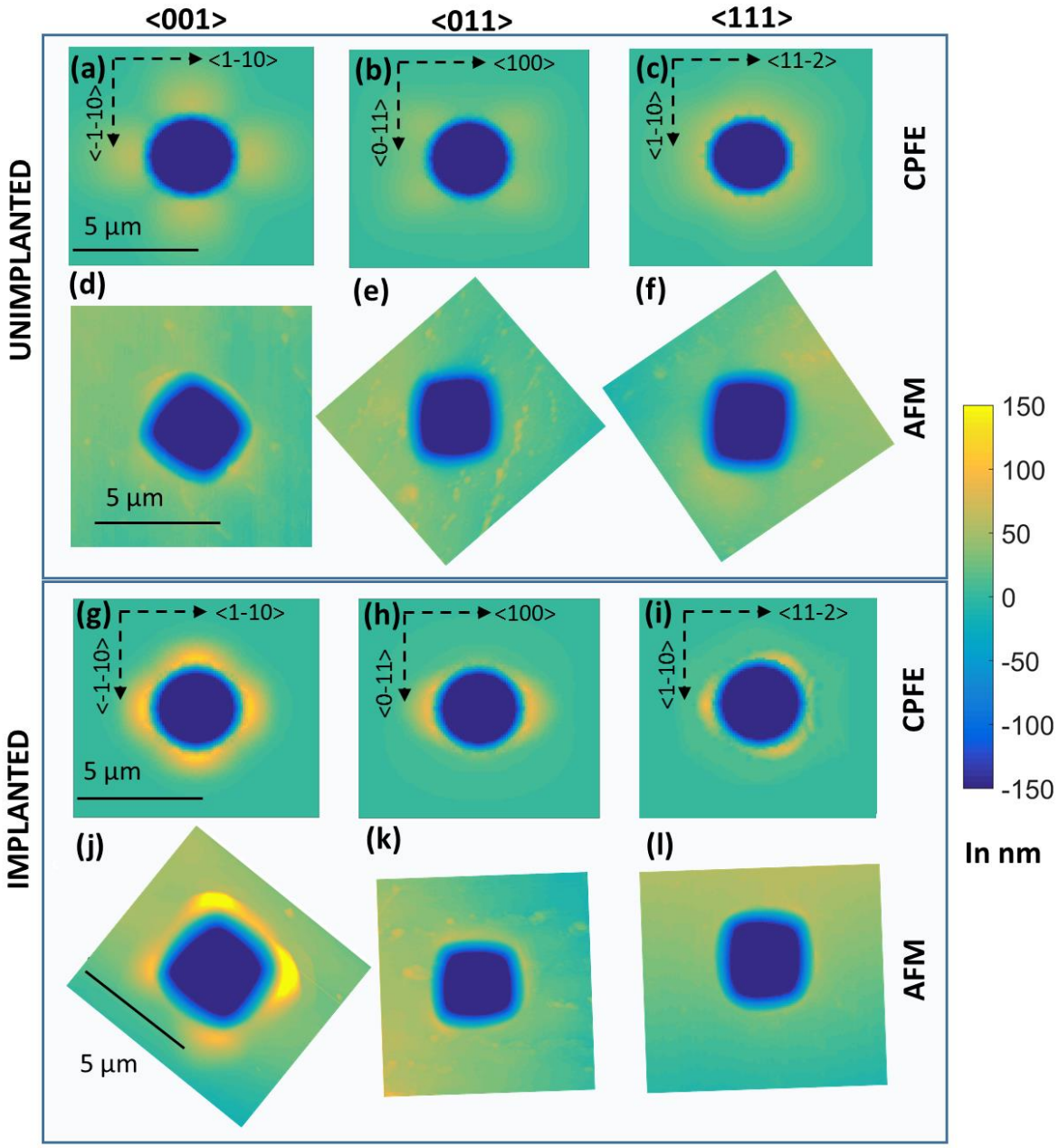


Figure 5.3.1 – Surface profiles of residual out-of-plane displacement after indentation. CPFE simulations for the unimplanted (a) – (c) and the helium-implanted sample (g) – (i) for <001>, <011> and <111> out-of-plane crystal orientations respectively. AFM for the unimplanted (d) – (f) and the helium-implanted sample (j) – (l) for <001>, <011> and <111> out-of-plane crystal orientations respectively. The AFM micrographs have been rotated to match the in-plane orientations as labelled on the CPFE plots. The colour scale and 5 µm scale bar are the same for all plots. Although the indent depth below the surface, after unloading, is ~ 400 nm, a colour-scale of -150 to 150 nm is used as we concentrate on investigating pile-up morphology on the sample surface.

Orientation-dependent differences are also seen in the load-displacement curves shown in Figure 5.3.2. Each curve is the average load-displacement response recorded from the four indents per orientation. In the unimplanted grains there is little difference between the different crystal orientations. In the helium-implanted material, on the other hand, the load for <001> orientation is ~ 20% higher than for <011> and ~ 30% higher than for <111>.

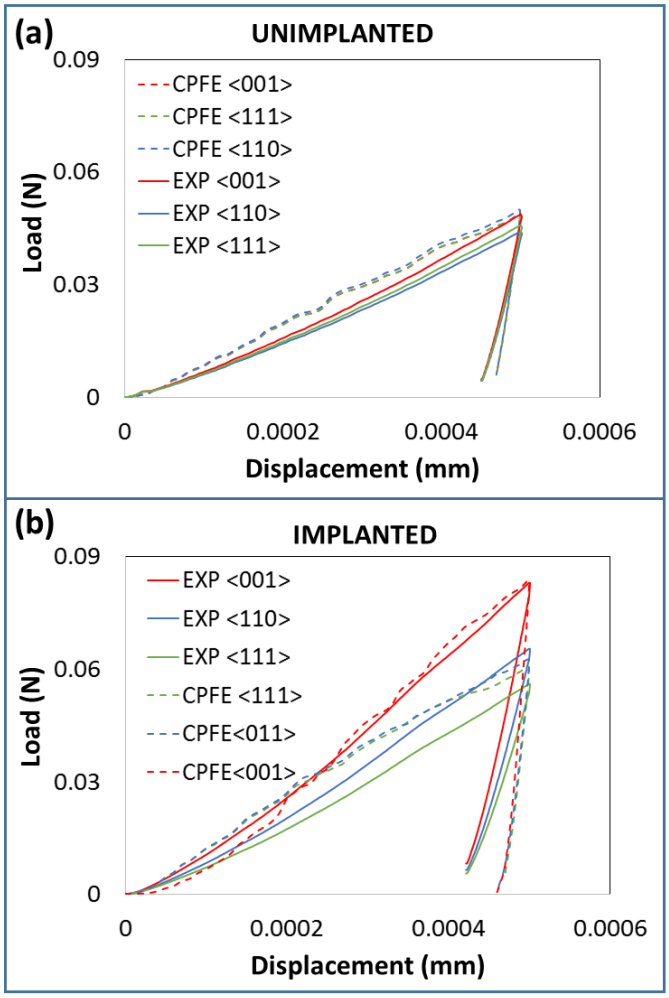


Figure 5.3.2 – Load versus displacement curves (a) unimplanted sample and (b) helium-implanted sample for the <001>, <011> and <111> from the nano-indentation experiment and CPFE simulation superimposed. The solid curves, i.e. those measured from nano-indentation experiments, are the average of four measurements performed on four different indents.

5.3.5. CPFE formulation and comparison with experiments

To explore the origin of the orientation-dependence of indentation behaviour in the helium-implanted material we consider a CPFE model of the indentation process. Recently we developed a CPFE formulation to simulate nano-indentation of a helium-implanted <001> oriented tungsten single crystal (Section 5.2). The formulation is based on a hypothesis derived from a comparative study of nano-indentation and micro-beam Laue diffraction measurements performed on helium-implanted and unimplanted parts of a tungsten <001> crystal (Chapter 4). Here, we use the same CPFE formulation with the appropriate orientation matrix to simulate indentation of the <011> and <111> grain of the polycrystalline tungsten sample. All other parameters of the model were kept constant. Below we briefly discuss the model and the underlying hypothesis. Further details can be found in Section 5.2.

Micro-beam Laue diffraction measurements of the deformation zone beneath indents in a <001> single crystal showed a more tightly confined plastic zone in the helium-implanted sample than in the unimplanted material (Chapter 4). Increased pile-up, slip steps and increased indentation load were observed in the implanted material. Based on these observations, we hypothesised the following mechanism for the interaction of glide dislocations and helium-implantation-induced defects (known to consist predominantly of Frenkel pairs that cannot recombine as helium occupies the vacancy [42]). We propose that initially, helium-defects strongly obstruct gliding dislocations and cause a pronounced hardening. However, with progressive deformation, passing dislocations facilitate release of helium from the helium-vacancy-self-interstitial defect complex and consequently recombination of Frenkel pairs. Reduced defect density channels are thus formed that allow

easier propagation of subsequent dislocations. This leads to a localisation of deformation, which in turn is the origin of the large pile-up and slip steps observed for the <001> orientation. A model based on this hypothesis was implemented in a CPFE user material subroutine (UMAT) for Abaqus where strain softening was applied to the helium-implanted layer.

The UMAT is based on a user-element developed by Dunne et al. [130] and is founded on the theory of multiplicative decomposition of the deformation gradient into elastic and plastic components [188], [225]. Briefly, the CPFE formulation constrains slip to applicable slip-systems (assumed to be the 12 {110} slip planes with a/2<111> slip vector directions [231] (Appendix G)). The slip rate is governed by a physically-based constitutive law that considers the glide of thermally activated dislocations in a field of pinning obstacles (Section 5.1.4.2) [130]. Taylor hardening is implemented, where the critically resolved shear stress (CRSS), with initial value τ_c^0, is increased as a function of evolving densities of geometrically necessary dislocations (GNDs) [236]. The CRSS in the unimplanted sample is $\tau_c = \tau_c^0 + CG\, b \sqrt{\rho_{GND}}$, where G is the shear modulus of tungsten, b the Burgers' vector and ρ_{GND} the sum of the GNDs produced across all slip-systems. A modified form of this equation is used in the helium-layer; $\tau_c = \tau_c^0 + CG\, b \sqrt{\rho_{GND}} + \tau_H$ where the additional τ_H term accounts for the increased resistance to dislocation glide due to helium-defects. To account for the strain softening, τ_H is reduced at the end of each time increment, Δt, if the material point was deformed plastically. The reduction in τ_H represents the gradual formation of defect-free regions, and consequently easier dislocation glide. τ_H is considered to be a function of the total accumulated crystallographic slip and the rate at which it decreases is estimated to be

proportional to its current value i.e. the current helium-defect concentration[6]. This suggests an exponential softening:

$$\tau_H^{t+\Delta t} = \tau_H^0 \, e^{-(\beta_p^{t+\Delta t}/\gamma)} \tag{5.3.1}$$

$$\beta_p^{t+\Delta t} = \beta_p^t + \sum_{\lambda=1}^{n} \dot{\beta}_p^{\lambda} \Delta t \tag{5.3.2}$$

where $\dot{\beta}_p^{\lambda}$ is the crystallographic slip rate on slip system λ , β_p^t and $\beta_p^{t+\Delta t}$ are the total accumulated crystallographic slip, summed over all slip systems, at the start and end of the time increment, and τ_H^0 is the initial value of τ_H . Only three UMAT parameters were fitted to the nano-indentation and AFM results of the <001> grain: the initial unimplanted CRSS, τ_c^0, the hardening prefactor C and only one additional parameter for the helium-layer, the softening-rate γ. All other UMAT parameters, including τ_H^0 were physically-derived, or taken from literature (Table H.1).

The geometry for CPFE simulations was a 3D, 20×20×20 μm^3 sample block and a 5 μm radius spherical indenter simulated in Abaqus (Dassault Systèmes, Providence, RI, USA). Based on symmetry, for the <001> and <011> grains, the model simulated one quarter of the experimental setup. For the <111> grain, a model simulating a third of the experimental setup was used (Figure I.3). The boundary conditions applied to the indentation model in Abaqus included symmetric XZ and YZ planes, a traction free top surface, and fixed displacement and rotation boundary conditions on the remaining surfaces.

[6] $\left.\frac{\partial \tau_H}{\partial \beta_p}\right|_{t+\Delta t} = -\tau_H/\gamma$

The 20 μm high block was partitioned into two layers: a 3 μm thick top layer and 17 μm thick bottom layer. When simulating indentation on the helium-implanted tungsten, the top layer was assigned material parameters of implanted tungsten and the bottom layer those of pure tungsten. Additional boundary conditions, $\sigma_{xx}^{BC} = \sigma_{yy}^{BC}$ = -260 MPa, were applied to the helium-implanted layer to account for helium-implantation induced residual stresses. These stresses arise out of the need to maintain geometrical continuity between the implanted layer and substrate (Section 3.4). Derivation of these stress boundary conditions is given in Appendix H.

The indenter was subjected to a displacement of 0.5 μm into the sample block followed by complete unloading to account for relaxation of the elastic part of the deformation and any reverse plastic deformation that may be taking place. The contact surface between the sample block and the indenter tip was assumed to be frictionless as a prior study [182] showed that the mechanical response of the substrate is not significantly affected by the coefficient of friction. A structured finite element biased mesh with >39500 20-noded quadratic hexahedral elements with reduced integration was used (C3D20R) (Appendix I); with an element size of 50 nm at the indent.

The simulated indent surface-profiles, after unloading, for both samples are shown in Figure 5.3.1. The AFM micrographs in Figure 5.3.1 are rotated to have the same in-plane orientation as the profiles predicted by CPFE. Four, two and three-fold symmetry can be seen in the CPFE predicted surface profiles of the <001>, <011> and <111> grains respectively (Figure 5.3.1 (a)-(c)). The CPFE model reproduces the experimental pile-up for all three grains in the implanted sample remarkably well. In particular, the model captures the much lower pile-up in the <011> and the <111> grains compared to the <001> grain.

We note in Figure 5.3.1 that the AFM measurements of the indent impressions are not perfectly circular. This is due to imperfections of the spherical indenter tip geometry. Flawless spherical indenter tips, especially with such a small tip radius, are difficult to manufacture. However, good agreement between the CPFE predictions (where a perfectly spherical tip was simulated) and the experimental results shows that the deviations in the indent tip geometry do not significantly affect the indentation response. This is an important advantage of using a spherical indenter tip over Berkovich tips, where the sharp tip makes the indentation response very sensitive to imperfections in tip geometry.

The simulated load-displacement curves for each grain orientation in both the implanted and unimplanted samples are shown superimposed on the experimental measurements in Figure 5.3.2. A good quantitative agreement is observed between CPFE and experimental results for the unimplanted sample. In terms of the mechanical response for the implanted samples, CPFE predictions for the <001> grain reaches ~ 14% higher load than the <011> and <111> grains; with the latter two producing a very similar load response. It is important to note that the parameters of the model were determined solely based on the indentation results of the <100> oriented crystal. For the simulations of the <011> and <111> oriented grains all parameters except for the input crystal orientation were kept unchanged.

Anisotropy in indentation behaviour has been previously noted in ∝-Ti [262] and Be [263] polycrystals, where modulus and hardness decreased significantly with increasing angle of inclination between the c-axis and the indentation axis. Orientation-dependent mechanical performance has been seen in tungsten too, where <001> single crystals were found to be the best performing kinetic energy penetrators, owing to favourable slip during loading and shear localisation [264]. It is interesting that orientation-dependent differences

in indentation response are as pronounced at the nano-scale. The results highlight the importance of determining the crystallographic orientation of the ion-implanted sample for accurate evaluation of the ion-induced alteration in deformation behaviour.

Quantitative agreement between CPFE predictions and experimental results for the implanted sample inspires some confidence in the hypothesis that localised deformation through slip channels, formed by dislocations interacting with helium-defects, can cause the large pile-up and increased hardening. In the 1960s' Makin et al. proposed a mathematical theory linking the creation of large pile-up and slip-steps to an accelerating fall in the force resisting dislocation glide [187]. As the defect reduction rate will depend on the number density of defects, an exponential decrease in τ_H, as implemented in the CPFE formulation in Eq. (5.3.2), is reasonable. The model uniquely captures the four-fold pile-up increase in the <001> grain in the implanted samples, affirming the strain-softening hypothesis. Strain-softening and consequent slip channel formation in irradiated materials, both fcc and bcc, has been experimentally observed in numerous studies [265]–[267]. This is of particular concern as it may lead to untimely failure due to loss of ductility.

The CPFE predictions also provide further insight into the underlying deformation zone beneath indents. Comparison of the field of effective plastic strain beneath indents in each grain for both samples (Figure 5.3.3) shows an orientation-independent trend. The deformation field becomes more confined near the indent in all grains in the implanted material, compared to a more widespread deformation zone in the unimplanted material.

Put together, these results, suggest that the underlying mechanism responsible for the modified behaviour of the implanted material, i.e. the interaction of dislocation with helium-induced defects, is orientation-independent. The changes in pile-up morphology for

different crystal orientations are simply a product of the relative orientations of the active slip systems, the indenter and the sample surface.

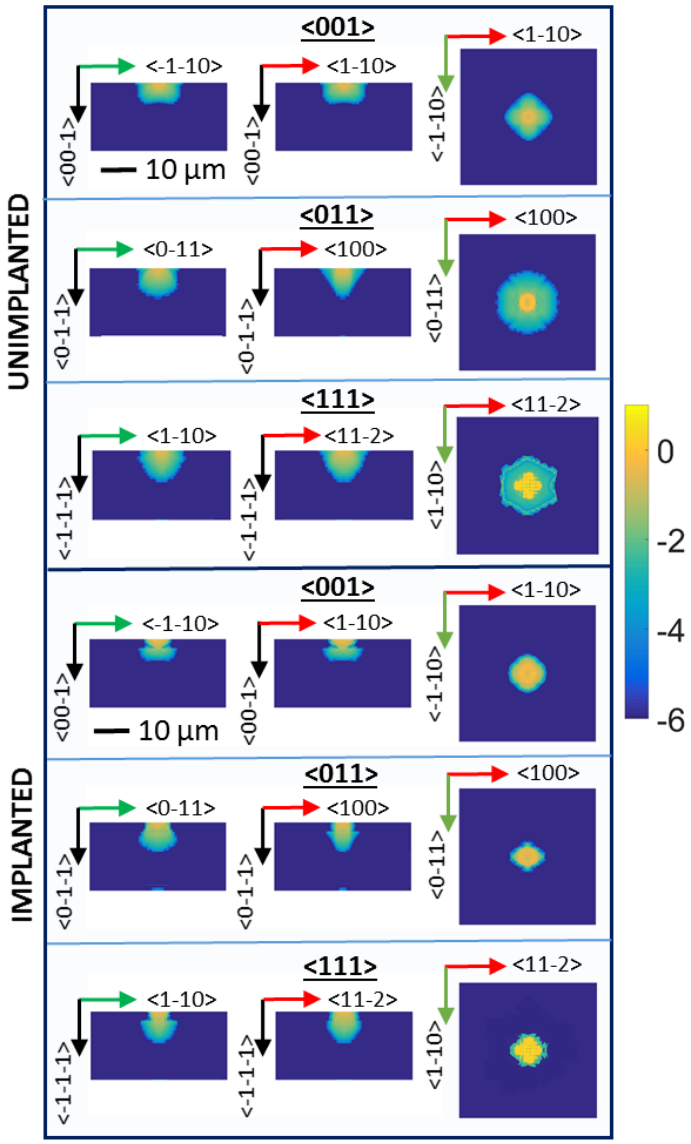


Figure 5.3.3 – A comparison of the effective plastic strain (in logarithmic scale) beneath indents in all three grains for both the unimplanted and the helium-implanted sample as predicted by the CPFE simulation. In each case, strain is shown on the YZ, XZ and the XY cross-sections from left to right.

In summary, we have examined the effect of helium-implantation in grains of three different orientations. It was found that <001>-oriented grains showed ~ 70% increased hardness and ~ 172% increased pile-up compared to unimplanted tungsten. In contrast, <011> and <111> grains show negligible change in pile-up and only a ~ 30% increase in

hardness compared to the unimplanted sample. CPFE based on the application of strain-softening in the helium-implanted layer, was able to reproduce the experimental results for all three grains with surprising accuracy. The fact that significantly different indentation behaviour is observed for different grain orientations in the implanted material highlights the importance of considering crystal orientation when interpreting nano-indentation data.

Chapter 6

Conclusions

This thesis presents several advances in the understanding of irradiation damage in tungsten, the main candidate material for armour components in future fusion reactors. Helium ion implanted tungsten was used here as a model to study irradiated tungsten armour component. This provides a convenient way of simultaneously mimicking damage formed by energetic neutron irradiation and introducing helium into the tungsten matrix so that its interaction with defects may be studied. Using a combination of experimental and modelling techniques, important insights were gained into irradiation induced dimensional change, the mechanism of interaction of irradiation defects with mobile dislocations and consequent changes in mechanical properties.

In association with this, a comprehensive review of the theory of computation of the dislocation tensor and GND density has been presented. The theory was demonstrated through 3D analysis of lattice distortions, induced by spherical nano-indentation in pure tungsten, using CPFE simulations and Laue measurements. Important conclusions derived thereby will be reviewed first. Following this, the observations made and conclusions drawn from examination of irradiated tungsten will be summarised.

Computation of dislocation tensor & GND density: Key points

The dislocation tensor ($\boldsymbol{\alpha}$) is linked to the density of GNDs causing closure failure, and can also be equated to lattice distortions in the deformed material. As such, $\boldsymbol{\alpha}$ provides a very useful link between GND density and the lattice curvature it accommodates.

- By exploring the different curl definitions used to compute the dislocation tensor, it has been shown that if applied consistently, all definitions give the same result.
- Contribution of the curl of the volumetric part of the elastic strain tensor to $\boldsymbol{\alpha}$ is small. Thus, strain measurements from experimental techniques (for example white-beam Laue diffraction and HR-EBSD) which can only measure the deviatoric component of strain, can be safely used to compute $\boldsymbol{\alpha}$.
- L^1 optimisation recovers a more heterogeneous distribution of GND density over individual slip systems while L^2 optimisation distributes GND density almost uniformly over all slip systems. If GND density on specific slip systems is required, the physically-based L^1 minimisation should be used.
- The total GND density determined by either L^1 or L^2 minimisation is remarkably similar. Thus, the computationally simpler L^2 optimisation may be preferred if only total GND density is required.

The conclusions drawn above laid the foundation for analysing plastic deformation fields in helium-irradiated tungsten. For example, clarity developed about the usage of the curl computation technique ensured correct calculation of GND density; an analysis which has highlighted important irradiation-induced changes in deformation behaviour. Important conclusions drawn from characterising helium-implanted tungsten are discussed below.

Helium-irradiation damage in tungsten: Key points

Of the large population of Frenkel pair defects created by helium-implantation at room temperature, only a small percentage of defects is retained. However, examining the helium-defects and their evolution with dose is challenging as the few atom large defects remain invisible in TEM. Instead energy- and depth-resolved synchrotron X-ray micro-diffraction was used here to probe these defects by measuring the lattice strains they cause.

With this technique, the impact of even quite low dose helium-implantation (~ 300 appm) could be examined. It was found that:

- Defect retention and thereby the strains induced are not simply a linear function of dose.
- A ten-fold increase in helium-implantation dose (from 300 to 3000 appm) caused only ~ 240% increase in volumetric eigenstrain, indicating that defect retention per injected helium atom is ~ 3 times higher at low helium doses.
- Increased defect retention at lower doses may be caused by impurities, in particular carbon, whilst at higher doses the injected helium dominates defect retention. Thus, material composition and impurities which have been known to affect tungsten's BDTT, could also be playing a key role in determining the defect retention and thereby the irradiation-induced lattice swelling.
- Grain orientation only caused minor changes in defect retention. Thus, at least as far as implantation-induced strains are concerned, tight control of the texture of tungsten armour components may not be necessary.
- Comparison with helium-implanted W-1at.wt% Re alloy samples showed that the presence of rhenium has a relatively small effect on defect retention. However, past studies on tungsten samples with higher concentration of rhenium, have shown substantial increase in hardening due to formation of rhenium clusters. Thus, further exploration of irradiated tungsten samples with varying concentrations of rhenium is necessary to draw more conclusive statements about the effect of this transmutation element.

Helium was also found to significantly impact the deformation behaviour of tungsten. Deformation behaviour of <001>-oriented tungsten, implanted with 3000 appm of helium

at room temperature, was examined by a combination of experimental techniques and compared with that of pure tungsten.

- Nano-indentation allowed examination of the hardness of the implanted layer which is only 3 μm thick. Surprisingly a ~ 75% increase in hardness was found in these samples.
- Large localised pile-up was noticed around the nano-indents in the helium-implanted samples with distinct formation of slip steps. AFM measurements showed a ~ 172% increase in pile-up height.
- The changes were found to extend to the deformation zone beneath indents. Changes in the lattice distortion fields beneath indents, could be measured with a strain resolution of ~ 1×10^{-4}, using depth-resolved white-beam X-ray micro-diffraction. Both lattice rotation and lattice strain fields under indents in the implanted samples were found to be localised, compared to a more widespread deformation zone under indents in the unimplanted material. These observations agree with HR-EBSD measurements on a FIB-lift-out made from the indent centre in the helium-implanted sample. A complete picture of the near-field (having steep strain gradients) and far-field, of the lattice distortion distribution beneath indents, could be obtained by combining the high spatial resolution of HR-EBSD and the high sensitivity of Laue measurements.
- Strain-softening during deformation, implied by these observations, was qualitatively confirmed by TEM which showed that dislocations “sweep out” helium-implantation-induced defects, leaving behind low defect density zones/channels.

Based on the experimental observations from indentation of the <001>-oriented helium-implanted tungsten sample, a mechanism of interaction between helium-defects and gliding dislocations was proposed; where helium-implantation-induced defects initially act as efficient obstacles to dislocation motion, but are removed by interaction with passing dislocations. A physically-based CPFE formulation, for helium-implanted tungsten, was developed based on this hypothesis, which accounted for initial hardening due to interaction of dislocation with helium-defects, as well as subsequent softening.

- Importantly only one fitting parameter (the rate of softening or defect removal) was used in the model for simulating helium-implanted tungsten. Shear resistance of the helium-defects was physically-based.
- The CPFE formulation was used to simulate indentation of <001>-oriented 3000 appm helium-implanted tungsten. Experimentally observed helium-induced changes in deformation behaviour such as increased hardness, large pile-up, localised distortion fields and confinement of GND density field, could all be well captured by the CPFE simulation.

Agreement between the CPFE predictions and the experimental results inspire confidence in the developed formulation. Together, the experimental and modelling results highlight that even a comparatively small concentration of irradiation/implantation induced defects can produce dramatic changes in the mechanical properties of tungsten; a large increase in the initial hardness followed by strain softening. This irradiation-induced strain localisation was found to be orientation-independent.

- Indentation simulated for <011> and <111> oriented grains of tungsten implanted with 3000 appm of helium, by the same CPFE model, showed a confined deformation field near the indent for both orientations.

- However, orientation-dependent changes were observed in the indent surface morphology. In contrast to the large pile-up and ~ 75% hardness increase seen in the <001>-oriented helium-implanted tungsten grains, <011> and <111> grains were found to show little change in pile-up and only a ~ 30% increase in hardness compared to the unimplanted sample.
- Together the observations suggest that the interaction of dislocation with helium-induced defects is orientation-independent and orientation-dependent changes in pile-up morphology arise due to the relative orientations of the active slip systems, the indenter and the sample surface.
- The fact that significantly different indentation behaviour is observed for different grain orientations in the implanted material highlights the importance of considering crystal orientation when interpreting nano-indentation data from ion-implanted materials. It is also noted that the large increase in the hardness seen for the <001> oriented grains may be due to the change in contact area caused by the large pile-up noticed in this case. This highlights the importance of accounting for contact area changes in hardness measurements.

The experimental observations made in this thesis provide conclusive evidence of the significant changes that can be induced by helium irradiation in tungsten armour components. Owing to its strong affinity of interaction with lattice defects, helium promotes the retention of irradiation-induced defects in the form of small helium-vacancy-self-interstitial defect complexes. The alterations in the mechanical properties induced by the retained helium-defects, such as increased hardness and reduced work hardening capacity are detrimental to material ductility, a key concern for long-term structural integrity of future tungsten-based diverter concepts. As such physically-based models that capture these effects will be key to determining the evolution of mechanical properties in fusion

reactor armour components and assessing their in-service performance. The feasibility of such models is inspired by the successful predictions of the CPFE model developed in this thesis for helium-implanted tungsten. The future outlook is to improve the accuracy of such models by integrating discrete dislocation dynamics, accounting for spatial variation in the distribution of the defect densities and extending them to polycrystals where increased defect retention due to grain boundaries must be considered.

The effective combination of experimental and modelling techniques is now being extended to self-ion implanted tungsten models to develop an understanding of the mechanism of interaction of the loop-dominated microstructure (as induced in this case) with dislocations. The broader outlook is to build an integrated model which accounts for the presence of helium- and self-ion- induced defects to predict the performance and lifetime of tungsten components irradiated by helium and neutrons in the fusion reactor.

Appendices

A. Ion energies and fluence for helium-implantation

Ion Energy (MeV)	3000 appm He	300 appm He
	Fluence (ions/cm^2)	Fluence (ions/cm^2)
0.05	3.60E+15	1.50E+14
0.1	1.50E+15	2.50E+14
0.2	1.00E+15	3.50E+14
0.3	5.00E+15	1.50E+14
0.4	5.00E+15	4.00E+14
0.6	5.00E+15	4.75E+14
0.8	5.00E+15	4.50E+14
1	5.00E+15	4.75E+14
1.2	5.00E+15	4.75E+14
1.4	5.00E+15	5.00E+14
1.6	5.50E+15	5.50E+14
1.8	6.00E+15	5.50E+14

Table A.1 – List of 12 ion energies used and the corresponding fluence for the helium ion implantations.

B. Supplementary materials for Chapter 3

EBSD maps of samples

Micro-diffraction measurements were carried out in each of the pre-determined grains of each sample. Overall, eight points were investigated experimentally, as shown by the black dots in Figure B.1.

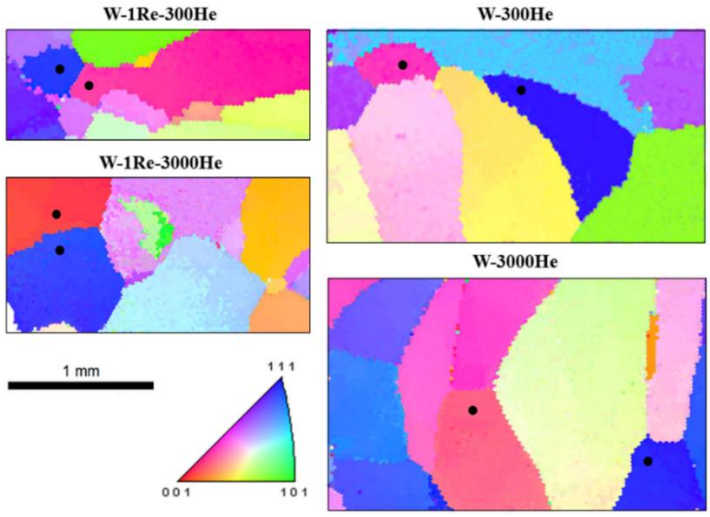


Figure B.1 - EBSD images of the four samples used in the study. The black spots indicate the positions in each sample where the micro-diffraction measurement was carried out.

Depth resolved strain measurements

Figure B.2 and Figure B.3 show the line plots for the direct strains over the depth range of 0-10 μm for the 300 and 3000 appm helium-implanted samples respectively. Figure B.4 and Figure B.5 show the line plots for the shear strains over the depth range of 0-10 μm for the 300 and 3000 appm helium-implanted samples respectively.

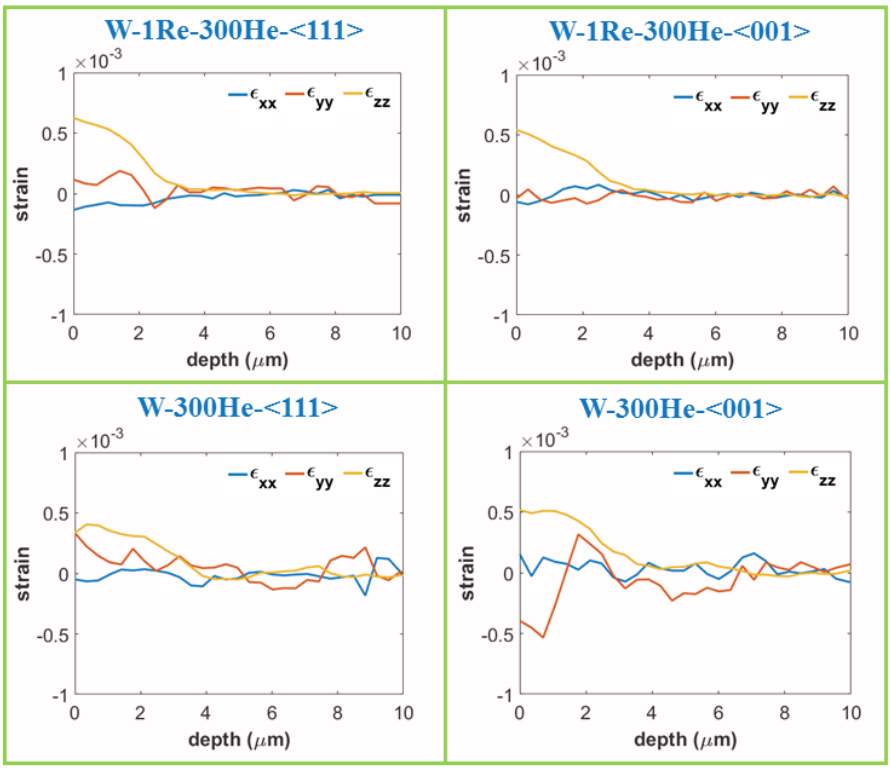


Figure B.2 – Direct strains measured for samples implanted with 300 appm of helium plotted vs sample depth.

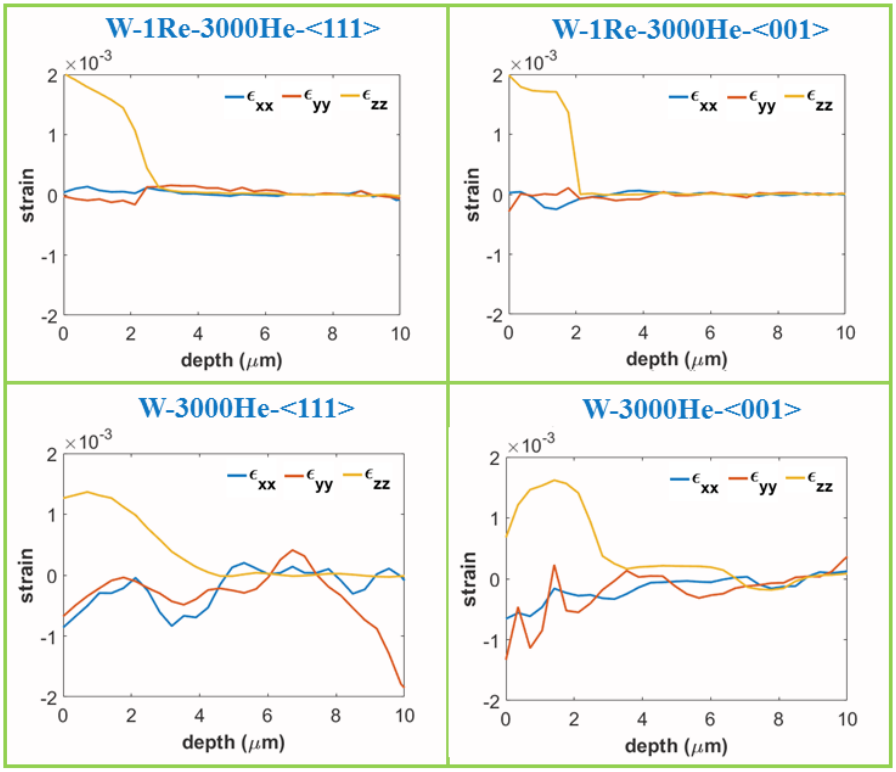


Figure B.3 – Direct strains measured for samples implanted with 3000 appm of helium plotted vs sample depth.

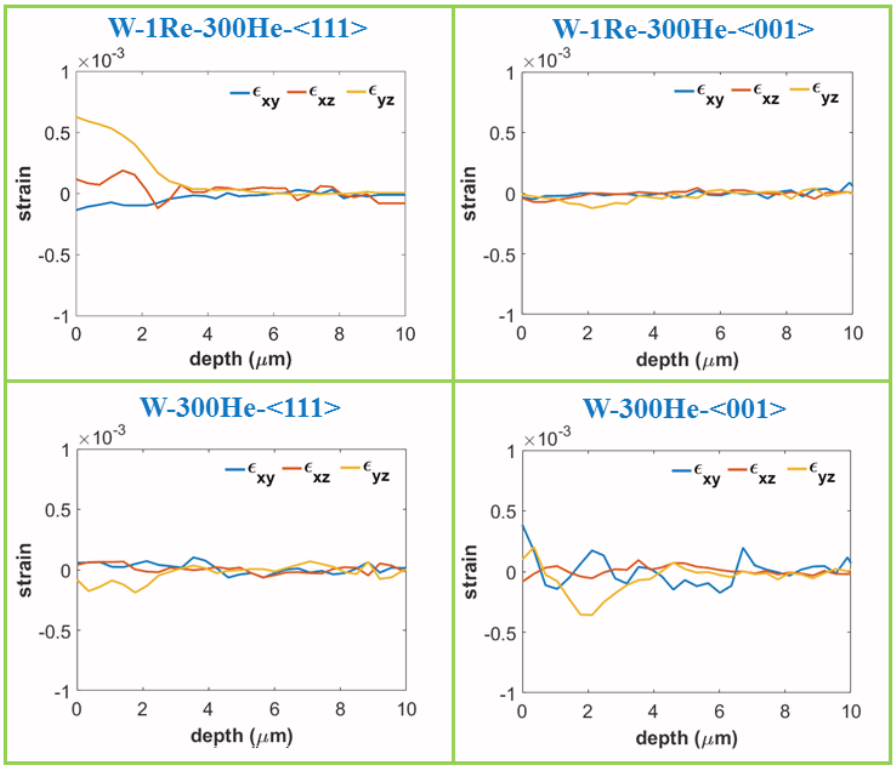


Figure B.4 – Shear strains measured in samples implanted with 300 appm of helium plotted vs sample depth.

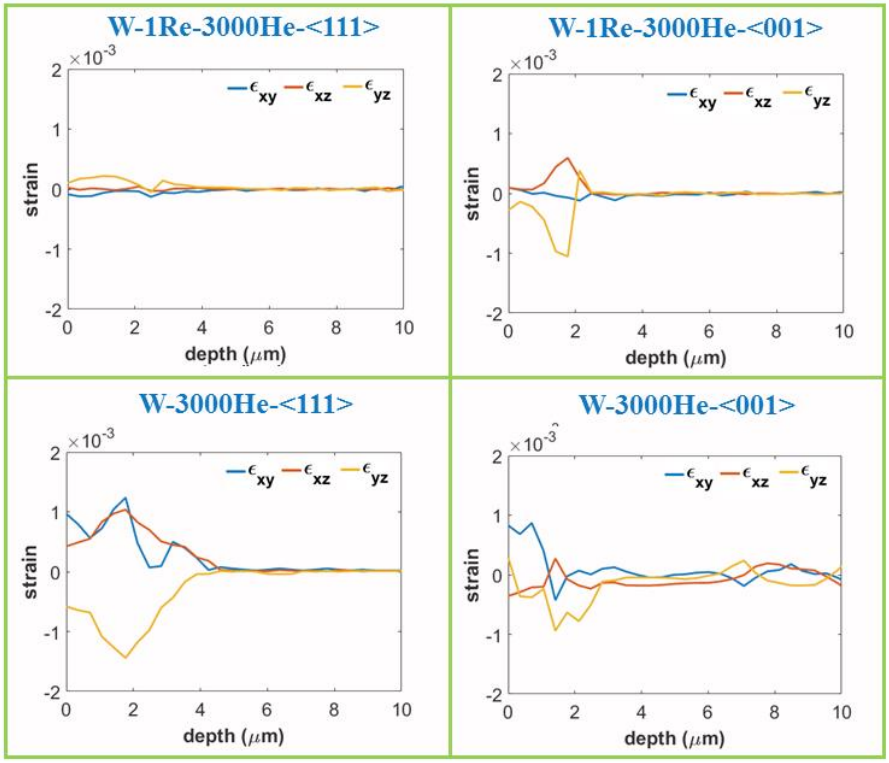


Figure B.5 – Shear strains measured in samples implanted with 3000 appm of helium plotted vs sample depth.

C. Supplementary materials for Chapter 4

Why we need to probe beneath indents?

Although pile up and channel formation could be observed by SEM and AFM measurements, the spread of the plastic zone underneath the indent cannot be unambiguously concluded from these methods. A study by Kiener et al. [268], reviews the different characterisation techniques (etch-pit, EBSD and in-situ TEM) used to analyse nano-indentation induced plasticity. Their report illustrates the limitations of each method (restricted to surface analysis, extensive sample preparation, lack of sensitivity to dislocations parallel to surface, restricted sample size etc.) and stresses on the need to use multiple techniques to fully understand the deformation mechanisms [268].

To illustrate why surface observations are not sufficient, the results from a simple 2D finite element simulation of a nano-indentation experiment are provided below. They show that different combinations of yield stress and hardening (Figure C.1 (a)) can result in very similar surface profiles (Figure C.1 (b)) but very different plastic deformation underneath the indent (Figure C.1 (c), (d)). 3D Laue micro diffraction measurements uniquely allow access to the complex 3D lattice distortion fields beneath specific indents without altering the residual stress state.

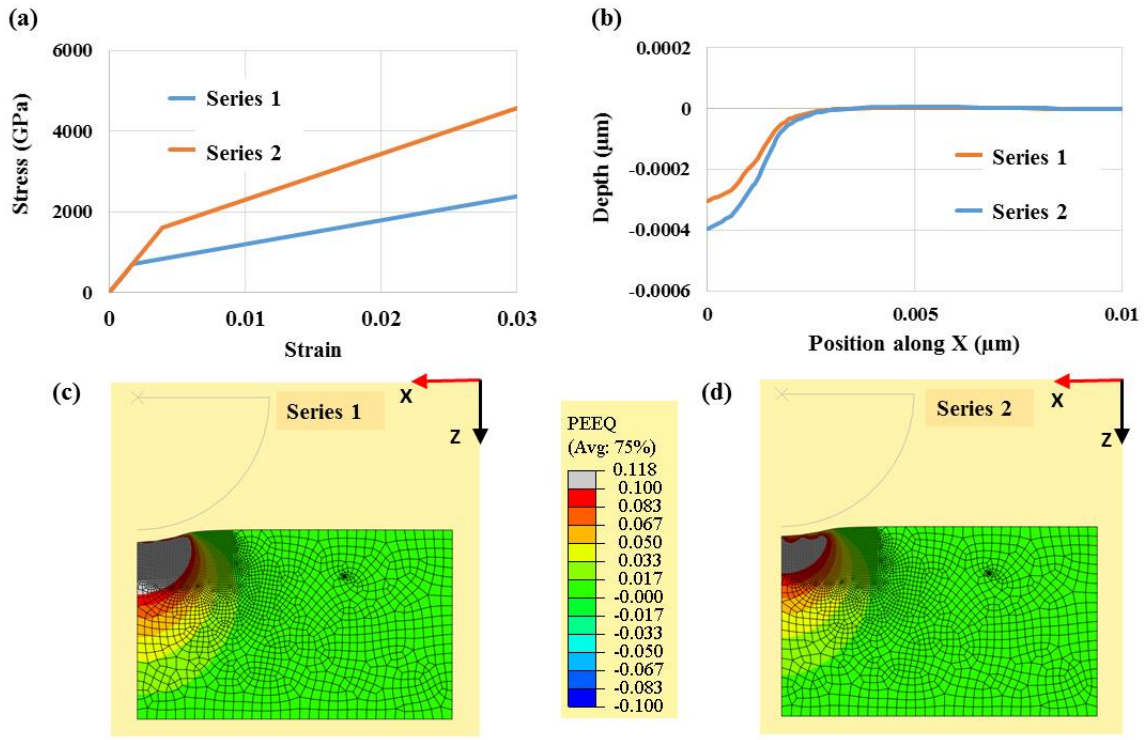


Figure C.1 – (a) Stress-strain curves for 2 chosen values of yield stress and linear hardening; (b) Indent-depth profile for the 2 chosen sets of yield stress and linear hardening; The equivalent plastic strain field beneath the indent after unloading as simulated in Abaqus using a 2D axisymmetric model with Von Mises yield criterion and linear hardening (c) for Series 1 and (d) for Series 2.

Detailed map of evolving lattice rotations

Figure C.2 shows the changes in lattice rotations, plotted on the YZ plane, for all three components, θ_x, θ_y and θ_z, in incremental positions along the X direction. Figure 4.2 in the main text illustrates these changing lattice rotations on only three chosen slices, before and after the indent centre. Figure C.2 further elucidates the progressive evolution of the lattice rotations along the X direction by depicting it on 0.9 µm incremental positions at distances of up to 5.4 µm from the indent centre. Lattice rotations for the helium-implanted tungsten are displayed using a reduced colour-scale as compared to the unimplanted sample. This has been done to clearly show the pattern of the smaller lattice rotations caused by helium-implantation and to get a pronounced view of their progressive evolution along the X-axis.

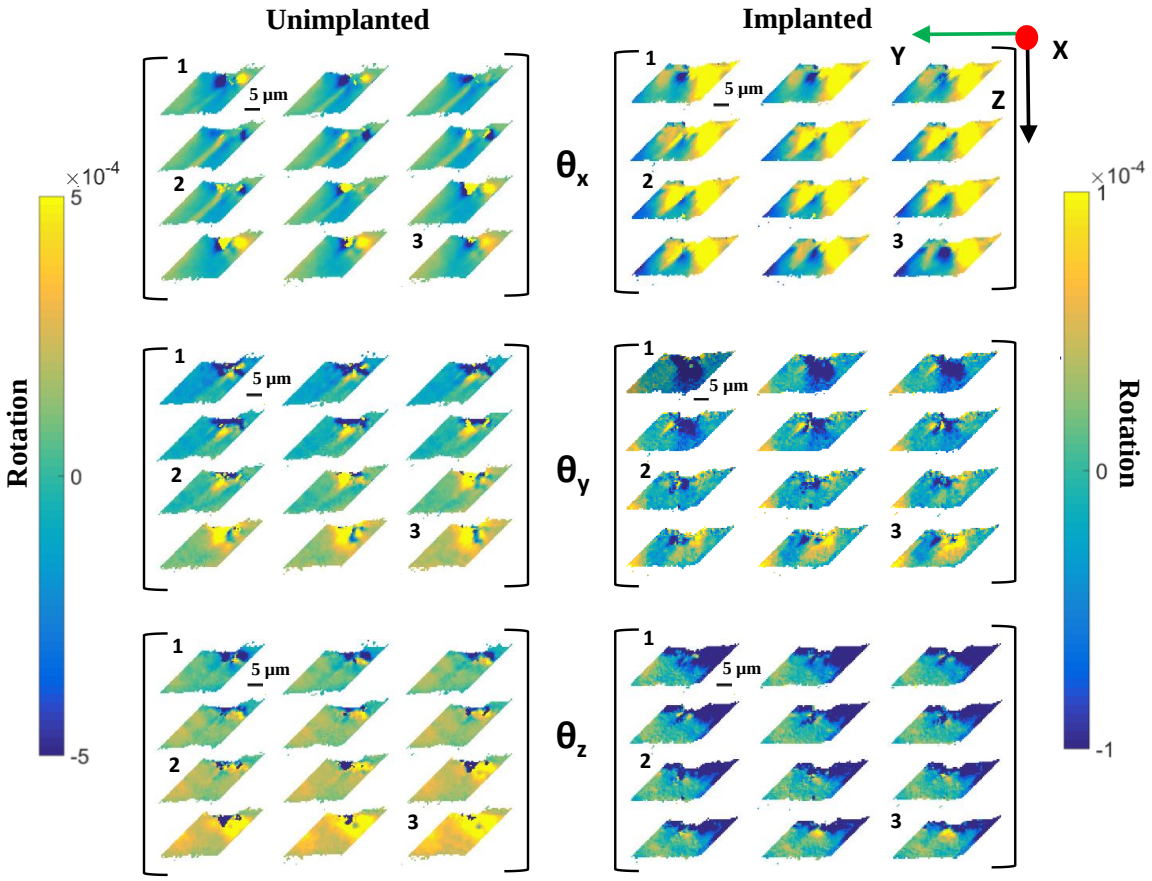


Figure C.2 – Lattice rotations in radians at incremental positions (0.9 µm between slices) along the X direction plotted on the YZ sample plane; Positions 1, 2 and 3 correspond to cross section slices shown in Figure 4.2. Position 1 corresponds to a point on the X-axis before the indent centre, position 2 is at the indent centre and position 3 is a slice after the indent centre. Scale bars correspond to 5 µm.

Deviatoric strain on XZ cross-section

Figure C.3 shows all components of the deviatoric strain, plotted on the XZ plane, at the indent centre. As observed in the YZ and XY planes (Figure 4.3), the strain fields are larger in magnitude in the unimplanted sample than in the helium-implanted sample. This is particularly noticeable for the ε_{xx}, ε_{xy} and the ε_{zz} components.

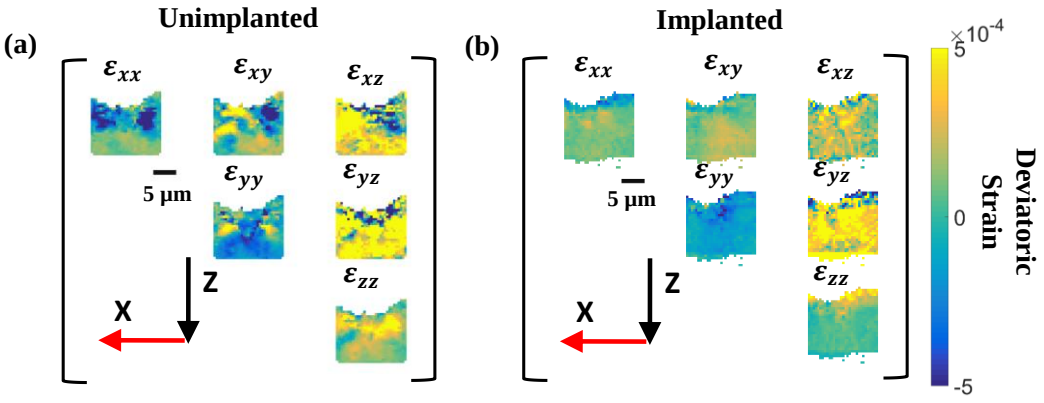


Figure C.3 – Experimentally measured elastic strains at the indent centre on the XZ plane. Scale bars correspond to 5 µm.

D. Schematic of lattice rotations during indentation

As the block deforms due to indentation, it is expected that lattice rotations about the X-axis, will be positive and negative (right-handed rotation) on either side of the indent centre (depicted by the dotted blue line). Similarly, it can be expected that θ_y will be negative in the region labelled before indent centre and positive after the indent centre. Rotations about the Z-axis are anticipated to be small.

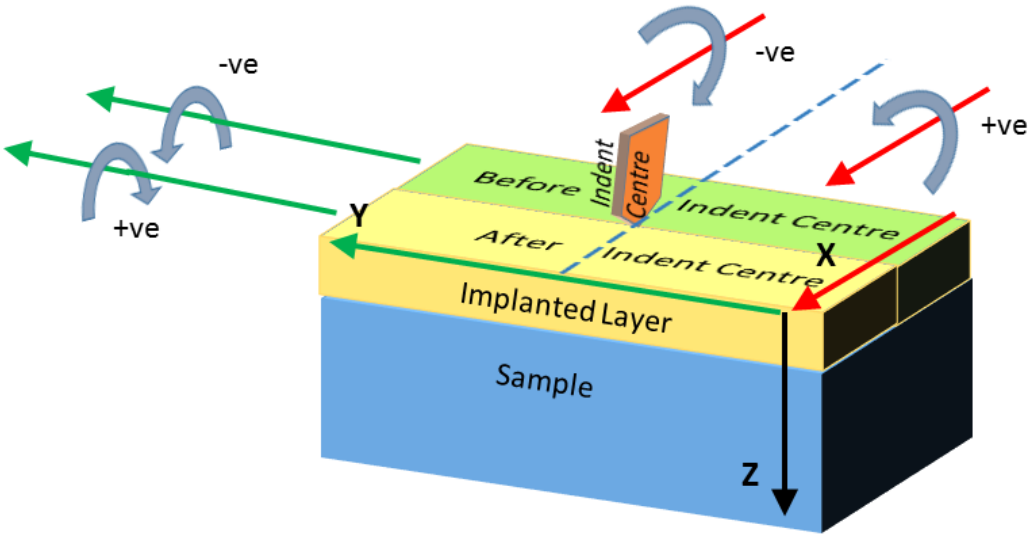


Figure D.1 – Schematic of the lattice rotations expected due to nano-indentation.

E. Supplementary materials for Chapter 5.1

Detailed derivation of three curl definitions

Derivation of the three common definitions of the curl of a second order tensor.

Precurl

$$\begin{aligned} \boldsymbol{R} = (\nabla \times \boldsymbol{P}) &= \left(\widehat{e_\iota}\frac{\partial}{\partial x_i}\right) \times P_{jm}\widehat{e_j} \otimes \widehat{e_m} = \left(\widehat{e_\iota} \times \widehat{e_j}\right) \otimes \widehat{e_m}\frac{\partial P_{jm}}{\partial x_i} \\ &= \widehat{e_k} \otimes \widehat{e_m} \in_{kij} P_{jm,i} \end{aligned} \tag{E. 1}$$

Thus, $\boldsymbol{R}_{km} = (\nabla \times \boldsymbol{P})_{km} = \in_{ijk} P_{jm,i}$

Postcurl

$$\begin{aligned} \boldsymbol{S} = (\boldsymbol{V} \times \nabla) &= V_{kj}\widehat{e_k} \otimes \widehat{e_j} \times \left(\widehat{e_\iota}\frac{\partial}{\partial x_i}\right) = V_{kj}\,\widehat{e_k} \otimes \left(\widehat{e_j} \times \widehat{e_\iota}\right)\frac{\partial}{\partial x_i} \\ &= V_{kj}\,\widehat{e_k} \otimes \widehat{e_m} \in_{mji} \frac{\partial}{\partial x_i} = \in_{mji} V_{kj,i}\,\widehat{e_k} \otimes \widehat{e_m} \end{aligned} \tag{E.2}$$

Thus, $\boldsymbol{S}_{km} = (\boldsymbol{V} \times \nabla)_{km} = \in_{mji} V_{kj,i} = -\in_{ijm} V_{kj,i}$

Curl3

If $\boldsymbol{c}$ is a constant vector then using the definition that $\nabla \times (\boldsymbol{c}.\boldsymbol{V}) = (\nabla \times \boldsymbol{V}).\boldsymbol{c}$ and recalling that

$$\boldsymbol{v} = \boldsymbol{c}.\boldsymbol{V} = c_m V_{mj}\widehat{e_j} \tag{E.3}$$

we can formulate the curl of a matrix using the familiar definition of the curl of a vector

$$(\nabla \times \boldsymbol{v})_k = \left(\widehat{e_i}\frac{\partial}{\partial x_i}\right) \times c_m V_{mj}\widehat{e_j} = \left(\widehat{e_i} \times \widehat{e_j}\right) c_m \frac{\partial V_{mj}}{\partial x_i} = \in_{kij} c_m V_{mj,i}\widehat{e_k}$$
$$= (\in_{ijk} V_{mj,i}\widehat{e_k} \otimes \widehat{e_m}).\boldsymbol{c} = (\nabla \times \boldsymbol{V}).\boldsymbol{c} \quad \text{(E.4)}$$

Thus, $\boldsymbol{Q}_{km} = (\nabla \times \boldsymbol{V})_{km} = \in_{ijk} V_{mj,i}$

Derivation of relation between the three curl definitions

Let $\boldsymbol{P}$ be defined as a second order tensor

$$\boldsymbol{P} = \begin{bmatrix} a_1 & a_2 & a_3 \\ b_1 & b_2 & b_3 \\ c_1 & c_2 & c_3 \end{bmatrix} \quad \text{(E.5)}$$

Proof of curl3 ($\boldsymbol{V}$) = Precurl ($\boldsymbol{V}^{\mathrm{T}}$)

Given the definition of $\boldsymbol{P}$ in Eq. (E.5), as per the above postulated statement, $\boldsymbol{V}$ will then be defined as

$$\boldsymbol{V} = \boldsymbol{P}^{\mathrm{T}} = \begin{bmatrix} a_1 & b_1 & c_1 \\ a_2 & b_2 & c_2 \\ a_3 & b_3 & c_3 \end{bmatrix} \quad \text{(E.6)}$$

Now, using the "curl3" definition, Q_{km}, can be written explicitly as

$$Q_{km} = (\nabla \times \boldsymbol{V})_{km} = \in_{ijk} V_{mj,i} = \begin{bmatrix} \frac{\partial V_{13}}{\partial x_2} - \frac{\partial V_{12}}{\partial x_3} & \frac{\partial V_{23}}{\partial x_2} - \frac{\partial V_{22}}{\partial x_3} & \frac{\partial V_{33}}{\partial x_2} - \frac{\partial V_{32}}{\partial x_3} \\ \frac{\partial V_{11}}{\partial x_3} - \frac{\partial V_{13}}{\partial x_1} & \frac{\partial V_{21}}{\partial x_3} - \frac{\partial V_{23}}{\partial x_1} & \frac{\partial V_{31}}{\partial x_3} - \frac{\partial V_{33}}{\partial x_1} \\ \frac{\partial V_{12}}{\partial x_1} - \frac{\partial V_{11}}{\partial x_2} & \frac{\partial V_{22}}{\partial x_1} - \frac{\partial V_{21}}{\partial x_2} & \frac{\partial V_{32}}{\partial x_1} - \frac{\partial V_{31}}{\partial x_2} \end{bmatrix} \quad \text{(E.7)}$$

Substituting the defined components of $\boldsymbol{V}$ (Eq. (E.6)) in Eq. (E.7), gives

$$Q_{km} = \begin{bmatrix} \frac{\partial c_1}{\partial x_2} - \frac{\partial b_1}{\partial x_3} & \frac{\partial c_2}{\partial x_2} - \frac{\partial b_2}{\partial x_3} & \frac{\partial c_3}{\partial x_2} - \frac{\partial b_3}{\partial x_3} \\ \frac{\partial a_1}{\partial x_3} - \frac{\partial c_1}{\partial x_1} & \frac{\partial a_2}{\partial x_3} - \frac{\partial c_2}{\partial x_1} & \frac{\partial a_3}{\partial x_3} - \frac{\partial c_3}{\partial x_1} \\ \frac{\partial b_1}{\partial x_1} - \frac{\partial a_1}{\partial x_2} & \frac{\partial b_2}{\partial x_1} - \frac{\partial a_2}{\partial x_2} & \frac{\partial b_3}{\partial x_1} - \frac{\partial a_3}{\partial x_2} \end{bmatrix} \tag{E.8}$$

Likewise, the precurl definition may be explicitly written as

$$R_{km} = (\nabla \times \boldsymbol{P})_{km} = \in_{ijk} P_{jm,i} = \begin{bmatrix} \frac{\partial P_{31}}{\partial x_2} - \frac{\partial P_{21}}{\partial x_3} & \frac{\partial P_{32}}{\partial x_2} - \frac{\partial P_{22}}{\partial x_3} & \frac{\partial P_{33}}{\partial x_2} - \frac{\partial P_{23}}{\partial x_3} \\ \frac{\partial P_{11}}{\partial x_3} - \frac{\partial P_{31}}{\partial x_1} & \frac{\partial P_{12}}{\partial x_3} - \frac{\partial P_{32}}{\partial x_1} & \frac{\partial P_{13}}{\partial x_3} - \frac{\partial P_{33}}{\partial x_1} \\ \frac{\partial P_{21}}{\partial x_1} - \frac{\partial P_{11}}{\partial x_2} & \frac{\partial P_{22}}{\partial x_1} - \frac{\partial P_{12}}{\partial x_2} & \frac{\partial P_{23}}{\partial x_1} - \frac{\partial P_{13}}{\partial x_2} \end{bmatrix} \tag{E.9}$$

By substituting the components of $\boldsymbol{P}$ from Eq. (E.5), R_{km} may be re-stated as

$$R_{km} = \begin{bmatrix} \frac{\partial c_1}{\partial x_2} - \frac{\partial b_1}{\partial x_3} & \frac{\partial c_2}{\partial x_2} - \frac{\partial b_2}{\partial x_3} & \frac{\partial c_3}{\partial x_2} - \frac{\partial b_3}{\partial x_3} \\ \frac{\partial a_1}{\partial x_3} - \frac{\partial c_1}{\partial x_1} & \frac{\partial a_2}{\partial x_3} - \frac{\partial c_2}{\partial x_1} & \frac{\partial a_3}{\partial x_3} - \frac{\partial c_3}{\partial x_1} \\ \frac{\partial b_1}{\partial x_1} - \frac{\partial a_1}{\partial x_2} & \frac{\partial b_2}{\partial x_1} - \frac{\partial a_2}{\partial x_2} & \frac{\partial b_3}{\partial x_1} - \frac{\partial a_3}{\partial x_2} \end{bmatrix} \tag{E.10}$$

Comparing Eq. (E.8) and Eq. (E.10), it is seen that $Q_{km} = R_{km}$, thus proving that precurl of $\boldsymbol{V}$ is equal to the curl of $\boldsymbol{P}$, provided $\boldsymbol{V} = \boldsymbol{P}^{\mathrm{T}}$.

Proof of curl3($\boldsymbol{V}$) = $-\left(\text{Postcurl }(\boldsymbol{V})\right)^{\text{T}}$

$$S_{km} = (\boldsymbol{V} \times \nabla)_{km} = -\in_{ijm} V_{kj,i} = \begin{bmatrix} \frac{\partial V_{12}}{\partial x_3} - \frac{\partial V_{13}}{\partial x_2} & \frac{\partial V_{13}}{\partial x_1} - \frac{\partial V_{11}}{\partial x_3} & \frac{\partial V_{11}}{\partial x_2} - \frac{\partial V_{12}}{\partial x_1} \\ \frac{\partial V_{22}}{\partial x_3} - \frac{\partial V_{23}}{\partial x_2} & \frac{\partial V_{23}}{\partial x_1} - \frac{\partial V_{21}}{\partial x_3} & \frac{\partial V_{21}}{\partial x_2} - \frac{\partial V_{22}}{\partial x_1} \\ \frac{\partial V_{32}}{\partial x_3} - \frac{\partial V_{33}}{\partial x_2} & \frac{\partial V_{33}}{\partial x_1} - \frac{\partial V_{31}}{\partial x_3} & \frac{\partial V_{31}}{\partial x_2} - \frac{\partial V_{32}}{\partial x_1} \end{bmatrix} \quad \text{(E.11)}$$

Substituting the components $\boldsymbol{V}$ of as per Eq. (E.6),

$$S_{km} = \begin{bmatrix} \frac{\partial b_1}{\partial x_3} - \frac{\partial c_1}{\partial x_2} & \frac{\partial c_1}{\partial x_1} - \frac{\partial a_1}{\partial x_3} & \frac{\partial a_1}{\partial x_2} - \frac{\partial b_1}{\partial x_1} \\ \frac{\partial b_2}{\partial x_3} - \frac{\partial c_2}{\partial x_2} & \frac{\partial c_2}{\partial x_1} - \frac{\partial a_2}{\partial x_3} & \frac{\partial a_2}{\partial x_2} - \frac{\partial b_2}{\partial x_1} \\ \frac{\partial b_3}{\partial x_3} - \frac{\partial c_3}{\partial x_2} & \frac{\partial c_3}{\partial x_1} - \frac{\partial a_3}{\partial x_3} & \frac{\partial a_3}{\partial x_2} - \frac{\partial b_3}{\partial x_1} \end{bmatrix} \quad \text{(E.12)}$$

From Eq. (E.8), $-(Q_{km})^T$ is

$$-(Q_{km})^T = \begin{bmatrix} \frac{\partial b_1}{\partial x_3} - \frac{\partial c_1}{\partial x_2} & \frac{\partial c_1}{\partial x_1} - \frac{\partial a_1}{\partial x_3} & \frac{\partial a_1}{\partial x_2} - \frac{\partial b_1}{\partial x_1} \\ \frac{\partial b_2}{\partial x_3} - \frac{\partial c_2}{\partial x_2} & \frac{\partial c_2}{\partial x_1} - \frac{\partial a_2}{\partial x_3} & \frac{\partial a_2}{\partial x_2} - \frac{\partial b_2}{\partial x_1} \\ \frac{\partial b_3}{\partial x_3} - \frac{\partial c_3}{\partial x_2} & \frac{\partial c_3}{\partial x_1} - \frac{\partial a_3}{\partial x_3} & \frac{\partial a_3}{\partial x_2} - \frac{\partial b_3}{\partial x_1} \end{bmatrix} = S_{km} \quad \text{(E.13)}$$

Stokes' theorem

When Stokes' theorem is applied to higher order tensors, a transpose sign is introduced unlike in the case of a vector. The proof provided by Cermelli and Gurtin [222] is explained here in brief. For all constant vectors $\boldsymbol{c}$ and a tensor field $\boldsymbol{T}$, the identity $(\text{curl}\,\boldsymbol{T}).\boldsymbol{c} = \text{curl}(\boldsymbol{T}^T.\boldsymbol{c})$ holds. Now considering a smooth vector field $\boldsymbol{f}$, the Stokes' theorem applies as

$$\oint_C \boldsymbol{f}.\mathrm{d}\boldsymbol{x} = \iint_S \text{curl}(\boldsymbol{f}).\boldsymbol{n}\mathrm{d}S \tag{E.14}$$

If $\boldsymbol{f} = \boldsymbol{T}^T.\boldsymbol{c}$, then

$$\oint_C \boldsymbol{T}^T.\boldsymbol{c}\,.\mathrm{d}\boldsymbol{x} = \iint_S \text{curl}(\boldsymbol{T}^T.\boldsymbol{c}).\boldsymbol{n}\mathrm{d}S = \iint_S \text{curl}(\boldsymbol{T}).\boldsymbol{c}.\boldsymbol{n}\mathrm{d}S \tag{E.15}$$

Since $\boldsymbol{c}$ is a constant therefore, taking transpose on both sides of Eq. (E.15)

$$\oint_C \boldsymbol{T}\,.\mathrm{d}\boldsymbol{x} = \iint_S (\text{curl}\,\boldsymbol{T})^T.\boldsymbol{n}\mathrm{d}S \tag{E.16}$$

Values of UMAT parameters

Material Property	Value	Reference
Elastic modulus E	410 GPa	[88], [166], [269], [270]
Shear modulus G	164.4 GPa	[88], [166], [269], [270]
Poisson's ratio υ	0.28	[88], [166], [269], [270]
Burgers' vector magnitude b	2.7×10^{-10} m	[271]
Activation energy ΔF	3.4559×10^{-20} J	Chosen to reduce strain-rate sensitivity
Boltzmann constant k	1.381×10^{-23} J/K	[272]
Temperature T	293 K	Room temperature assumed similar to experimental conditions
Attempt frequency ν	1×10^{11} s^{-1}	[273]
Density of statistically stored dislocations, ρ_{SSD}	1×10^{10} m^{-2}	[272]
CRSS, τ_c	900 MPa	Fitted to experimental data
Density of mobile dislocations ρ_m	5×10^{10} m^{-2}	[217]
Probability of pinning Ψ	1.457×10^{-4}	Chosen and kept fixed

Table E.1 – Material properties for tungsten taken from literature and the CRSS from fitting to load-displacement experimental data obtained from nano-indentation.

F. Use of the effective modulus in indentation

Elastic properties of tungsten used in the model are given in Table F.1. The stiffness of tungsten (material for the sample block) is a significant fraction (~ 36%) of that of diamond (material for the indenter tip). However simulations using a rigid sharp indenter showed that the simulation results matched the experimental results very well when the results were scaled using the effective modulus, E_{eff} $\left(\frac{1}{E_{eff}} = \frac{1-\upsilon_{diamond}^2}{E_{diamond}} + \frac{1-\upsilon_{tungsten}^2}{E_{tungsten}}\right)$ [202] i.e.

$$P\ (exp.) = \frac{E_{eff\ (exp.)}}{E\ (FEA)}\ P(FEA) \qquad \text{(F. 1)}$$

$E_{diamond}$	$E_{tungsten}$	$\upsilon_{diamond}$	$\upsilon_{tungsten}$	E_{eff}	$R_{indenter}$
1143 GPa	410 GPa	0.0691	0.28	322.58 GPa	4.2 µm

Table F.1 – Values of Young's modulus and Poisson's ratio for diamond (indenter tip) and tungsten (indented sample) as obtained from literature [88], [166], [270]. With the assumption of isotropic, linear elastic solid, the Young's modulus and Poisson's ratio are related to the elastic constant as follows: $E = c_{11} - 2\left(\frac{c_{12}^2}{c_{11}+c_{12}}\right)$ and $\upsilon = c_{12}/(c_{11}+c_{12})$.

Thus, to avoid a full meshing and increase in simulation size, the indenter was designed as a discrete rigid wire frame. The results of indentation load reached, were scaled with an effective modulus E_{eff} to account for the fact that elastic displacements may occur in both the indenter tip and the specimen [202].

G. Burgers' vector & line direction for GND calculation

The combination of Burgers' vector and line direction used for GND density calculation.

Dislocation type	Density	Burgers' vector : $\boldsymbol{b}$	Slip Normal : $\boldsymbol{n}$	Line Direction : $\boldsymbol{l}$
Edge 1	ρ_1	[-111]	(110)	[-1 1 -2]
Edge 2	ρ_2	[1-11]	(110)	[-1 1 2]
Edge 3	ρ_3	[111]	(-101)	[1 -2 1]
Edge 4	ρ_4	[1-11]	(-101)	[-1 -2 -1]
Edge 5	ρ_5	[111]	(-110)	[-1 -1 2]
Edge 6	ρ_6	[11-1]	(-110)	[1 1 2]
Edge 7	ρ_7	[111]	(01-1)	[-2 1 1]
Edge 8	ρ_8	[-111]	(01-1)	[-2 -1 -1]
Edge 9	ρ_9	[1-11]	(011)	[-2 -1 1]
Edge 10	ρ_{10}	[11-1]	(011)	[2 -1 1]
Edge 11	ρ_{11}	[-111]	(101)	[1 2 -1]
Edge 12	ρ_{12}	[11-1]	(101)	[1 -2 -1]
Screw 1	ρ_{13}	[-111]	(110)	[-1 1 1]
Screw 2	ρ_{14}	[1-11]	(110)	[1 -1 1]
Screw 3	ρ_{15}	[111]	(-101)	[1 1 1]
Screw 4	ρ_{16}	[11-1]	(-110)	[1 1 -1]

Table G.1 – Combination of Burgers' vector and line direction used for the calculation of the GND.

H. Supplementary materials for Chapter 5.2

Computation of stress boundary conditions

Additional boundary conditions, $\sigma_{xx}^{BC} = \sigma_{yy}^{BC}$ are applied to the helium-implanted layer to account for the restricted in-plane displacement to maintain geometrical continuity between the implanted layer and substrate. The ε_{zz}^{dev} component of the deviatoric lattice strain in the helium-implanted sample, as measured by the white-beam Laue diffraction, is ~ 550 × 10^{-6}. This value was obtained by averaging the measured ε_{zz}^{dev} over 1.5 μm of the helium-implanted layer. The total strain tensor, $\boldsymbol{\varepsilon}^{e}$, is related to the deviatoric component $\boldsymbol{\varepsilon}_{dev}^{e}$ as

$$\boldsymbol{\varepsilon}^{e} = \boldsymbol{\varepsilon}_{dev}^{e} + 1/3 \text{ Tr } (\boldsymbol{\varepsilon}^{e})\boldsymbol{I} \tag{H.1}$$

where $\boldsymbol{I}$ is the identity matrix. The ε_{xx} and ε_{yy} components of the total lattice strain tensor are expected to be zero, as deformation along X and Y directions is restricted in order to maintain geometrical continuity between the implanted layer and the substrate (Section 3.4). Thus, $\text{Tr } (\boldsymbol{\varepsilon}^{e}) = \varepsilon_{zz}$. Therefore, Eq. (H.1) can be re-written as

$$\varepsilon_{zz} = \varepsilon_{zz}^{dev} + 1/3\, \varepsilon_{zz} \tag{H.2}$$

$$\varepsilon_{zz}^{dev} = 2/3\, \varepsilon_{zz} \tag{H.3}$$

Using Eq. (H.3), $\varepsilon_{zz} = 825 \times 10^{-6}$. ε_{zz} can be related to ε_{vol}^{*} using Eq. (3.8). Using the computed ε_{vol}^{*}, boundary conditions are calculated as per Eq. (3.6) i.e. $\sigma_{xx}^{BC} = \frac{-E*\varepsilon_{vol}^{*}}{3(1-\upsilon)} = \sigma_{yy}^{BC}$ to be -260 MPa.

Values of UMAT parameters

Material Property	Value	Reference
Elastic modulus E	410 GPa	[88], [166], [269], [270]
Shear modulus G	164.4 GPa	[88], [166], [269], [270]
Poisson's ratio υ	0.28	[88], [166], [269], [270]
Burgers' vector magnitude b	2.7×10^{-10} m	[271]
Stress boundary conditions $\sigma_{xx}^{BC} = \sigma_{yy}^{BC}$	-260 MPa	See Section on Computation of stress boundary conditions on Page 202
τ_H^0	750 MPa	Section 5.2.3.6
Activation energy ΔF	3.4559×10^{-20} J	Chosen to reduce strain-rate sensitivity
Boltzmann constant k	1.381×10^{-23} J/K	[272]
Temperature T	298 K	Room temperature assumed similar to experimental conditions
Attempt frequency v	1×10^{11} s^{-1}	[273]
Density of statistically stored dislocations, ρ_{SSD}	1×10^{10} m^{-2}	See Section on Values for $\boldsymbol{\rho_{SSD}}$ and $\boldsymbol{\rho_m}$ on Page 204
Density of mobile dislocations ρ_m	3.5×10^{10} m^{-2}	See Section on Values for $\boldsymbol{\rho_{SSD}}$ and $\boldsymbol{\rho_m}$ on Page 204
Probability of pinning Ψ	0.657×10^{-2}	Value chosen and kept fixed
τ_c^0	360 MPa	Fitted to experimental data of unimplanted sample
γ	0.025	Fitted to experimental data of helium-implanted sample
C'	0.0065	Fitted to experimental data of unimplanted sample

Table H.1 – List of parameters used in the constitutive law in the CPFE formulation and their corresponding values.

Values for ρ_{SSD} and ρ_m

Laue diffraction measurements performed on nano-indented pure tungsten showed the presence of GND density on the order of ~ 10^{17} m^{-2}. This value agreed well with CPFE predictions of the indentation experiment (Section 5.1.5.3). The SSD densities assumed here, ρ_{SSD} and ρ_m, for the CPFE calculations were taken to be much smaller than the GND density estimate, on the order of 10^{10} m^{-2}.

CPFE vs Continuum-mode FEM

The CPFE predicted surface pile-up around the nano-indent in the helium-implanted material agrees very well with the AFM measurements quantitatively and in terms of pile-up patterns (Figure 5.2.3 in main text). CPFE uniquely allows this prediction of the deformation pattern by accounting for crystallographic slip. A continuum plasticity simulation, performed on the same model, is unable to reproduce the orientation dependence of pile-up as shown in Figure H.1.

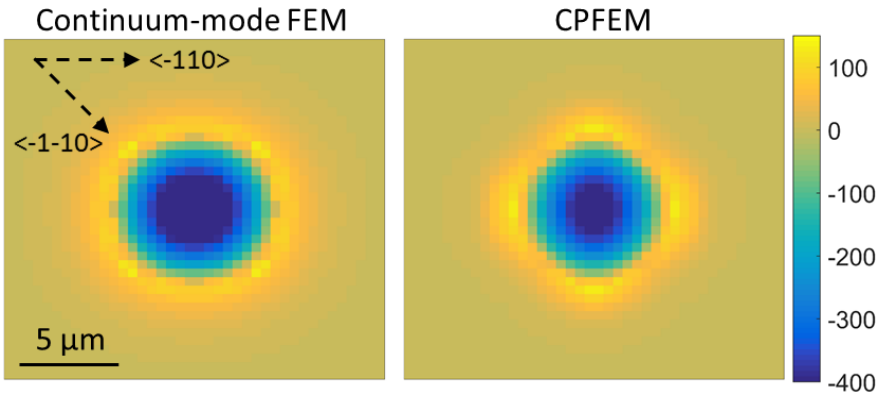


Figure H.1 – Surface pile-up around nano-indents in 001-oriented helium-implanted tungsten single crystal as predicted by continuum-based simulation (left, which does not account for crystal orientation) and by CPFE (right).

Line plots from CPFE and Laue strain measurements

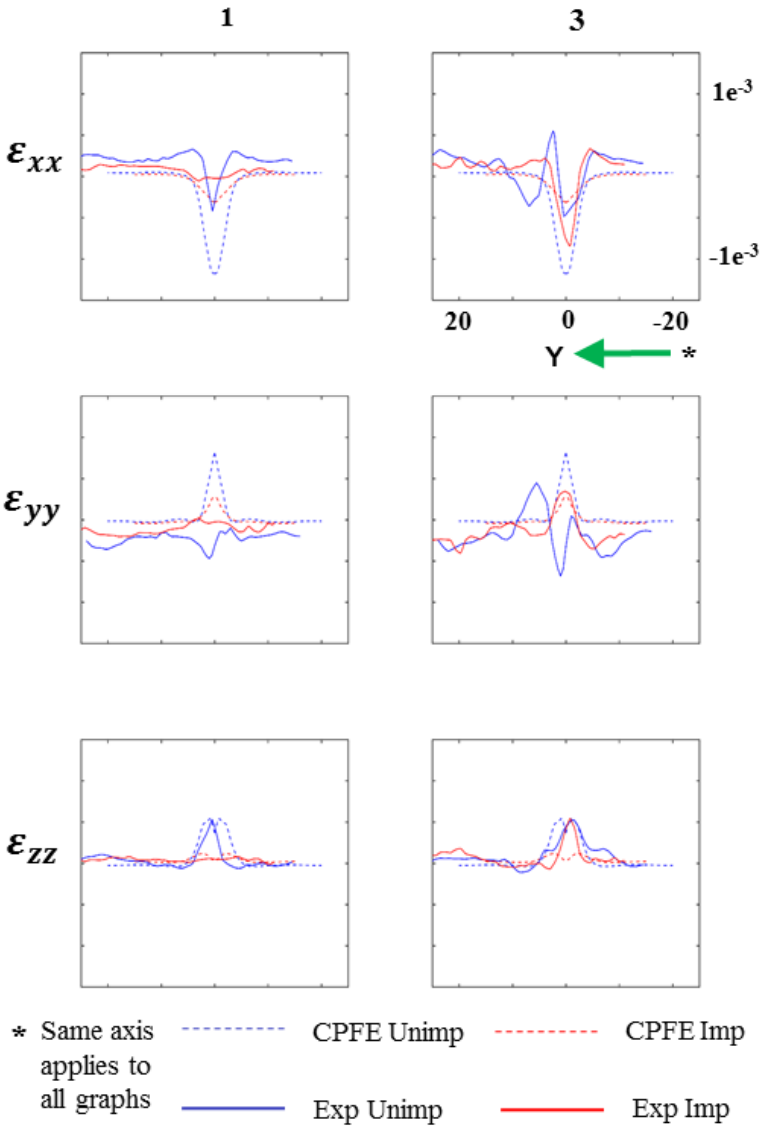


Figure H.2 – Line plots corresponding to the contour plots in Figure 5.2.6 (c) and (d). Direct lattice strains are plotted along a horizontal line 4.5 μm below the indent (shown by dotted white lines in Figure 5.2.6 (a) and (b) in main text). Slices 1 and 3 correspond to YZ sections drawn 5 μm away from the indent centre, on either side, along the X-axis.

I. Supplementary materials for Chapter 5.3

SEM micrographs of nano-indents

Figure I.1 and Figure I.2 show SEM micrographs of the spherical indents made in <001>, <011> and <111> grains in the unimplanted and helium-implanted sample respectively. Four indents were made for each orientation in each sample (with 50 µm spacing between indents for indents in the same grain). SEM micrographs of the indent topography show consistent results across each orientation and implantation condition.

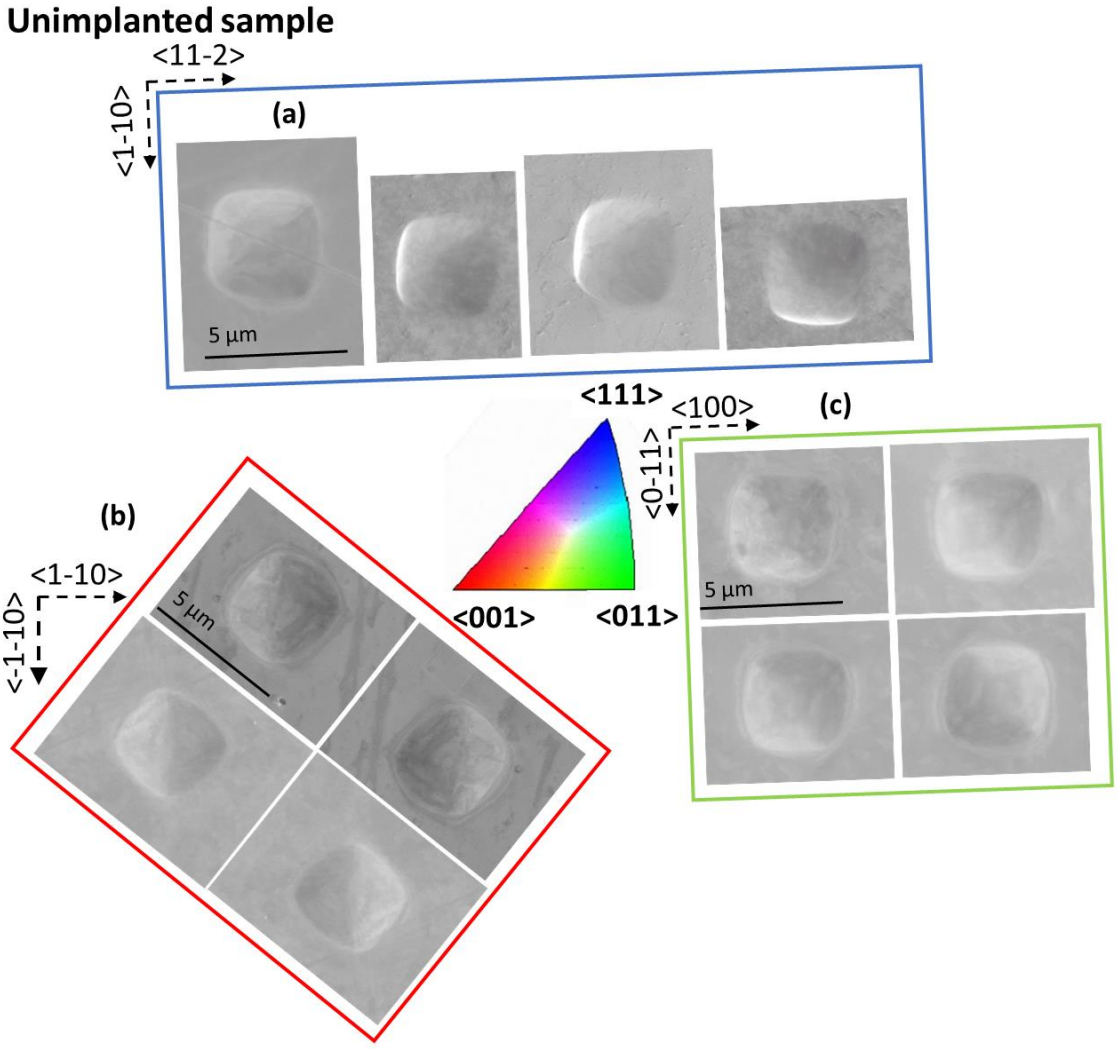


Figure I.1 - SEM micrographs of four indents in (a) <001>, (b) <011> and (c) <111> grains in the unimplanted sample; The SEM micrographs have been rotated to match the in-plane crystal orientation as indicated by dotted black labelled arrows.

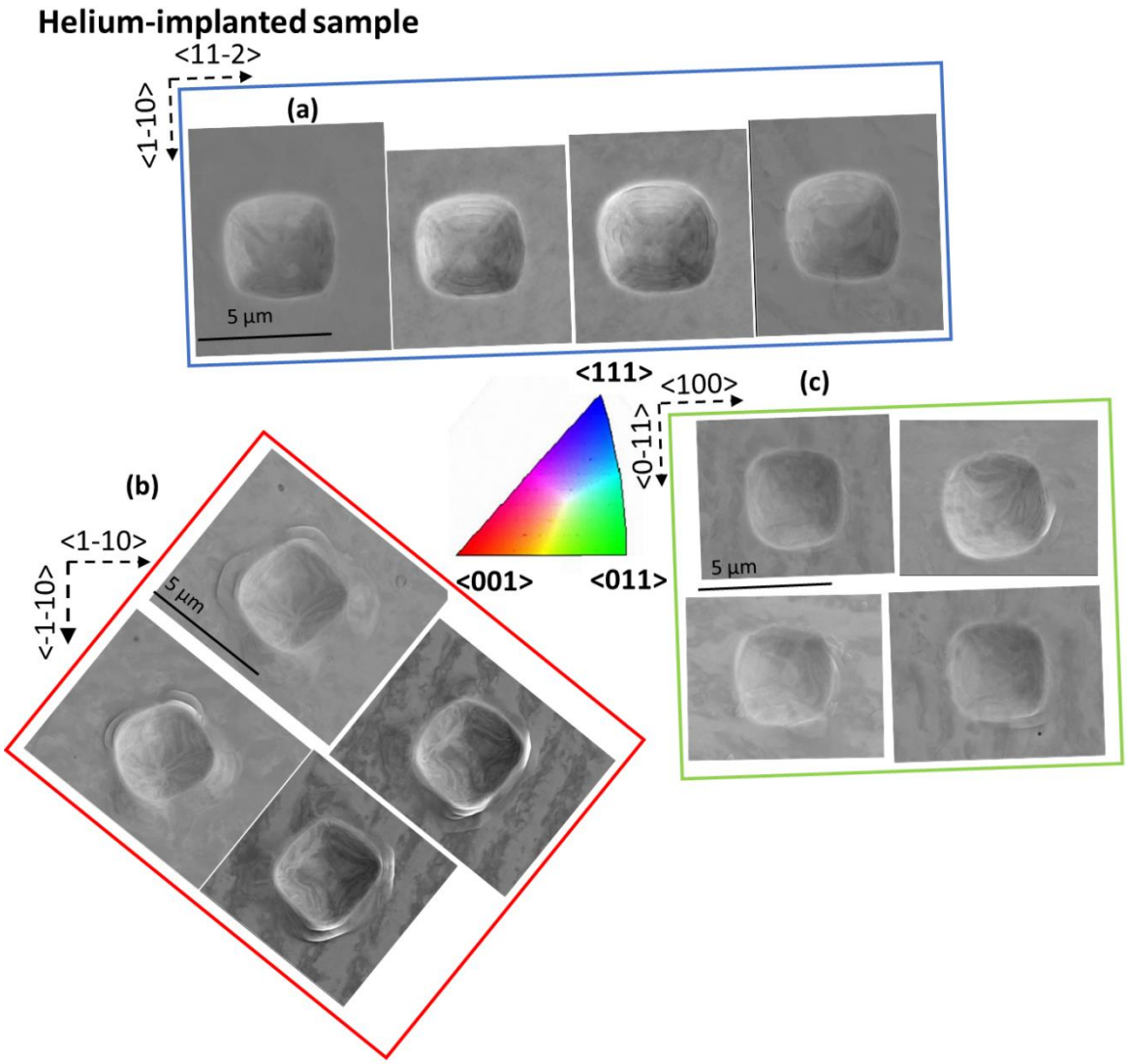


Figure I.2 – SEM micrographs of four indents in (a) <001>, (b) <011> and (c) <111> grains in the helium-implanted sample; The SEM micrographs have been rotated to match the in-plane crystal orientation as indicated by dotted black labelled arrows.

CPFE mesh

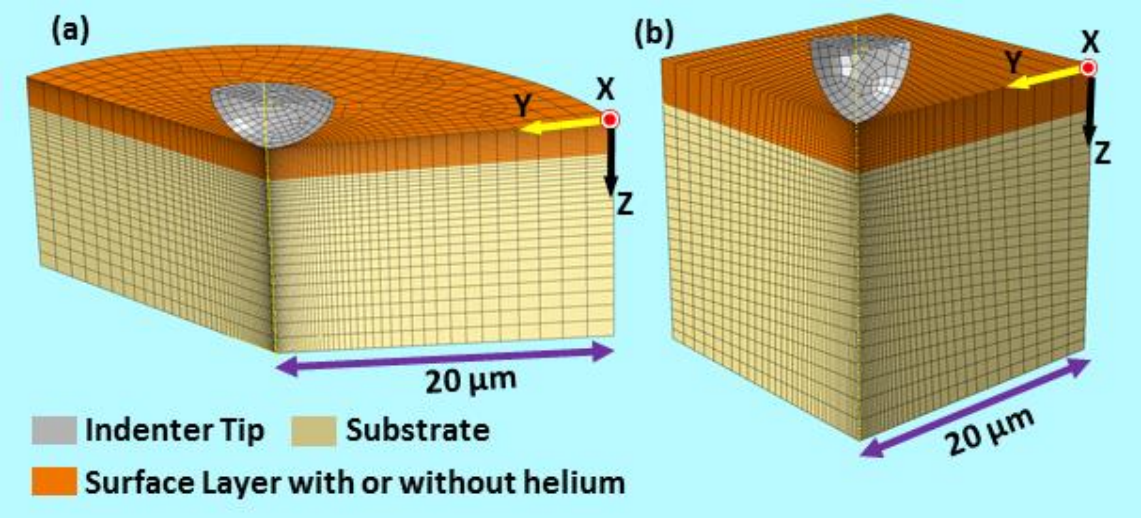


Figure I.3 – Rendering of the finite element mesh used for 3D crystal plasticity simulations of the tungsten sample indented by a 4.2 µm radius spherical indenter (a) one-third model for the <111> orientation and (b) quarter model for the <001> and <011> orientations. The X, Y, Z coordinate frame used throughout this work is superimposed.

References

[1] U.S. Energy Information Administration, *International Energy Outlook 2016*, vol. 0484(2016), no. May 2016. 2016.

[2] https://www.euro-fusion.org/jet/jets-main-features/, "EUROFusion - Jet's main features," *Webpage*, 2019. .

[3] https://www.iter.org/proj/inafewlines, "What will ITER do?," *Webpage*, 2019. .

[4] H. Bolt, a. Brendel, D. Levchuk, H. Greuner, and H. Maier, "Materials for plasma facing components of fusion reactors," *Energy Mater. Mater. Sci. Eng. Energy Syst.*, vol. 1, pp. 121–126, 2006.

[5] https://www.iter.org/sci/whatisfusion, "What is Fusion?," *Webpage*, 2019. .

[6] M. Rieth *et al.*, "Recent progress in research on tungsten materials for nuclear fusion applications in Europe," *J. Nucl. Mater.*, vol. 432, no. 1, pp. 482–500, 2013.

[7] X. Yi, M. L. Jenkins, M. Briceno, S. G. Roberts, Z. Zhou, and M. A. Kirk, "*In situ* study of self-ion irradiation damage in W and W–5Re at 500 °C," *Philos. Mag.*, vol. 93, no. 14, pp. 1715–1738, May 2013.

[8] M. R. Gilbert, S. L. Dudarev, S. Zheng, L. W. Packer, and J. C. Sublet, "An integrated model for materials in a fusion power plant: Transmutation, gas production, and helium embrittlement under neutron irradiation," *Nucl. Fusion*, vol. 52, no. 8, p. 83019, Aug. 2012.

[9] M. R. Gilbert and J.-C. Sublet, "Neutron-induced transmutation effects in W and W-alloys in a fusion environment," *Nucl. Fusion*, vol. 51, no. 4, p. 43005, Apr. 2011.

[10] Y. Zayachuk, M. H. J. 'T Hoen, P. A. Zeijlmans Van Emmichoven, D. Terentyev, I. Uytdenhouwen, and G. Van Oost, "Surface modification of tungsten and tungsten-tantalum alloys exposed to high-flux deuterium plasma and its impact on deuterium retention," *Nucl. Fusion*, vol. 53, no. 1, pp. 13013–7, 2013.

[11] S. Sharafat, A. Takahashi, K. Nagasawa, and N. Ghoniem, "A description of stress driven bubble growth of helium implanted tungsten," *J. Nucl. Mater.*, vol. 389, no. 2, pp. 203–212, 2009.

[12] I. de Broglie, C. E. E. Beck, W. Liu, and F. Hofmann, "Temperature dependence of helium-implantation-induced lattice swelling in polycrystalline tungsten: X-ray micro-diffraction and Eigenstrain modelling," *Scr. Mater.*, vol. 107, pp. 96–99, 2015.

[13] E. T. Cheng, "Assessment of low activation materials," *[Proceedings] 14th IEEE/NPSS Symp. Fusion Eng.*, pp. 621–625, 1991.

[14] M. Ekman, K. Persson, and G. Grimvall, "Phase diagram and lattice instability in tungsten ± rhenium alloys," *J. Nucl. Mater.*, vol. 278, pp. 276–279, 2000.

[15] N. Wei, T. Jia, X. Zhang, T. Liu, Z. Zeng, and X. Yang, "First-principles study of the phase

stability and the mechanical properties of W-Ta and W-Re alloys," *AIP Adv.*, vol. 4, no. 5, p. 57103, May 2014.

[16] P. Gumbsch, "Controlling Factors for the Brittle-to-Ductile Transition in Tungsten Single Crystals," *Science (80-.).*, vol. 282, no. 5392, pp. 1293–1295, Nov. 1998.

[17] S. J. Zinkle and N. M. Ghoniem, "Operating temperature windows for fusion reactor structural materials," *Fusion Eng. Des.*, vol. 51–52, no. 2000, pp. 55–71, 2000.

[18] L. Singheiser, T. Hirai, J. Linke, G. Pintsuk, and M. Rödig, "Plasma-facing materials for thermo-nuclear fusion devices," *Trans. Indian Inst. Met.*, vol. 62, no. 2, pp. 123–128, 2009.

[19] J. Roth *et al.*, "Tritium inventory in ITER plasma-facing materials and tritium removal procedures," *Plasma Phys. Control. Fusion*, vol. 50, no. 10, p. 103001, Oct. 2008.

[20] A. R. Raffray, L. El-Guebaly, G. Federici, D. Haynes, F. Najmabadi, and D. Petti, "Dry-Wall Survival under IFE Conditions," *Fusion Sci. Technol.*, vol. 46, no. 3, pp. 417–437, 2017.

[21] S. Pestchanyi, V. Safronov, and I. Landman, "Estimation of carbon fibre composites as ITER divertor armour," *J. Nucl. Mater.*, vol. 329–333, no. 1–3 PART A, pp. 697–701, 2004.

[22] "Tungsten uses," *International Tungsten Industry Association.*, 2011. .

[23] A. Giannattasio and S. G. Roberts, "Strain-rate dependence of the brittle-to-ductile transition temperature in tungsten," *Philos. Mag.*, vol. 87, no. 17, pp. 2589–2598, 2007.

[24] Tran-Huu-Loi, J. P. Morniroli, M. Gantois, and M. Lahaye, "Brittle fracture of polycrystalline tungsten," *J. Mater. Sci.*, vol. 20, no. 1, pp. 199–206, 1985.

[25] W. T. Sanders, "Peierls Stress for an Idealized Crystal Model," *Phys. Rev.*, vol. 128, no. 4, pp. 1540–1549, Nov. 1962.

[26] R. W. Hertzberg, *Deformation and Fracture Mechanics of Engineering Materials*, 4th ed. 1976.

[27] Caillard.D and J. . Martin, *Thermally Activated Mechanisms in Crystal Plasticity*, 1st ed., vol. 8. 2003.

[28] P. A. Gordon, T. Neeraj, Y. Li, and J. Li, "Screw dislocation mobility in BCC metals: the role of the compact core on double-kink nucleation," *Model. Simul. Mater. Sci. Eng.*, vol. 18, no. 8, p. 85008, 2010.

[29] J. P. Hirth and J. Lothe, *Theory of dislocations*. 2016.

[30] R. . Margevicius, J. Riedle, and P. Gumbsch, "Fracture toughness of polycrystalline tungsten under mode I and mixed mode I/II loading," *Mater. Sci. Eng. A*, vol. 270, no. 2, pp. 197–209, 1999.

[31] A. Giannattasio, Z. Yao, E. Tarleton, and S. G. Roberts, "Brittle–ductile transitions in polycrystalline tungsten," *Philos. Mag.*, vol. 90, no. 30, pp. 3947–3959, 2010.

[32] L. Romaner, C. Ambrosch-Draxl, and R. Pippan, "Effect of rhenium on the dislocation core

structure in tungsten," *Phys. Rev. Lett.*, vol. 104, no. 19, 2010.

[33] C.-H. Huang, M. R. Gilbert, and J. Marian, "Simulating irradiation hardening in tungsten under fast neutron irradiation including Re production by transmutation," *J. Nucl. Mater.*, vol. 499, pp. 204–215, 2018.

[34] Y. Zheng *et al.*, "Investigation of Radiation Damage in Stainless steel, Tungsten and Tantalum by Heavy Ion Irradiations," *Nucl. Phys. A*, vol. 834, no. 1–4, p. 761c–763c, 2010.

[35] C. H. Huang, L. Gharaee, Y. Zhao, P. Erhart, and J. Marian, "Mechanism of nucleation and incipient growth of Re clusters in irradiated W-Re alloys from kinetic Monte Carlo simulations," *Phys. Rev. B*, vol. 96, no. 9, pp. 1–18, 2017.

[36] M. Rieth and A. Hoffmann, "Influence of microstructure and notch fabrication on impact bending properties of tungsten materials," *Int. J. Refract. Met. Hard Mater.*, vol. 28, no. 6, pp. 679–686, Nov. 2010.

[37] J. Du, T. Höschen, M. Rasinski, and J.-H. You, "Shear debonding behavior of a carbon-coated interface in a tungsten fiber-reinforced tungsten matrix composite," *J. Nucl. Mater.*, vol. 417, no. 1, pp. 472–476, 2011.

[38] G. He *et al.*, "Preparation of tungsten fiber reinforced-tungsten/copper composite for plasma facing component," *J. Nucl. Mater.*, vol. 455, no. 1, pp. 225–228, 2014.

[39] L. Veleva, "Contribution to the production and characterisation of W-Y, W-Y2O3 and W-TiC materials for fusion reactors," 2011.

[40] J. Fan, Y. Han, P. Li, Z. Sun, and Q. Zhou, "Micro/nano composited tungsten material and its high thermal loading behavior," *J. Nucl*, vol. 455, no. 1–3, pp. 717–723, 2014.

[41] J. Knaster, A. Moeslang, and T. Muroga, "Materials research for fusion," *Nature Physics*, vol. 12, no. 5. pp. 424–434, 2016.

[42] F. Hofmann *et al.*, "Lattice swelling and modulus change in a helium-implanted tungsten alloy: X-ray micro-diffraction, surface acoustic wave measurements, and multiscale modelling," *Acta Mater.*, vol. 89, pp. 352–363, 2015.

[43] C. D. Hardie, C. A. Williams, S. Xu, and S. G. Roberts, "Effects of irradiation temperature and dose rate on the mechanical properties of self-ion implanted Fe and Fe-Cr alloys," *J. Nucl. Mater.*, vol. 439, no. 1–3, pp. 33–40, 2013.

[44] J. W. Morris, "Chapter 4 : Defects in Crystals," *Mater. Sci.*, pp. 76–107, 2007.

[45] T. Troev, N. Nankov, and T. Yoshile, "Simulation of defects in fusion plasma first wall materials," *J. Phys. Conf. Ser.*, vol. 516, p. 12022, 2014.

[46] Ł. Ciupiński *et al.*, "TEM observations of radiation damage in tungsten irradiated by 20MeV W ions," *Nucl. Instruments Methods Phys. Res. Sect. B Beam Interact. with Mater. Atoms*, vol. 317, no. PART A, pp. 159–164, Dec. 2013.

[47] http://ec.europa.eu/research/energy/euratom/index_en.cfm?pg=fusion&section=iter-future, "ITER Future and DEMO," *Webpage*, 2019. .

[48] P. Vladimirov and A. Möslang, “Comparison of material irradiation conditions for fusion, spallation, stripping and fission neutron sources,” *J. Nucl. Mater.*, vol. 329–333, no. 1–3 PART A, pp. 233–237, 2004.

[49] “International Fusion Materials Irradiation Facility.” [Online]. Available: http://www.ifmif.org/?page_id=28.

[50] A. I. Ryazanov and E. V. Semenov, “Radiation damage formation in fusion structural materials due to elastic and inelastic processes,” *J. Nucl. Mater.*, vol. 417, no. 1–3, pp. 1074–1077, 2011.

[51] N. Sekimura, “Primary knock-on atom energy dependence of cascade damage formation and interaction,” *Jounal Nucl. Mater.*, vol. 233–237, no. 96, pp. 1080–1084, 1996.

[52] A. I. Ryazanov, E. V. Metelkin, and E. V. Semenov, “Modeling of cascade and sub-cascade formation at high PKA energies in irradiated fusion structural materials,” *J. Nucl. Mater.*, vol. 386–388, no. C, pp. 132–134, 2009.

[53] A. De Backer, A. E. Sand, K. Nordlund, L. Luneville, D. Simeone, and S. L. Dudarev, “Subcascade formation and defect cluster size scaling in high-energy collision events in metals,” *EPL (Europhysics Lett.*, vol. 115, no. 2, p. 26001, Jul. 2016.

[54] M. E. Sawan, “Damage parameters of structural materials in fusion environment compared to fission reactor irradiation,” *Fusion Eng. Des.*, vol. 87, no. 5–6, pp. 551–555, Aug. 2012.

[55] R. G. Abernethy, “Predicting the performance of tungsten in a fusion environment: a literature review,” *Mater. Sci. Technol. (United Kingdom)*, vol. 33, no. 4, pp. 388–399, 2017.

[56] M. Shimada *et al.*, “Overview of the US?Japan collaborative investigation on hydrogen isotope retention in neutron-irradiated and ion-damaged tungsten,” *Fusion Eng. Des.*, vol. 87, no. 7–8, pp. 1166–1170, Aug. 2012.

[57] X. Yi, M. L. Jenkins, M. A. Kirk, Z. Zhou, and S. G. Roberts, “In-situ TEM studies of 150 keV W+ ion irradiated W and W-alloys: Damage production and microstructural evolution,” *Acta Mater.*, vol. 112, pp. 105–120, 2016.

[58] D. E. J. Armstrong, X. Yi, E. A. Marquis, and S. G. Roberts, “Hardening of self ion implanted tungsten and tungsten 5-wt% rhenium,” *J. Nucl. Mater.*, vol. 432, no. 1–3, pp. 428–436, Jan. 2013.

[59] J. Gibson, D. Armstrong, and S. Roberts, “The micro-mechanical properties of ion irradiated tungsten,” *Phys. Scr.*, vol. T159, 2014.

[60] D. E. J. Armstrong, A. J. Wilkinson, and S. G. Roberts, “Mechanical properties of ion-implanted tungsten–5 wt% tantalum,” *Phys. Scr.*, vol. T145, no. T145, p. 14076, Dec. 2011.

[61] F. A. Garner, H. L. Heinisch, R. L. Simons, and F. M. Mann, “Implications of neutron spectrum and flux differences on fission-fusion correlations at high neutron fluence,” *Radiat. Eff. Defects Solids*, vol. 113, no. 1–3, pp. 229–255, 1990.

[62] H. Iwakiri, K. Morishita, and N. Yoshida, “Effects of helium bombardment on the deuterium behavior in tungsten,” *J. Nucl. Mater.*, vol. 307–311, no. 1 SUPPL., pp. 135–138, 2002.

[63] C. S. Becquart and C. Domain, “Solute–point defect interactions in bcc systems: Focus on first principles modelling in W and RPV steels,” *Curr. Opin. Solid State Mater. Sci.*, vol. 16, no. 3, pp. 115–125, Jun. 2012.

[64] Y. Oya *et al.*, “Comparison of deuterium retention for ion-irradiated and neutron-irradiated tungsten,” *Phys. Scr.*, vol. T145, p. 14050, Dec. 2011.

[65] X. Fang *et al.*, “Hydrogen embrittlement of tungsten induced by deuterium plasma: Insights from nanoindentation tests,” *J. Mater. Res.*, vol. 33, no. 20, pp. 3530–3536, 2018.

[66] D. Terentyev, A. Bakaeva, T. Pardoen, A. Favache, and E. E. Zhurkin, “Surface hardening induced by high flux plasma in tungsten revealed by nano-indentation,” *J. Nucl. Mater.*, vol. 476, pp. 1–4, Aug. 2016.

[67] Y. Zayachuk, D. E. J. Armstrong, K. Bystrov, S. Van Boxel, T. Morgan, and S. G. Roberts, “Nanoindentation study of the combined effects of crystallography, heat treatment and exposure to high-flux deuterium plasma in tungsten,” *J. Nucl. Mater.*, vol. 486, pp. 183–190, 2017.

[68] N. Hashimoto *et al.*, “Microstructural analysis on helium retention of ion-irradiated and annealed tungsten foils,” *J. Nucl. Mater.*, vol. 347, no. 3, pp. 307–313, Dec. 2005.

[69] N. Yoshida, H. Iwakiri, K. Tokunaga, and T. Baba, “Impact of low energy helium irradiation on plasma facing metals,” in *Journal of Nuclear Materials*, 2005, vol. 337–339, no. 1–3 SPEC. ISS., pp. 946–950.

[70] L. Yang, H. Liu, and Xi. Zu, “First-Principles Study of the Migration of Helium in Tungsten,” *Int. J. Mod. Phys. B*, vol. 23, no. 8, pp. 2077–2082, 2009.

[71] J. H. Evans, “An interbubble fracture mechanism of blister formation on helium-irradiated metals,” *J. Nucl. Mater.*, vol. 68, no. 2, pp. 129–140, 1977.

[72] S. TAKAMURA, N. OHNO, D. NISHIJIMA, and S. KAJITA, “Formation of Nanostructured Tungsten with Arborescent Shape due to Helium Plasma Irradiation,” *Plasma Fusion Res.*, vol. 1, pp. 051–051, 2006.

[73] M. J. Baldwin and R. P. Doerner, “Helium induced nanoscopic morphology on tungsten under fusion relevant plasma conditions,” *Nucl. Fusion*, vol. 48, no. 3, 2008.

[74] F. Maury, M. Biget, P. Vajda, A. Lucasson, and P. Lucasson, “Frenkel pair creation and stage I recovery in W crystals irradiated near threshold,” *Radiat. Eff.*, vol. 38, no. 1–2, pp. 53–65, 1978.

[75] S. J. Zenobia, L. M. Garrison, and G. L. Kulcinski, “The response of polycrystalline tungsten to 30 keV helium ion implantation at normal incidence and high temperatures,” *J. Nucl. Mater.*, vol. 425, no. 1–3, pp. 83–92, 2012.

[76] J. S. K.-L. Gibson, S. G. Roberts, and D. E. J. Armstrong, “High temperature indentation of helium-implanted tungsten,” *Mater. Sci. Eng. A*, vol. 625, pp. 380–384, 2015.

[77] J. Boisse, C. Domain, and C. S. Becquart, “Modelling self trapping and trap mutation in tungsten using DFT and Molecular Dynamics with an empirical potential based on DFT,” *J. Nucl. Mater.*, vol. 455, no. 1–3, pp. 10–15, Dec. 2014.

[78] C. S. Becquart, M. F. Barthe, and A. De Backer, “Modelling radiation damage and He production in tungsten,” *Phys. Scr.*, vol. T145, no. T145, p. 14048, Dec. 2011.

[79] D. E. J. Armstrong, P. D. Edmondson, and S. G. Roberts, “Effects of sequential tungsten and helium ion implantation on nano-indentation hardness of tungsten,” *Appl. Phys. Lett.*, vol. 251901, no. 25, pp. 1–5, 2013.

[80] F. Hofmann, D. R. Mason, J. K. Eliason, A. A. Maznev, K. A. Nelson, and S. L. Dudarev, “Non-Contact Measurement of Thermal Diffusivity in Ion-Implanted Nuclear Materials,” *Sci. Rep.*, vol. 5, p. 16042, 2015.

[81] C. E. Beck *et al.*, “Correcting for contact area changes in nanoindentation using surface acoustic waves,” *Scr. Mater.*, vol. 128, pp. 83–86, 2017.

[82] Z. Zhou *et al.*, “Simulations of weak-beam diffraction contrast images of dislocation loops by the many-beam Howie – Basinski equations,” *Philos. Mag.*, vol. 86, no. 29–31, pp. 4851–4881, 2006.

[83] F. Hofmann *et al.*, “Lattice Swelling and Modulus Change in a Helium - -Implanted Tungsten Alloy : X- - ray Micro- - Diffraction , Surface Acoustic Wave Measurements , and Multiscale modelling,” no. 14, 2014.

[84] C. Oliver and M. Pharr, “An improved technique for determining hardness and elastic modulus using load and displacement sensing indentation experiments,” *Journal of Materials Research*, vol. 7, no. 11. pp. 1564–1583, Jun-1992.

[85] W. C. Oliver and G. M. Pharr, “Measurement of hardness and elastic modulus by instrumented indentation: Advances in understanding and refinements to methodology,” *J. Mater. Res.*, vol. 19, no. 1, pp. 3–20, 2004.

[86] S. Pathak and S. R. Kalidindi, “Spherical nanoindentation stress–strain curves,” *Mater. Sci. Eng. R*, vol. 91, pp. 1–36, 2015.

[87] N. A. Fleck and J. w. Hutchinson, “Strain Gradient Plasticity,” *Advances in Applied Mechanics*, vol. 33. pp. 295–361, 1997.

[88] F. H. Featherston and J. R. Neighbours, “Elastic constants of tantalum, tungsten, and molybdenum,” *Phys. Rev.*, vol. 130, no. 4, pp. 1324–1333, 1963.

[89] L. Martiradonna, “A photograph of crystal order,” *Nature*, vol. 11, no. 1, p. 1, 2014.

[90] W. H. Bragg and W. L. Bragg, “The Reflection of X-rays by Crystals,” *Proc. R. Soc. London*, vol. 88, no. 605, pp. 428–438, 1913.

[91] K. S. Chung and G. E. Ice, “Automated indexing for texture and strain measurement with broad-bandpass x-ray microbeams,” *J. Appl. Phys.*, vol. 86, no. 9, pp. 5249–5255, 1999.

[92] N. Tamura, “XMAS: a versatile tool for analyzing synchrotron X-ray microdiffraction data,” *Strain Dislocation Gradients from Diffr.*, no. January, pp. 125–155, 2014.

[93] J.-S. Micha, “LaueTools,” *https://sourceforge.net/projects/lauetools/?source=navbar*. [Online]. Available: https://sourceforge.net/projects/lauetools/?source=navbar.

[94] W. Liu, G. E. Ice, B. C. Larson, W. Yang, J. Z. Tischler, and J. D. Budai, "The three-dimensional X-ray crystal microscope: A new tool for materials characterization," *Metall. Mater. Trans. A*, vol. 35, no. 7, pp. 1963–1967, Jul. 2004.

[95] W. Yang, B. C. Larson, J. Z. Tischler, G. E. Ice, J. D. Budai, and W. Liu, "Differential-aperture X-ray structural microscopy: A submicron-resolution three-dimensional probe of local microstructure and strain," *Micron*, vol. 35, no. 6, pp. 431–439, 2004.

[96] Z. Zhou, M. L. Jenkins, S. L. Dudarev, A. P. Sutton, and M. A. Kirk, "Simulations of weak-beam diffraction contrast images of dislocation loops by the many-beam Howie-Basinski equations," *Philos. Mag.*, vol. 86, no. 29–31, pp. 4851–4881, 2006.

[97] F. Hofmann, S. Eve, J. Belnoue, J. S. Micha, and A. M. Korsunsky, "Analysis of strain error sources in micro-beam Laue diffraction," *Nucl. Instruments Methods Phys. Res. Sect. A Accel. Spectrometers, Detect. Assoc. Equip.*, vol. 660, no. 1, pp. 130–137, 2011.

[98] B. C. Larson, W. Yang, G. E. Ice, J. D. Budai, and J. Z. Tischler, "Three-dimensional X-ray structural microscopy with submicrometre resolution," *Nature*, vol. 415, no. 6874, pp. 887–890, 2002.

[99] W. Liu *et al.*, "Achromatic nested Kirkpatrick-Baez mirror optics for hard X-ray nanofocusing," *J. Synchrotron Radiat.*, vol. 18, no. 4, pp. 575–579, 2011.

[100] R. Barabash, G. E. Ice, B. C. Larson, G. M. Pharr, K. S. Chung, and W. Yang, "White microbeam diffraction from distorted crystals," *Appl. Phys. Lett.*, vol. 79, no. 6, pp. 749–751, 2001.

[101] R. I. Barabash *et al.*, "Quantitative analysis of dislocation arrangements induced by electromigration in a passivated interconnect," *J. Appl. Phys.*, vol. 93, no. 5701, 2003.

[102] R. I. Barabash and G. E. Ice, "Microdiffraction Analysis of Hierarchical Dislocation Organization," *Encycl. Mater. Technol. Updat. Elsevier, Oxford.*, pp. 1–18, 2007.

[103] A. J. Wilkinson, G. Meaden, and D. J. Dingley, "High-resolution elastic strain measurement from electron backscatter diffraction patterns: New levels of sensitivity," *Ultramicroscopy*, vol. 106, no. 4–5, pp. 307–313, 2006.

[104] A. J. Wilkinson, "Measurement of elastic strains and small lattice rotations using electron back scatter diffraction," *Ultramicroscopy*, vol. 62, no. 4, pp. 237–247, 1996.

[105] T. B. Britton and J. L. R. Hickey, "Understanding deformation with high angular resolution electron backscatter diffraction (HR-EBSD)," *IOP Conf. Ser. Mater. Sci. Eng.*, vol. 304, no. 1, p. 12003, 2018.

[106] W. Pantleon, "Resolving the geometrically necessary dislocation content by conventional electron backscattering diffraction," *Scr. Mater.*, vol. 58, no. 11, pp. 994–997, Jun. 2008.

[107] J. Jiang, T. Zhang, F. P. E. Dunne, and T. Ben Britton, "Deformation compatibility in a single crystalline Ni superalloy," *Proc. R. Soc. A Math. Phys. Eng. Sci.*, vol. 472, no. 2185, 2016.

[108] J. . Nye, "Some geometrical relations in dislocated crystals," *Acta Metall.*, vol. 1, no. 2, pp. 153–162, 1953.

[109] B. S. El-Dasher, B. L. Adams, and A. D. Rollett, “Viewpoint: Experimental recovery of geometrically necessary dislocation density in polycrystals,” *Scr. Mater.*, vol. 48, no. 2, pp. 141–145, Jan. 2003.

[110] D. P. Field, P. B. Trivedi, S. I. Wright, and M. Kumar, “Analysis of local orientation gradients in deformed single crystals,” *Ultramicroscopy*, vol. 103, no. 1, pp. 33–39, 2005.

[111] D. Wallis, L. N. Hansen, T. Ben Britton, and A. J. Wilkinson, “Dislocation Interactions in Olivine Revealed by HR-EBSD,” *J. Geophys. Res. Solid Earth*, vol. 122, no. 10, pp. 7659–7678, Oct. 2017.

[112] J. Jiang, T. Ben Britton, and A. J. Wilkinson, “The orientation and strain dependence of dislocation structure evolution in monotonically deformed polycrystalline copper,” *Int. J. Plast.*, vol. 69, pp. 102–117, 2015.

[113] D. Wallis, L. N. Hansen, T. Ben Britton, and A. J. Wilkinson, “Geometrically necessary dislocation densities in olivine obtained using high-angular resolution electron backscatter diffraction,” *Ultramicroscopy*, vol. 168, pp. 34–45, Sep. 2016.

[114] F. J. Humphreys, “Characterisation of fine-scale microstructures by electron backscatter diffraction (EBSD),” *Scr. Mater.*, vol. 51, no. 8, pp. 771–776, 2004.

[115] M. F. Ashby, “The deformation of plastically non-homogeneous materials,” *Philos. Mag.*, vol. 21, no. 170, pp. 399–424, 1970.

[116] J. Jiang, T. B. Britton, and A. J. Wilkinson, “Measurement of geometrically necessary dislocation density with high resolution electron backscatter diffraction: Effects of detector binning and step size,” *Ultramicroscopy*, vol. 125, pp. 1–9, 2013.

[117] A. K. Ghosh and R. Raj, “Grain size distribution effects in superplasticity,” *Acta Metall.*, vol. 29, no. 4, pp. 607–616, 1981.

[118] M. Zhou and F. P. E. Dunne, “Mechanisms-based constitutive equations for the superplastic behaviour of a titanium alloy,” *J. Strain Anal. Eng. Des.*, vol. 31, no. 3, pp. 187–196, 1996.

[119] A. C. F. Cocks, “Inelastic deformation of porous materials,” *J. Mech. Phys. Solids*, vol. 37, no. 6, pp. 693–715, 1989.

[120] P. P. Castañeda, “The effective mechanical properties of nonlinear isotropic composites,” *J. Mech. Phys. Solids*, vol. 39, no. 1, pp. 45–71, 1991.

[121] A. Manonukul, F. P. E. Dunne, and D. Knowles, “Physically-based model for creep in nickel-base superalloy C263 both above and below the gamma solvus,” *Acta Mater.*, vol. 50, no. 11, pp. 2917–2931, 2002.

[122] H. . Frost and F. Ashby, M, *Deformation-mechanism maps: the plasticity and creep of metals and ceramics*. 1982.

[123] G. Z. Voyiadjis and R. K. A. Al-Rub, “Thermodynamic based model for the evolution equation of the backstress in cyclic plasticity,” *Int. J. Plast.*, vol. 19, no. 12, pp. 2121–2147, 2003.

[124] F. Dunne and N. Petrinic, *Introduction to Computational Plasticity*. Oxford University

Press, 2004.

[125] W. Callister, *Materials Science and Engineering - An introduction*, 7th ed. .

[126] N. K. Chen and R. Maddin, "Slip planes and the energy of dislocations in a bodycentered cubic structure," *Acta Metall.*, vol. 2, no. 1, pp. 49–51, 1954.

[127] K. Srivastava, R. Gröger, D. Weygand, and P. Gumbsch, "Dislocation motion in tungsten: Atomistic input to discrete dislocation simulations," *Int. J. Plast.*, vol. 47, pp. 126–142, 2013.

[128] D. Peirce, R. J. Asaro, and A. Needleman, "An analysis of nonuniform and localized deformation in ductile single crystals," *Acta Metall.*, vol. 30, no. 6, pp. 1087–1119, 1982.

[129] T. O. Erinosho and F. P. E. Dunne, "Strain localization and failure in irradiated zircaloy with crystal plasticity," *Int. J. Plast.*, vol. 71, pp. 170–194, Aug. 2015.

[130] F. P. E. Dunne, D. Rugg, and A. Walker, "Lengthscale-dependent, elastically anisotropic, physically-based hcp crystal plasticity: Application to cold-dwell fatigue in Ti alloys," *Int. J. Plast.*, vol. 23, no. 6, pp. 1061–1083, 2007.

[131] N. a. Fleck, G. M. Muller, M. F. Ashby, and J. W. Hutchinson, "Strain gradient plasticity: Theory and experiment," *Acta Metall. Mater.*, vol. 42, no. 2, pp. 475–487, 1994.

[132] H. Gao, Y. Hang, W. D. Nix, and J. W. Hutchinson, "Mechanism-based strain gradient plasticity - I. Theory," *J. Mech. Phys. Solids*, vol. 47, no. 6, pp. 1239–1263, Apr. 1999.

[133] A. Arsenlis and D. . M. Parks, "Crystallographic aspects of geometrically-necessary and statistically-stored dislocation density," *Acta Mater.*, vol. 47, no. 5, pp. 1597–1611, 1999.

[134] E. P. Busso, F. T. Meissonnier, and N. P. O'Dowd, "Gradient-dependent deformation of two-phase single crystals," *J. Mech. Phys. Solids*, vol. 48, no. 11, pp. 2333–2361, 2000.

[135] M. E. Gurtin and L. Anand, "A theory of strain-gradient plasticity for isotropic, plastically irrotational materials. Part II: Finite deformations," *Int. J. Plast.*, vol. 21, no. 12, pp. 2297–2318, Jul. 2005.

[136] W. D. Nix and H. Gao, "Indentation size effects in crystalline materials: A law for strain gradient plasticity," *J. Mech. Phys. Solids*, vol. 46, no. 3, pp. 411–425, Mar. 1998.

[137] Z. Zhao, M. Ramesh, D. Raabe, A. M. Cuitiño, and R. Radovitzky, "Investigation of three-dimensional aspects of grain-scale plastic surface deformation of an aluminum oligocrystal," *Int. J. Plast.*, vol. 24, no. 12, pp. 2278–2297, Dec. 2008.

[138] H. M. Zbib, M. Hiratani, and M. Shehadeh, "Multiscale Discrete Dislocation Dynamics Plasticity," in *Continuum Scale Simulation of Engineering Materials*, no. 1956, Weinheim, FRG: Wiley-VCH Verlag GmbH & Co. KGaA, 2005, pp. 201–229.

[139] D. Li, H. Zbib, X. Sun, and M. Khaleel, "Predicting plastic flow and irradiation hardening of iron single crystal with mechanism-based continuum dislocation dynamics," *Int. J. Plast.*, vol. 52, pp. 3–17, 2014.

[140] H. Lim, J. D. Carroll, C. C. Battaile, T. E. Buchheit, B. L. Boyce, and C. R. Weinberger,

"Grain-scale experimental validation of crystal plasticity finite element simulations of tantalum oligocrystals," *Int. J. Plast.*, vol. 60, pp. 1–18, Sep. 2014.

[141] X. Song, F. Hofmann, and A. M. Korsunsky, "Dislocation-based plasticity model and micro-beam Laue diffraction analysis of polycrystalline Ni foil: A forward prediction," *Philos. Mag.*, vol. 90, no. 30, pp. 3999–4011, Oct. 2010.

[142] T. Zhang, J. Jiang, B. Britton, B. Shollock, and F. Dunne, "Crack nucleation using combined crystal plasticity modelling, high-resolution digital image correlation and high-resolution electron backscatter diffraction in a superalloy containing non-metallic inclusions under fatigue," *Proc. R. Soc. A Math. Phys. Eng. Sci.*, vol. 472, no. 2189, p. 20150792, May 2016.

[143] S. Das, W. Liu, R. Xu, and F. Hofmann, "Helium-implantation-induced lattice strains and defects in tungsten probed by X-ray micro-diffraction," *Mater. Des.*, vol. 160, pp. 1226–1237, 2018.

[144] S. Das, D. E. J. Armstrong, Y. Zayachuk, W. Liu, R. Xu, and F. Hofmann, "The effect of helium implantation on the deformation behaviour of tungsten: X-ray micro-diffraction and nanoindentation," *Scr. Mater.*, vol. 146, pp. 335–339, Mar. 2018.

[145] M.-F. Barthe *et al.*, "Positron annihilation characteristics in UO 2 : for lattice and vacancy defects induced by electron irradiation," *Phys. status solidi*, vol. 4, no. 10, pp. 3627–3632, Sep. 2007.

[146] J. Wiktor, X. Kerbiriou, G. Jomard, S. Esnouf, M. F. Barthe, and M. Bertolus, "Positron annihilation spectroscopy investigation of vacancy clusters in silicon carbide: Combining experiments and electronic structure calculations," *Phys. Rev. B - Condens. Matter Mater. Phys.*, vol. 89, no. 15, p. 155203, Apr. 2014.

[147] L. Sandoval, D. Perez, B. P. Uberuaga, and A. F. Voter, "Competing kinetics and he bubble morphology in W," *Phys. Rev. Lett.*, vol. 114, no. 10, 2015.

[148] R. A. Duncan *et al.*, "Increase in elastic anisotropy of single crystal tungsten upon He-ion implantation measured with laser-generated surface acoustic waves," *Appl. Phys. Lett.*, vol. 109, no. 15, 2016.

[149] F. Hofmann *et al.*, "Micro-beam Laue alignment of multi-reflection Bragg coherent diffraction imaging measurements," *J. Synchrotron Radiat.*, vol. 24, no. 5, pp. 1048–1055, Sep. 2017.

[150] S. Suresh, *Fatigue of Materials*, 2nd ed. Cambridge University Press, 1998.

[151] K. Nordlund *et al.*, "Improving atomic displacement and replacement calculations with physically realistic damage models," *Nat. Commun.*, vol. 9, no. 1, pp. 1–8, 2018.

[152] A. E. Sand, S. L. Dudarev, and K. Nordlund, "High-energy collision cascades in tungsten: Dislocation loops structure and clustering scaling laws," *EPL*, vol. 103, no. 4, p. 46003, Aug. 2013.

[153] C. S. Becquart and C. Domain, "An object Kinetic Monte Carlo Simulation of the dynamics of helium and point defects in tungsten," *J. Nucl. Mater.*, vol. 385, no. 2, pp. 223–227, 2009.

[154] C. E. Beck, S. G. Roberts, P. D. Edmondson, and D. E. J. Armstrong, "Effect of alloy

composition & helium ion-irradiation on the mechanical properties of tungsten, tungsten-tantalum & tungsten-rhenium for fusion power applications," in *Materials Research Society Symposium Proceedings*, 2013, vol. 1514, pp. 99–104.

[155] J. F. Ziegler and J. Biersack, "SRIM – The stopping and range of ions in matter (2010)," *Nucl. Inst. Methods Phys. Res. B*, vol. 268, pp. 1818–1823, 2010.

[156] "ASTM E521–96(2009) e1, Standard Practice for Neutron Radiation Damage Simulation by Charged-Particle Irradiation, ASTM International, West Conshohocken, PA, 2009, USA."

[157] W. Liu, P. Zschack, J. Tischler, G. Ice, and B. Larson, "X-ray laue diffraction microscopy in 3D at the advanced photon source," in *AIP Conference Proceedings*, 2010, vol. 1365, no. 108, pp. 108–111.

[158] F. Hofmann *et al.*, "X-ray micro-beam characterization of lattice rotations and distortions due to an individual dislocation.," *Nat. Commun.*, vol. 4, p. 2774, 2013.

[159] O. Robach, J. S. Micha, O. Ulrich, and P. Gergaud, "Full local elastic strain tensor from Laue microdiffraction: Simultaneous Laue pattern and spot energy measurement," *J. Appl. Crystallogr.*, vol. 44, no. 4, pp. 688–696, 2011.

[160] L. E. Levine, C. Okoro, and R. Xu, "Full elastic strain and stress tensor measurements from individual dislocation cells in copper through-Si vias," *IUCrJ*, vol. 2, no. 6, pp. 635–642, Nov. 2015.

[161] F. Hofmann, S. Keegan, and A. M. Korsunsky, "Diffraction post-processing of 3D dislocation dynamics simulations for direct comparison with micro-beam Laue experiments," *Mater. Lett.*, vol. 89, pp. 66–69, 2012.

[162] S. L. Dudarev and P. Ma, "Elastic fields, dipole tensors, and interaction between self-interstitial atom defects in bcc transition metals," *Phys. Rev. Mater.*, vol. 2, no. 3, p. 33602, 2018.

[163] T.-S. Jun and A. M. Korsunsky, "Evaluation of residual stresses and strains using the Eigenstrain Reconstruction Method," *Int. J. Solids Struct.*, vol. 47, no. 13, pp. 1678–1686, 2010.

[164] S. L. Dudarev, D. R. Mason, E. Tarleton, and A. E. Sand, "Multi-scale model for stresses , strains and swelling of reactor components under irradiation," *Nucl. Fusion*, vol. 58, no. 12, 2018.

[165] C. Liu *et al.*, "Fabrication of nested elliptical KB mirrors using profile coating for synchrotron radiation X-ray focusing," *Appl. Surf. Sci.*, vol. 258, no. 6, pp. 2182–2186, 2012.

[166] D. I. Bolef and J. De Klerk, "Elastic Constants of Single-Crystal Mo and W between 77° and 500°K," *J. Appl. Phys.*, vol. 33, no. 7, pp. 2311–2314, Jul. 1962.

[167] M. Gilbert, "Transmutation and He Production in W and W-alloys," 2010.

[168] A. Richard *et al.*, "Strains in light-ion-implanted polycrystals: Influence of grain orientation," *J. Appl. Crystallogr.*, vol. 45, no. 4, pp. 826–833, 2012.

[169] P. E. Lhuillier *et al.*, "Trapping and release of helium in tungsten," *J. Nucl. Mater.*, vol. 416, no. 1–2, pp. 13–17, 2011.

[170] T. Suzudo, M. Yamaguchi, and A. Hasegawa, "Stability and mobility of rhenium and osmium in tungsten: First principles study," *Model. Simul. Mater. Sci. Eng.*, vol. 22, no. 7, 2014.

[171] L. Gharaee, J. Marian, and P. Erhart, "The role of interstitial binding in radiation induced segregation in W-Re alloys," *J. Appl. Phys.*, vol. 120, no. 2, 2016.

[172] A. Khan *et al.*, "Effect of rhenium irradiations on the mechanical properties of tungsten for nuclear fusion applications," *J. Nucl. Mater.*, vol. 477, pp. 42–49, Aug. 2016.

[173] T. Suzudo and A. Hasegawa, "Suppression of radiation-induced point defects by rhenium and osmium interstitials in tungsten," *Sci. Rep.*, vol. 6, no. 1, p. 36738, Dec. 2016.

[174] A. Xu *et al.*, "Ion-irradiation induced clustering in W-Re-Ta, W-Re and W-Ta alloys: An atom probe tomography and nanoindentation study," *Acta Mater.*, vol. 124, pp. 71–78, 2017.

[175] M. H. J. T'Hoen *et al.*, "Saturation of deuterium retention in self-damaged tungsten exposed to high-flux plasmas," *Nucl. Fusion*, vol. 52, no. 2, 2012.

[176] M. Rasinski, A. Kreter, Y. Torikai, and C. Linsmeier, "The microstructure of tungsten exposed to D plasma with different impurities," *Nucl. Mater. Energy*, vol. 12, pp. 302–306, 2017.

[177] V. S. Voitsenya *et al.*, "Effect of sputtering on self-damaged recrystallized W mirror specimens," *J. Nucl. Mater.*, vol. 434, no. 1–3, pp. 375–381, 2013.

[178] A. Debelle, M. F. Barthe, and T. Sauvage, "First temperature stage evolution of irradiation-induced defects in tungsten studied by positron annihilation spectroscopy," *J. Nucl. Mater.*, vol. 376, no. 2, pp. 216–221, 2008.

[179] D. Nguyen-Manh, A. P. Horsfield, and S. L. Dudarev, "Self-interstitial atom defects in bcc transition metals: Group-specific trends," *Phys. Rev. B - Condens. Matter Mater. Phys.*, vol. 73, no. 2, 2006.

[180] L. Ma, L. Levine, R. Dixson, D. Smith, and D. Bahr, "Effect of the Spherical Indenter Tip Assumption on the Initial Plastic Yield Stress," *Nanoindentation Mater. Sci.*, vol. 22, no. 6, pp. 1656–1661, 2012.

[181] D. G. Flom and R. Komanduri, "Some indentation and sliding experiments on single crystal and polycrystalline materials," *Wear*, vol. 252, no. 5–6, pp. 401–429, Mar. 2002.

[182] Y. Wang, D. Raabe, C. Klüber, and F. Roters, "Orientation dependence of nanoindentation pile-up patterns and of nanoindentation microtextures in copper single crystals," *Acta Mater.*, vol. 52, no. 8, pp. 2229–2238, May 2004.

[183] D. Kiener, P. Hosemann, S. A. Maloy, and A. M. Minor, "In situ nanocompression testing of irradiated copper," *Nat. Mater.*, vol. 10, no. 8, pp. 608–613, 2011.

[184] S. R. Kalidindi and S. Pathak, "Determination of the effective zero-point and the extraction of spherical nanoindentation stress-strain curves," *Acta Mater.*, vol. 56, no. 14, pp. 3523–

3532, 2008.

[185] N. Hashimoto, T. S. Byun, K. Farrell, and S. J. Zinkle, "Deformation microstructure of neutron-irradiated pure polycrystalline metals," *J. Nucl. Mater.*, vol. 329–333, no. 1–3 PART B, pp. 947–952, 2004.

[186] P. M. M. Rice and S. J. J. Zinkle, "Temperature dependence of the radiation damage microstructure in V±4Cr±4Ti neutron irradiated to low dose," *J. Nucl. Mater.*, vol. 258–263, pp. 1414–1419, Oct. 1998.

[187] M. J. Makin and J. V. Sharp, "A Model of Lattice Hardening in Irradiated Copper Crystals with the External Characteristics of Source Hardening," *Phys. status solidi*, vol. 9, no. 1, pp. 109–118, 1965.

[188] S. Das, F. Hofmann, and E. Tarleton, "Consistent determination of geometrically necessary dislocation density from simulations and experiments," *Int. J. Plast.*, vol. 109, pp. 18–42, May 2018.

[189] H. S. Khan, Akhtar.S, *Continuum theory of Plasticity*. John Wiley & Sons, Inc., 1995.

[190] F. Roters, P. Eisenlohr, L. Hantcherli, D. D. Tjahjanto, T. R. Bieler, and D. Raabe, "Overview of constitutive laws, kinematics, homogenization and multiscale methods in crystal plasticity finite-element modeling: Theory, experiments, applications," *Acta Mater.*, vol. 58, no. 4, pp. 1152–1211, Feb. 2010.

[191] E. C. Aifantis, "On the Microstructural Origin of Certain Inelastic Models," *J. Eng. Mater. Technol.*, vol. 106, no. 4, pp. 326–330, Oct. 1984.

[192] D. Raabe, M. Sachtleber, H. Weiland, G. Scheele, and Z. Zhao, "Grain-scale micromechanics of polycrystal surfaces during plastic straining," *Acta Mater.*, vol. 51, no. 6, pp. 1539–1560, Apr. 2003.

[193] F. T. Meissonnier, E. P. Busso, and N. P. O'Dowd, "Finite element implementation of a generalised non-local rate-dependent crystallographic formulation for finite strains," in *International Journal of Plasticity*, 2001, vol. 17, no. 4, pp. 601–640.

[194] P. S. Bate and W. B. Hutchinson, "Grain boundary area and deformation," *Scr. Mater.*, vol. 52, no. 3, pp. 199–203, Feb. 2005.

[195] F. P. E. Dunne, R. Kiwanuka, and A. J. Wilkinson, "Crystal plasticity analysis of micro-deformation, lattice rotation and geometrically necessary dislocation density," *Proc. R. Soc. A Math. Phys. Eng. Sci.*, vol. 468, no. 2145, pp. 2509–2531, 2012.

[196] B. Chen, J. Jiang, and F. P. E. Dunne, "Is stored energy density the primary meso-scale mechanistic driver for fatigue crack nucleation?," *Int. J. Plast.*, vol. 101, pp. 213–229, Feb. 2017.

[197] C. F. O. Dahlberg, Y. Saito, M. S. Öztop, and J. W. Kysar, "Geometrically necessary dislocation density measurements associated with different angles of indentations," *Int. J. Plast.*, vol. 54, pp. 81–95, Mar. 2014.

[198] S. Balasubramanian and L. Anand, "Plasticity of initially textured hexagonal polycrystals at high homologous temperatures: Application to titanium," *Acta Mater.*, vol. 50, no. 1, pp.

133–148, Jan. 2002.

[199] R. J. Asaro and J. R. Rice, “Strain localization in ductile single crystals,” *J. Mech. Phys. Solids*, vol. 25, no. 5, pp. 309–338, 1977.

[200] S. R. Kalidindi, “Incorporation of deformation twinning in crystal plasticity models,” *J. Mech. Phys. Solids*, vol. 46, no. 2, pp. 267273–271290, Feb. 1998.

[201] T. J. Vogler and J. D. Clayton, “Heterogeneous deformation and spall of an extruded tungsten alloy: plate impact experiments and crystal plasticity modeling,” *J. Mech. Phys. Solids*, vol. 56, no. 2, pp. 297–335, Feb. 2008.

[202] M. Li, D. J. Morris, S. L. Jennerjohn, D. F. Bahr, and L. Levine, “Finite element analysis and experimental investigation of the Hertzian assumption on the characterization of initial plastic yield,” *J. Mater. Res.*, vol. 24, no. 3, pp. 1059–1068, 2009.

[203] J. H. Behrmann, “Crystal plasticity and superplasticity in quartzite; A natural example,” *Tectonophysics*, vol. 115, no. 1–2, pp. 101–129, May 1985.

[204] F. Weber, I. Schestakow, F. Roters, and D. Raabe, “Texture evolution during bending of a single crystal copper nanowire studied by EBSD and crystal plasticity finite element simulations,” *Adv. Eng. Mater.*, vol. 10, no. 8, pp. 737–741, Aug. 2008.

[205] D. Raabe, B. Sander, M. Friák, D. Ma, and J. Neugebauer, “Theory-guided bottom-up design of β-titanium alloys as biomaterials based on first principles calculations: Theory and experiments,” *Acta Mater.*, vol. 55, no. 13, pp. 4475–4487, Aug. 2007.

[206] D. J. Luscher, J. R. Mayeur, H. M. Mourad, A. Hunter, and M. A. Kenamond, “Coupling continuum dislocation transport with crystal plasticity for application to shock loading conditions,” *Int. J. Plast.*, vol. 76, pp. 111–129, Jan. 2016.

[207] J. R. Rice, “Inelastic constitutive relations for solids: An internal variables theory and its application to metal plasticity,” *J. Mech. Phys. Solids*, vol. 19, no. 6, pp. 433–455, 1971.

[208] N. A. Fleck and J. R. Willis, “A mathematical basis for strain-gradient plasticity theory. Part I: Scalar plastic multiplier,” *J. Mech. Phys. Solids*, vol. 57, no. 7, pp. 1045–1057, Jan. 2009.

[209] N. A. Fleck and J. R. Willis, “A mathematical basis for strain-gradient plasticity theory. Part II: Tensorial plastic multiplier,” *J. Mech. Phys. Solids*, vol. 57, no. 7, pp. 1045–1057, 2009.

[210] H. Lyu, A. Ruimi, and H. M. Zbib, “A dislocation-based model for deformation and size effect in multi-phase steels,” *Int. J. Plast.*, vol. 72, pp. 44–59, Sep. 2015.

[211] V. A. Lubarda, “On the recoverable and dissipative parts of higher order stresses in strain gradient plasticity,” *Int. J. Plast.*, vol. 78, pp. 26–43, Mar. 2016.

[212] D. Liu *et al.*, “Toward a further understanding of size effects in the torsion of thin metal wires: An experimental and theoretical assessment,” *Int. J. Plast.*, vol. 41, pp. 30–52, Feb. 2013.

[213] E. Martínez-Pañeda and C. F. Niordson, “On fracture in finite strain gradient plasticity,” *Int. J. Plast.*, vol. 80, pp. 154–167, May 2016.

[214] D. Liu and D. J. Dunstan, “Material length scale of strain gradient plasticity: A physical interpretation,” *Int. J. Plast.*, vol. 98, pp. 156–174, Nov. 2017.

[215] A. J. Wilkinson and D. Randman, “Determination of elastic strain fields and geometrically necessary dislocation distributions near nanoindents using electron back scatter diffraction,” *Philos. Mag.*, vol. 90, no. 9, pp. 1159–1177, Mar. 2010.

[216] J. W. Kysar, Y. Saito, M. S. Oztop, D. Lee, and W. T. Huh, “Experimental lower bounds on geometrically necessary dislocation density,” *Int. J. Plast.*, vol. 26, no. 8, pp. 1097–1123, Aug. 2010.

[217] M. E. Kartal, R. Kiwanuka, and F. P. E. Dunne, “Determination of sub-surface stresses at inclusions in single crystal superalloy using HR-EBSD, crystal plasticity and inverse eigenstrain analysis,” *Int. J. Solids Struct.*, vol. 67–68, pp. 27–39, Aug. 2015.

[218] T. J. Ruggles, D. T. Fullwood, and J. W. Kysar, “Resolving geometrically necessary dislocation density onto individual dislocation types using EBSD-based continuum dislocation microscopy,” *Int. J. Plast.*, vol. 76, pp. 231–243, Jan. 2016.

[219] Y. Guan, B. Chen, J. Zou, T. Ben Britton, J. Jiang, and F. P. E. Dunne, “Crystal plasticity modelling and HR-DIC measurement of slip activation and strain localization in single and oligo-crystal Ni alloys under fatigue,” *Int. J. Plast.*, vol. 88, pp. 70–88, Jan. 2017.

[220] R. I. Barabash, G. E. Ice, M. Kumar, J. Ilavsky, and J. Belak, “Polychromatic microdiffraction analysis of defect self-organization in shock deformed single crystals,” *Int. J. Plast.*, vol. 25, no. 11, pp. 2081–2093, 2009.

[221] R. W. Soutas-Little, *Elasticity*. 1999.

[222] P. Cermelli and M. E. Gurtin, “On the characterization of geometrically necessary dislocations in finite plasticity,” *J. Mech. Phys. Solids*, vol. 49, no. 7, pp. 1539–1568, 2001.

[223] E. Kroner, “Der fundamentale Zusammenhang zwischen Versetzungsdiehte und Spannungsfunktionen,” vol. 475, no. 142, 1955.

[224] M. Lazar and Y. P. Pellegrini, “Distributional and regularized radiation fields of non-uniformly moving straight dislocations, and elastodynamic Tamm problem,” *J. Mech. Phys. Solids*, vol. 96, pp. 632–659, 2016.

[225] E. H. Lee, “Elastic-Plastic Deformation at Finite Strains,” *J. Appl. Mech.*, vol. 36, no. 1, pp. 1–6, Mar. 1969.

[226] A. Acharya and J. L. Bassani, “Lattice incompatibility and a gradient theory of crystal plasticity,” *J. Mech. Phys. Solids*, vol. 48, no. 8, pp. 1565–1595, Aug. 2000.

[227] E. Demir, D. Raabe, N. Zaafarani, and S. Zaefferer, “Investigation of the indentation size effect through the measurement of the geometrically necessary dislocations beneath small indents of different depths using EBSD tomography,” *Acta Mater.*, vol. 57, no. 2, pp. 559–569, 2009.

[228] S. Sun, B. L. Adams, and W. E. King, “Observations of lattice curvature near the interface of a deformed aluminium bicrystal,” *Philos. Mag. A*, vol. 80, no. 1, pp. 9–25, Jan. 2000.

[229] G. G. Slabaugh, "Computing Euler angles from a rotation matrix," *http://www.gregslabaugh.net/publications/euler.pdf*, vol. 6, no. 2000, pp. 1–6, 1999.

[230] A. Irastorza-Landa, N. Grilli, and H. Van Swygenhoven, "Laue micro-diffraction and crystal plasticity finite element simulations to reveal a vein structure in fatigued Cu," *J. Mech. Phys. Solids*, vol. 104, pp. 157–171, Jul. 2017.

[231] C. Marichal, H. Van Swygenhoven, S. Van Petegem, and C. Borca, "{110} Slip with {112} slip traces in bcc Tungsten.," *Sci. Rep.*, vol. 3, no. 211, p. 2547, 2013.

[232] S. Das, H. Yu, E. Tarleton, and F. Hofmann, "Hardening and Strain Localisation in Helium-Ion-Implanted Tungsten," *arXiv Prepr. arXiv1901.00745*, Dec. 2018.

[233] Z. Zhou, M. L. Jenkins, S. L. Dudarev, A. P. Sutton, and M. A. Kirk, *Simulations of weak-beam diffraction contrast images of dislocation loops by the many-beam Howie-Basinski equations*, vol. 86, no. 29–31. 2006.

[234] P. M. Derlet, D. Nguyen-Manh, and S. L. Dudarev, "Multiscale modeling of crowdion and vacancy defects in body-centered-cubic transition metals," *Phys. Rev. B - Condens. Matter Mater. Phys.*, vol. 76, no. 5, 2007.

[235] A. J. Wilkinson and P. B. Hirsch, "Electron diffraction based techniques in scanning electron microscopy of bulk materials," *Micron*, vol. 28, no. 4, pp. 279–308, 1997.

[236] G. I. Taylor, "The Mechanism of Plastic Deformation of Crystals. Part I. Comparison with Observations," *Proc. R. Soc. A Math. Phys. Eng. Sci.*, vol. 145, no. 855, pp. 388–404, 1934.

[237] K. M. Davoudi and J. J. Vlassak, "Dislocation evolution during plastic deformation: Equations vs. discrete dislocation dynamics study," *J. Appl. Phys.*, vol. 123, no. 8, 2018.

[238] C. C. Fu and F. Willaime, "Ab initio study of helium in α-Fe: Dissolution, migration, and clustering with vacancies," *Phys. Rev. B - Condens. Matter Mater. Phys.*, vol. 72, no. 6, p. 64117, Aug. 2005.

[239] J. C. Slater, "Atomic radii in crystals," *J. Chem. Phys.*, vol. 41, no. 10, pp. 3199–3204, 1964.

[240] T. . Simes, S. . Mellor, and D. . Hills, "Research Note: A note on the influence of residual stress on measured hardness," *J. Strain Anal.*, vol. 19, no. 2, pp. 135–137, 1984.

[241] J. . Sharp, "Deformation of Neutron Irradiated Copper Alloys," *Acta Metall.*, vol. 22, p. 449, 1974.

[242] J. Kacher, G. Liu, and I. Robertson, "In situ and tomographic observations of defect free channel formation in ion irradiated stainless steels," *Micron*, vol. 43, no. 11, pp. 1099–1107, 2012.

[243] R. Tulluri and D. J. Morrison, "Effects of ion irradiation on fatigue of Fe-12Cr-20Mn stainless steel for fusion reactor applications," *J. Mater. Eng. Perform.*, vol. 6, no. 4, pp. 454–460, 1997.

[244] S. J. Zinkle and B. N. Singh, "Microstructure of neutron-irradiated iron before and after tensile deformation," *J. Nucl. Mater.*, vol. 351, no. 1, pp. 269–284, 2006.

[245] N. Hashimoto, T. S. Byun, K. Farrell, and S. J. Zinkle, “Deformation microstructure of neutron-irradiated pure polycrystalline vanadium,” *J. Nucl. Mater.*, vol. 336, no. 2, pp. 225–232, 2005.

[246] T. Byun and N. Hashimoto, “Strain Localization in Irradiated Materials,” *Nucl. Eng. Technol.*, vol. 38, no. 7, pp. 619–638, 2006.

[247] R. J. Wasilewski, “B.C.C. stacking fault energies,” *Scr. Metall.*, vol. 1, no. 1, pp. 45–47, 1967.

[248] J. A. Knapp, D. M. Follstaedt, J. C. Barbour, and S. M. Myers, “Finite-element modeling of nanoindentation for determining the mechanical properties of implanted layers and thin films,” *Nucl. Instruments Methods Phys. Res. Sect. B Beam Interact. with Mater. Atoms*, vol. 127–128, pp. 935–939, 1997.

[249] G. M. Pharr and W. C. Oliver, “Measurement of Thin Film Mechanical Properties Using Nanoindentation,” *MRS Bull.*, vol. 17, no. 7, pp. 28–33, Jul. 1992.

[250] W. D. Nix, “Elastic and plastic properties of thin films on substrates: nanoindentation techniques,” *Mater. Sci. Eng. A*, vol. 234–236, pp. 37–44, 1997.

[251] H. Ogiwara, A. Kohyama, H. Tanigawa, and H. Sakasegawa, “Irradiation-induced hardening mechanism of ion irradiated JLF-1 to high fluences,” *Fusion Eng. Des.*, vol. 81, no. 8–14, pp. 1091–1097, Feb. 2006.

[252] C. Heintze, C. Recknagel, F. Bergner, M. Hernández-Mayoral, and A. Kolitsch, “Ion-irradiation-induced damage of steels characterized by means of nanoindentation,” *Nucl. Instruments Methods Phys. Res. Sect. B Beam Interact. with Mater. Atoms*, vol. 267, no. 8, pp. 1505–1508, 2009.

[253] M. Ando *et al.*, “Evaluation of hardening behaviour of ion irradiated reduced activation ferritic/martensitic steels by an ultra-micro-indentation technique,” *J. Nucl. Mater.*, vol. 307–311, pp. 260–265, Dec. 2002.

[254] S. Das, H. Yu, E. Tarleton, and F. Hofmann, “Orientation-dependent indentation response of helium-implanted tungsten,” *Appl. Phys. Lett.*, vol. 114, no. 22, p. 221905, 2019.

[255] I. DeBroglie, C. E. Beck, W. Liu, and F. Hofmann, “Temperature Dependence of Helium--Implantation--Induced Lattice Swelling in Polycrystalline Tungsten: X--ray Micro--Diffraction and Eigenstrain Modelling,” *Scr. Mater.*, vol. 107, p. 4, 2015.

[256] P. Hosemann *et al.*, “Nanoindentation on ion irradiated steels,” *J. Nucl. Mater.*, vol. 389, no. 2, pp. 239–247, 2009.

[257] C. D. Hardie, S. G. Roberts, and A. J. Bushby, “Understanding the effects of ion irradiation using nanoindentation techniques,” *J. Nucl. Mater.*, vol. 462, pp. 391–401, 2015.

[258] Y. Gaillard, C. Tromas, and J. Woirgard, “Study of the dislocation structure involved in a nanoindentation test by atomic force microscopy and controlled chemical etching,” *Acta Mater.*, vol. 51, no. 4, pp. 1059–1065, 2003.

[259] D. F. Bahr, D. E. Kramer, and W. W. Gerberich, “Non-linear deformation mechanisms during nanoindentation,” *Acta Mater.*, vol. 46, no. 10, pp. 3605–3617, 1998.

[260] M. Hollatz, M. Bobeth, W. Pompe, and V. Marx, “Orientation dependent crack patterns in alumina films on NiAl single crystals due to spherical indentation,” *Acta Mater.*, vol. 44, no. 10, pp. 4149–4159, 1996.

[261] J. Li, K. J. Van Vliet, T. Zhu, S. Yip, and S. Suresh, “Atomistic mechanisms governing elastic limit and incipient plasticity in crystals,” *Nature*, vol. 418, p. 307, Jul. 2002.

[262] T. B. Britton, H. Liang, F. P. E. Dunne, and A. J. Wilkinson, “The effect of crystal orientation on the indentation response of commercially pure titanium: experiments and simulations,” *Proc. R. Soc. A Math. Phys. Eng. Sci.*, vol. 466, no. 2115, pp. 695–719, Mar. 2010.

[263] V. Kuksenko, S. Roberts, and E. Tarleton, “The hardness and modulus of polycrystalline beryllium from nano-indentation,” *Int. J. Plast.*, vol. 116, pp. 62–80, 2019.

[264] P. W. . Bruchey, W.J; Horwath, E.J.;Kingman, “Orientation dependence of deformation and penetration behavior of tungsten single-crystal rods,” *Tungsten tungsten Alloy.*, vol. 23, no. 23061891, pp. 121–128, 1991.

[265] A. J. Bushby, S. G. Roberts, and C. D. Hardie, “Nanoindentation investigation of ion-irradiated Fe-Cr alloys using spherical indenters,” *J. Mater. Res.*, vol. 27, no. 1, pp. 85–90, 2012.

[266] M. Victoria *et al.*, “The microstructure and associated tensile properties of irradiated fcc and bcc metals,” *J. Nucl. Mater.*, vol. 276, no. 1, pp. 114–122, 2000.

[267] Y. Dai and M. Victoria, “Defect Cluster Structure and Tensile Properties of Copper Single Crystals Irradiated With 600 MeV Protons,” *MRS Online Proc. Libr. Arch.*, vol. 439, p. 319, 1996.

[268] D. Kiener, K. Durst, M. Rester, and A. M. Minor, “Revealing deformation mechanisms with nanoindentation,” *JOM*, vol. 61, no. 3. pp. 14–23, 2009.

[269] R. A. Ayres *et al.*, “Elastic constants of tungsten−rhenium alloys from 77 to 298 °K,” *J. Appl. Phys.*, vol. 46, no. 4, pp. 1526–1530, Apr. 1975.

[270] C. A. Klein and G. F. Cardinale, “Young’s modulus and Poisson’s ratio of CVD diamond,” *Diam. Relat. Mater.*, vol. 2, no. 5–7, pp. 918–923, Apr. 1993.

[271] B. N. Dutta and B. Dayal, “Lattice Constants and Thermal Expansion of Palladium and Tungsten up to 878 C by X-Ray Method,” *Phys. status solidi*, vol. 3, no. 12, pp. 2253–2259, Jan. 1963.

[272] C. A. Sweeney, W. Vorster, S. B. Leen, E. Sakurada, P. E. McHugh, and F. P. E. Dunne, “The role of elastic anisotropy, length scale and crystallographic slip in fatigue crack nucleation,” *J. Mech. Phys. Solids*, vol. 61, no. 5, pp. 1224–1240, May 2013.

[273] A. Cottrell, *An introduction to metallurgy*. Universities Press, 1990.